Studies on the Background of the Wide Field Imager aboard the IXO and ATHENA X-Ray Telescopes

TECHNISCHE
UNIVERSITÄT
DARMSTADT

Fachbereich Physik
Institut für Kernphysik
Astrophysik
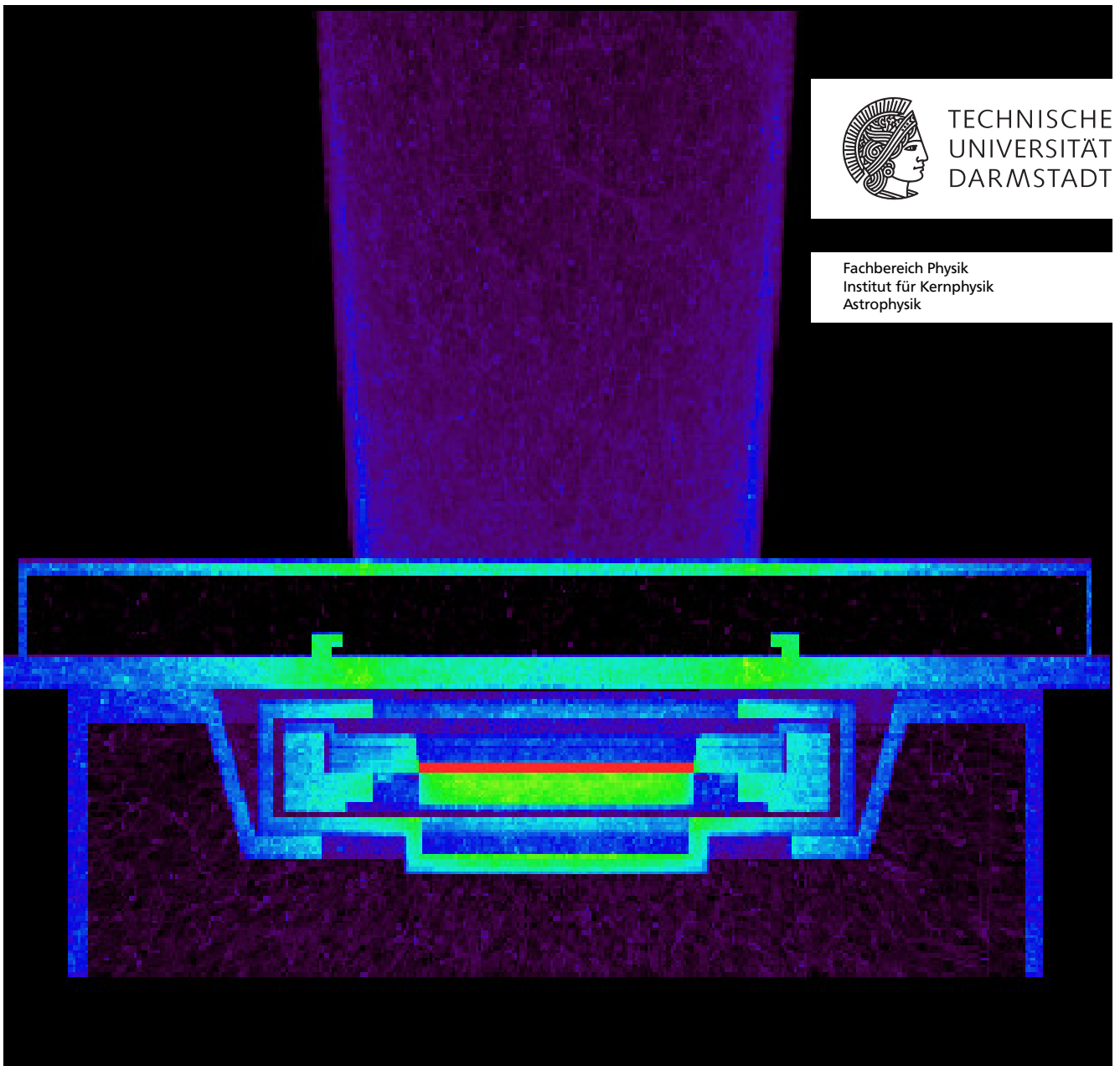
Studies on the Background of the Wide Field Imager aboard the IXO and ATHENA X-Ray Telescopes
Studien zum Hintergrund des Wide Field Imager an Bord der IXO und ATHENA Röntgenteleskope

Genehmigte Dissertation von Steffen Hauf, M.Sc. aus Darmstadt

1. Gutachten: Prof. Dr. Dr. h.c./RUS Dieter H.H. Hoffmann
2. Gutachten: Dr. Markus Kuster

Tag der Einreichung: September 2012
Tag der Prüfung: 04.07.2012

Darmstadt — D 17
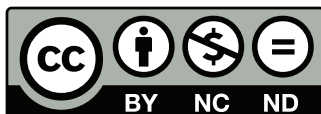
Erklärung zur Dissertation

Hiermit versichere ich, die vorliegende Dissertation ohne Hilfe Dritter nur mit den angegebenen Quellen und Hilfsmitteln angefertigt zu haben. Alle Stellen, die aus Quellen entnommen wurden, sind als solche kenntlich gemacht. Diese Arbeit hat in gleicher oder ähnlicher Form noch keiner Prüfungsbehörde vorgelegen.

Darmstadt, den 18. September 2012

_____

(S. Hauf, M.Sc.)

Zusammenfassung

Das International X-ray Observatory (IXO) war ein von der ESA, NASA und JAXA geplantes, satellitengestütztes Röntgenteleskop und der designierte Nachfolger der erfolgreichen XMM Newton und Chandra Missionen. Ziel war es räumlich, zeitlich und spektral hochaufgelöste Observationen im Energiebereich von 0.1 keV – 40 keV mit hoher Sensitivität durchzuführen. Infolge des durch Budgetkürzungen bedingten Rückzugs der NASA im Jahr 2010 entschied sich die ESA ein kleineres, rein Europäisches Projekt in Form eine L-Klasse Mission weiterzuführen: A Telescope for High ENergy Astrophysics (ATHENA).

Beiden Missionen gemein ist der Wide Field Imager (WFI), ein DePFET basierter Halbleiterdetektor, welcher räumlich hochauflösende ($\leq$ 10 arcsec) bildgebende Observationen mit moderate spektroskopischer ($\Delta E \approx$ 70 eV@1 keV) und hoher Zeitauflösung ($<$ 20μs) im Energiebereich von 0.1 keV – 15 keV ermöglichen würde. Die geplante hohe Sensitivität von $\approx 10^{-17}$ erg cm^{-2} s^{-1} für eine Beobachtungszeit von 100 ks setzt einen maximalen teilcheninduzierten Hintergrund von $\approx 10^{-4}$ cts keV^{-1} cm^{-2} s^{-1} – 10^{-3} cts keV^{-1} cm^{-2} s^{-1} voraus. Eine solche Hintergrundrate ist für den geplanten Orbit am zweiten Lagrange Punkt des Erde-Sonne Systems nur mit einem optimierten Abschirmungskonzept und effizienten Hintergrund-Reduktionsalgorithmen als Teil der Datenprozessierung erreichbar. Die Erforschung und Charakterisierung solcher Reduktionsmöglichkeiten mit Hilfe von Geant4 Monte-Carlo Simulationen ist das Kern-Thema dieser Arbeit.

Nach einer kurzen Einleitung in die Röntgenastronomie und die IXO/ATHENA Missionsparameter wird ein Überblick über das Geant4 Monte-Carlo Tool-kit und die Anforderungen an die Simulationsumgebung gegeben. Im Zuge dessen wird festgestellt, dass die in Geant4 enthaltenen Möglichkeiten zur Simulation von radioaktiven Zerfällen und Langzeitaktivierung für die Domäne der Röntgenastronomie nicht ausreichend sind. Basierend auf einer Analyse der experimentellen Anforderungen und vorhandener Zerfallssimulationen wurde im Rahmen dieser Arbeit deshalb ein neuer radioaktiver Zerfallscode für Geant4 entwickelt. Diese neue Software ist genauer als der existierende Geant4 Zerfallscode, was mit weitreichenden Verfikationstests und einer selbst-konsistenten Validierung mittels Germaniumdetektormessungen überprüft wurde. Im speziellen wurde hierzu ein neuartiges, an die experimentelle Wirklichkeit angelehntes, statistisches Sampling-Verfahren entwickelt, welches die Intensitätsabweichungen von zerfallsbedingter Rönten- und Gammastrahlung um bis zu 50% reduziert. Gleichzeitig werden für die Simulation einzelner Zefälle Geschwindigkeitssteigerungen von 50% und für die Simulation von Zerfallsketten Steigerungen von bis zu 400% erreicht. Dieser neue Code und die zugehörige Langzeitaktivierungssimulation wurden in die IXO/ATHENA Simulationsumgebung integriert. Diese Simulationsumgebung, deren Genauigkeit sowohl mit XMM Newton Hintergrundmessungen, als auch mit Space Shuttle STS-53 CREAM Langzeitaktivierungsdaten überprüft wurde, ermöglicht eine genaue Charakterisierung des IXO/ATHENA Hintergrundes. Basierend auf diesen Studien wurde eine optimierte Graded-Z Abschirmung entwickelt, welche effizient Fluoreszenzstrahlung unterdrückt. Eine weitere Reduktion des Hintergrundes um $>$ 99% auf $(6.42 \pm 2.03) \times 10^{-4}$ cts keV^{-1} cm^{-2} s^{-1} wird durch die im Rahmen dieser Arbeit entwickelten Mustererkennungsalgorithmen erreicht. Mit Hilfe eines elektrischen Feldes, welches Sekundärelektronen, die stärkste Hintergrundkomponente, zu Energien außerhalb des Detektionsbereiches beschleunigt, kann diese Rate zusätzlich um $\approx$ 50% auf $(2.70 \pm 2.67) \times 10^{-4}$ cts keV^{-1} cm^{-2} s^{-1} gesenkt werden. Zu beiden Hintergrundraten muss noch der durch Langzeitaktivierung verursachte verzögerte Hintergrund hinzu gezählt werden. Dieser wurde zu $(0.21 \pm 0.05) \times 10^{-4}$ cts keV^{-1} cm^{-2} s^{-1}, nach einer Missionsdauer von 10 Jahren, abgeschätzt. Die Hintergrundvorhersagen sind somit innerhalb der IXO/ATHENA Toleranzgrenze.

Allgemeinen gilt, dass die im Rahmen dieser Arbeit vorgestellte Hintergrundabschätzung und Optimierung für viele Siliziumpixeldetektor-basierte Anwendungen nützlich sein wird. Von der ebenfalls erfolgten Geant4 Softwareentwicklung dürfte eine noch größere Gruppe von Experimenten profitieren. Sie umfasst Anwendungsmöglichkeiten auf den Gebieten der Niederhintergrund-Detektoren, der Materialforschung, der Reaktor- und Fusionsforschung, des Strahlenschutzes sowie der nuklearen Überwachung.

Abstract

The planned International X-ray Observatory (IXO) was the designated successor to the extremely successful XMM Newton and Chandra X-ray observatories. Aiming to provide high sensitivity, high spatial, spectral and timing resolution observations in the 0.1 keV – 40 keV energy range, the mission would have greatly extended our knowledge of the universe. The international project was canceled due to the pullout of NASA in 2010. Subsequently, ESA pursued an European-only mission: A Telescope for High ENergy Astrophysics (ATHENA).

Both missions foresaw the use of a DePFET-based Wide Field Imager (WFI) for spectroscopic imaging observations in the energy range between 0.1 keV – 15 keV. The WFI would offer a high quantum efficiency, high spatial ($\leq$ 10 arcsec), moderate spectral ($\Delta E \approx$ 70 eV@1 keV) and high timing resolution ($<$ 20μs) for imaging observations. The planned high sensitivity of $\approx$ 10^{-17} erg cm^{-2} s^{-1} for a 100 ks observation translates into a maximum cosmic particle-induced background rate of $\approx$ 10^{-4} cts keV^{-1} cm^{-2} s^{-1} – 10^{-3} cts keV^{-1} cm^{-2} s^{-1}. A rate which at the second Lagrangian point of the Earth-Sun system is only feasible if an optimized shielding concept and efficient background detection and reduction algorithms are employed. The study and optimization of these background reduction concepts, using a Geant4 Monte-Carlo simulation and the accompanying software development, is the core topic of this work.

After an introduction to X-ray astronomy in which the requirements for a next-generation X-ray observatory are discussed and an overview of the IXO and ATHENA missions is given the simulation environment and the Geant4 Monte-Carlo toolkit are introduced. In the course of doing so the requirements for the simulation are defined and it is asserted that the radioactive decay simulation of Geant4 does not provide adequate functionality for an X-ray astronomy application. In particular, it is found that the code is not well verified and validated and that an appropriate means of simulating the cosmic-ray induced delayed background is not provided. As a response to this problem an extensive verification and self-consistent validation effort on radioactive decays in Geant4 was undertaken which has resulted in a new radioactive decay code for Geant4. This software is more accurate and significantly faster than the existing code. It includes a novel statistical sampling approach which appreciates the fact that for most experiments radioactive decays and the resulting radiation are a statistical observable. Furthermore, a self-consistent long-term activation simulation which requires minimal user input is included. The new code was extensively verified with Evaluated Nuclear Structure Data File (ENSDF) data and validated with High Purity Germanium (HPGe) detector measurements.

As a concrete application example this code was included into the IXO/ATHENA simulation environment. Using this environment which was validated with XMM Newton EPIC-pn background measurements and cosmic ray activation measurements from the Space Shuttle STS-53 mission an extensive characterization of the prompt and delayed on-orbit background was performed. These studies resulted in an optimized graded-Z shielding design which is needed for a fluorescence emission free background; flexible pattern detection and rejection algorithms with $>$ 99% rejection efficiency; as well as a novel approach utilizing an electric field to accelerate secondary electrons to energies above the detection limit thereby additionally reducing the background by $\approx$ 50%.

In conclusion, a background estimate of $(6.42 \pm 2.03) \times 10^{-4}$ cts keV^{-1} cm^{-2} s^{-1} has been obtained for the ATHENA WFI. If a 200 kV cm^{-1} accelerating field is used a lower rate of $(2.70 \pm 2.67) \times 10^{-4}$ cts keV^{-1} cm^{-2} s^{-1} can be achieved. The contribution of the delayed background component was estimated at $(0.21 \pm 0.05) \times 10^{-4}$ cts keV^{-1} cm^{-2} s^{-1} after a 10 year mission time. All rates are within the WFI background requirements.

The background studies reported upon in the work are deemed applicable and beneficial for a wide range of silicon pixel detector applications. The code development work which has resulted in a new radioactive decay simulation for Geant is considered useful for an even broader range of experiments including applications in low background detectors, material sciences, radiation safety, nuclear non-proliferation studies, medical physics and homeland security.

Contents

Preface

The background estimates and code developments presented as part of this work were conducted with different versions of the Geant4* Monte-Carlo toolkit (Agostinelli et al., 2003; Allison et al., 2006). If not noted otherwise these were versions `Geant4.9.1-p01` and `Geant4.9.1-p03` for the IXO simulations and `Geant4.9.3-p01` and `Geant4.9.4-p01` for the ATHENA part of this work. If radiation energy or intensity values are given they were taken from the NuDat database (Sonzogni, 2005) if not otherwise noted.

The Geant4 development work was carried out as part of the nano5[†] team, a group of researchers aiming to improve Geant4 in critical areas through the use of modern coding and design practices, verification and validation efforts.

---

*   GEometry And Tracking
†   `http://www.ge.infn.it/geant4/nano5/index.html`

1 Introduction

1.1 A Very Short History of Astronomy

The human eye is only sensitive to optical light, e.g. photon-radiation at wavelengths between 380 nm – 780 nm. Accordingly, if we look at the night sky with the unaided eye what we will see is emission from planetary, galactic and cosmic objects at these wavelengths. This is possible because Earth's atmosphere is largely transparent for optical light as is shown in Figure 1. Due to the fact that other cosmic objects are at great distances from us, an unaided viewer will not be able to resolve details of these objects. Exceptions to this are the Moon and large structures such as galaxies like the Milky Way.
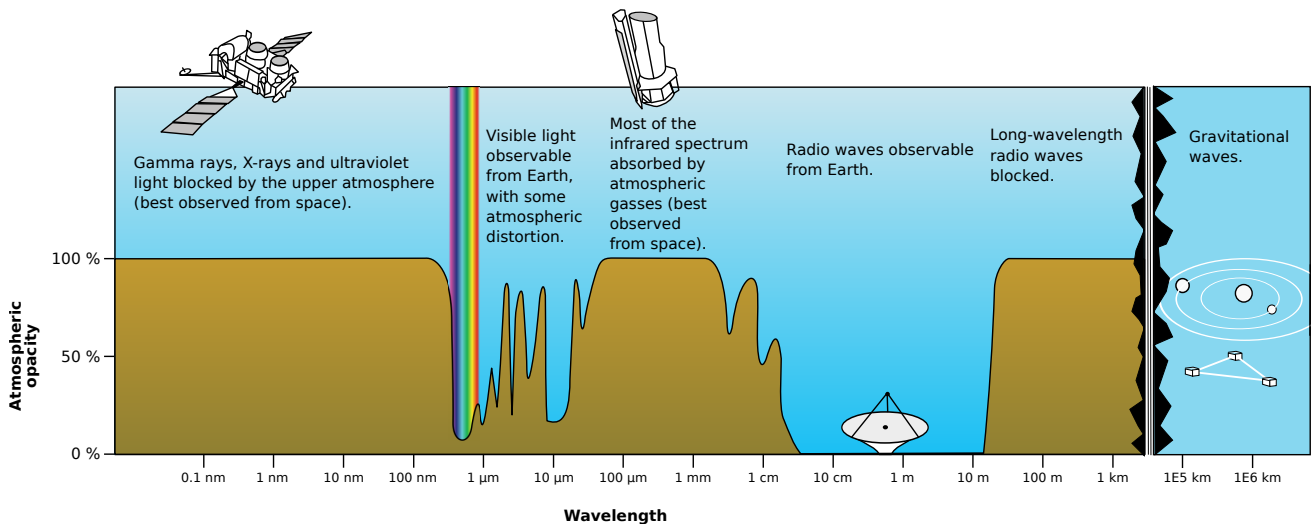
Figure 1: The electromagnetic spectrum in comparison with atmospheric opacity. Original artwork taken from Mysid, 2012 and extended to include gravitational waves.

Only beginning with the construction of optically high quality refracting telescopes by Hans Lippershey, Sacharias Jansen, Jacob Metius, Gallileo Galilei and Christiaan Huygens at the beginning of the 17th century have we obtained the technical capabilities to magnify what we see and thereby explore our universe in more detail. Shortly thereafter reflecting-type telescopes started appearing. Work on these was initiated by Marin Mersenne and continued by James Gregory; leading to the Gregorian telescope design - named after the latter. The reflecting design was further improved by Isaac Newton (Newtonian telescope) and Laurent Cassegrain resulting in the Cassegrain reflectors in common use today.

During the 19th and especially the 20th century reflecting telescopes caught the advantage over refracting designs as long focal lengths and large apertures could be realized in a much more compact way. The resolution power and sensitivity of these telescopes was determined by their mirror diameters. By the end of the 20th century telescopes had reached sizes of over 5 m in diameter. From the 1990s onward, the achievable resolution was further increased by the use of adaptive optics, circumventing the limits imposed by atmospheric refraction and turbulence.

Other parts of the electromagnetic spectrum had become accessible some 100 years earlier. The advent of radio-technology at the beginning of the 20th century allowed the study of the universe at wavelengths other than the optical — radio-astronomy had been born. Nevertheless, large parts of the electromagnetic spectrum were still inaccessible, blocked by the Earth's opaque atmosphere as shown in Figure 1.

It was the beginning of the space age in the 1950s which provided new opportunities for astronomers and astrophysicists. By introduction of the technological means needed to reach the high altitudes needed for an non-attenuated view wavelengths previously unaccessible, became observable. Starting with sounding rockets and balloon experiments scientists had the first X-ray, infrared, UV and gamma-ray

observatories orbiting our planet by the 1970s. Since then space launches have become common place and powerful telescopes orbit the Earth and the Sun. At the same time single ground based observatories are being replaced by extensive arrays of multiple instruments further pushing the resolution and sensitivity limits for optical, radio and high energy gamma-ray observations. Relatively recently neutrino telescopes have become operational (e.g. Achterberg et al., 2006), leaving gravitational waves as one of the last wavelengths currently inaccessible to scientists. Or as Robert C. Bless put it: *"There's no question that astronomers will look back on this period as a golden age; and there's no way it could have happened except by getting above the Earth's atmosphere"*(Broad, 1984).

"Getting above Earth's atmosphere" also marks the beginning of X-ray astronomy, which by now has a long history of successful missions, all of which have greatly expanded our scientific understanding of the universe. The heritage of these observatories heavily influences the scientific requirements and design of next-generation telescopes such as the Advanced Telescope for High ENergy Astrophysics (ATHENA) and the International X-ray Observatory (IXO) which are discussed in this work. Accordingly, a short overview of X-ray astronomy is given in the following section, outlining the mission parameters of ATHENA and IXO in the course of doing so.

1.2 The X-ray Universe and X-ray Astronomy

In the following a short history of X-ray astronomy will be presented. In order to give a better impression of the evolution of the detectors and observatories discussed, a qualitative comparison of spatial and energy resolution capabilities using the example of the Crab nebula is provided in Figure 2.

1.2.1 From Sub-Orbital Flights to Imaging Observatories

Scientific observations of the X-ray universe began in the early 1960s. An X-ray detector on board an Aerobee sounding rocket launched by a team from American Space and Engineering and led by Riccardo Giacconi detected the first cosmic X-ray source: Scorpius X-1; the first X-ray source in the constellation of Scorpius (Figure 3, Giacconi, Gursky, Paolini, and Rossi, 1962). This first detector was a collimated proportional counter, without any spectral or spatial resolution. It could determine the presence and intensity of an X-ray source; positional information could be deduced from the orientation of the spacecraft at the time of observation. Owing to the fact that this was a suborbital flight the observation time was limited to 350 s. Although the detector was quite a crude instrument from a modern point of view the mission proved the existence of cosmic X-ray sources and strongly motivated the development of more sophisticated detectors.

The development of orbital observatories was the logical next step in X-ray astronomy as these would allow for much longer observation times. The first of these satellites was the Uhuru (SAS-A[*]) mission, launched from Kenya in 1970 and named after the Swahili word for *freedom* (Giacconi et al., 1971b). Uhuru was equipped with two sets of proportional counters, sensitive in the energy range from 2 keV – 20 keV. Each of these collimated counters had an effective area of $\approx 0.084\,\mathrm{m}^2$. Complete sky coverage with a sensitivity of $\approx 1\,\mathrm{mCr}^{\dagger}$ was achieved by constantly rotating the complete satellite with a period of $\approx 12\,\mathrm{min}$. This provided a spatial resolution of a few arc-minutes for strong sources and a few tenths of a degree for sources at the sensitivity limit (NASA, 2012a). Over a mission duration of three years more than 300 discrete sources were discovered in the first X-ray all-sky survey (Forman et al., 1978). The discovery of a variability of some sources led e.g. to the determination of the rotational period of neutron stars (Figure 4, Giacconi et al., 1971a). Concurrently, Uhuru X-ray observations were compared with studies at optical wavelengths, leading to the first multi-spectral "pictures" of the universe (Bradt and McClintock, 1983). Finally Uhuru results introduced the Crab Nebula as a common calibration source for future X-ray and gamma-ray missions (Toor and Seward, 1974).

A more sensitive successor of Uhuru, SAS-3, was launched in 1975. During its four year mission it took Uhuru-like proportional counter observations, determining the precise location of 60 X-ray sources.

---

[*]   Small Astronomical Satellite
[†]   1 mCrab, one milli-Crab: $2.4 \times 10^{-11}\,\mathrm{W\,m^{-2}}$ in the energy range from 2 keV – 10 keV
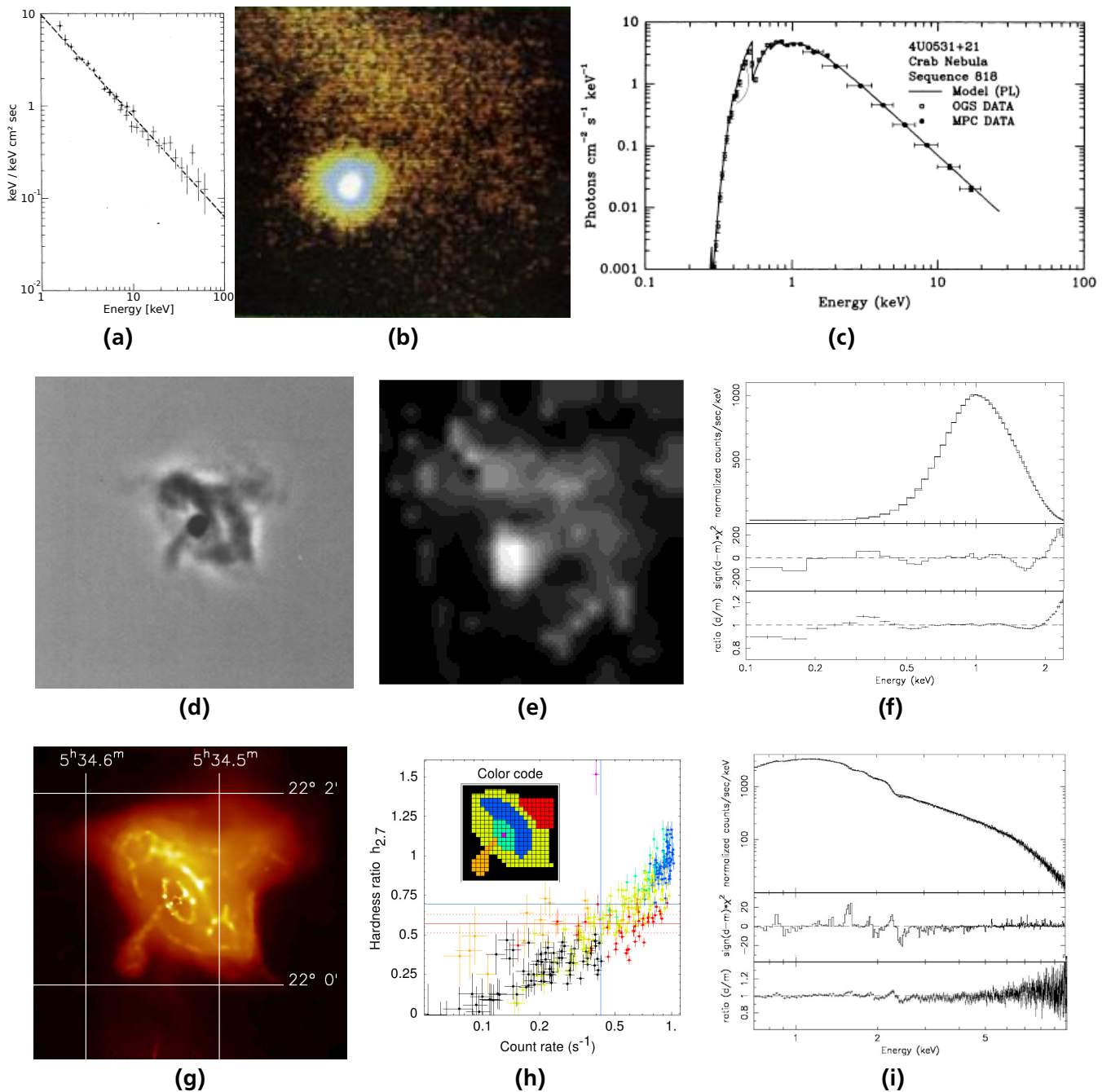
Figure 2: Evolution of the imaging and spectroscopic capabilities of X-ray observatories highlighted with observations of the Crab nebula. The first row shows a multi-detector spectrum obtained with the Uhuru satellite by Toor and Seward, 1974 (a). Image (b) is an Einstein HRI image by Harnden and Seward, 1984 next to an OGS spectrum (c) by Vrtilek et al., 1991. In the second row a RoSAT HRI (d) and the corresponding PSPC image (e) of Crab from Chen, Li, and Wu, 1997 are shown alongside a PSPC spectrum (f, top panel) by Weisskopf et al., 2010. The two lowers panels show the residues in terms χ^2 and ratios when fitting a power law model. In the third row a Chandra image (g) and corresponding position dependent hardness ratio plot (h) by Weisskopf et al., 2000 are shown. The hardness plot highlights the spectral resolution of single pixels. Next to the Chandra images is a Crab spectrum (i) obtained by Weisskopf et al., 2010 from the EPIC-pn camera of XMM Newton.
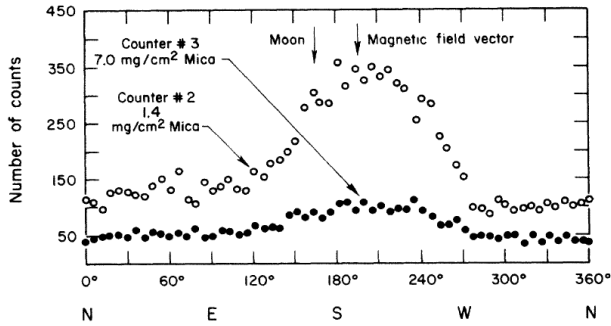
Figure 3: The original observation of Scorpius-X1 by Giacconi, Gursky, Paolini, and Rossi, 1962, marking the discovery of the first cosmic X-ray source. The plot shows the X-ray counts measured at a given orientation of the detector. The counts were accumulated over 350 s.
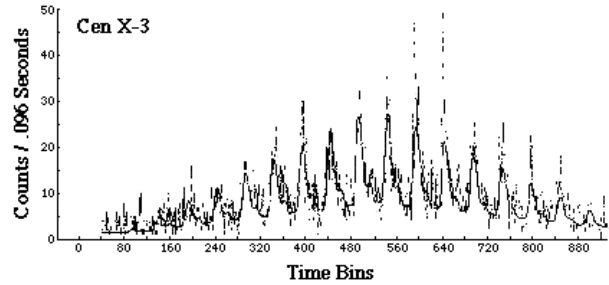
Figure 4: Original light curve resulting from the Uhuru observation of the Centaurus X-3 binary system by Giacconi et al., 1971a. The variability of the intensity over time was used to determine the rotational period of the neutron star in the system. Plot taken from NASA, 2012a.

It also surveyed the soft X-ray background from 0.1 keV – 0.28 keV with a dedicated low energy detector system (Marshall and Clark, 1984; NASA, 2012d).

The 1970s saw additional X-ray missions with proportional counter detectors: the British run Ariel-V mission which established Seyfert I galaxies (Active Galactic Nuclei - AGN) as X-ray emitters and discovered iron line emission from extra-galactic sources (Cooke et al., 1978; Elvis et al., 1978; Mitchell and Culhane, 1977) and the OSO-8[*] observatory which detected black body radiation in the spectrum of X-ray bursts (Swank et al., 1977). The era of proportional counters culminated with the launch of the large HEAO-1[†] observatory by NASA in 1977 with a total of 15 X-ray detectors on board for different energy ranges from 0.25 keV – 10000 keV (NASA, 2012c). Scientific landmarks for this mission included a complete high galactic latitude survey (Piccinotti et al., 1982), measurements of the X-ray background from 0.3 keV – 50 keV (Marshall et al., 1980), as well as the identification of several hundred optical companions for previously identified X-ray sources (Bradt and McClintock, 1983).

While the early observatories were extremely successful at first identifying many bright X-ray sources and generating additional scientific interest through the observation of temporal variabilities as well as line emission, they still had a coarse spatial resolution. It was determined by the collimator opening angle and was at best in the arc-minute range. In order to identify the regions where X-ray emission was produced and to determine the physical processes involved, an order of magnitude improvement in resolution and sensitivity was required. In 1978 these requirements resulted in the Einstein Observatory (HEAO-2), the first fully imaging X-ray telescope launched into space (Giacconi et al., 1979).

The Einstein observatory featured six detectors, four of which could be rotated into the focal plane of a Wolter Type I grazing incidence telescope capable of focusing X-rays in the energy range from 0.1 keV – 4.0 keV. Two of these detectors had imaging capabilities: the Imaging Proportional Counter (IPC) with a field of view (FOV) of 75 arcmin, a spatial resolution of 1 arcmin in the energy range from 0.4 keV – 4.0 keV as well as a small degree of spectral resolution. The second was the High Resolution Imager (HRI) with a FOV of 25 arcmin and a spatial resolution of 2 arcsec in the energy range from 0.1 keV – 3.0 keV. The first mentioned instrument was largely used for surveys (e.g. Maccacaro et al., 1988; Stocke et al., 1991) while the latter could provide high resolution X-ray imaging of X-ray point sources (Harnden and Seward, 1984). It was usually used in conjunction with one of the fixed, non focal

---

[*]   8th Orbiting Solar Observatory
[†]   High Energy Astronomy Observatory

instruments, the Objective Grading Spectrometer (OGS). This combination allowed for high resolution imaging observations while at the same time obtaining spectral information. The two additional focal plane instruments were the Solid State Spectrometer (SSS, $0.5\,\text{keV} - 4.5\,\text{keV}$, $E/\Delta E \approx 3 - 25$) and the Focal Plane Crystal Spectrometer (FPCS, $0.42\,\text{keV} - 2.6\,\text{keV}$, $E/\Delta E \approx 100 - 1000$). Additionally a Monitor Proportional Counter (MPC) with an energy range of $1.5\,\text{keV} - 20.0\,\text{keV}$ was installed co-aligned with the telescope.

The science return from Einstein was enormous and therefore only a few prominent examples will be given here. It includes the first morphological studies of supernova remnants (e.g. Tuohy and Garmire, 1980, Tuohy, Burton, and Clark, 1982), the first studies of X-ray emission from galaxies and galactic clusters which gave insight into cluster evolution (e.g. Forman et al., 1979) as well as studies of X-ray emission from jets in AGN which had previously been observed in the radio regime (Schreier, Gorenstein, and Feigelson, 1982). Additionally, the Einstein observatory can be seen as archetypal for many X-ray telescopes to come: all dedicated X-ray observatories afterwards have used focal plane detectors, either fixed or movable, placed behind grazing incidence optics. This fact motivates a brief introduction of the principle physics governing the optical assembly of such telescopes at this point.

X-ray Optics

X-ray telescopes like Einstein need to focus the incident radiation to achieve their high spatial resolution and sensitivity. Normal refractive or reflective optics will not work for X-rays as they are either transparent in this energy range (refractive designs) or absorb rather than reflect radiation at large incidence angles (reflective designs). A solution to this problem is the use of grazing incidence optics, of which the most common is the *Wolter*-type design (Wolter, 1952). For X-ray observatories Wolter type-I optics are typically used (see Figure 5). To achieve a high reflectivity and large effective areas[*] multiple hyperbolic and parabolic shells are nested into each other. For effective reflection to occur the surface roughness has to be in order of the wavelength, i.e. a few nanometers.
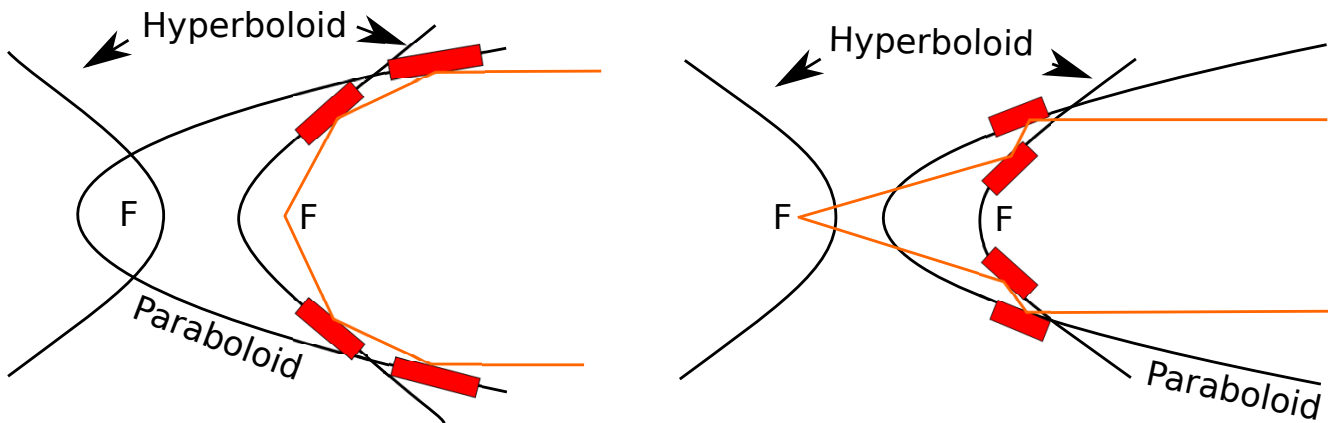
Figure 5: Sketches of the light path (orange) for Wolter Type-I (left) and Type-II (right) telescope designs. The reflective elements are shown in red. X-ray telescopes commonly use a Wolter Type-I design for the optics. A third design (Wolter Type-III) exists but its usage is uncommon for telescopes and accordingly, it is not shown here.

This can be achieved by using highly polished glass or ceramic carrier substrates, grounded to the Wolter geometry, which are then coated with a metal reflection surface. These "more traditional" optics, used e.g. for Einstein, ROSAT (Trümper, 1982) and Chandra (Weisskopf et al., 2002), are generally heavy due to the thick mirror substrates required and as such allow for only a limited number of nested mirrors. This imposes limits on the maximum effective area achievable.

---

[*] The telescope area defined by the aperture times the reflectivity at a given wavelength. It decreases with energy as total reflection occurs at smaller incidence angles.

An alternative approach is the use of thin metal coated foils, which are light weight and can thus be extensively nested. This results in larger collecting areas and thus higher sensitivities. Missions using such systems are e.g. the ASCA (Tanaka, Inoue, and Holt, 1994) and Suzaku (Mitsuda et al., 2007) observatories. The downside of these designs is that current manufacturing processes do not allow to shape the shells into a perfect Wolter-geometry. This currently limits the resolution of such systems to about 1 arcmin. Two additional new approaches exist, slumped glass (Ghigo et al., 2010) and silicon pore optics (Collon et al., 2010), the latter of which is briefly discussed in Section 2.

It can be shown that, regardless of the mirror design, the maximum X-ray energy which can be focused is proportional to the focal length of the optical assembly (Aschenbach, 2009). If the interaction of radiation with matter is described using the complex index of refraction

$$n = 1 - \delta - i \cdot \beta \tag{1}$$

with phase change δ and the absorption coefficient β, the reflectivity of a surface is determined by the reflection coefficients for p and s polarization, given by the Fresnel equations[*] as

$$r_p = \left(\frac{E_r}{E_i}\right)_p = \frac{n^2 \sin\alpha - \sqrt{n^2 - \cos^2\alpha}}{n^2 \sin\alpha + \sqrt{n^2 - \cos^2\alpha}} \tag{2}$$

$$r_s = \left(\frac{E_r}{E_i}\right)_s = \frac{\sin\alpha - \sqrt{n^2 - \cos^2\alpha}}{\sin\alpha + \sqrt{n^2 - \cos^2\alpha}}. \tag{3}$$

In these equations E_r/E_i is the ratio of the amplitudes of reflected and incident electric fields and α is the incidence angle as measured from the reflecting surface. For radiation at short wavelengths the real part of the index of refraction is less than one, which greatly decreases the reflectivity at surface normal incidence angles. Applying Snell's law however, one finds that for $n_r = 1 - \delta < 1$ the refraction angle measured from the normal is greater than 90°. In other words, total reflection occurs for grazing incidence angles of $\alpha \leq \alpha_c$ with

$$\cos\alpha_c = 1 - \delta. \tag{4}$$

A rough estimate of δ can be made if the wavelength λ sufficiently differs from the electron binding energies of the mirror materials, i.e. coupling effects can be neglected,

$$\delta = \frac{r_e}{2\pi} \frac{N_0 \rho}{A} Z \lambda^2 \tag{5}$$

with Avogadro's number N_0, electron radius r_e, atomic number Z, atomic mass A and the mass density ρ. For heavy elements $Z/A \approx 0.5$ which simplifies equations 4 and 5 for $\delta << 1$ to

$$\alpha_c = 5.6\lambda \sqrt{\rho}. \tag{6}$$

Equation 6 yields maximum incidence angles α_c of about one degree. Denser materials such as gold, platinum or iridium will result in larger angles but have a decreased reflectivity between $2\,\text{keV} - 4\,\text{keV}$ due to M-shell absorption. Depending on the desired energy range other materials may thus be more suited. An additional consequence of Equation 6 is that for a given material the radiation energy which

---

[*]   Explanations and details on p- and s-polarization and the Fresnel equations can be found in most physics books, see e.g. Feynman, 1965.

can be focused depends on the focal length of the telescope. A point on a detector at a distance L from the mirror can be illuminated if

$$L \geq d \tan^{-1} \alpha_c \tag{7}$$

where d is the shortest distance between an axis perpendicular to the detector plane and the reflection point on the mirror. Assuming d is limited by mechanical design constraints this yields

$$L \propto \lambda^{-1} \propto E. \tag{8}$$

The necessary focal length L is thus proportional to the energy E of the radiation which is to be focused. Accordingly, X-ray observatories which aim to image the hard X-ray region will need to be have long focal lengths[*].

1.2.2 From Einstein to Chandra and XMM Newton

In the late 1980s and 1990s a multitude of smaller X-ray telescopes, often with dedicated payloads, were launched. It would go beyond the scope of this introduction to present each of these with due detail, which is why for the remainder of this section focus will be laid upon three extremely successful observatories: ROSAT, XMM Newton and Chandra. For more information about other telescopes like ASCA (Tanaka, Inoue, and Holt, 1994), GINGA (Koyama, 1988), BeppoSAX (Boella et al., 1997) and Suzaku (Mitsuda et al., 2007), all of which were successful missions in their own right, further information can easily be found in the literature.

The next "milestone" to be introduced here is the ROSAT observatory (Trümper, 1982), launched in 1990 and operational until 1999. ROSAT featured a Position Sensitive Proportional Counter (PSPC), similar to the one aboard Einstein, but with a field of view of $2°$ and an energy resolution of $\Delta E/E = 0.43$. The spatial resolution was energy dependent and ranged from $\approx$ 1 arcmin – 10 arcmin. The second instrument which could be rotated into the field of view was a High Resolution Imager (HRI) with a 2 arcsec spatial resolution but no spectroscopic capabilities. ROSAT earned its scientific merits with an all sky survey listing over 150,000 new objects (Voges et al., 1999, 2000) — an almost 100-fold increase in known X-ray sources compared to previous observations. Additional prominent research includes detailed morphological studies of supernova remnants and clusters of galaxies as well as the discovery of X-ray emission from comets (Lisse et al., 1996).

The two last observatories to be discussed as part of this introduction are ESA's XMM Newton (Jansen et al., 2001) and NASA's Chandra (Weisskopf et al., 2002) mission. Launched in 1999, they continue to operate to date and still mark the state-of-the-art for X-ray telescopes in many categories. The requirements for a next generation observatory like IXO or ATHENA thus are of direct lineage from these two observatories, which is why they will be discussed in more detail here. An overview of both telescopes' parameters is given in Table 1.

XMM Newton

The European Space Agency's X-ray Multi Mirror Mission (XMM-Newton) provides for a large FOV combined with a good spectral resolution, sensitivity and long uninterrupted exposures as a result of its highly elliptical orbit (apogee $114,00$ km)[†]. It benefits from the large effective area of its three Wolter type-I telescopes which each illuminate a separate detector. This allows for simultaneous observations with all three focal plane instruments. XMM Newton further distinguishes itself from other observatories by including an optical monitor, a dedicated micro-channel-plate pre-amplified CCD [‡] behind a 30 cm telescope. In consequence, simultaneous optical observations of the X-ray regions are possible.

---

[*] There actually have been studies of designs which use two spacecrafts, e.g. SIMBOL-X (Ferrando et al., 2004). Here the focal length is determined by the separation of the two spacecrafts which are in close formation flight.

[†] If no additional sources are given then data for XMM is taken from the XMM User's Handbook (ESA, 2012)

[‡] Charge Coupled Device

XMM Newton's three X-ray telescopes are virtually identical, consisting of 58 coaxially and confocaly nested Wolter type-I mirror shells with grazing incidence angles between 17 armin – 42 armin (Aschenbach et al., 2000). The focal length is 7.5 m and the effective area ranges from 1500 cm^2 at $E < 2$ keV to still above 300 cm^2 at $E = 10$ keV. The point spread function (PSF) varies, depending on the telescope so that each detector has a slightly different spatial resolution but it is generally in the order of 15 arcsec. The FOV of the telescopes is 30 arcmin in diameter and X-rays with energies ranging from 0.1 keV – 10 keV are efficiently focused by the optics. XMM's X-ray detectors consist out of the following:

- Two EPIC[*]-MOS[†] CCD detectors, each positioned behind a dedicated telescope (Turner et al., 2001). The EPIC-MOS cameras consist of seven CCDs each, six of which radially surround the seventh central one. The outer chips are stepped up compared to the center CDD following the field curvature of the focal plane. This allows for better focusing of off-axis sources. The detector assembly covers the complete FOV of 28.4 arcmin, albeit small unusable areas at the individual CCD borders exist, a fact which has to be taken into account for point source observations (they should not lie on these "gaps"). The MOS detectors consist of 600×600, $40\,\mu m^2$ pixels, with one pixel covering 1.1×1.1 arcsec of the FOV. Thus the mirror PSF of 15 arcsec HEW[‡] is sampled by 15 pixels.

  The energy resolution of the MOS-based detectors ranges between 20 eV – 190 eV (FWHM) in the detector energy range from 0.1 keV – 10 keV. The quantum efficiency lies between 0.1 at 0.1 keV up to a maximum of ≈ 0.9 at 3.6 keV and shows distinct absorption edges throughout the energy range. The quantum efficiency and telescope effective area limit the maximum observable X-ray energy to 10 keV for the EPIC-MOS.

  The MOS based detectors offer three observation modes: *full frame* with a time resolution of 2.6 s, *large window* with a time resolution of 0.9 s and *small window* with a time resolution of 0.3 s. Depending on the energy range the EPIC-MOS chips have a sensitivity limit of $\approx 10^{-15} - 10^{-14}$ erg cm^{-2} s^{-1} for a 100 ks observation.

- One EPIC-pn imager which consists of a single silicon wafer with 12 integrated CCD chips (Strüder et al., 2000). Similar to the MOS-chips small gaps between the 200×64 pixel^2 CCDs exist which need to be taken into account for source positioning. The EPIC-pn chips cover the complete field of view, whereas the edges of the rectangular imager are not illuminated by the telescopes circular aperture. Data from these areas may be used for background approximations. With a pixel size of 4.1×4.1 arcsec^2 the PSF of the telescope is slightly over-sampled.

  The EPIC-pn features a high quantum efficiency ranging between $\approx 0.6 - 1$ in the energy range from 0.15 keV – 15.0 keV with a prominent absorption feature near the silicon K-edge at 1.838 keV. The quantum efficiency is much more homogeneous than that of the EPIC-MOS and close to 1 from 0.3 keV – 10 keV. The energy resolution is between ≈ 70 eV – 200 eV. One of the main features of the EPIC-pn chip is its timing resolution which, depending on the observation mode, lies between 73.4 ms (full frame) and 5.7 ms (window mode) for full imaging observations. In timing mode (1D-observation of the source) 0.03 ms can be reached. Even faster is a burst mode without source position information which has a relative timing capability of $7\,\mu s$. The high timing resolution modes suffer from the fact that the on-board data processing limits absolute timing (e.g. with respect to UTC[§]). The absolute timing resolution is at minimum $300\,\mu s - 600\,\mu s$ (Kirsch et al., 2004; Martin-Carrillo et al., 2012).

  Due to the higher quantum efficiency the EPIC-pn also has a slightly higher sensitivity than the MOS chips. A limit of $\approx 0.5 \times 10^{-15} - 0.5 \times 10^{-14}$ erg cm^{-2} s^{-1} is reached for a 100 ks observation.

---

[*]   European Photon Imaging Camera
[†]   Metal Oxide Semiconductor
[‡]   Half Energy Width
[§]   Universal Time Coordinated

Freyberg *et al.* highlighted a problem in the design of the EPIC-pn in (Freyberg et al., 2004; Pfeffermann et al., 2004). The CCDs are situated above the electronics board which has integrated circuits on its backside. These circuits are clearly distinguishable by their fluorescence emission visible in EPIC-pn spectra as it is imaged on the detector at the respective fluorescence energies.

- In addition to the three imaging detectors a Reflecting Grating Spectrometer (RGS) can be used for spectroscopic studies in the energy range from 0.33 keV – 2.5 keV. The RGS is mounted in the light paths of the two telescopes illuminating the EPIC-MOS chips and intercepts about 58% of the light directed towards the EPIC when used. The RGS consists of a linear array of 9 MOS CCDs similar to those of the EPIC. It offers a high spectral resolution of 500 – 1000 across its energy range. This corresponds to an energy resolution of $\Delta E \approx 2$ eV.

An overview of XMM's and Chandra's capabilities in comparison to the future IXO and ATHENA missions is given in Table 1. The mission lifetime of XMM was originally intended at five years and has continuously been extended since. It will reach a definite end in 2018 when the on board consumables have been used.

In summary XMM's large collection area, FOV and spectroscopic capabilities make it an ideal observatory for studying extended sources such as supernova remnants, accretion discs around black holes and AGN[*]. This has led to new insights into the energy budget of the radiation emitted from accretion discs, isotope production in nova remnants and the afterglow of gamma ray bursts as well as the production of detailed spectra of AGN (Schartel, 2008, 2009).

Chandra

NASA's Chandra[†] mission is in many fields an ideal complement to XMM. Similarly launched in 1999 it is active to date. The focus of the Chandra mission is to provide a very high resolution X-ray camera with good spectroscopic capabilities and a high sensitivity. In order to achieve these goals a trade-off concerning mirror effective area had to be made. In contrast to XMM's thinner metal substrate mirrors, Chandra uses highly accurately polished glass as a substrate for the mirror system. Whilst this allows for more accurate replication of an ideal Wolter geometry it is also heavy because the substrate has to be quite thick. This limits the number of nested mirror shells and thus the effective area of the optical assembly to 800 cm^2 at 0.25 keV and 100 cm^2 at 8.0 keV. The focal length is 10 m. On the upside the high grinding and polishing accuracy results in a small PSF of < 0.5 arcsec, a 10-fold higher resolution than e.g. XMM Newton. The field of view diameter is 30 arcmin. This single telescope illuminates two interchangeable X-ray detectors as well as a grating system.

- The Advanced CCD Imaging Spectrometer (ACIS) (Garmire et al., 2003) can acquire high resolution X-ray images while at the same time providing moderate resolution spectroscopic information, similar to XMM's EPIC instruments. The ACIS consists of 10 planar 1024×1024 pixel^2 CCDs. Four of these are arranged in a 2×2 array (ACIS-I) and are solely used for imaging observations. The remaining six are arranged in a 6×1 array (ACIS-S) and can be used either for imaging or for readout of the High Energy Transmission Grating (HETG) or Low Energy Transmission Grating (LETG) systems, both of which will be introduced later. A flexible combination of any six CCDs is possible for a given observation, although the use of all six will increase the thermal background rates and chances of telemetry saturation. Two of the ACIS-S CCDs are back-illuminated, i.e. the sensitive volume is facing the FOV and not obscured by the logic components on the chip.

  The quantum efficiency of the front-illuminated chips is > 30% between 0.7 keV – 11.0 keV and > 80% between 3.0 keV – 6.5 keV. The back-illuminated chips have a higher quantum efficiency in the soft X-ray regime. It is > 30% between 0.4 keV – 11.0 keV and > 80% between

---

[*] Active Galactic Nuclei

[†] The information presented here is taken from (Weisskopf et al., 2002) and the Chandra User's Guide (NASA, 2012b).

0.8 keV – 10.0 keV. With a pixel size of 23.985 μm the ACIS CDDs slightly oversample the telescopes PSF. Frame times are variable between 0.2 s – 10 s; the nominal frame time is 3.2 s. The ACIS instrument offers a sensitivity of 4×10^{-15} ergs cm^{-2} s^{-1} for a 10 ks observation. The spectral resolution is energy and position dependent and in the range of 30 eV – 160 eV for the front-illuminated chips and 110 eV – 230 eV for the back illuminated chips.

- The second Chandra focal plane instrument is the High Resolution Camera (HRC) which is a microchannel plate based imaging detector. Similar to ACIS the instrument actually consists of two separate detectors, an imaging detector (HRC-I) and a second lengthy detector for the Low Energy Transmission Grating readout (HRC-S). The HRC fills the complete field of view provided by the telescope and is sensitive to energies ranging from 0.08 keV – 10.0 keV which is below the ACIS threshold. With a spatial resolution of 0.4 arcsec it slightly over-samples the mirror's PSF. At 9×10^{-16} ergs cm^{-2} s^{-1} for a 100 ks observation it has a similar sensitivity as the ACIS but lacks the spectral resolution ($\Delta E/E \approx 1$ at 1 keV).

  By design the HRC would have a high timing resolution of 16 μs. Regretfully, a wiring error leads to the time information being associated with the next event. If this event is not telemetered the timing information is lost. This error practically limits the timing resolution to the mean time between events or $\approx$ 4 ms. By using only the central component of HRC-S a work-around has been found which reestablishes the full timing resolution for certain observation scenarios.

- As was already mentioned, the two imaging instruments are supplemented by two transmission grading assemblies: the High Energy Transmission Grating and Low Energy Transmission Grating systems. Depending on the imaging instrument in use these either illuminate a CCD or a MCP detector. The HETG consists of two sets of gratings with different periods: the Medium Energy Grating is optimized for the energy range from 0.4 keV – 5.0 keV; the High Energy Grating is optimized for the energy range from 0.8 keV – 10.0 keV. Both provide a high spectral resolving power ranging from 1070 – 65 (HEG) and 970 – 80 (MEG) in their respective energy ranges which corresponds to an energy resolution of 0.4 eV $-$ 77 eV. The HETG can only be used in conjunction with the ACIS instrument.

  In contrast, the Low Energy Transmission Grating is available for both the HRC and ACIS. It allows high resolution spectroscopic measurements in the energy range between 0.07 keV – 0.15 keV and moderate resolution at higher energies up to 10 keV. The resolving power $\Delta E/E$ is greater 1000 at energies between 0.07 $-$ 0.25 keV.

Due to its high spatial resolution the Chandra observatory continues to be an important science driver in black hole and accretion physics, stellar and supernova evolution, evolution of galaxy clusters, dark matter searches as well as AGN and relativistic jet studies (Swartz, Wolk, and Fruscione, 2010). Chandra will reach the end of its life-time in 2014 when it runs out of consumables.

The Path to IXO and ATHENA

With the definitive end of XMM's and Chandra's life cycle approaching within this decade it is only prudent to plan for a follow-up mission, especially when considering the scientific success of these two observatories. In order to better motivate the requirements for a next-generation telescope this introduction concludes with a short overview of the current science objectives in X-ray astronomy and the respective requirements for a next-generation X-ray mission.

		Chandra	XMM Newton	IXO	ATHENA
General	Agencies Mission type Orbit	NASA Great Observatory-Class Highly elliptical	ESA L-Class Highly elliptical	ESA, NASA, JAXA L-Class Second Lagrangian	ESA L-Class Second Lagrangian
Mirrors	Focal length Mirror effective area	$10.0\,\mathrm{m}$ $0.08\,\mathrm{m}^2$ @ $2.5\,\mathrm{keV}$, $0.01\,\mathrm{m}^2$ @ $8\,\mathrm{keV}$	$7.5\,\mathrm{m}$ $0.15\,\mathrm{m}^2$ @ $2\,\mathrm{keV}$, $0.035\,\mathrm{m}^2$ @ $10\,\mathrm{keV}$	$20\,\mathrm{m}$ $2.5\,\mathrm{m}^2$ @ $2\,\mathrm{keV}$, $0.2\,\mathrm{m}^2$ @ $10\,\mathrm{keV}$, $0.015\,\mathrm{m}^2$ @ $30\,\mathrm{keV}$	$11.5\,\mathrm{m}$ $1.2\,\mathrm{m}^2$ @ $1.25\,\mathrm{keV}$, $0.7\,\mathrm{m}^2$ @ $6\,\mathrm{keV}$
	Angular resolution Observatory energy range	$< 0.5\,\mathrm{arcsec}$ $0.08\,\mathrm{keV}$–$10\,\mathrm{keV}$	$15\,\mathrm{arcsec}$ $0.1\,\mathrm{keV}$–$15\,\mathrm{keV}$	$\leq 5\,\mathrm{arcsec}$ $0.1\,\mathrm{keV}$–$40\,\mathrm{keV}$	$\leq 10\,\mathrm{arcsec}$ $0.1\,\mathrm{keV}$–$15\,\mathrm{keV}$
	Max. obs. sensitivity	$\approx 10^{-16}\,\mathrm{erg\,cm^{-2}\,s^{-1}}$	$\approx 10^{-15}\,\mathrm{erg\,cm^{-2}\,s^{-1}}$	$\approx 10^{-17}\,\mathrm{erg\,cm^{-2}\,s^{-1}}$	$\approx 10^{-17}\,\mathrm{erg\,cm^{-2}\,s^{-1}}$
Detectors	Spectroscopy imaging detector	ACIS $0.4\,\mathrm{keV} - 10\,\mathrm{keV}$, any 6 of 10 modules: $1024 \times 1024\,\mathrm{pixel}^2$, $\Delta E = 30\,\mathrm{eV}$@$0.7\,\mathrm{keV}$, FOV: $< 30\,\mathrm{arcmin}$	EPIC-pn $(0.15\,\mathrm{keV} - 15\,\mathrm{keV})$, 12 quad w. $200 \times 64\,\mathrm{pixel}^2$, $\Delta E = 70\,\mathrm{eV}$@$1\,\mathrm{keV}$, FOV: $30\,\mathrm{arcmin}$	WFI $0.1 - 15\,\mathrm{keV}$, $1024 \times 1024\,\mathrm{pixel}^2$, $\Delta E = 70\,\mathrm{eV}$@$1\,\mathrm{keV}$, FOV: $18\,\mathrm{arcmin}$ HXI $6\,\mathrm{keV} - 40\,\mathrm{keV}$, $1024 \times 1024\,\mathrm{pixel}^2$, $\Delta E = 1\,\mathrm{keV}$@$40\,\mathrm{keV}$, FOV: $18\,\mathrm{arcmin}$	WFI $0.1\,\mathrm{keV} - 15\,\mathrm{keV}$, $640 \times 640\,\mathrm{pixel}^2$, $\Delta E = 70\,\mathrm{eV}$@$1\,\mathrm{keV}$, FOV: $25\,\mathrm{arcmin}$
	Spectroscopy detector	HETG & LETG $0.07\,\mathrm{keV} - 5.0\,\mathrm{keV}$, $\Delta E = 0.4\,\mathrm{eV}$ @ $0.07\,\mathrm{keV}$, $\Delta E = 77\,\mathrm{eV}$ @ $5.0\,\mathrm{keV}$, non-imaging	RGS $0.33\,\mathrm{keV} - 1\,\mathrm{keV}$, $\Delta E = 2\,\mathrm{eV}$, non-imaging	XGS $0.3\,\mathrm{keV} - 1\,\mathrm{keV}$, $\Delta E = 0.25\,\mathrm{eV}$, non-imaging	XMS $0.2\,\mathrm{keV} - 6\,\mathrm{keV}$, $\Delta E = 2\,\mathrm{eV}$, FOV: $2\,\mathrm{arcmin}$
	Dedicated imaging detector	HRC $0.08\,\mathrm{keV} - 10\,\mathrm{keV}$, FOV: $30\,\mathrm{arcmin}$	none	none	none
	Relative timing resolution	HRC $dt \leq 16\,\mu s$	EPIC-pn $dt = 73.4\,\mathrm{ms}$ full frame, $7\,\mu s$ burst	HTRS $dt = 10\,\mu s$	WFI $dt = 16\,\mu s$
	X-ray polarimetry	none	none	XPOL	none

In the previous section a short overview of the history of X-ray astronomy was given and major science accomplishments in X-ray astronomy were briefly pointed out. It was shown that X-ray observatories have up to now provided scientists with information about e.g black holes, neutron stars, clusters of galaxies, active galactic nuclei, nucleosynthesis, supernova remnants and acceleration mechanisms therein. In this section current questions in X-ray astronomy, which result from previous studies, will be summarized alongside the resulting mission requirements for a future X-ray observatory. The information presented here is taken from the initial IXO assessment document, the IXO Yellow Book (Barcons et al., 2011), which should be consulted for additional details.

A. Evolution of Galaxies and therein contained Supermassive Black Holes (SMBH)
Task: Acquire a deeper understanding of the growth and evolution of SMBH. This objective can be subdivided into the following tasks:

1. Find young, unobscured supermassive black holes and measure their radiation and spin characteristics. These measurements will require extensive surveys with a large field of view detector which at the same time provides the spatial and spectral resolution needed to study and distinguish accretion features.

2. Study growing SMBH which are already obscured, these include Compton-thick AGN. This objective will require highly sensitive detectors with moderate spatial and high spectral resolution up to hard X-ray energies above 20 keV. Very high spectral resolution is needed to distinguish line emission from AGN.

3. Measure the influence of SMBH on their host galaxies, e.g. star formation rates and gas motions in clusters and galaxies. This will require detectors with high sensitivity capable of studying faint, extended sources with adequate spatial and high spectral resolution.

B. Studies of the Large-Scale Structure of the Universe and the Creation of Elements

1. Find missing baryons in the intergalactic medium by observing absorption spectra against bright background sources. These observations will require detectors with a very high spectral resolution. Spatial resolution is less important as extended sources will be studied.

2. Study gas motions and turbulence in cluster gas. This will give insight on cluster physics and evolution as well as dark matter interacting with the gas. Additionally, the physical processes behind cosmic ray production in clusters can be studied. These studies require detectors with a high spectral resolution capable of resolving the small Doppler shifts resulting from the gas motion. Additionally, observations in the hard X-ray regime are necessary to study radiation emitted from highly relativistic particles.

3. Measure the dark energy density in galaxy clusters by surveying these at different epochs. This will require a detector with a large field of view as well as moderate spatial and high spectral resolution in order to determine gas cluster gas temperatures and distribution.

4. Study the chemical evolution of the universe on a cosmic time scale by observing the abundances in intra cluster gas at different epochs. In order to distinguish the emission lines from a large number of elements a very high spectral resolution is required.

C. Study Matter under Extreme Conditions

1. Study accretion physics and matter influenced by strong gravitational forces. This involves the observation of accretion discs, determining their spin and timing as well as the polarity of the

emitted radiation. An important aspect is to also determine the kinematics of disc outflows and the core regions of the disc, where highly relativistic velocities are reached. Such studies require detectors capable of providing very high timing resolution, high spatial resolution, high spectral resolution as well as information about radiation polarimetry. The energy range to be studied extends into the hard X-ray regime.

2. Determine parameters for the neutron star equation of state. This involves a survey of neutron star mass and radius by use of timing and spectroscopic measurements as well as polarization measurements for highly magnetized neutron stars. Accordingly, detectors suited for these studies must provide very high timing and spectroscopic resolution as well as polarimetric information.

D. The Life Cycle of Matter and Energy in the Universe

1. Study the explosion mechanisms of supernovas by measuring temperatures, velocities and turbulences in the remnants. This will require high precision spectroscopic studies alongside imaging capabilities.

2. Study the nucleosynthesis occurring in supernovas by detecting emission from radioactive elements. Detectors will need to allow for high precision spectroscopic measurements with high sensitivity up to hard X-ray energies in order to observe emission lines from heavier elements.

3. Study cosmic ray acceleration mechanisms in supernova remnants by measuring synchrotron-emission occurring in the presence of fluctuating magnetic fields. These observations should be spatially and spectroscopically resolved and also include polarimetric information.

4. Study the occurrence of molecular, atomic and solid matter in the interstellar medium by measuring the edge energy of bound-free transitions. This task will require detectors with a very high spectral resolution.

5. Study the vicinity of the SMBH at the galactic center by determining its energetics and geometry with a high spatial and spectroscopic resolution detector.

6. Study the characteristics of proto-planetary discs around young stars using high resolution, time resolved spectroscopic measurements.

7. Study the atmospheres of planetary bodies within our own solar system by measuring the emission resulting from particle acceleration in the upper layers. This will require high resolution spectroscopy measurements which include spatial information.

As is apparent from the above list, the science requirements for a next-generation X-ray observatory mandate detectors capable of high timing, high spatial and high spectroscopic resolution while at the same time measuring the polarization of the radiation, favorably over a large field for view. Combining all these requirements into a single detector is currently unfeasible. Accordingly, dedicated detectors for specific tasks will be needed, an approach in use on all current observatories (e.g. gratings for high spectral but no spatial resolution and CCDs for moderate spectral but high spatial resolution). Possible examples for such detectors is discussed in the next chapter, in which the International X-ray Observatory (IXO) and its successor design the Telescope for High ENergy Astrophysics - ATHENA are introduced.
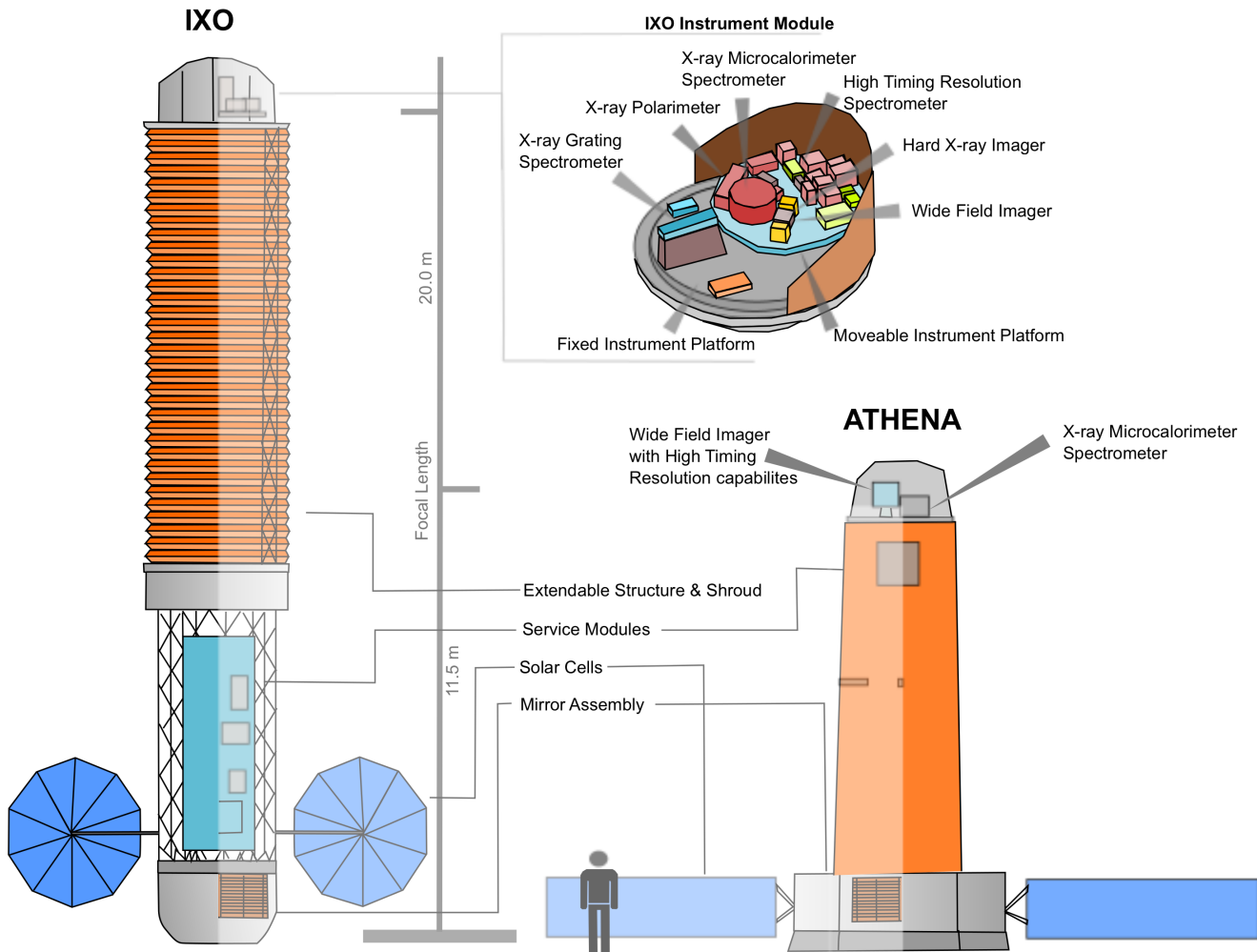
Figure 6: A general overview of the IXO and ATHENA observatories. For IXO the fully extended state and a more detailed view of the instrument module is shown. The IXO mirror assembly would have consisted of a single large mirror while ATHENA has two mirrors, one for each detector, much like XMM Newton. Please note that the figure only shows one possibly configuration for each spacecraft, as so far no final design has been agreed upon.

With the end of the life time of the current state of the art X-ray telescopes approaching in the foreseeable future, ESA and NASA have been planning replacements for XMM Newton and Chandra since the 1990s. These studies originally developed into the very ambitious XEUS* project on the ESA side (Bavdaz et al., 2006) and the Constellation-X program from NASA (Tananbaum et al., 1999). In 2008 the two projects were merged into the International X-ray Observatory (IXO). IXO was to have a very large effective mirror area of $2.5\,\mathrm{m}^2$ at $2\,\mathrm{keV}$ and $0.2\,\mathrm{m}^2$ at $10\,\mathrm{keV}$ which would have lead to order of magnitude improvements in sensitivity in comparison to XMM Newton (mirror area: $0.15\,\mathrm{m}^2$ and $0.035\,\mathrm{m}^2$ at the aforementioned energies) and Chandra (mirror area: $0.044\,\mathrm{m}^2$ and $0.001\,\mathrm{m}^2$ at the aforementioned energies). Simultaneously IXO's focal length of $20\,\mathrm{m}$ (XMM Newton: $7.5\,\mathrm{m}$, Chandra: $10\,\mathrm{m}$) and improved mirror design would have provided a spatial resolution of $< 5\,\mathrm{arcsec}$ in the energy range from

---

*   X-ray Evolving Universe Spectroscopy

0.1 keV – 40 keV for the focal plane detectors. This compares to XMM's energy range of 0.15 keV – 15 keV at a resolution of 5 arcsec and Chandra's energy range of 0.1 keV − 10 keV at a resolution of < 0.5 arcsec. In order to cover the science requirements presented in Section 1.3 six dedicated detectors as well as a grating assembly were planned:

- The X-ray Polarimeter (XPOL) which would be used for polarization measurements in the energy range between 2 keV – 10 keV. Additionally, it would feature a modest field of view of 2.6×2.6 arcmin^2, a medium energy resolution of 1.2 keV at 6 keV and an angular resolution of 5 arcsec. The timing resolution of 5 μs is comparable to the WFI and HXI detectors which will be introduced shortly, but a dead time of 10 μs has to be taken into account between events (Bellazzini et al., 2010). XPOL uses a gaseous pixel detector, which is able to follow the tracks of the photo electrons created when X-rays interact with the gas. The track directions are related to the polarization of the X-ray by a $\cos^2$ law. XPOL would meet the requirements for tasks: C.1, C.2, D.3 and D.5.

- The High Time Resolution Spectrometer (HTRS) which would be non-imaging and cover the 0.3 keV – 15 keV energy range with very high count-rate capabilities (> 10 Crab[*]) and good energy resolution ($\approx$ 150 eV at 6 keV). The timing resolution was planned to be 10 μs (Barret et al., 2010). Design-wise the HTRS consists of an arrangement of 31 silicon drift detectors which are coupled to high speed ASICs[†]. The HTRS would meet requirements C.1, C.2.

- The X-ray imaging Micro-calorimeter Spectrometer which would offer a very high energy resolution of $\Delta E \leq 2.5$ eV in a 2×2 arcmin FOV pixel array and $\Delta E \leq 10.0$ eV for a 5×5 arcmin^2 FOV array both of which in the 0.3 keV – 12 keV energy range. The sensitivity would be limited to 2^{-2} cts keV^{-1} cm^{-2} s^{-1} by the non-X-ray background. The maximum event rate planned is $100,000$ cts s^{-1} array^{-1} (Kelley et al., 2009). To achieve this high energy resolution the calorimeter has to be cooled to 50 mK which would require a large and heavy cryogenic system. Ideally, this system does not need any life time limiting cryogens. For the detector itself two designs were studied, one using transition edge sensor (TES) thermometers, the other using metal-insulator based (MIS) sensor arrays. In the TES design a Mo/Au bilayer is operated in the range of its transition temperature between normal and superconducting behavior; the photon energy is then measured via the temperature dependent resistance change. The MIS design works by measuring the change of the tunneling current through an insulator situated between a metal and a semi-conducting layer. Photons interacting with the insulator affect this current. The XMS would meet requirements A.2, A.3, B.1, B.2, B.4, C.1, C.2, D.1, D.2, D.7.

- The X-ray Grating Spectrometer (XGS) would offer a resolving power > 3000 in the soft energy band from 0.3 keV – 1.0 keV (McEntaffer et al., 2009). It is complementary to the XMS since it has a higher resolution at lower energies. Similar to the spectroscopic instruments used aboard XMM and Chandra the detector relies on gratings, placed along the optical axis of the mirror, to illuminate a set of CCDs. As such the XGS is not mounted on the movable instrument platform in the focal plane. It is designed to meet requirements B.1, D.4, D.6.

- The Hard X-ray Imager (HXI) which would cover a 8 arcmin FOV with a resolution of 5 arcsec in the 10 keV – 40 keV energy range. It would further have good energy resolution of $\Delta E \leq 1$ keV (FWHM) and count rate performance (Nakazawa et al., 2010). The sensitivity would be limited by the non X-ray background to 5×10^{-4} cts keV^{-1} cm^{-2} s^{-1}. The detector consists of 0.5 mm thick silicon strips for lower energies in front of a 0.5 mm – 0.75 mm thick cadmium-tellurium detector array responsible for higher X-ray energies. The HXI would meet requirements A.2, B.2, C.1, D.2, D.3.

---

[*]   For the HTRS this is about $170,000$ cts s^{-1} with 2% dead time.
[†]   Application Specific Integrated Circuits

- The Wide Field Imager which would cover the 0.1 keV – 15 keV energy range with a 18 arcmin FOV, high spatial and good energy resolution and a high sensitivity. The Wide Field Imager would be placed in front of the HXI and thus simultaneous observations with both detectors of the same source would be possible (Stefanescu et al., 2010). As this is the detector of most concern for this work a more detailed description of the WFI will be given in Section 2.1. It would meet requirements A.1, A.2, B.3, C.1, D.3, D.5.

These six detectors together with their supporting components as well as the long focal length needed to focus 40 keV X-rays would have resulted in a rather large space-craft as it is shown in Figure 6 — too large to fit into any existing space launch vehicle fairing. This is why IXO was designed to be extensible. During launch the mirror assembly would be backed against the instrument module. Only in orbit would an extensible truss structure separate the two, enlarging the spacecraft to its full focal length.

With a planned launch date in the 2020–2022 time frame design studies for IXO were progressing rapidly in 2010, when NASA opted out of the project due to budgeting constraints. ESA decided not to entirely cancel the project but place a new call for proposals for a smaller ESA-only L-class mission. This design would become known as ATHENA - A Telescope for High ENergy Astrophysics. For this ESA-only mission the launch mass had to be lowered which meant that both the mirror system's weight and the number of instruments had to be reduced. From the original six instruments only the Wide Field Imager and the X-ray Micro-calorimeter Spectrometer were to remain on-board; not coincidently those two instruments which would have met the most science requirements in the original IXO mission concept. The WFI was modified to preserve most of IXO's high timing resolution capabilities. Both instruments would be illuminated by an individual telescope with a focal length of 11.5 m and an effective area of $1.2\,m^2$ at 1.25 keV and $0.7\,m^2$ at 6 keV. The spatial resolution requirement was relaxed to initially 10 arcsec with a 5 arcsec goal (Bavdaz et al., 2011).

ATHENA's mirror system would be a novelty with respect to its construction method. For the first time it is planned to use silicon pore optics (Collon et al., 2010), a design which was also discussed for IXO alongside the more traditional slumped glass carrier substrate (Ghigo et al., 2010). Silicon pore optics use "off the shelf" commercial grade silicon wafers as mirror substrate. These are ground and polished to a high accuracy, cut in a wedged fashion to form a petal and etched to have ribs on the backside for easier bending. A coating is applied to the front. Each of these processed wafers then constitutes part of a mirror shell. Multiple shells are stacked and bonded together while at the same time being formed into the required Wolter type-I geometry. The result is a compact, largely self-supporting substrate which is lightweight enough to allow for large effective areas but at the same time can be formed to the precision necessary for a high spatial resolution.

Lastly, both the canceled IXO mission and the planned ATHENA mission share an ambitious sensitivity goal of $\approx 10^{-17}\,erg\,cm^{-2}\,s^{-1}$ for a 100 ks observation. While this is already within the limits of Chandra for a 2 Ms observation, IXO/ATHENA offers this sensitivity across the complete field of view and not just a central region while simultaneously reducing the necessary observation time by a factor of 20. This will greatly accelerate larger surveys (Barret et al., 2011; Luo et al., 2008). A comparison of the main parameters discussed in this section for both missions and the current XMM Newton and Chandra observatories is given in Table 1.

2.1 The Wide Field Imager

DePFET Active Pixel Sensors

IXO and ATHENA share the common Wide Field Imager; the detector for which background estimates were made as part of this work. The WFI is an active pixel detector based on Depleted P-Channel Field Effect Transistors - DePFETs (Lechner et al., 2003) - a sketch of which is shown in Figure 7. A DePFET is an active pixel sensor: each pixel is connected to its own amplifier. This limits the signal path length of unamplified signals and thereby greatly reduces electronic noise. At the same time amplified signals are less likely to be significantly distorted by cross-talk from neighboring pixel connections allowing for shorter readout cycles.
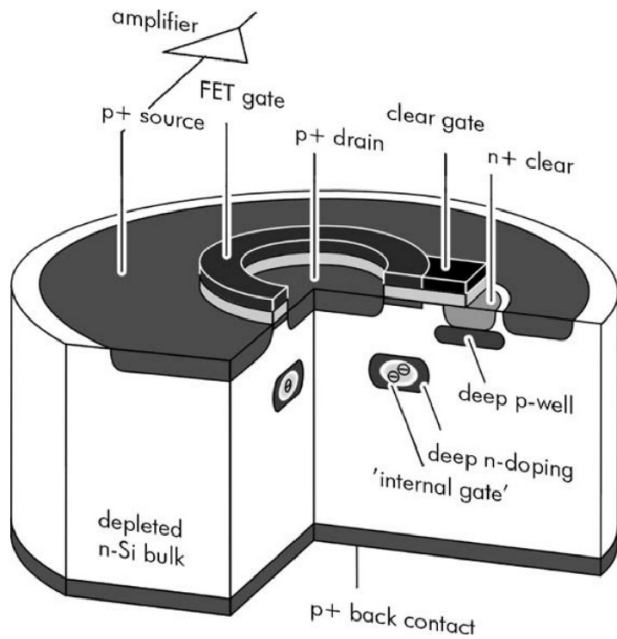
Figure 7: A functional sketch of a single DePFET in circular geometry. Ionizing radiation generates electrons in the depleted bulk which will then drift to the potential minimum of the internal gate. For each electron a positive mirror charge is induced in the FET channel which in turn enhances the transistor current by $\approx 200\,\text{pA}$. The device is reset by applying a positive voltage to the clear contact an the clear gate. Image taken from Lechner et al., 2003.

A DePFET consists of a fully depleted backside illuminated silicon bulk. Depletion is achieved by a backside diode which creates a potential minimum for electrons near the surface. This minimum is additionally confined in the lateral direction to the area beneath the FET-gate by a deep n-doped implantation of similar extend. Electrons produced by ionizing radiation will drift to the potential minimum and induce positive mirror charges in the FET-gate, which in turn increases the transistor current. As such the transistor conductivity is a function of the charge accumulated in the potential minimum which acts as an "internal gate."

The deep n-doping exists independently of the current flowing through the FET channel. This persistent potential minimum allows for charge collection even if the transistor is turned off, greatly reducing the power consumption of the device. During readout the current is switched on via an external readout gate. After readout the electrons which have accumulated at the internal gate are drained by applying a positive voltage to a deep n^+-doped clear contact via the clear gate. This contact is separated from the bulk by a p-doped well during integration and can thus not be reached by the electrons. After the internal gate has been reset a second baseline readout is performed with an empty internal gate. Now the FET-gate current is switched off again and the DePFET is ready for the next integration cycle.

The above functional principle has significant advantages. Because of the near simultaneous charge and baseline measurements as well as the in pixel amplification, sub-electron noise levels and an energy resolution near the Fano-limit* can be achieved. Furthermore, the potential well visible to the electrons can easily be extended by silicon drift detector arrangements consisting of p-n junctions. This allows for very variable pixel sizes without the need to alter the central DePFET design. The backside illumination allows for a seamless sensitive area with an unity fill factor; no signal lines or logic components subdivide the charge collection volume. Instead the individual pixels are defined by the arrangement of the potential wells. The detector is also inherently radiation-hard as the bulk shields the logic structures from radiation and particles entering through the FOV.

By choosing an appropriate thickness for the bulk ($450\,\mu$m in case of the WFI), high quantum efficiencies, even at higher energies, can be achieved (Figure 8). At the low energy end the quantum efficiency is limited by the need for optical and ultra-violet light blocking filters. These ensure that the sensor is not saturated by light from strong optical sources such as AGN, clusters containing bright galaxies or

---

* The best achievable energy resolution as determined by the fluctuation on the number of electrons created as the result of the absorption of a photon.

Figure 8: The expected IXO WFI quantum efficiency with and without optical and UV light blocking filters. The XMM quantum efficiency with a thin blocking filter is shown as a comparison. The positions of the K-absorption edges of the wafer and filter materials are marked. Replot of original taken from Treis et al., 2009b
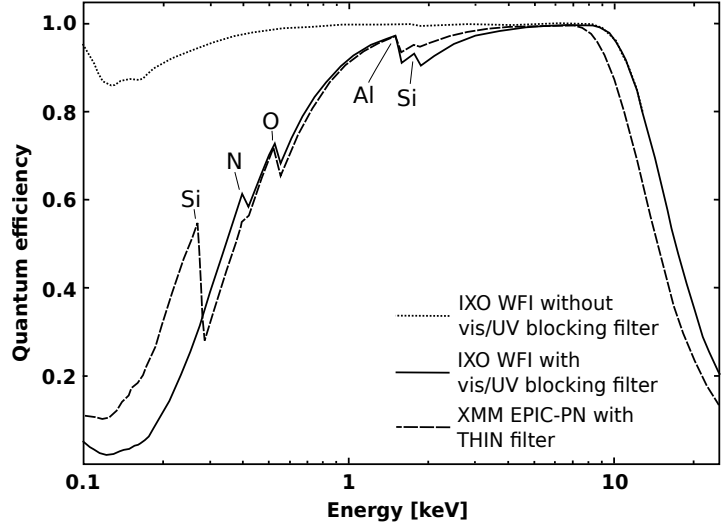
foreground objects. The current WFI design foresees a 70 nm aluminum filter for blocking optical and SiO_x/SiN_x layers for blocking UV light.

Another noteworthy advantage of the WFI design is that due to the single silicon bulk the detector is homogeneously transparent for radiation at higher energies. In case of IXO this fact makes the integration of the Hard X-ray Imager behind the WFI possible without impeding its resolution or sensitivity characteristics.

DePFET Readout

The conductivity change in the DePFET transistor channel is commonly converted to a measurable signal either using a source follower or a drain based current readout. For the source follower design a constant current source is applied to the pixel source contact. Accumulated electrons at the internal gate result in a voltage step proportional to the amount of charges collected. By comparing the voltage level before and after the clearing process the charge number can be recovered using the relation

$$\Delta V_s = \frac{g_q}{g_m} \cdot \Delta Q_s, \tag{9}$$

with the DePFET's external gate's transconductance g_m and the charge transconductance g_q, which is the ratio of the current change in a given pixel δI_{pixel} and the charges accumulated at the internal gate $\delta q_{int.gate}$,

$$g_q = \frac{\delta I_{pixel}}{\delta q_{int.gate}} \tag{10}$$

and the amount of charges removed during the clearing of the internal gate, ΔQ_s. For the alternative drain based readout approach the transistor source and drain contacts are kept at a constant voltage. Charges accumulating at the internal gate will now result in a change in current, which if converted to an output voltage by a current-to-voltage converter with gain g_c results in a voltage change of

$$\Delta V_{out} = g_c \cdot g_q \cdot \Delta Q_s. \tag{11}$$

The advantage of the drain based approach is its speed. All the transistors terminal voltages are fixed and thus the source capacitance does not have to be recharged. Whilst the source follower based readout needs to recharge this capacitance it is more robust to the variations in transistor parameters and operating conditions. More details can be found in Treis et al., 2009b.
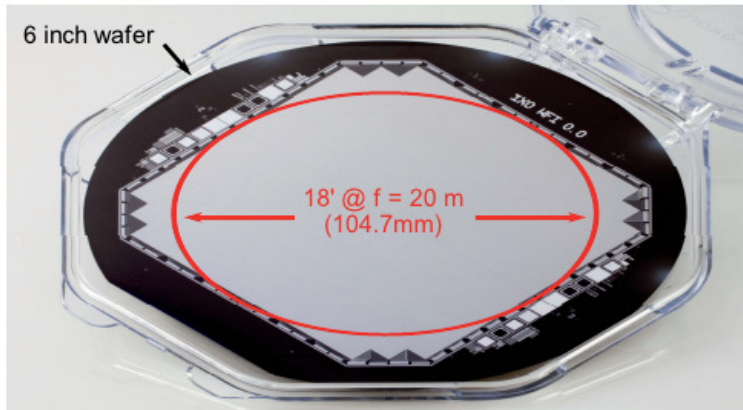
Figure 9: A mechanical model of the WFI wafer as it would be sized for IXO. The fill factor is 100% and the detector is completely monolithic. Image taken from Bellazzini et al., 2010.

For IXO both readout approaches have been studied by using either VELA source follower ASICs (Bombelli et al., 2008) or ASTEROID drain based ASICs (Porro et al., 2007). At the point of switch over to ATHENA no decision had been made as to which is preferable because both designs would have been capable of handling the readout rate of 400 Hz.

The IXO Wide Field Imager

In case of IXO the Wide Field Imager consists of a $1024 \times 1024\,pixel^2$ DePFET matrix; yielding a total of 1 M pixel on a $450\,\mu m$ thick silicon bulk. A mechanical model of this wafer is shown in Figure 9. Each pixel has a side length of $100\,\mu m$ resulting in a total sensitive area of $10 \times 10\,cm^2$ which completely covers the 18 arcmin FOV provided by the telescope. For readout the pixels are divided into two hemispheres of 8 sectors at $128 \times 512\,pixel^2$ each. Within any combination of these sectors the pixels can be read out with using arbitrary selection of rows. This limiting of the read out area to the region of interest allows higher readout rates ($\approx 2.5\,\mu s$ p. row) than would be possible for the full frame (400 Hz). As a result, the readout of bright sources is possible without the risk of pile-up effects (Treis et al., 2009b). Depending on the readout scheme an absolute time resolution between 1 ms (full-frame) and $16\,\mu s$ (window mode) can be reached.

The initial mechanical design of the WFI is shown in Figure 10. The wafer with the sensitive area is supported by a frame made out of Al_2O_3-ceramic. Along the side of the sensitive area the front-end ASICs placed upon the circuit board are visible. The wafer and board are held in place by a set of springs, which press them against the detector frame. Also shown are the flex leads which lead from the ASICs to the back-end electronics. On the non-FOV side a filter frame and filter against radiation reflected and emitted by the HXI is visible. This initial design iteration does not yet include the graded-Z shielding which was studied as part of this work.
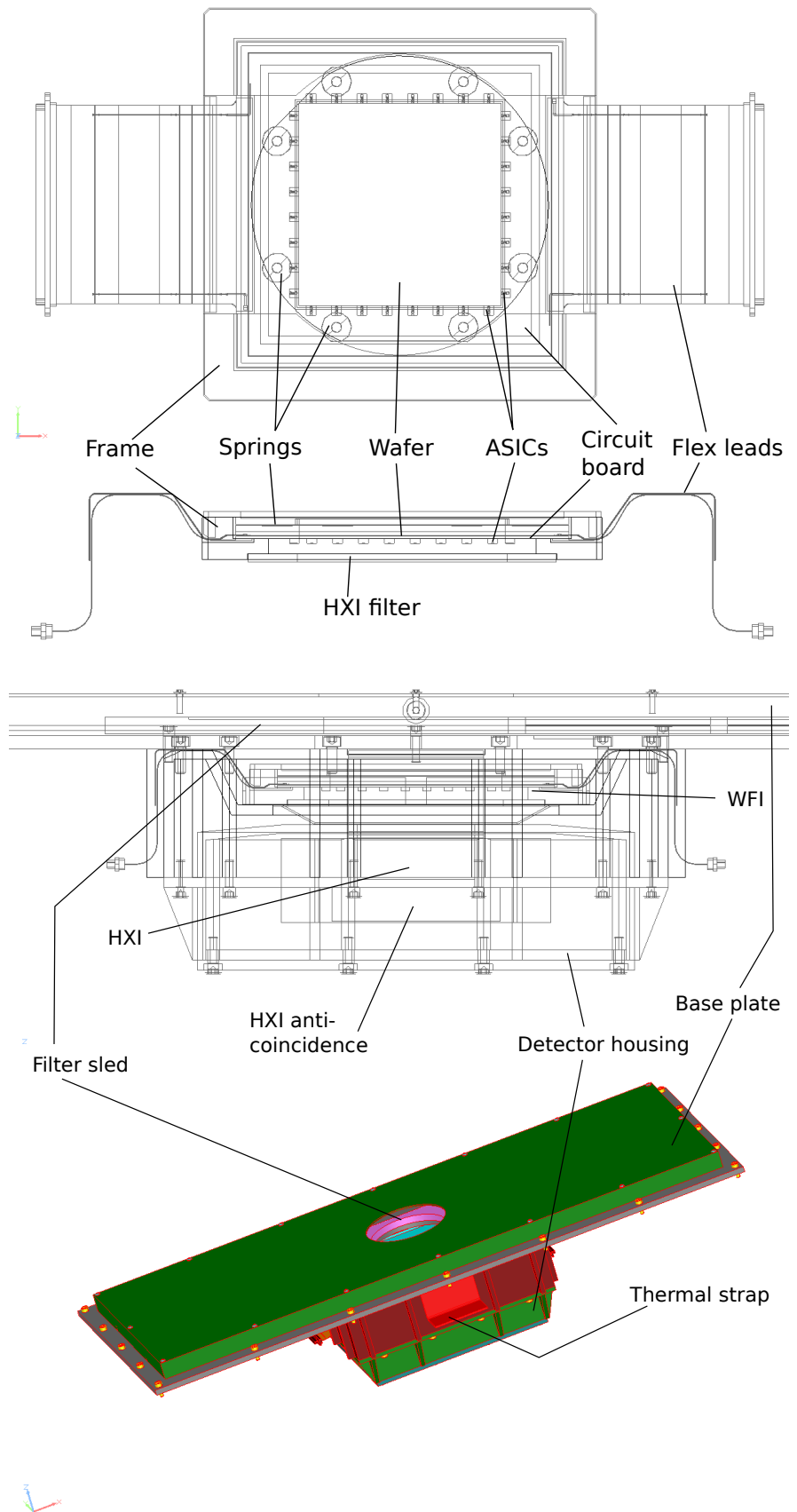
The WFI assembly is housed inside a detector casing mounted on top of a base plate, which is the interface to the movable instrument platform. This casing is mostly made out of aluminium except for steel screws and the non-aluminum filters of the filter-sled. Figure 10 also shows a mass dummy for the Hard X-ray imager made from CdTe and the surrounding BGO[*] anti-coincidence detector (AC). The AC would veto non-FOV events registered on the HXI. Generally, low-Z elements prevail in the WFI part of the detector assembly, while high-Z materials exist in and near the HXI.

The ATHENA Wide Field Imager

The ATHENA Wide-Field Imager is very similar to that of IXO but has been adjusted to accommodate the larger field-of-view and faster timing requirements of ATHENA. By reducing the number of pixels to 640×640 a frame rate of 1562.5 Hz is obtainable. This is nearly 4 times faster than the IXO baseline design. A slower option of 781.25 Hz has also been studied. The FOV was increased from 18 arcmin to

---

[*] Bismuth-Germanium-Oxide, $Bi_4Ge_3O_{12}$

Figure 10: A CAD model of the IXO Wide Field Imager without (top) and with (bottom) the exterior casing, supplied by Max Planck Halbleiterlabor. In the top drawing the detector frame, flex leads, ASICs and the wafer itself are shown. In the bottom drawing the detector case, base plate and the HXI housing as well as the HXI are shown.

Frame   Springs   Wafer   ASICs   Circuit board   Flex leads

HXI filter

WFI

HXI

HXI anti-coincidence

Detector housing

Base plate

Filter sled

Thermal strap

25 arcmin, resulting in a pixel size of $130 \times 130\,\mu m^2$ on a $8 \times 8\,cm^2$ detector. The spatial resolution of the ATHENA WFI would be limited by the mirror system to 10 arcsec with a 5 arcsec goal. The other parameters such as thickness, filter layers and the resulting quantum efficiency are the same as for IXO. Similar readout modes would be used with a maximum windowed read-out rate of $16\,\mu s$.

Because of the shorter focal length of the ATHENA telescopes a dedicated Hard X-ray Imager has become obsolete. Accordingly, the ATHENA WFI does not foresee an interface for another FOV detector situated behind it. Additionally, the absence of the HXI allows for a simpler cooling approach. With no need to keep the sensitive area homogeneously transparent for hard X-ray radiation a cold finger can be placed on the non-FOV side. The cold finger material is not yet decided upon and is a point of study for the simulations presented as part of this work. As a consequence of the above alterations the mechanical design of the detector casing was altered to reflect the size changes and removal of the HXI. Otherwise it remains similar to that of the IXO baseline design.

IXO and ATHENA Orbit

Another point which was to be addressed with IXO and ATHENA is the observation-limiting traverses of Earth's shadow and radiation fields that occur for the highly elliptic Earth-bound orbits of XMM Newton and Chandra. During these periods the observed source is either obscured by the Earth, or the background rises to intolerable levels within the Van-Allen radiation belts. In effect this greatly impedes observation times and results in a far less stable background environment. For IXO and ATHENA this problem is solved by placing the spacecraft in a Lissajous halo orbit around the second Lagrangian point of the Earth-Sun system as it is illustrated in Figure 11. The choice of such an orbit allows for almost continuous observations and guarantees that the field of view will never face the sun. This also results in a thermal environment less prone to variations. Additionally, the radiation background is expected to be more stable, except for strong solar events such as flares and coronal mass ejections but will also be more demanding to suppress, as the telescope is positioned outside Earth's geomagnetic field. The minimization of this on-orbit background, which will be introduced in detail in the following section, is the core topic of this work.
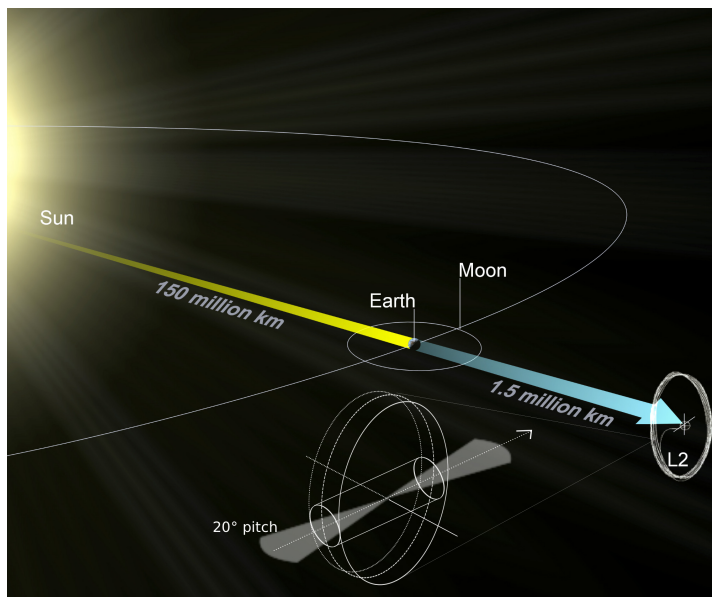

Figure 11: The IXO/ATHENA orbit: both telescopes would be placed in a Lissajous halo orbit around the second Lagrangian of the Earth-Sun system. The orientation would be such that the FOV never faces the sun, allowing for near continuous observations. The background picture was taken from NASA/ESA, 2012, the orbital path is taken from Barcons et al., 2011.

2.2 The Radiation Environment at the Second Lagrangian Point

The previous section concluded with a short description of the advantages of placing an X-ray observatory into an solar-synchronous orbit at the second Lagrangian (L2) point of the Earth-Sun system. These advantages are continuous observation times and a largely stable thermal and background radiation

environment. The benefits come at the price of being outside the Earth's geomagnetic field. This field is a potential background source in it's own right due to the ionized particles trapped therein, but also significantly shields from lower energy solar and cosmic particles. Due to the large numbers of satellites in Earth-bound orbits, the radiation environment within the Earth's magnetic "sphere of influence" has been extensively characterized (e.g. Heinrich, 1994; Heinrich and Spill, 1979; Heirtzler, 2002) and experience concerning its implications on space-based observatories has been acquired. This is not the case for the radiation environment at L2: few spacecrafts have been positioned here (e.g. Herschel & Planck, Pilbratt et al., 2010) and in consequence, experience is scarce. Accordingly, L2 missions such as IXO and ATHENA will need to rely on simulations to estimate their on-orbit particle and radiation background. The accuracy of these estimates will naturally depend on an appropriate input of expected radiation sources as well as a correct simulation of the interaction of the radiation with the detector and observatory. Both these topics are discussed in this section. Generally a spacecraft positioned at L2 will be subjected to the following radiation sources.

- Solar radiation consisting of X-rays, electrons, protons and light nuclei. The radiation intensity and particle flux is modulated proportional to the solar activity. In flare conditions and subsequent coronal mass ejections fluxes and intensities can increase up to 1000-fold in comparison to the quiescent values (e.g. Moses, Droege, Meyer, and Evenson, 1989; Shea and Smart, 1990; Feldman, Doschek, Behring, and Phillips, 1996). These strong variations can generally not be modeled well.

- Extra-solar (cosmic) radiation consisting of X-rays, electrons, protons and light nuclei. Charged particles are modulated anti-proportional to the solar activity and the thereon depending strength of the solar magnetic field. The intensity does not show extreme short-term variations and has successfully been modeled, e.g. with the CREME96 code (Tylka et al., 1997).

An overview of all background components at L2, along with examples of how they affect the detectors and spacecraft is given in Figure 12. Depending on the spacecraft's shielding design, the detectors' energy range and orientation towards the Sun, not all constituents presented in the figure will be of equal importance. Accordingly, an initial estimate of each component's influence should be performed before continuing with more detailed, and more time consuming, simulations. Based upon the properties of DePFET pixel detectors discussed in Section 2.1, electronic noise will not be included into the background model as it is expected to be on a sub-electron level. Field-of-view X-ray background emission will not be modeled either because strictly speaking it should be attributed to the observed source and not the background. This leaves non-FOV X-ray emission as well as solar and galactic particles as background sources. An estimate of their energy dependent potential for influencing the IXO/ATHENA background is the subject for the remainder of this section.

2.2.1 Importance of Background Constituents as Determined by Preparatory Simulations and Measurements

In order to estimate the influence of the cosmic X-ray and particle background on an observatory positioned at L2, knowledge about the energy dependent fluxes of the respective emissions is necessary. Both components have been extensively studied and accordingly, generally accepted spectra exist. Figure 13 shows a compilation of these spectra taken from a selection of measurements and models. It is evident from the figure that the cosmic radiation covers a wide energy range between $\approx 1\,\mathrm{MeV} - 10^{11}\,\mathrm{MeV}$. While more energetic cosmic rays exist they can generally be ruled out to significantly influence the detector background due to their extremely low fluxes. Accordingly, they will not be taken into account in the further proceeding.

In consequence, the spectra shown in the figure were used as input for preparatory simulations of a plane slab approximation of a silicon detector behind a graded-Z shielding which had previously been studied for the SIMBOL-X X-ray observatory (Ferrando et al., 2004). These simulations were then used
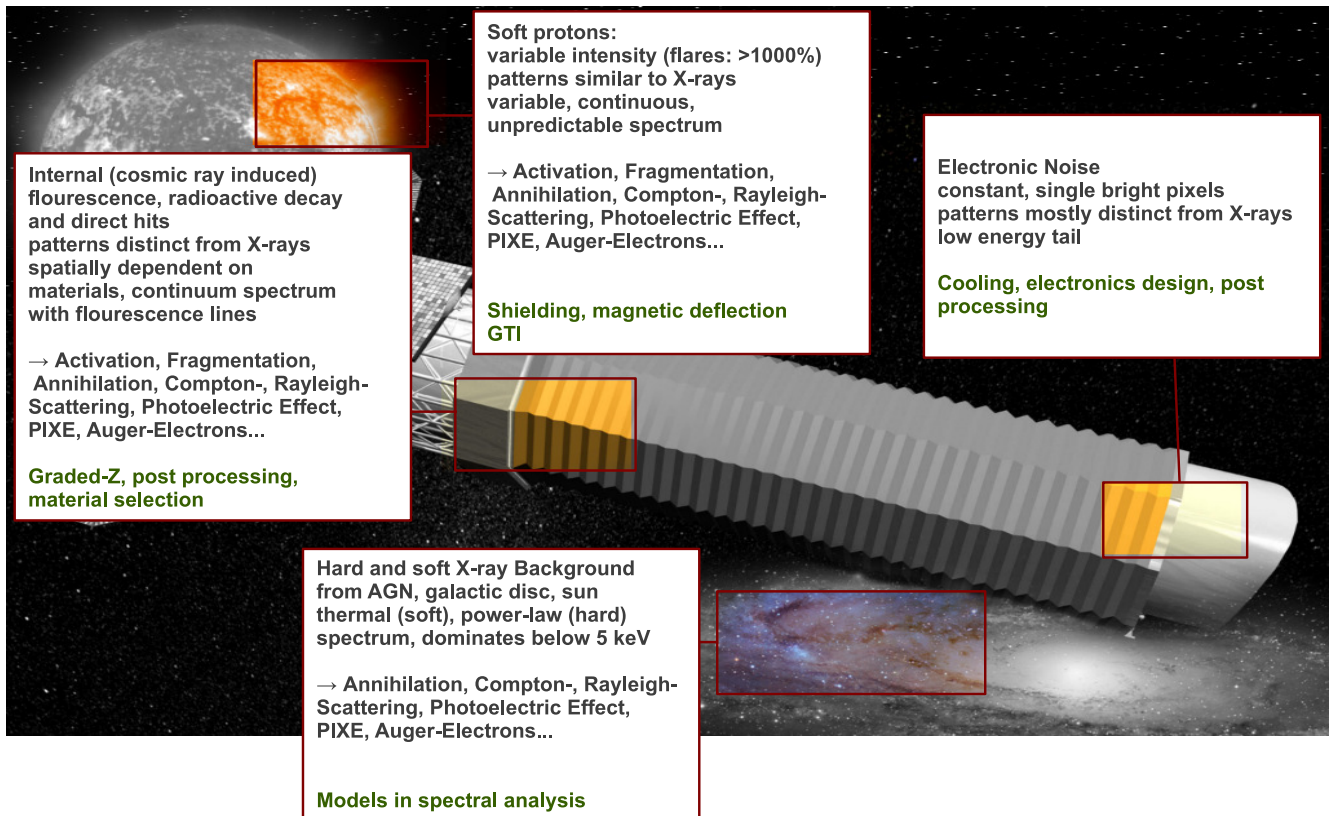
Figure 12: An overview of the potential background sources and observatory like IXO is subjected to at the second Lagrangian point. The background artwork was taken from the NASA website, `www.nasa.gov`.

to estimate the expected influence of the aforementioned sources on the WFI background. A sketch of the slab approximation is shown in Figure 14.

The simulations were run using the Geant4-based MULASSIS code (Lei et al., 2002). Whilst this code does not allow for the detailed geometry and information output necessary for a full scale simulation of the WFI, it has the advantage of an uncomplicated and tested setup. Each simulation consisted of 10^6 mono-energetic gammas or 10^7 protons emitted at discrete energy intervals onto the shielding. The MULASSIS-integrated analysis was then used to output basic quantities such as flux and deposited dose.

X-ray and Gamma-Radiation

As is apparent from Figure 15 X-rays with energies $E < 250\,\text{keV}$ are completely blocked by the graded-Z shielding. The influence of X-rays at higher energies was estimated by emitting photons with a flux of $1\,\text{photon}\,\text{cm}^{-2}\,\text{s}^{-1}\,\text{keV}^{-1}\,\text{sr}^{-1}$ onto a $450\,\mu\text{m}$ thick silicon slab behind the shielding layers (Figure 16). With increasing photon energy the event rate in the WFI energy range initially rises. If the energy is increased beyond $0.5\,\text{MeV}$ the event rate drops again and is already below $2 \times 10^{-5}\text{cts}\,\text{cm}^{-2}\,\text{s}^{-1}\,\text{keV}^{-1}$ at $50\,\text{MeV}$. This is due to the low quantum efficiency of the WFI at these energies.

Using these results the lower flux bound, at which gamma radiation will influence the detector background, was conservatively estimated from the gamma ray flux at the minimum energy for which the shielding was found to be transmissive ($\approx 10^{-2}\,\text{photons}\,\text{keV}^{-1}\text{cm}^{-2}\text{s}^{-1}\text{sr}^{-1}$ at $250\,\text{keV}$), the envisioned background rate ($10^{-4}\,\text{events}\,\text{keV}^{-1}\text{cm}^{-2}\text{s}^{-1}$) and the addition of one order of magnitude margin of error. This calculation yields a maximum flux of $\approx 12\,\text{photons}\,\text{keV}^{-1}\text{cm}^{-2}\text{s}^{-1}\text{sr}^{-1}$ against which the shielding is effective at all energies.

Taking into account that the cosmic photon flux at energies where the shielding is penetrated is below $10^{-2}\,\text{photons}\,\text{cm}^{-2}\,\text{s}^{-1}\,\text{keV}^{-1}\,\text{Sr}^{-1}$ (Figure 13), it is obvious that cosmic X-ray and gamma-radiation will
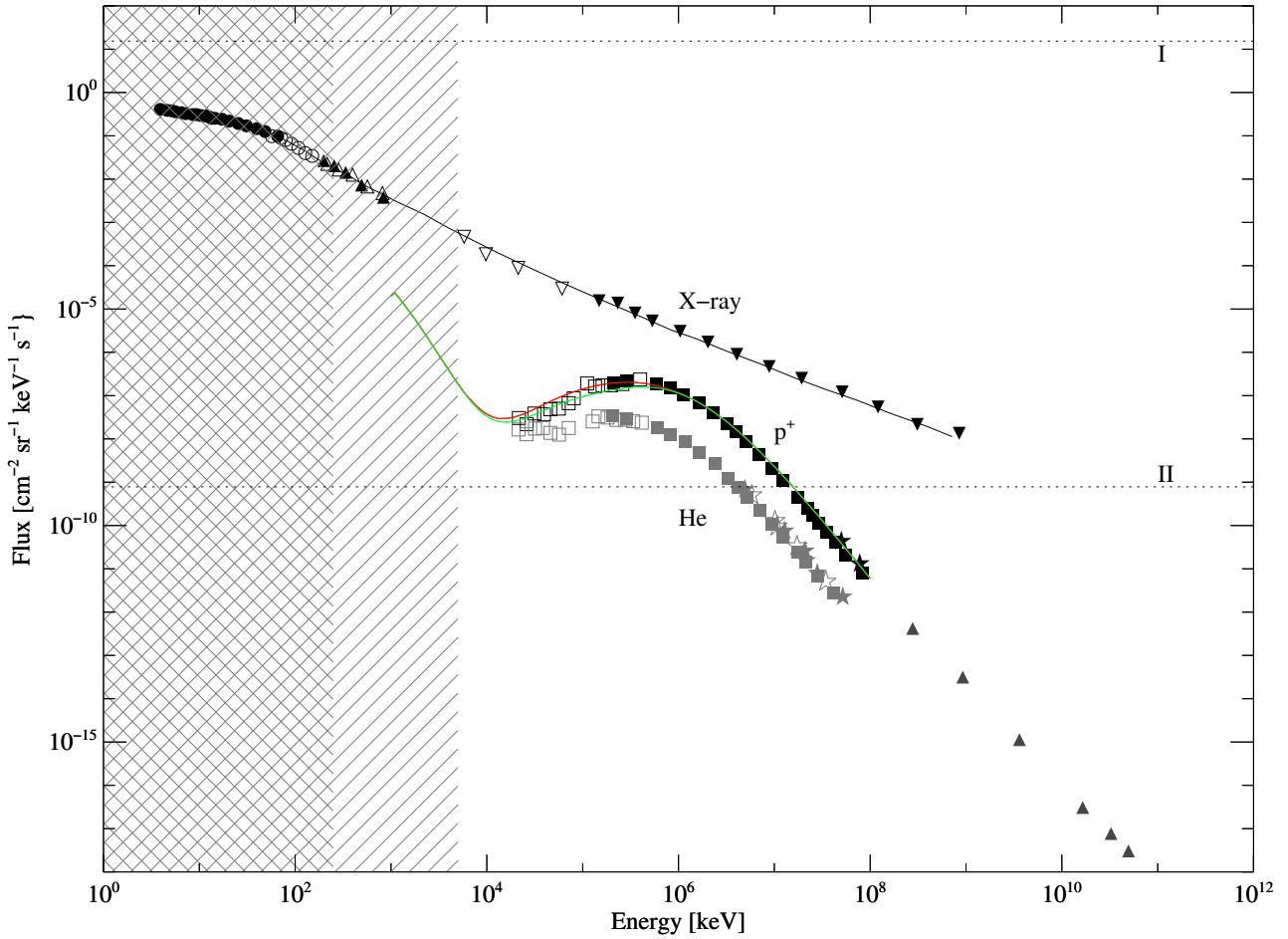
Figure 13: Cosmic background sources relevant to IXO/ATHENA. The cosmic X-ray and gamma-ray as well as the cosmic proton and Helium spectra are shown. Gamma-ray data is taken from Gruber, Matteson, Peterson, and Jung, 1999 and consists of HEAO-A2 HED (open circles), HEAO-A4 LED (filled circles), HEAO-A4 MED (open upright triangles), FUKATA (filled upright triangles), COMPTEL (open inverted triangles) and EGRET (filled inverted triangles) data as well as the fit by Gruber (solid line). The proton data shown is taken from Seo et al., 1991 and shows LEAP (filled squares), IMP8 (open squares), Webber et al. (open stars) and Ryan et Al (filled stars) data. It is supplemented at higher energies by additional LEAP data. The red and green curves are spectra obtained from the CREME 96 model (Tylka et al., 1997) for an 2022 IXO/A-THENA launch and the 1987 solar minimum covered by the measurements shown in the plot. The Helium spectrum is based on the same data sources as proton spectrum and is shown in a lighter shade. The shaded areas show the energy regions in which the planned graded-Z shielding is fully opaque for gamma-radiation (cross-shaded), and protons (diagonally shaded). The dashed lines mark conservative estimates for the gamma (I) and proton (II) fluxes the WFI will be sensitive to (see text for details).

not have a significant impact on the detector background. This assumption is supported by the experience gained from background estimates of the SIMBOL-X mission (Hauf, 2009a,b; Klose, 2007; Tenzer et al., 2006, 2009). In these works the shielding design was modeled in detail and a more realistic detector and satellite mass model were used. The reported fluxes of $\approx 10^{-5}\,\mathrm{keV}^{-1}\mathrm{cm}^{-2}\mathrm{s}^{-1}$ are in agreement with the preparatory MULASSIS-output.
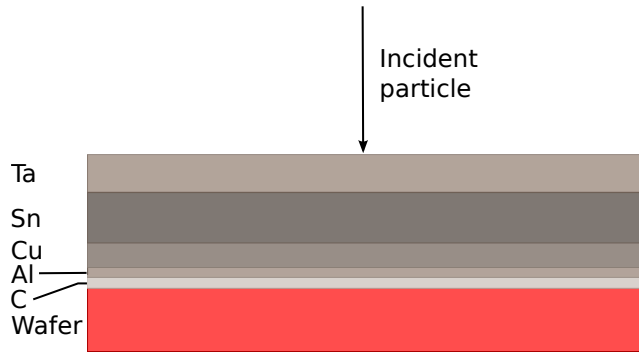
Figure 14: The plane slab approximation used for the preliminary background modeling and the shielding optimization. Note that the layer thicknesses are not shown to scale.
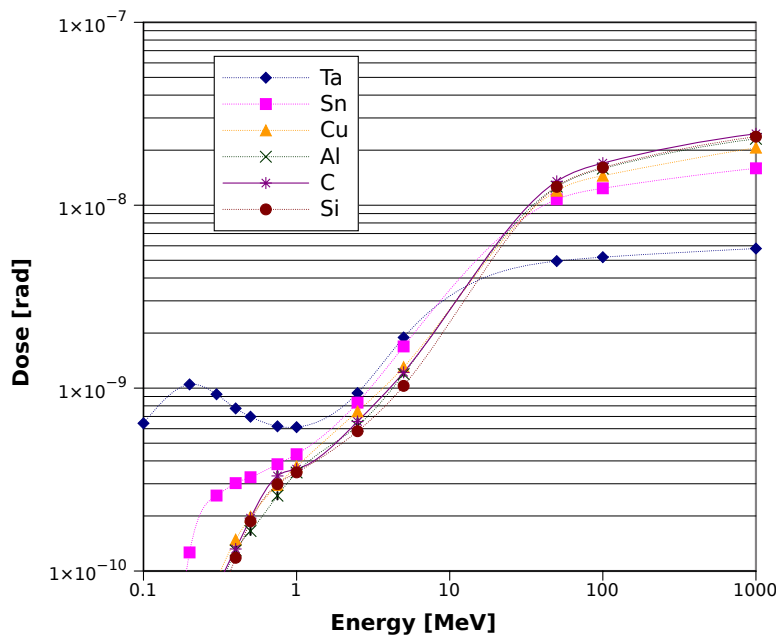

Figure 15: A simulation of the dose deposited by gamma rays in the individual shielding layers and the wafer. The gamma rays were emitted at discrete energies (data points, dotted lines are spline fits as a visual guideline) onto a plane slab approximation of the shielding layers and the silicon wafer of the WFI detector. The uncertainties are suffieciently small as not to be distinguishable in the plot.
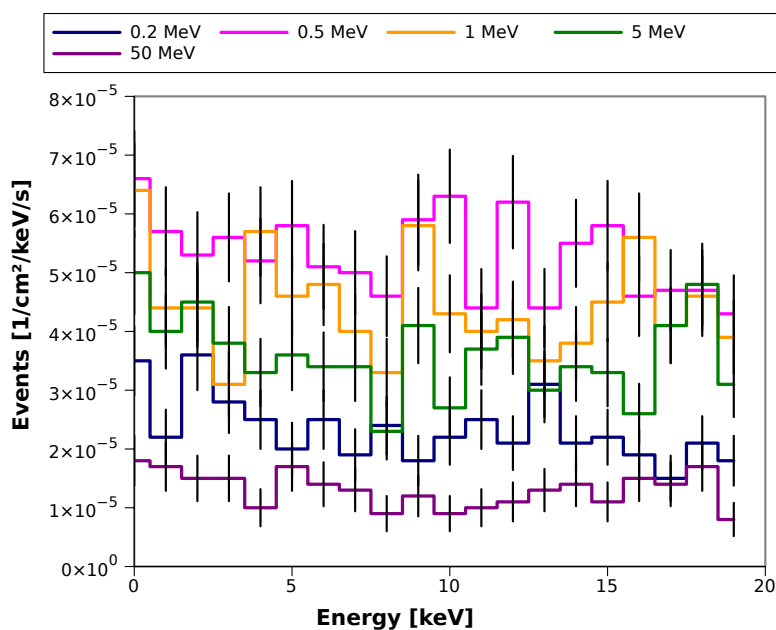

Figure 16: Simulated pulse height spectrum registered in the WFI wafer for gamma rays emitted at discrete energies (distinguished by the colors) onto a plane slab approximation of the shielding layers located in front of the wafer.

Figure 17: Background subtracted decay spectrum of a TNSA proton irradiated grading-Z shielding sample. The spectrum was acquired over a duration of 20 hours starting $\approx$ 10 min after the irradiation. Also shown are a lower limit of the ATHENA sensitivity goal and the background rate estimated from the ATHENA simulation at the time of the measurement. Plot previously published in Neff et al., 2011.
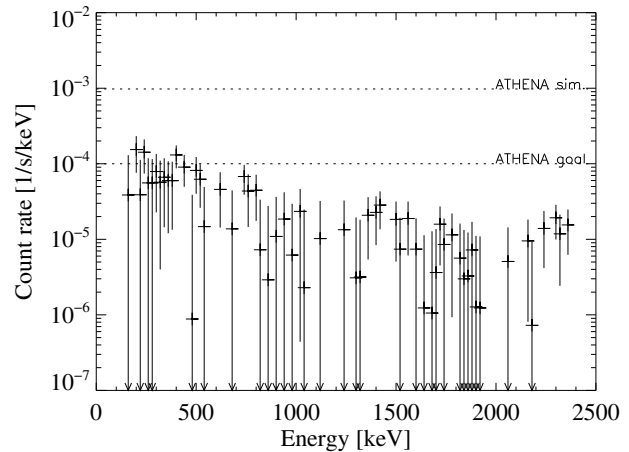
Solar Electrons

The influence of solar electrons, which generally have energies below $E < 10\,\text{keV}$ (Lin, 1985), was estimated in a similar manner, again using a plane shielding approximation. It was found that the baseline shielding is opaque for electrons with $E < 250\,\text{keV}$. The solar electron flux can be approximated using a power law with $dN/dE \approx E^{-\gamma}$ and $\gamma \approx 4$ (Lin, 1985). Taking the fluxes given in Lin, 1985, this yields an electron flux of $\approx 10^{-7}\,\text{keV}^{-1}\text{cm}^{-2}\text{s}^{-1}$ for electrons capable of passing the shielding. Using the same considerations as for the X-ray component this results in an absolute flux estimate of $\approx 10^{-9}\,\text{keV}^{-1}\text{cm}^{-2}\text{s}^{-1}$ for the electrons. This flux is low enough to have insignificant effects on the overall background flux.

Based on the above considerations, the decision was made to exclude both the cosmic X-ray and electron component from the background model. Simulations using the full detector model are very computing time intensive and not justified for these components due to their low impact on the overall background.

Cosmic Ray Protons

The two remaining background components are solar proton and cosmic rays. Because cosmic rays consist to 90% of protons (Gaisser, 1991), additional light nuclei were neglected. Following the same approach as used for the X-ray and electron component, preparatory simulations with a plane slab approximation of the shielding give an initial estimate of the protons' contribution to the background. For protons the flux behind the shielding was estimated at discrete energies between 1 MeV and 50 MeV

The simulations show that the variability of the solar proton flux during the Sun's 11-year cycle can be neglected for the IXO/ATHENA background model. Figure 18 shows the proton flux behind the graded-Z shielding for different proton energies. The shielding blocks protons below 5 MeV. This finding is supported by TNSA* proton irradiation measurements of the graded-Z shielding which were taken at the PHELIX laser of the Gesellschaft für Schwerionenforschung. The experiment, presented in Neff et al., 2011, evaluated the transmittance of protons through the shielding up to a maximum energy of 18 MeV. This was done by using Germanium detectors to measure the spectrum of the gamma radiation emitted from the irradiated samples. A measurement for a complete shielding sample taken from the detector-facing side of the shielding is exemplary shown in Figure 17. If a significant amount of protons were to penetrate the shielding this would result in the activation of inner-lying shielding layers. In consequence, the decay radiation of these activated materials would be visible in the spectrum. This is not the case.

Softer protons thus can only enter through the unshielded FOV. For solar protons this is unlikely because the telescope will be facing away from the Sun during observations. In consequence, the modulation of the *solar* proton flux due to the Sun's 11 year cycle will not have significant impact on the overall detector background.

---

*   Target Normal Sheath Acceleration

The solar cycle however also modulates the *cosmic* ray component, which peaks in the solar activity minimum, when the solar magnetic field, which acts against inbound galactic particles, is at its weakest. For a conservative background estimate this maximum in cosmic ray flux should be assumed, as the IXO/ATHENA mission will span large parts of the solar cycle.

The estimate of the energy up to which cosmic ray protons need to be included in the simulation model takes into account that protons and resulting secondary radiation can be detected by the WFI over the energy range of $0.1 \, \text{keV} - 15 \, \text{keV}$ on a detector area area of $\approx 100 \, \text{cm}^2$. Furthermore, a conservative estimate for the secondary radiation yield (e.g. through PIXE*) of $10 \, \text{particles} \, \text{proton}^{-1}$ was used, based upon Allen, 1939; Borovsky, McComas, and Barraclough, 1988; Dehaes and Dubus, 1993. With an additional one order of magnitude margin of error these considerations yield a minimum detectable flux of $\approx 9 \times 10^{-9} \, \text{protons} \, \text{keV}^{-1} \text{cm}^{-2} \text{s}^{-1} \text{sr}^{-1}$. A comparison with the proton spectrum shown in Figure 13 results in an energy range of $5 \, \text{MeV} - 10^4 \, \text{MeV}$ over which cosmic ray particles might influence the detector background. For a conservative estimate this range was extended by approximately one order of magnitude on both sides.

In consequence, a model of the solar and cosmic proton spectrum from $100 \, \text{keV} - 100 \, \text{GeV}$ is used as the basis of the background simulations. Such a spectrum was generated for the IXO/ATHENA orbit at L2 using the CREME96 code and the tools available on the Vanderbilt University web page (Tylka et al., 1997). This model yields a mean proton flux of $2.318 \, \text{protons} \, \text{cm}^{-2} \text{s}^{-1}$ without giving uncertainties. By calculating a spectrum near the solar minimum an upper limit of the cosmic ray induced background can be given.

2.2.2 Physical Processes Relevant to the Simulations

For a correct estimate of the particle induced IXO/ATHENA background the underlying (Monte-Carlo) simulation has to take into account all relevant physical processes the cosmic ray protons and resulting secondary particles might be subjected to. The energy range over which interactions are of interest extends from the lower bound of the detector sensitivity at $0.1 \, \text{keV}$ to the upper energy bound of the cosmic rays included in the model which is at $100 \, \text{GeV}$. It would go beyond the scope of this work to detail upon the broad variety of electromagnetic and hadronic interactions which are possible in this range. Instead a summary of the most important processes is given in Table 2.

It is apparent from the variety of processes listed in the table that simulation tools which focus on specific physical niches can be ruled out for the estimation of the IXO/ATHENA background. Instead a general-purpose tool-kit is required, which on the one hand can model a great variety of physical processes in a wide energy range and on the other hand is capable of handling complex geometries, such as that of the Wide Field Imager. The Geant4 Monte-Carlo toolkit(Agostinelli et al., 2003; Allison et al., 2006) is such a simulation environment; it will be introduced in more detail in the following chapter.

---

*   Particle Induced X-ray Emission
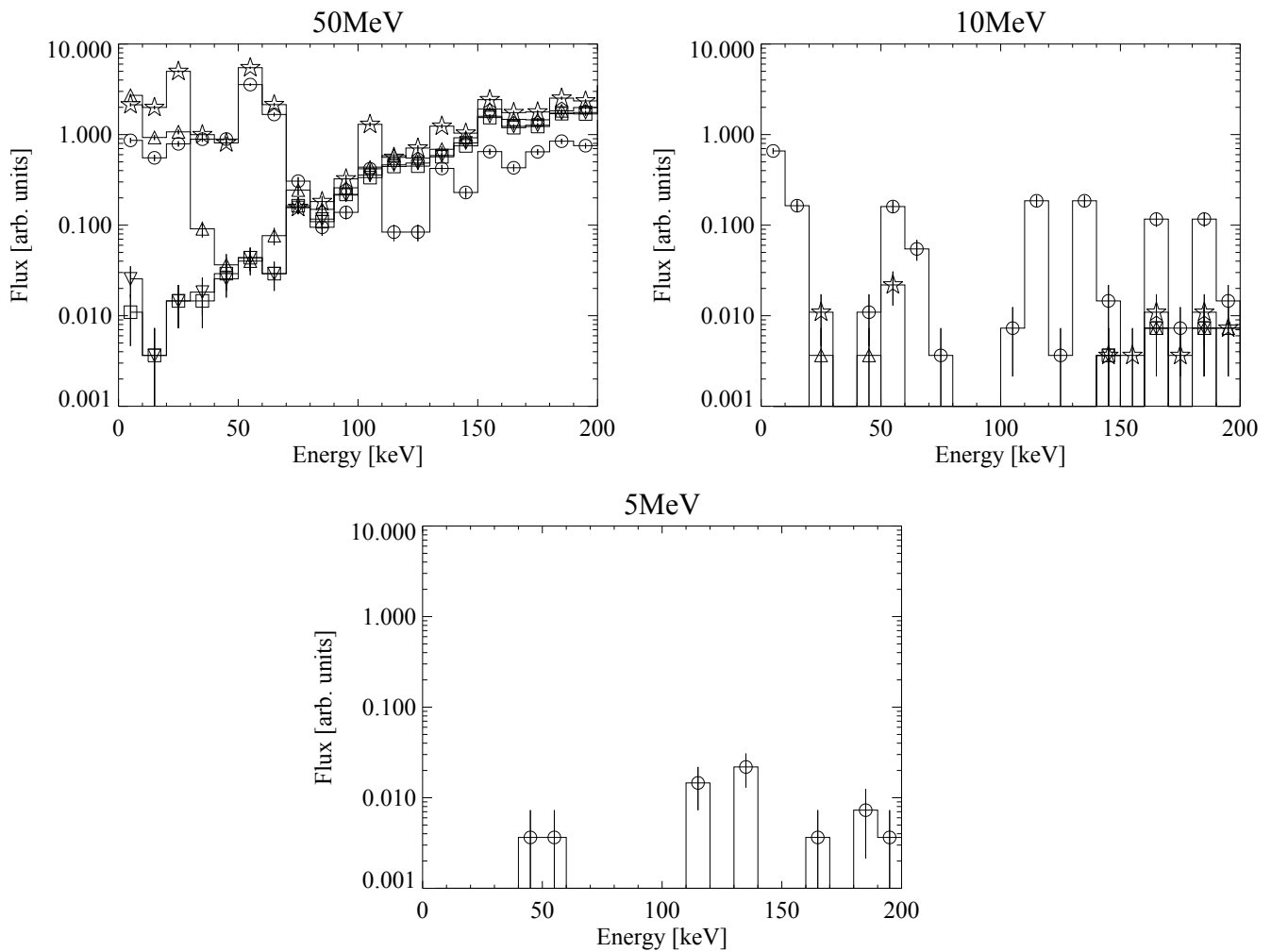
Figure 18: The simulated flux of protons behind each shielding layer which were emitted at discrete energies and are incident on a plane slab approximation of the shielding layers and the silicon wafer of the WFI detector. The layers are marked as follows: tantalum (circles), tin (stars), copper (upright triangles), aluminum (inverse triangles) and carbon (squares). At an energy of 1 MeV no protons penetrated through the tantalum or subsequent layers.

Table 2: A selection of electromagnetic and hadronic processes a space based detector is subjected to in the energy range from $0.1\,\text{keV} - 100\,\text{GeV}$.

Process	Effects	Secondaries	Energy range
Photoelectric effect	Ejection of an electron from material after a photon has been absorbed.	Electron	$\approx 1\,\text{eV} - 1\,\text{MeV}$, depending on material
Compton scattering	A photon scatters inelastically off an unbound electron, the energy and direction of the photon are altered.	-	Upwards of a few keV
Rayleigh scattering	A photon scatters elastically off an atom or molecule, the direction of the photon is altered.	-	Upwards of a few eV
Coulomb scattering	Two charged particles scatter off each other. The Coulomb force dominates the interaction.	-	Upwards of a few keV
Electron-positron pair production	A gamma with an energy above $1022\,\text{keV}$ is converted to an electron–positron pair.	Electrons, Positron	$\geq 1022\,\text{keV}$
Muon pair production	A gamma with sufficient energy is converted to a muon-antimuon pair.	Muon, Anti-Muon pair	$\geq 211\,\text{MeV}$, $\geq 44\,\text{GeV}$ when interacting with atomic electrons.
Ionization	A charged particle traverses a material and looses energy by ionizing atoms or molecules therein.	Electrons/delta-rays	
Bremsstrahlung	A charged particle is accelerated in the Coulomb field of a nucleus resulting in the production of photons.	X-rays, Gamma-rays	Upwards of a few keV
Annihilation	A positron-electron pair annihilates, in effect producing gamma radiation.	Gamma-rays	Gamma radiation at $E > 511\,\text{keV}$
Atomic relaxation	An ionized atom relaxes, X-ray fluorescence and Auger electrons are produced.	X-rays, Electrons	A few keV
PIXE	Production of X-ray fluorescence emission when the ionization occurred by heavier particle.	X-rays	a few keV
Cerenkov radiation	Photon radiation which occurs if a particles exceeds the speed of light within a medium.	X-rays	
Hadronic scattering	Elastic scattering of hadrons off nuclei.		Above a few MeV
Hadronic collisions / Spallation	Hadron-nucleus collisions result in hadronic ejectiles as a result of the collision and the subsequent deexcitation of the stricken nucleus. Cascades may occur and unstable nuclei may result from these collisions.	Protons, neutrons	Above approx. 1 GeV
Fission	Hadronic collisions may result in the production of heavy instable nuclei prone to fission, thermal neutrons may catalyze this process	Lighter nuclei	Energy release: a few 100 MeV
Fermi breakup	Extremely high excited light nuclei break up into lighter fragments.		A few MeV
Neutron capture	One or more neutrons merge into the nucleus in a hadronic collision. The resulting nucleus may be unstable.		A few MeV
Proton capture	One or more protons merge into the nucleus in a hadronic collision. The resulting nucleus may be unstable.		A few MeV
Radioactive decays	Hadronic collisions, p/n-captures, fission and Fermi breakup may result in radioactive nuclei which emit radiation and particles when they decay.		

3 Simulation Environment

As a result of the preparatory simulations presented in Section 2.2, it was found that a simulation of the cosmic ray induced IXO/ATHENA background would require a simulation environment capable of modeling a large number of electromagnetic and hadronic processes in the energy range between 0.1 keV and 100 GeV. The Geant4 Monte-Carlo toolkit (Agostinelli et al., 2003; Allison et al., 2006), developed at CERN*, was identified as a candidate capable of these tasks.

In order to facilitate the comprehension of the terminology used in the remainder of this work, this section will commence with a short technical overview of the Geant4 tool-kit and Monte-Carlo simulations. The actual IXO/ATHENA simulation environment is introduced thereafter.

The Monte Carlo Method

The problem of estimating the particle induced background of a space-born observatory, such as IXO and ATHENA, is archetypal for the need to model increasingly complex and sensitive experiments. These models usually need to account for a variety of physical processes, often in a geometrically complex environment. In such scenarios analytical approaches quickly reach their limits, even if equations are solved numerically.

Monte-Carlo simulations address this problem. Instead of trying to find a single deterministic solution, small, but solvable subproblems are repeatedly and randomly sampled. The result is then determined by a statistical analysis of the outcome of a large number of samples, e.g. the most likely solution is found.

The concrete scenario of tracking a particle through a material can be implemented as a Monte-Carlo simulation by subdividing the particle's path into small steps. For each step changes in the particle's characteristics due to physical interactions are evaluated. To each interaction type, or physical process, a probability of occurrence is attributed, defined by the characteristics of the particle, the material and other external conditions. This probability is compared against a random number[†] and the particle's parameters (e.g. energy, momentum or direction) are altered in accordance with the process which defined the step. The evaluation is repeated for each following step until a position is reached at which the particle's characteristics are either output for analysis or the particle has left the bounds of the simulation.

By evaluating a sufficiently large number of particles the most likely parameter set for a given particle and its interactions can be determined (e.g. its final position and momentum or where energy losses have occurred).

Due to the constant increase in computational performance and the concurrent reduction of the "cost per calculation" over the last decades Monte-Carlo simulations have become feasible for a broad field of applications. This reflects itself in the number of publications per year which reference to Monte-Carlo methods (Figure 19). Today general purpose Monte-Carlo toolkits are capable of modeling almost the entire spectrum of physics at energies ranging from electron volts to TeV and scales from nanometers to cosmic sizes. The Geant4 tool-kit which is used in this work is one example.

A Short Introduction Into Geant4 Design

Geant4 is written in C++ and follows object-orientated programming paradigms. The tool-kit kernel is responsible for the tracking of particles through a user-defined geometry and supplies different, often virtual base classes which can be overwritten to include application specific code. Physical interactions are termed *processes* in Geant4 and are usually represented by distinct classes or modules. They derive from a small number of base classes which provide an interface for the kernel to query a mean free path or cross-section from the process. Based on these cross sections the process which defines the current

---

*   Conseil Européen pour la Recherche Nucléaire

†   Two common comparison scenarios are the comparison with the normalized cumulative probability of competing processes and the comparison with the normalized probability of an exclusive process. In first case one process is definitively picked, in the latter case nothing might be done if the random number does meet the probability criterion.
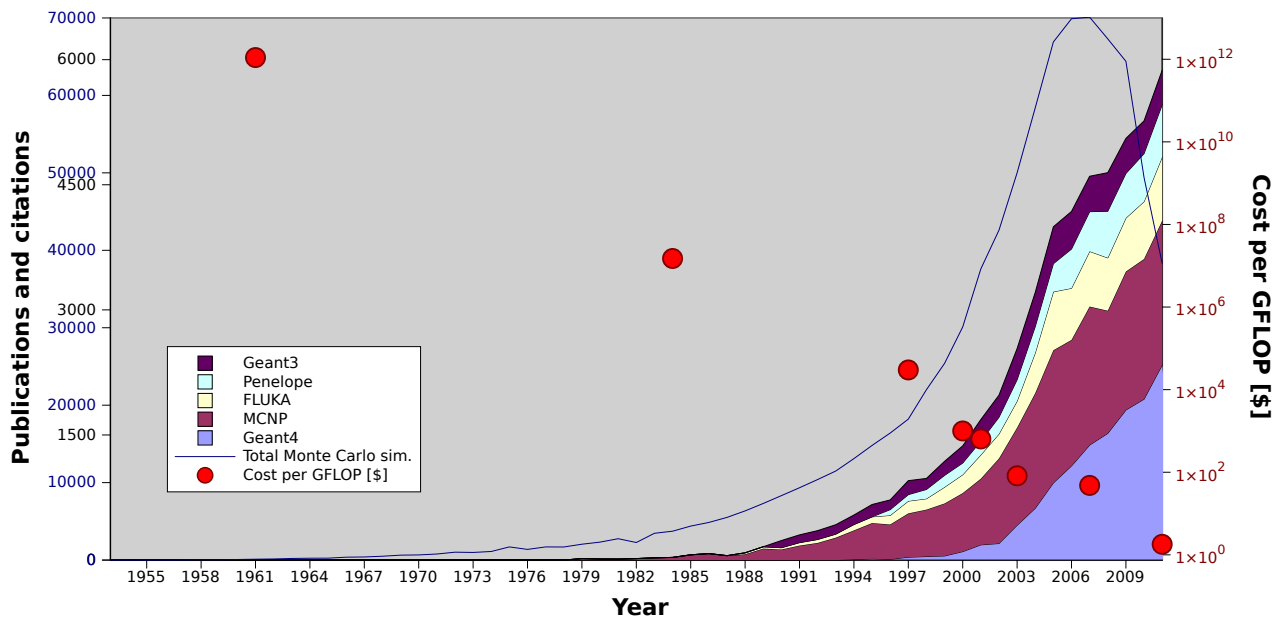
Figure 19: The number of publications referencing Monte-Carlo methods in general (blue line and blue axis) or a specific Monte-Carlo toolkit (colored areas and black axis) compared to the cost in dollars of one Giga Floating Point Operation per second (GFLOPS, red axis). The publication data was evaluated from `scholar.google.com`, the cost per GFLOP was taken from Wikipedia.org, 2012. The drop in total publication rate in the years past 2008 is likely due to delays in the inclusion of publications into Google's database.

tracking step is evaluated by the kernel. Not all processes included in Geant4 have to be registered[*] with the kernel in a given application, instead only those of interest to the problem domain are included as part of a *physics list*.

The geometric setup of an application is handled in a similar fashion. Structures are defined as *volumes* which have materials associated to them. A volume can be freely derived from base classes as long as the kernel can query its extend, orientation, material and similar properties through a standardized interface. Geant4 already provides a number of primitive volume types such as boxes, annuli, spheres, cones and segments thereof. Additionally, extruded solids as well as (closed) polygon mesh surfaces can be defined. In combination with boolean operations on these volumes a detailed detector model can be implemented.

The definition of a volume occurs on three levels: the definition of a *primitive* representing the shape of the volume, the definition of a logical volume which associates a material to this primitive, and the placement of the volume, which reveals it to the tracking and positions it in the simulation's coordinate grid. This three tier system makes reusing of volumes simple. A given shape can be used as the basis of multiple logical volumes with different materials, which in turn can be positioned at different locations.

Geant4 is programmed as a state machine: a simulation or *run* is managed by the `G4RunManager` class, which is responsible for the interaction with the kernel. In the *pre-initialization* state physics lists and the geometry are registered with the run manager, as are user provided implementations of the `G4StackingAction`, `G4EventAction`, `G4SteppingAction`, `G4TrackingAction` and `G4PrimaryGeneratorAction`. Following the initialization and the change to the *Init*, *Idle* and *Geom_closed* states, these actions provide an interface to the simulation at run time; the geometry and physics may not be altered in this state any more.

---

[*]   In this meaning: making the kernel aware of the fact that this process should be used in the simulation. More general: making a program part aware an object which is to be instantiated.

When the run manager switches to the *EventProc* state it commences with event processing. The `G4PrimaryGeneratorAction` class now produces a *primary event* which is associated with user-defined *primary* particles with characteristics such as particle type and momenta. The positional and time information is associated to the particle by a separate `G4PrimaryVertex` object. The new event is then handed to the `G4EventManager` class which converts the primaries to `G4Track` objects. These *tracks* are sent to the `G4StackingManager` class which may be interfaced by the user with `G4StackingAction`. The stack manager has three stacks, *urgent*, *waiting* and *postpone to next event*, which are treated in a first-in, last-out fashion. The top-most track is now popped off the *urgent* stack and passed to the `G4TrackingManager` class, again user-interfaceable by the corresponding "action" class. Despite its name: `G4TrackingManager` does not perform the tracking, instead it brokers between the event manager and the `G4SteppingManager` which is responsible for tracking. The stepping manager evaluates the particle properties before and after each tracking step and determines the physical process defining the step but also if a particle will come to rest due to continuous or discrete energy losses. Afterwards these changes are passed to the associated `G4Track` object and new tracks for the secondaries which were produced during the evaluation of the step may be created. The secondary production is determined by production thresholds set during the initialization phase either as energy or range *cuts*. Below these thresholds no secondaries are created, instead the corresponding energy is deposited in the current volume.

All `G4Track` objects are then pushed onto the stack again and the `G4EventManager` class initiates the processing of the next track. An event is completely processed if the stack is empty. Before the creation of new primary tracks commences, hits which may have registered on *sensitive detectors* and user-defined end-of-event-action code are evaluated.

After a predefined number of events has been processed the run manager invokes the *Quit* state. The kernel is now ready for the next run, with the possibility of changing physical and geometrical parameters in between.

For a more detailed information, especially on the user action classes, the reader should consult the *Geant4 User's Guide: For Application Developers* and the *Geant4 User's Guide: For Tool-Kit Developers*, both of which can be found at Geant4 collaboration, 2012.

3.1 The Simulation Geometry in Geant4

A CAD model of the IXO Wide Field Imager was used as the basis for the simulation geometry. The model was transferred to a set of geometric primitives which were further refined using boolean operations. The materials of each component where defined in close collaboration with the detector design team at Max–Planck Halbleiterlabor. The general approach was to model the detector with a high level of detail in the proximity of the sensitive area and to simplify components positioned at larger distances thereof. Greatest detail was applied to the wafer itself, where the aluminium, silicon-oxide and silicon-nitrate filter layers of the entrance window side were included in a later design iteration (see Figure 20). This approach guarantees that even the influence of small detector-near components on the homogeneity of the background is taken into account by the simulation. At the same time no unnecessary processing time is spent on components which are distant enough that only their overall shape and mass will be of effect.

For the ATHENA simulations the Geant4 model was altered by excluding the HXI and its corresponding anti-coincidence and adjusting the pixel and wafer size to the larger FOV. Furthermore, a cold finger was added to the backside of the wafer, which could be simulated with varying material composition. Additional small changes included reducing the number of ASICs from 8 to 6 per sensitive area edge and the exclusion of the thermal strap which had become obsolete due to the cold finger. A comparison of the CAD model and the two Geant4 implementations is shown in Figure 21. It is supplemented by a rendering of the geometry shown in Figure 22.

Both for IXO and ATHENA the sensitive area is represented in a fully pixelized fashion, i.e. charge collection is modeled separately for each pixel. The individual pixels are associated with a *sensitive*
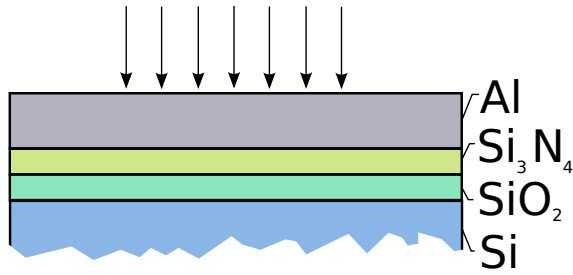
Figure 20: A sketch of the Wide Field Imager entrance window showing the optical and UV-filter layers with the arrows marking the FOV-side. The layer thicknesses are in the order of a few 10 nm (the exact thickness was obtained from Max–Planck Halbleiterlabor by private communication).

detector which keeps track of hits. Details on the data aggregated for each registered event are given in Section 3.4.

In addition to the Wide Field Imager very simplified models of the X-ray Micro-calorimeter Spectrometer (XMS), movable instrument platform, fixed instrument platform and sun shield were implemented in the simulation. The usage of these models was designed to be optional with the purpose of estimating the influence of these components on the background flux and homogeneity. A rendering of this simplified model is shown in Figure 23.
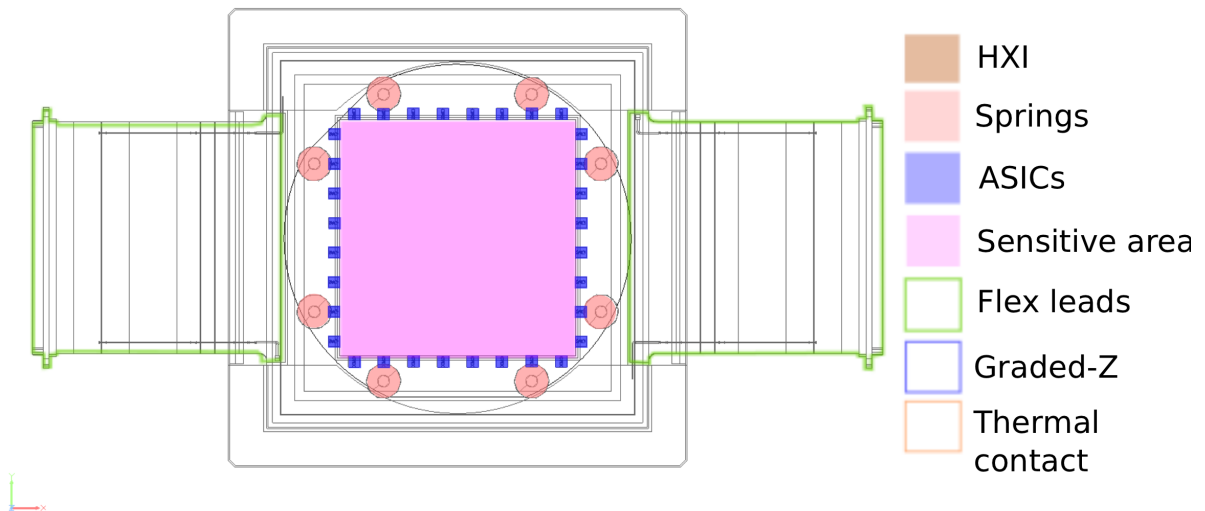
The Graded-Z Shield

An integral part of the simulation geometry is the addition of a graded-Z shielding, which was not foreseen in the original IXO design. The baseline design of this shielding is derived from previous work carried out for the SIMBOL-X X-ray observatory (Hauf, 2009a,b; Klose, 2007; Tenzer et al., 2006, 2009) and is shown in Table 3. The shielding is used to effectively suppress fluorescence emission from detector and satellite components in proximity of the sensitive area. This is accomplished by a layered design in which the atomic number of the individual layer materials decreases towards the detector. The dense, high-Z materials in the outer layers are effective in suppressing X-ray and gamma emission, solar electrons as well as soft protons. Due to the ionization of the material resulting from its interaction with these particles the shielding material will emit fluorescence emission. Subsequent layers are adjusted in thickness to absorb this fluorescence emission which again leads to ionization. With the decreasing atomic number of each layer the fluorescence emission line energies are consecutively shifted to lower energies. Ideally, the last layer is of such low atomic number that it emits radiation outside the detector's energy range. In consequence, a properly optimized graded-Z shield effectively eliminates line emissions. These are present in the spectra of previous X-ray telescopes such as XMM Newton (Strüder et al., 2003), Suzaku (Mitsuda et al., 2007) and Chandra (Hickox and Markevitch, 2006) and may pose a problem in data analysis. This is why an optimization of the IXO/ATHENA shielding is performed as part of this work.

In addition to the passive graded-Z shielding the simulation geometry foresees the definition of two variants of an electric field where the shielding layers act as anodes and cathodes. A sketch of the possible field implementations is shown in Figure 26. More details on this approach will be given in Chapter 7.7.

3.2 Generation of Primaries and Corresponding Result Normalization

The primary particles for the IXO/ATHENA background simulation are cosmic ray protons. Their energy spectrum, produced with the CREME96 model, has already been discussed in Section 2.2. This spectrum is read into the simulation by a parser implemented as part of the `G4PrimaryGeneratorAction` class. This parser fills an energy-flux distribution which is passed to the General Particle Source (GPS, Ferguson, C, 2000) of Geant4. The primary particles are then emitted at a maximum opening angle of $\alpha = 0.0175$ rad from the inward facing surface of a sphere with a radius of $R = 50$ m. The intersections of emission cones result in a second virtual sphere which tightly encloses the simulation geometry and has the radius $r = R \tan \alpha$. For a detector situated within this second sphere it seems as if it isotropically receives radiation from a 4π solid angle. A sketch of the approach is supplied in Figure 24.

Original CAD

HXI
Springs
ASICs
Sensitive area
Flex leads
Graded-Z
Thermal contact

Geant4 IXO
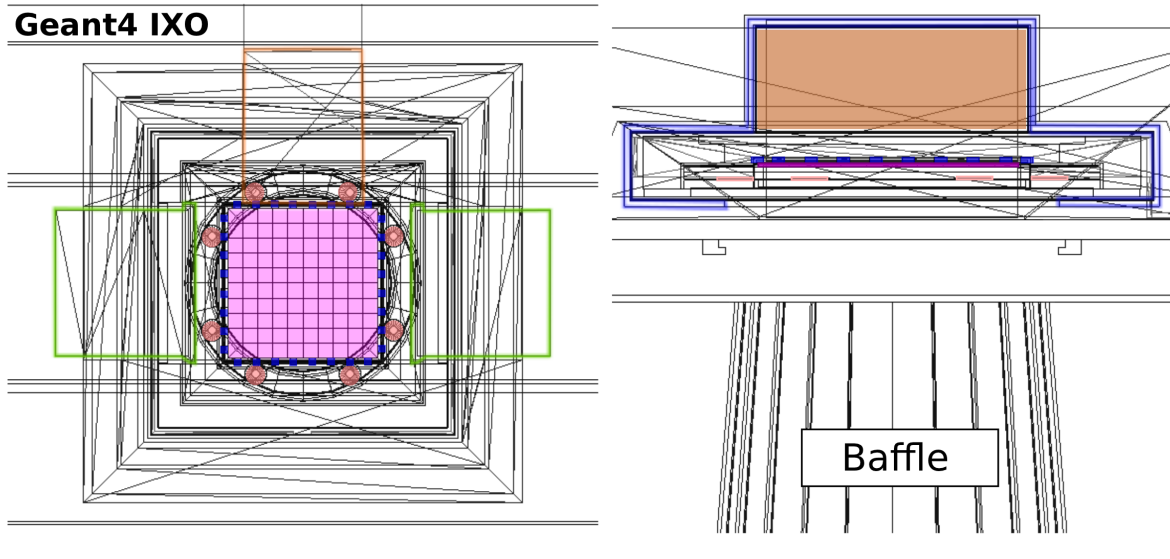
Baffle
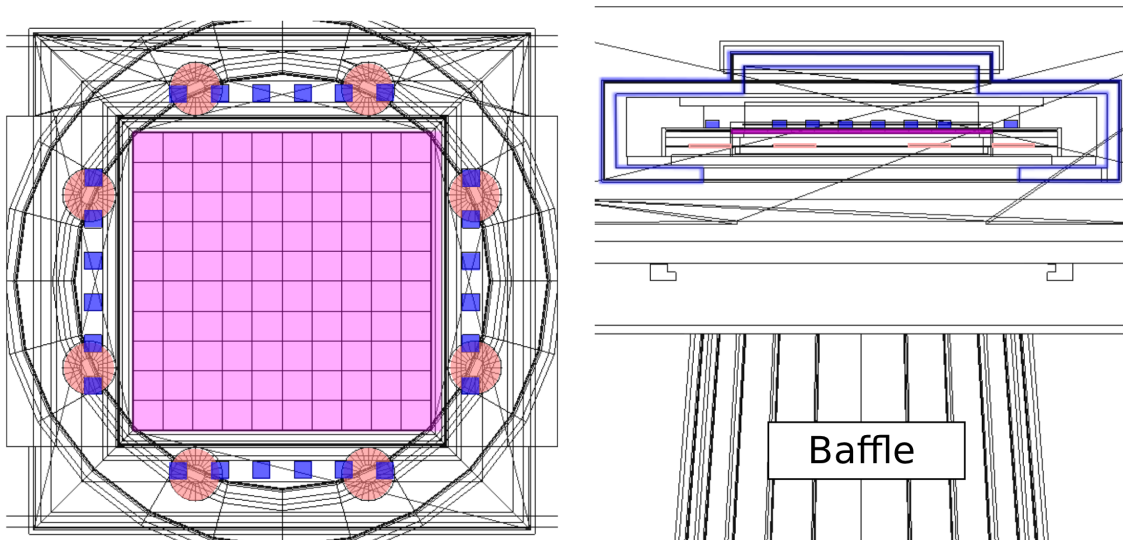
Geant4 ATHENA

Baffle

Figure 21: A comparison of the original WFI CAD model and the Geant4 implementations thereof in the IXO and ATHENA variants. The annular structure visible in the top views of both the IXO and ATHENA versions is the baffle.
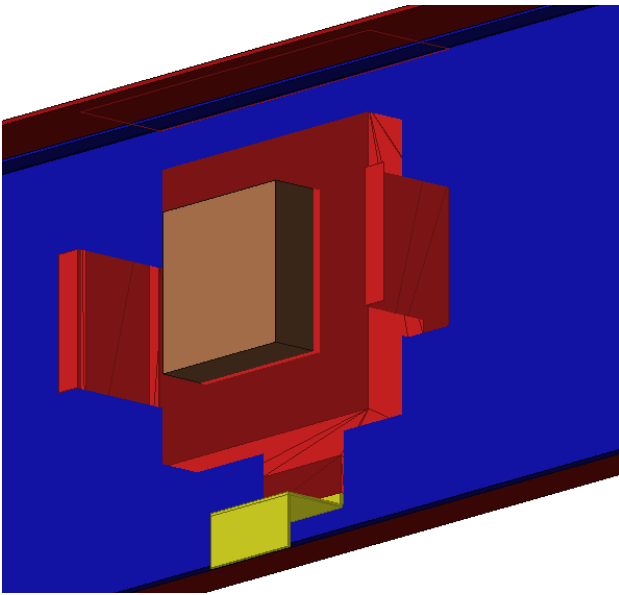
Figure 22: A view of the Geant4 implementation of the IXO WFI with the outer casing removed. Visible are the thermal strap (yellow), the flex leads (red), the HXI (brown) and the WFI frame (red) as well as the mounting plate (blue).
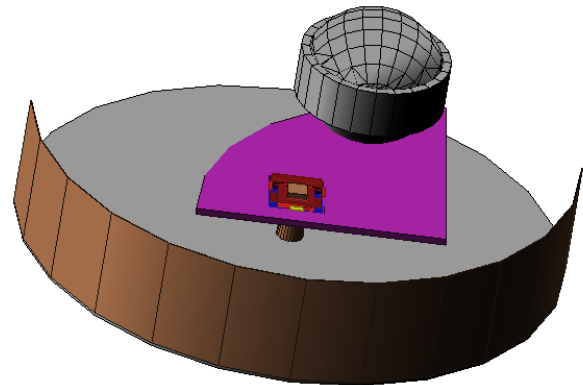

Figure 23: The full satellite setup which can optionally included in the IXO WFI Geant4 simulation. The WFI (largely red) is shown at the center. The large spherical structure is a mass dummy of the XMS. Also shown are the movable instrument platform (purple) and the sun shield (brown).

Table 3: Optimized thicknesses of the graded-Z shielding layers from the outermost to the innermost layer. Instead of graphite other carbon-rich materials such as Kapton may be used.

Material	Thickness	$K_{\alpha 1,2}$ emission energies [keV]
Tantalum	1.5 mm	57.532 / 56.277 keV
Tin	2.2 mm	25.271 / 25.044 keV
Copper	1.2 mm	8.047 / 8.027 keV
Aluminium	0.3 mm	1.486 / 1.486 keV
Graphite	0.1 mm	0.277 / − keV
Beryllium (added later)	0.1 mm	108.5 / − keV

Figure 24: A sketch of the primary particle generation approach. The primary protons are emitted from the inner surface of the larger sphere at an opening angle $\alpha = 0.0175\,\mathrm{rad}$. This results in a smaller virtual sphere, within which emission is isotropically emitted from all directions.
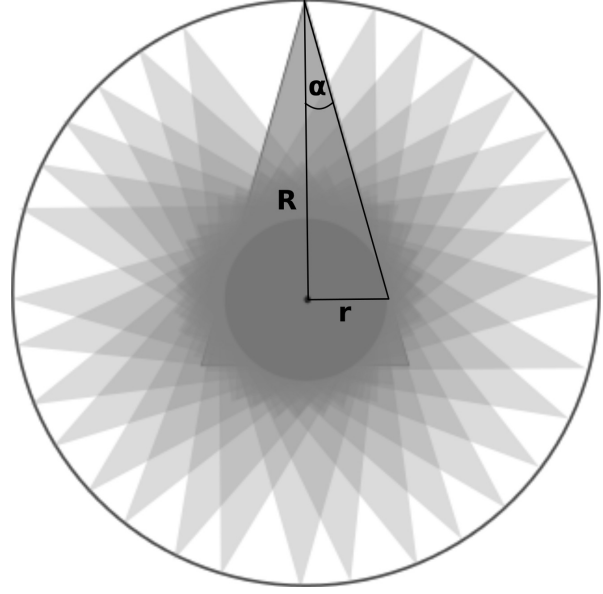
For the normalization of the final simulation results, knowledge about the correlation between the number of emitted primaries and the time period covered by the simulation is necessary. If the integral source flux Φ in the energy interval $[\mathrm{E}_1, \mathrm{E}_2]$ is known, the time t_{sim} can be calculated from the source geometry:

$$n|_{\mathrm{E}_1}^{\mathrm{E}_2} = A \cdot t_{\mathrm{sim}} \Phi = A \cdot t_{\mathrm{sim}} \cdot 2.318 \, \mathrm{protons\, cm^{-2}\, s^{-1}} \tag{12}$$

where $n|_{\mathrm{E}_1}^{\mathrm{E}_2}$ is the number of simulated primaries emitted from an area A. It was shown in Hauf, 2009b that for the above source geometry this equation can be rewritten as

$$t_{\mathrm{sim}} = \frac{n|_{\mathrm{E}_1}^{\mathrm{E}_2}}{\Phi \cdot \pi R^2 \sin^2 \alpha}. \tag{13}$$

As a result of the knowledge of t_{sim}, the number of events registered in the simulated detector model can be converted into a flux.

3.3 The Physics List

The primary protons emitted from the source sphere described in Section 3.2 will interact with the observatory via the physical processes discussed in Section 2.2.2. Accordingly, an accurate background estimate requires the underlying simulation to account for these processes. In Geant4 this is possible due to the diverse range of electromagnetic and hadronic interactions implemented therein. Table 4 extends the list of processes given in Table 2 to include information about the Geant4 implementation and existing verifications/validations. For the electromagnetic interactions the Low-Energy Livermore-library driven processes were used which were found to be in good agreement with experimental data in Lechner, Mantero, Pia, and Sudhakar, 2008. The hadronic processes are based on the *QGSP_BIC_HP* physics list, which uses a Quark-Gluon String Precompound model (Folger and Wellisch, 2003) to handle high energy collisions and the *Geant4 Binary Cascade* (Folger, Ivanchenko, and Wellisch, 2004) for interactions of primary protons and neutrons below $\approx 10\,\mathrm{GeV}$. Additionally, the high precision neutron package (*NeutronHP*) handles neutron transport from thermal neutron energies up to $20\,\mathrm{MeV}$. These hadronic processes have been validated with LHC[*] data in Apostolakis et al., 2009; Boyko, 2008; Dotti, Lupi, and Roda, 2006; Ribon et al., 2004, 2010; Wellisch, 2005. Generally deviations of less than 30%

---

[*]   Large Hadron Collider

are observed. A validation with atmospheric cosmic ray measurements in Astbury and Axen, 2006 shows agreements within a factor of 2.

The *QGSP_BIC_HP* list was extended to include PIXE[*] via the `G4hImpactIonisation` process, which has been validated and verified in Pia et al., 2009; Pia et al., 2009; Weidenspointner, Pia, and Zoglauer, 2008 and found to qualitatively reproduce the XMM Newton background fluorescence features in Tenzer, Kendziorra, and Santangelo, 2008. This was additionally validated for the simulation environment used in this work (see Section 3.5). Finally radioactive decay physics were incorporated via the `G4RadioactiveDecay` process which is responsible for the correct decay of unstable nuclei produced by the other hadronic interactions and the contribution of these nuclei to the delayed background component. It was found that sufficient verification or validation of a large set of radioactive isotopes does not exist in the literature. Additionally, the process does not provide adequate functionality for the simulation of activity buildup. These shortcomings motivate the development of a new radioactive decay code for Geant4, which is discussed in detail in Chapter 3.5, alongside extensive verification and self-consistent validation measurements.

3.4 Simulation Output and Analysis Routines

As was briefly discussed in the description of the geometry, particles and radiation which deposit energy in the sensitive area (i.e. *hits*) are aggregated by a sensitive detector object. The information kept for each hit consists of the particle type, its energy, the momentum direction before the hit, if it has passed through the field of view, the primary event number, the primary particle's energy as well as the production process and location which defined the particle. This information is output into a compact binary file. The content area of this file is preceded by a header which holds simulation attributes such as filename and the number of primaries.

In addition to the *hit* information the simulation can optionally output the location, processes and energies for all secondary producing interactions occurring within the simulation geometry. While this output results in large amounts of data, it allows to determine how different components and materials in the geometry contribute to the background.

Both types of output data are analyzed using custom IDL[†] routines. The hit data is first transferred from the raw binary format into a FITS[‡] format, common in astrophysics. This format is readable by a large number of programs and is thus better suited as an archival format. The FITS files are then used as input for a series of analysis tools, which can output detailed spectra for the simulated data, including information on the particle types contributing to the background. The analysis additionally implements a flexible pattern detection algorithm, which classifies pixel patterns into those resulting for X-rays and those classified as background (see Figure 25). This is done by comparing the pattern's size, shape and energy distribution. If the total energy of the pattern constituents is above the maximum X-ray energy which can be focused by the mirrors or at which the WFI has a sufficient quantum efficiency for detecting X-rays (both bounds set to 20 keV for ATHENA) it is also classified as an invalid event which is to be attributed to a minimum ionizing particle (MIP). For large simulated data sets the IDL implementation of the pattern analysis is computationally expensive. A C++ version of the detection algorithms, with less intermediate information output, is then used instead. After the pattern recognition different rejection schemes may be applied, either excluding complete frames if they contain invalid patterns, or only a specified area around a rejected pattern. Finally an estimate of the WFI's energy resolution, based on prototype measurements, is optionally applied to the simulated data.

3.5 Validation of Geant4 and the Simulation Environment with XMM Newton Measurements

In Section 3.3 it has become apparent that while many physics processes included in Geant4 have been validated with experimental data, validations in the X-ray observatory application domain, especially

---

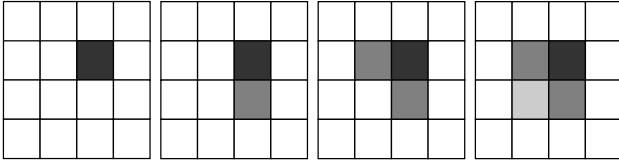[*]   Particle Induced X-ray Emission
[†]   Interactive Data Language
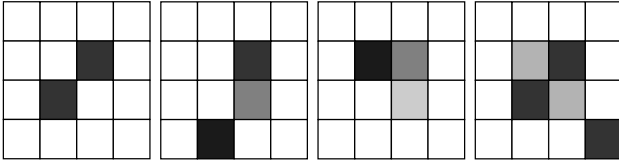[‡]   Flexible Image Transport System

Table 4: An overview of the Geant4 electromagnetic and hadronic processes used in the IXO/ATHENA simulation. Additionally, verification and validation examples are given.

	Process	Energy range	Geant4 Process	Validation/Verification results
Electromagnetic physics	**Photoelectric effect**	$> 100\,\mathrm{eV}$	G4LivermorePhoto ElectricModel	Energy deposit validation of Livermore-physics in Lechner, Mantero, Pia, and Sudhakar, 2008, χ^2-tests, 99% confidence interval, 15 pass, 9 fails. Verification of Compton scattering models in Augelli et al., 2009, Validation with XMM data in Tenzer, Kendziorra, and Santangelo, 2008, good reproduction of quantum efficiency.
	Compton scattering		G4LivermoreCompton Model	
	Rayleigh scattering		G4LivermoreRayleigh Model	
	Coulomb scattering		G4ComptonScattering	
	Electron-positron pair production		G4Livermore Gamma-Conversion Model	
	Ionisation		G4LivermoreIonisationModel, G4hIonisation	
	Bremsstrahlung		G4Livermore-BremsstrahlungModel	
	Annihilation		G4eplusAnnihilation	
Had+EM	**Atomic relaxation**		G4AtomicDeexcitation, G4PhotonEvaporation	Verification with NIST reference in Guatelli et al., 2007, 5 statistical tests, Auger and X-ray emissions.
	PIXE		G4hImpactIonisation	Verification and validation in Pia et al., 2009; Pia et al., 2009; Weidenspointner, Pia, and Zoglauer, 2008, 46-85% agreement with experiment depending on model. Validation with XMM Background data in Tenzer, Kendziorra, and Santangelo, 2008, qualitative reproduction of features.
Hadronic physics	**Hadronic scattering**	$0 - 100\,\mathrm{GeV}$	QGSP_BIC_HP physics	Validation with LHC data in Apostolakis et al., 2009; Boyko, 2008; Dotti, Lupi, and Roda, 2006; Ribon et al., 2004, 2010; Wellisch, 2005, shower profiles, e/π ratios and calorimeter energy resolution agrees within 30%. Fission and spallation validated in Apostolakis et al., 2009, agreements within 10-50% reported, Validation with atmospheric cosmic ray measurements in Astbury and Axen, 2006, agreements within a factor of two. Validation with XMM background data in Tenzer, Kendziorra, and Santangelo, 2008, qualitative reproduction of features.
	Hadronic collisions / Spallation	High precision below $20\,\mathrm{MeV}$		
	Fission			
	Fermi Breakup			
	Neutron capture	High precision below $20\,\mathrm{MeV}$		
	Proton capture			
	Radioactive decays			

Valid patterns

Invalid patterns

Deposited energy

■ High   ■ Medium   ■ Low

II   I

Figure 25: Examples of valid and invalid patterns which can register on the detector. X-rays will generally generate patterns with characteristic energy depositions. Event patterns which deviate from these valid patterns are identified as background and rejected.
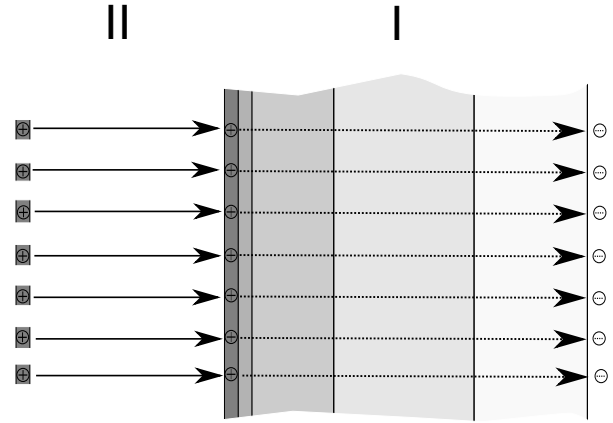
Figure 26: Sketch of the two electric field designs studied: I) The field extends within the graded-Z layers (dashed field lines) with the innermost and outermost layers acting as anode and cathode. II) The field extends between an additional graphite mesh anode placed 4 mm from the innermost layer (solid field lines).

for detectors similar to the WFI, are scarce. A notable exception are the comparisons between XMM-filter-wheel-closed observations and Geant4 simulations by Tenzer, Kendziorra, and Santangelo, 2008. Here a good agreement between measured and simulated quantum efficiency was reported and the main background fluorescence lines could be reproduced. The *eROSITA* simulation environment used in these simulations shares a common heritage with the IXO/ATHENA simulation environment presented in this work — both were originally independently programmed for the use in SIMBOL-X background simulations. Accordingly, a similar performance is to be expected when comparing against XMM measurements; a task which was undertaken with the aim of validating the presented code for an X-ray astronomy application.

As the implementation of a complex XMM geometry is a dedicated project in its own right, a simplified model was used for the validation. This model includes a parametrized version of the EPIC-pn camera consisting of the PCB board, modeled as two $200\,\mu$m thick copper layers enclosing a $800\,\mu$m molybdenum core, and the $300\,\mu$m thick silicon wafer bulk with the addition of a $30\,$nm SiO_2 passivation layer.

Instead of accurately positioning the individual SMDs[*] and ASICs their placement was determined by a grid superimposed on the PCB board. Care was taken that this approach reproduces the background relevant characteristics of the EPIC-pn, such as the origins of fluorescence emission, e.g. the Au and Ni deposits on the FOV side behind each SMD and the voids in the PCB (Figure 27). The shielding and satellite components were simplified even further. They were modeled as an aluminium box with a wall strength of $1\,$cm, which encloses the PCB and wafer.

In order to significantly reduce the processing times a two tiered simulation approach was chosen. At first, a simulation with a range cut of $1\,\mu$m and with the aluminium shielding was run. This simulation would determine the aluminium fluorescence emission and the secondary electron emission resulting
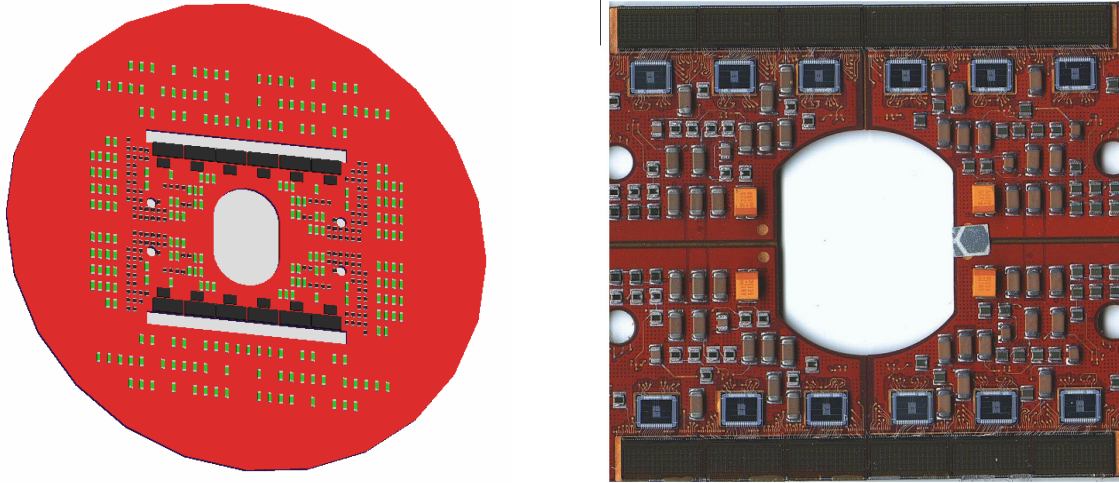
---

[*]   Surface Mounted Devices

Figure 27: Left panel: a rendering of the simplified XMM EPIC-pn focal plane model used for the valida-
tion simulations. Note the regular spacing of the SMDs due to the gridded parametrization
(see text). Right panel: A picture of a section of the XMM EPIC-pn PCB board with ASICs an
SMD components taken from Tenzer, Kendziorra, and Santangelo, 2008.

from the shielding. A second run with a reduced range cut of $0.1 \, \mu$m was then conducted without the
shielding. This simulation would allow do obtain better statistics for the radiation resulting from the
SMDs and the PCB board.

In the analysis the first simulation was normalized by the proton flux and simulated time in accordance
with the normalization scheme presented in Section 3.2. The second simulation was then scaled in
such a fashion that the continuum intensities of both simulations agree. The two data sets were than
superimposed on each other. Hereby the data for energies below 4 keV, i.e in the region influenced by
the aluminium fluorescence emission from the shielding, was taken from the first simulation. The data
for the fluorescence features of the PCB and SMDs at energies above 4 keV was taken from the scaled
second simulation. Finally the energy resolution of the EPIC-pn was approximated by convolving the
resulting spectrum with a Gaussian. This spectrum was then compared with experimental data taken
from Tenzer, Kendziorra, and Santangelo, 2008.

The results of this procedure are shown in Figure 28. It is apparent from the Figure that the back-
ground intensity, determined largely by the first simulation run, is represented well. The fluorescence
emission line resulting from the aluminium is present, as is that from gold and copper. The nickel emis-
sion is not represented well which is probably results from the simplified detector model used for the
simulation.

In conclusion, the IXO/ATHENA simulation environment is able to qualitatively replicate the measured
XMM background spectrum in a similar fashion as the quantitative analysis by Tenzer et. al. did. The
uncertainties reported there will therefore be taken into consideration for the IXO/ATHENA simulation
environment.

In addition to the reproduction of the prominent fluorescence lines the EPIC-pn quantum efficiency was
validated by emitting $10,000$ photons of a specified energy onto the sensitive area. This was repeated
at intervals of 100 eV in the energy range from 0.1 keV – 15 keV. At energies where micro-structuring of
the quantum efficiency might occur the interval was reduced to 2 eV – 20 eV. As is apparent from Fig-
ure 29 the simulation is in excellent agreement ($< 10\%$ deviation) with the measurements from 250 eV
upwards. Below this threshold Geant4 does normally not track particles, a fact which is commented
upon in Section 7.5, and which explains the missing simulation data.

In addition to a good overall representation of the quantum efficiency the simulation also reproduces
the efficiency reduction at the silicon K-edge (1.838 keV) and at the absorption edge of the SiO_2 passi-
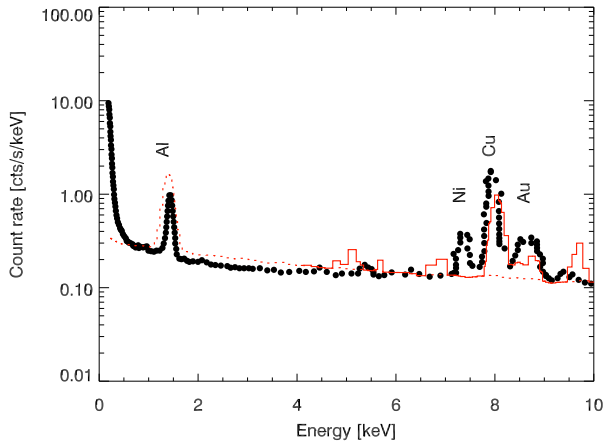
Figure 28: A comparison between an XMM simulation run with the IXO/ATHENA environment and XMM background data (filled circles) taken from Tenzer, Kendziorra, and Santangelo, 2008. The dashed red line represents data taken from the first simulation which included the aluminium shielding. The solid red line highlights the data obtained from a second simulation run without the shielding. More details on this approach are given in the text. Additionally, the position of fluorescence emission from the detector materials is marked.
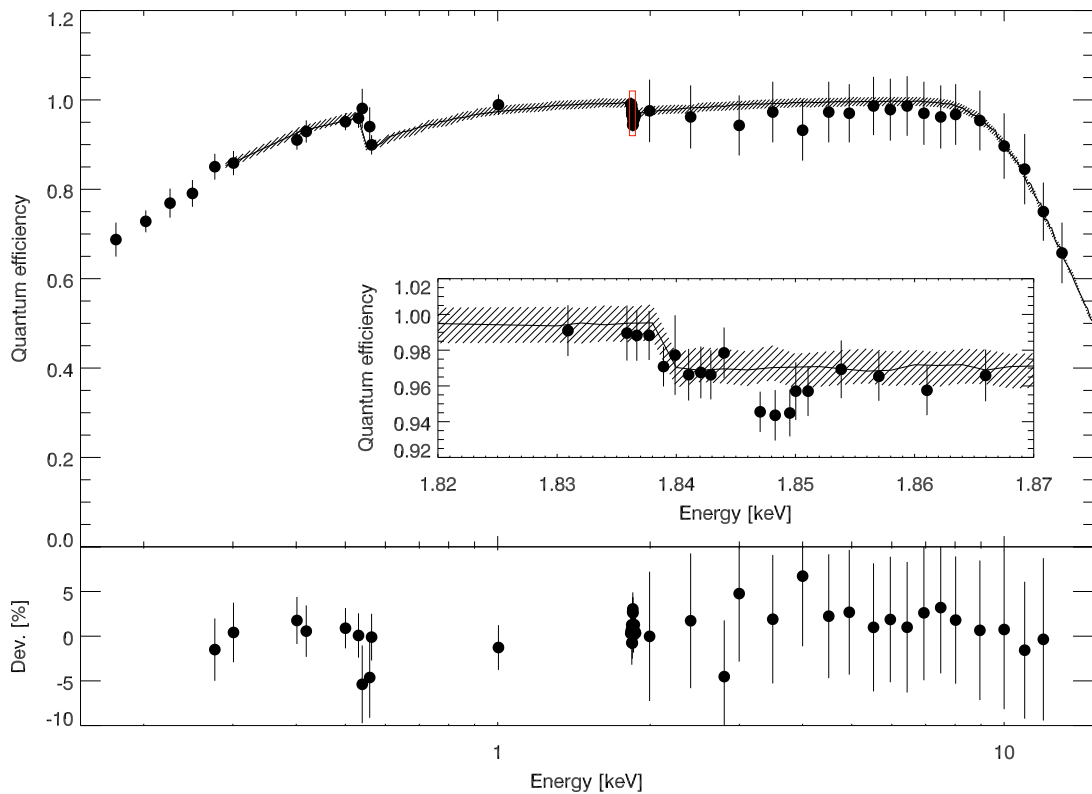

Figure 29: A comparison of the simulated XMM EPIC-pn quantum efficiency (solid line with shaded uncertainties) and measured data (filled circles) taken from Strüder et al., 2000. The inset shows a detailed view of the region around the silicon K-edge; its location is marked with a red box in the main figure. Note that for the Si-K edge only one step of the two-stepped efficiency drop-off is reproduced by the simulation. The relative deviation between simulation and measurement is shown in the lower panel.

vation layer (528 eV). In conclusion, these two validation simulations yield confidence in the simulation environment and its applicability to the IXO/ATHENA problem domain.

4 Radioactive Decays in Monte Carlo Simulations

As has been described in Chapter 2.2.2, a correct estimate of the additional background introduced by the buildup of radioactive nuclei in orbit can be crucial for missions like IXO and ATHENA. Accordingly, any decay model implemented as part of a Monte-Carlo code should be well validated and able to simulate this process. For Geant4 versions up to 4.9.5 this is currently not the case.

4.1 Radioactive Decays in Geant4

Although a radioactive decay code for Geant4 exists it has to the author's best knowledge never been thoroughly verified against a complete set of evaluated data for the known radioisotopes. Whilst validations and calibrations exist (e.g. Hurtado, Garcia-Tenorio, and Garcia-Leon, 2009; Hurtado, García-León, and García-Tenorio, 2004; Laborie, Le Petit, Abt, and Girard, 2002; Golovko, Iacob, and Hardy, 2008 — see Table 5) they are often application-specific and only cover a limited range of nuclei for which often only photo-peak efficiencies and not the Compton continuum has been studied. In these works the usually good agreement between simulations and measurements is often achieved by iteratively altering the simulation geometry until it the simulation reproduces the measurement. This approach is valid within the error bounds attached to the parameters of the real-world detector, parameters such as dead layer thickness, entrance window thickness and source characteristics. Nevertheless it obscures how well a Geant4 simulation is capable of producing estimates for a detector in the design phase for which actual hardware is not yet available. In this case comparisons with experimental reality are not possible, and thus such adjustments cannot be made. Additionally, the result of a simulation of a complete detector setup is necessarily influenced by a complex geometry and the interactions resulting from many different physical processes of which the radioactive decay is just one. This makes it difficult to distinguish if any observed deviations result from geometric features or the accuracy of the modeled processes; and in the latter case from which process they result.

A verification of the code with a large number of isotopes would thus be beneficial as an initial, application independent indicator of radioactive decay simulation accuracy. In a second step these results can then be brought into a more specific context by comparing the model of a complete detector setup with measurements. In this chapter such a verification based on the ENSDF[*] data library (Tuli, 2010) and validation measurements with a High Purity Germanium (HPGe) detector will be presented. Both the verification and the validation were done for the *current* Geant4 code and a *new* code [†] with enhanced capabilities, which was developed as part of this work. A short summary of radioactive decay physics and an overview of model implementations in three major Monte-Carlo tool kits will be given. This summary is extended by an analysis of the current Geant4 decay code in particular. The results of these reviews are then used as the basis for formulating the requirements for a radioactive decay simulation within the context of a Monte-Carlo toolkit at the conclusion of this chapter. Based on this problem domain analysis a newly developed code is introduced in Chapter 5 before proceeding with the presentation of the verification and validation results for both Geant4 codes in Chapter 6.

4.2 Radioactive Decay Physics

Radioactive decays are a physical process during which atomic nuclei of unstable atoms transmute into lower energy states. In the course of doing so they spontaneously emit particles or ionizing radiation. The decays result from either nucleus-internal processes or interactions of the nucleus with shell electrons. An external trigger is not required and the occurrence of a single decay cannot be predicted.

Radioactive decays have been intensively studied for over a century, beginning with their discovery by Henry Bequerel in 1896 (Bequerel, 1896). Additional research by Ernest Rutherford, Paul Villard, Pierre and Marie Courie was subsequently placed on theoretical foundations by Enrico Fermi (Fermi, 1934)

---

[*]   Evaluated Nuclear Structure Data File

[†]   In the remainder the *current* code will be regarded as the published Geant4 code while the *new* code it the software developed as part of this work.

Table 5: A selection of previous works which have studied Geant4 radioactive decay simulations.

Source	Goal	Photo peak deviation[1]	Continuum deviation[2]	Comments	Geant4 comments
McNamara, Heijnis, Fierro, and Reinhard, 2012	The determination of the efficiency of a Compton suppressed HPGe detector using Monte Carlo simulations.	0%–27%	-	Larger deviations at lower energies, dead layer thickness estimated by comparison of accuracy at lower energies. No comparison of continuum shape and flux.	Low Energy
Gharbi, 2011	Inhomogeneity effects on HPGe gamma spectrometry detection efficiency using Monte Carlo techniques.	0.9%–21%	-	Optimized detector parameters.[3] Only full peak energy events evaluated. Deviations evenly distributed.	Low Energy
Hurtado, García-León, and García-Tenorio, 2004	A GEANT4 code for simulation of a germanium gamma-ray detector and its application to efficiency calibration.	0.4%–17% unoptimized, 0.04%–1.57% optimized	-	Optimized detector parameters (up to 25%), Spatial biasing.	Low Energy, 8.1
Vidmar et al., 2008	An inter-comparison of Monte Carlo codes used in gamma-ray spectrometry.	1%–10%	-	Comparison of GEANT3, GEANT4, MCNP and PENELOPE, large deviations between codes at low energies, less at higher. No comparison with experimental data.	-
Capogni, Meo, and Fazio, 2010	Simulation of radioactive decays in GEANT Monte Carlo codes: Comparison between spectra and efficiencies computed with sch2for and G4RadioactiveDecay.	0%–17% Monochromatic radiation, 0–3.44% for isotopes	<1% total efficiency	Comparison between sch2for implemented in GEANT3.21 and GEANT4. Codes deviate more at low energies.	Standard+LE-Rayleigh, 9.0
Lei, Rason, Ford, and Morris, 2009	Validation of Geant4-based dose computational tools with REEF Experiments.		2.1%–62.1% deviation	Comparison of radiation dose estimates with two GEANT4 base tools, GRAS and MULASSIS.	
Bissaldi et al., 2009	Ground-based calibration and characterization of the Fermi gamma-ray burst monitor detectors.	1%–40%	-	Comparison with NaI detector measurements, response taken into account, largest deviations at low energies. Detailed detector geometry.	Simulation with GRESS

[1] Relative photo peak intensity deviation.
[2] Continuum flux and shape deviation.
[3] The simulation geometry was altered to better fit the experimental data.

and others in the first half of the 20th century. Owing to this long history of research in-depth explanations along with the underlying models can be found in many physics books. Accordingly, it will be refrained from giving a detailed theoretical discussion of the topic and instead focus on a phenomenological overview, taking into account observables such as the radiation and secondary particles resulting from the process. Historically, the type of emitted particles was used to distinguish between different decay types.

- When undergoing an alpha-decay the parent nucleus emits a helium nucleus consisting out of two protons and two neutrons. These particles are now missing from the parent nucleus and accordingly, the atomic number Z and atomic mass number A change with $Z_d = Z_p - 2$, $A_d = A_p - 4$.

- The β^--decay is a weak process during which a neutron n is converted into a proton p. Additionally, an electron and an anti-neutrino are emitted by the parent nucleus:

$$n \rightarrow p + e^- + \bar{\nu}_e. \tag{14}$$

The atomic number of the daughter nucleus changes by $Z_d = Z_p + 1$ due to the electron emission and the atomic mass number stays constant, i.e. $A_d = A_p$. Since the electron and neutrino share the energy released during the decay and both particles are not bound in their final state, their energy distribution follows a continuous spectrum.

- During a β^+-decay a bound proton p of a nucleus is converted into a neutron n. Additionally, a positron and a neutrino are emitted by the parent nucleus:

$$p \rightarrow n + e^+ + \nu_e. \tag{15}$$

The atomic number changes according to $Z_d = Z_p - 1$ and the atomic mass number stays constant at $A_d = A_p$.

- If a daughter nucleus is left in an excited state, after a transmutation by the previously mentioned decay types, it can deexcite by emitting gamma-radiation. In case the excited daughter state is a longer-lived (metastable) state, its deexcitation is called *isomeric transition*, which will also result in gamma-radiation. In both cases the atomic number and atomic mass number remain unchanged.

Apart from these "classical" decay types two additional decay channels exist:

- During an electron capture,which is also called inverse beta decay, the parent nucleus absorbs an inner shell electron (usually K- and L-shell electrons) and simultaneously emits a neutrino. As a result, a proton is transmuted into a neutron

$$p + e^- \rightarrow n + \nu_e \tag{16}$$

and thus $Z_d = Z_p - 1$ and $A_d = A_p$. In contrast to a beta-decay, an electron capture is a two body decay, resulting in a discrete neutrino energy.

- As an alternative process to the emittance of gamma-emission an excited nucleus can return to its ground state by transferring its excitation energy to one of the lower shell electrons. This process is called internal conversion and results in the emission of an electron from the atom, now leaving the atom in an excited state. The electron carries a discrete fraction of the decay energy which distinguishes it from beta-particles with an continuous energy spectrum. As with gamma-decays no transmutation of the nucleus takes place and the atomic number and atomic mass number remain unchanged.

The discussed decay types are stochastic processes: the time at which a given unstable nucleus decays cannot be predicted and is not predetermined. Nevertheless, given a large enough sample of decaying nuclei, the decay constant λ can be determined by statistical means, usually by measuring the activity . This concept also leads to the definition of the half-life $t_{1/2}$, the time after which half of a population of nuclei has decayed. Both are related via

$$\lambda = \frac{ln\,2}{t_{1/2}}. \tag{17}$$

The number of unstable nuclei $N(t)$ remaining after a certain time t is given by

$$N(t) = N_0 \cdot \exp(-\lambda t). \tag{18}$$

Differentiating this equation then yields the number of decays per time interval, or activity

$$A(t) = -dN/dt = A_0 \cdot \exp(-\lambda t) \tag{19}$$

with $A_0 = \lambda N_0$. In many cases it is the activity which is the observable and the half-life is derived from its measurement. Furthermore no all-encompassing theory determining all characteristics of the decay products and radiation exists. Instead each decay type is governed by individual, often quantum-mechanical theories, which makes ad-hoc theory-driven calculations of decay properties computationally expensive, if not impossible. As a consequence, efficient and fast simulations of radioactive decays will necessarily have to rely on pre-calculated or empirical data for the determination of the decay characteristics.

4.3 Experimental Requirements

Not surprisingly the required output of a simulation often consists of observables which correspond to this empirical input; parameters such as radiation type and intensity, decay time and radiation energy. It was already stated that most experiments measure the time-accumulated statistical distribution of these observables or their influence on other measured data and not the results from a single decay. In general radioactive decay physics play an important role in a variety of fields, e.g.

- Measure and analyze the properties of decays and decay chains of naturally occurring radioactive isotopes. This task is frequently encountered in material sciences, radiation safety and nuclear proliferation monitoring, when an unknown sample consisting partially or fully of unstable isotopes is to be characterized.

- Determine material properties after previous irradiation. An otherwise not radioactive sample is e.g. activated by a neutron beam. The subsequent decays of the radioactive activation products can be observed and an analysis of their radioactive emission can determine the new and initial material composition. This scenario is often encountered in material sciences and metallurgy.

- Determine activation and build-up of radioactive nuclei occurring at fission reactors, fusion reactors, particle accelerators or intense laser sources. This knowledge is crucial for nuclear waste disposal and radiation safety precautions.

- Estimate the build-up of radio-nuclei due to high energy cosmic ray particles interacting with space born X-ray and gamma-ray instruments. Meta-stable states usually must be accounted for. This scenario is of concern for the IXO and ATHENA missions.

- Estimate the influence of the cosmic-ray induced background and natural radioactivity on low background experiments in astroparticle physics and nuclear physics. Examples include neutrino telescopes such as IceCube (Achterberg et al., 2006) and SuperKamiokande (Fukuda et

al., 2003), neutrino detectors like OPERA (Acquafredda et al., 2009) and axion telescopes such as CAST (Aalseth et al., 2002).

- Study possibilities to distinguish individual radioactive emission from an experiment's intended observables; e.g. the estimation of the in-orbit cosmic-ray induced background of space-based detectors or low background (under)ground experiments. This scenario applies to the experiments mentioned for the two previous tasks.

Although the above list is far from complete it summarizes the main application scenarios frequently encountered when modeling an experiment as a Monte-Carlo simulation. Hence, before proceeding with the development of a new code suitable for the above scenarios it is worthwhile to assess the capabilities of existing codes.

4.4 Radioactive Decay in Monte Carlo Codes

Models for the simulation of radioactive decays exist in most general-purpose Monte-Carlo codes either natively or as an external package. The following summary is not intended to give a complete overview of these codes but will instead highlight specific capabilities, limitations and the general implementation approach. Additionally, the overview is constrained to the three most common codes[*] according to the number of citations reported on Google scholar[†] at the time of this writing: MCNP(600), Geant4(4980) and FLUKA(510).

- MCNP(X) (Briesmeister, 1986; Hendricks, 2003) does not include a full radioactive decay simulation by default except for the generation of delayed gammas resulting from decays. In this case the data is extracted from the *phtlib* database[‡]. More often MCNP is linked via scripts to specialized codes such as ORIGEN2 (Croff, 1983) or CINDER90 (Giacri-Mauborgne et al., 2005; Wilson et al., 1995), both of which use their own data libraries. These codes are commonly used to model reactor fuel cycles and accelerator induced transmutations but also provide the functionality for simulating individual radioactive decays and decay chains. Due to the codes' natures they can include replenishment through activation. In contrast to the gamma radiation alpha- and beta-emission needs to be generated from tabulated user input. Generally, MCNP is specialized on the simulation of many decays and the resulting statistics, rather than simulating individual decays.

- FLUKA (Fassò, Ferrari, Sala, and Ranft, 2001) generates and transports beta- and gamma-radiation but currently not alpha-radiation. Decay chains are possible and include replenishment through activation. FLUKA uses its own data libraries, largely based on NNDC[§] data and thus ENSDF (Bhat, 1991). Similar to MCNP the emphasis lies on the simulation of a large number of decays rather than the simulation of the individual decay.

- In Geant4 (Agostinelli et al., 2003; Allison et al., 2006) radioactive decays are treated on a per-decay level, based on data from the ENSDF (Bhat, 1991) library. Decay chains including activation are possible and will produce the associated decay emission. Alpha and beta emission is sampled from the decay database. Deexcitation radiation of the daughter nucleus is not produced by the radioactive decay simulation itself but by other physics processes of Geant4 using their respective databases. The emphasis lies on the per-decay simulation and not on the sampling of a large number of decays. A more concise introduction to the Geant4 decay code will be given in Section 4.6.

---

[*] An additional criterion was that the code should be able to simulate a given radioactive nucleus in such a way that the user need not specify the individual radiations and intensities

[†] scholar.google.com

[‡] No concrete reference could be found, it is mentioned in all MCNP manuals though.

[§] National Nuclear Data Center

In general the above Monte-Carlo codes either emphasize the simulation of a large number of decays and the resulting statistical outcome or the physically correct simulation of individual decays. The latter is necessarily also correct for many decay scenarios but requires additional computational overhead. The generalization of the experimental requirements has shown that applications which require capabilities in both domains exist.

Such applications would directly benefit from a code which can utilize a statistical approach when appropriate but can also simulate single decays of special interest in a physically accurate fashion if necessary. The new radioactive decay code for Geant4 which was developed as part of this work is designed to cover these two problem domains; both of which will be analyzed in detail in this chapter.

4.5 Problem Domain Analysis

In a very general context the problem domain for a radioactive decay simulation consists of the task of decaying an unstable nucleus and producing any associated radiation and particles. This task has additionally been differentiated by introducing the underlying physics of different decay types in Section 4.2. Furthermore, experimental requirements and the shortcomings of existing simulation implementations have been added to the domain in Sections 4.3 and 4.4. In summary these considerations result in the following list of requirements.

- Decay one or many parent nuclei according to the physical parameters governing their decay (e.g. decay type, initial excitation, half-life).

- Produce daughter nuclei with the physical properties resulting from the decay (e.g. atomic number and mass determined by the decay type, excitation energy and kinetics determined by parent- and decay kinetics).

- Generate particles and radiation associated with the decay (e.g. beta-, gamma- and alpha-emission, neutrinos and conversion electrons).

- The above tasks will require information from empirical or pre-calculated data as ad-hoc theoretical calculation is not feasible.

In addition to these basic requirements it was shown that the experimental observable for radioactive decays is often the deexcitation emission from the associated daughter nucleus. Measurements of this quantity usually consist of observing a large number of decays of the parent isotope. Hence the above requirements can be extended to include

- The production of emission and radiation occurring during the deexcitation of the daughter nucleus (e.g. gamma-, X-rays and Auger-electrons)

- A possibility to efficiently simulate a large number of decays when overall statistics of the observables are important and not the individual decay.

- The inclusion of the capability to efficiently simulate decay chains and foresee that intermediate products in these chains may be of lesser importance.

- The three previous points will again need to rely on information from empirical or pre-calculated data if ad-hoc calculations are not possible.

Finally radioactive decays of nuclei are often associated with prior activation of stable nuclei in a given material. Examples of this case include shielding estimates, materials science and radiation safety analysis. As will be shown in Section 5.5 the algorithms necessary for the efficient computation of decay chains can be modified to include time dependent and independent nuclear activation. Consequently the following additional requirement should be addressed by a decay simulation.

- Include isotope replenishment by activation into the decay chain calculations. Take into account meta-stable states if required.

Aside from these *functional* requirements additional *structural* requirements are imposed by the fact that the code is to be part of a larger Monte-Carlo toolkit. These requirements are in part tool-kit specific but will generally include possibilities to interface with the Monte-Carlo code and physical processes implemented therein as well a ways for the user to alter the functionality of the code, e.g. biasing mechanisms and suppression of individual decay channels.

4.6 The Current Geant4 Radioactive Decay Code

As has been previously mentioned a radioactive decay code for Geant4 exists. In the following section this *current* code will be analyzed with respect to design capabilities and shortcomings. Building upon this analysis the development of a new radioactive decay code for Geant4 is motivated. The verification and validation results for this existing code will be presented in Section 6, alongside the results for the new software.

The code discussed here as *current* is that of Geant4.9.4-p01 but the following analysis should also apply to earlier Geant4 versions. It uses reprocessed ENSDF[*] data (Tuli, 2010) in the April 2006 version to determine the decay type, decay emission and daughter nucleus resulting from the transmutation of a given parent. It delegates the deexcitation of the daughter to the `G4Photonevaporation` process which uses ENSDF data libraries (Dec. 2010 version) and conversion electron probabilities compiled from Band, Trzhaskovskaya, and Listengarten, 1976; Hager and Seltzer, 1968; Rösel, Fries, Alder, and Pauli, 1978 as data sources. In case of electron capture decays a shell vacancy is generated using shell-capture probabilities from the radioactive decay database. The production of the subsequent fluorescence emission and Auger-electron is delegated to the `G4AtomicDeexcitation` process which has been previously validated in Guatelli et al., 2007 but has evolved since then.

Figure 30 shows an UML[†] class diagram of the current code; it is supplemented by the activity diagram shown in Figure 31. The diagrams share the same color coding which will be used in the following short "walk-through" on how a decay is processed:

1. The Geant4 tracking algorithms hand an unstable nucleus to the radioactive decay simulation and its main class, `G4RadioactiveDecay`. This class queries the radioactive decay database if decay entries for an isotope with the given Z, A and excitation energy exist. If this is not the case the nucleus is *stopped and killed*, i.e. all its energy is deposited at its current position but nothing else is done. If a decay entry is found the code initializes the information necessary for the decay of the nucleus. Note that database handling is a responsibility of the main class, while it could usually be associated to a dedicated object.

2. If the nucleus-species decays for the first time the `G4RadioactiveDecay` class loads the respective data from the on-disk data library and initializes an instance of `G4NuclearDecayChannel` which is loaded into an in-memory vector aggregate. Later occurrences of the same nucleus access this vector instead of the slower hard drive based library. If the decay type is either beta-minus or beta-plus the `G4RadioactiveDecay` class also instantiates the sampling of the corresponding Fermi-Function. Note that while a separate `G4BetaFermi` class exists it is not independent of the implementations in the main class.

3. After the data has been loaded/retrieved a decay channel is picked by the `G4RadioactiveDecay` class according to the branching ratios of the individual decay channels. The `G4NuclearDecay-Channel` class then samples the decay emission and resulting particles. Note that even though the physics behind the individual decay types are inherently different they are all sampled by the same

---

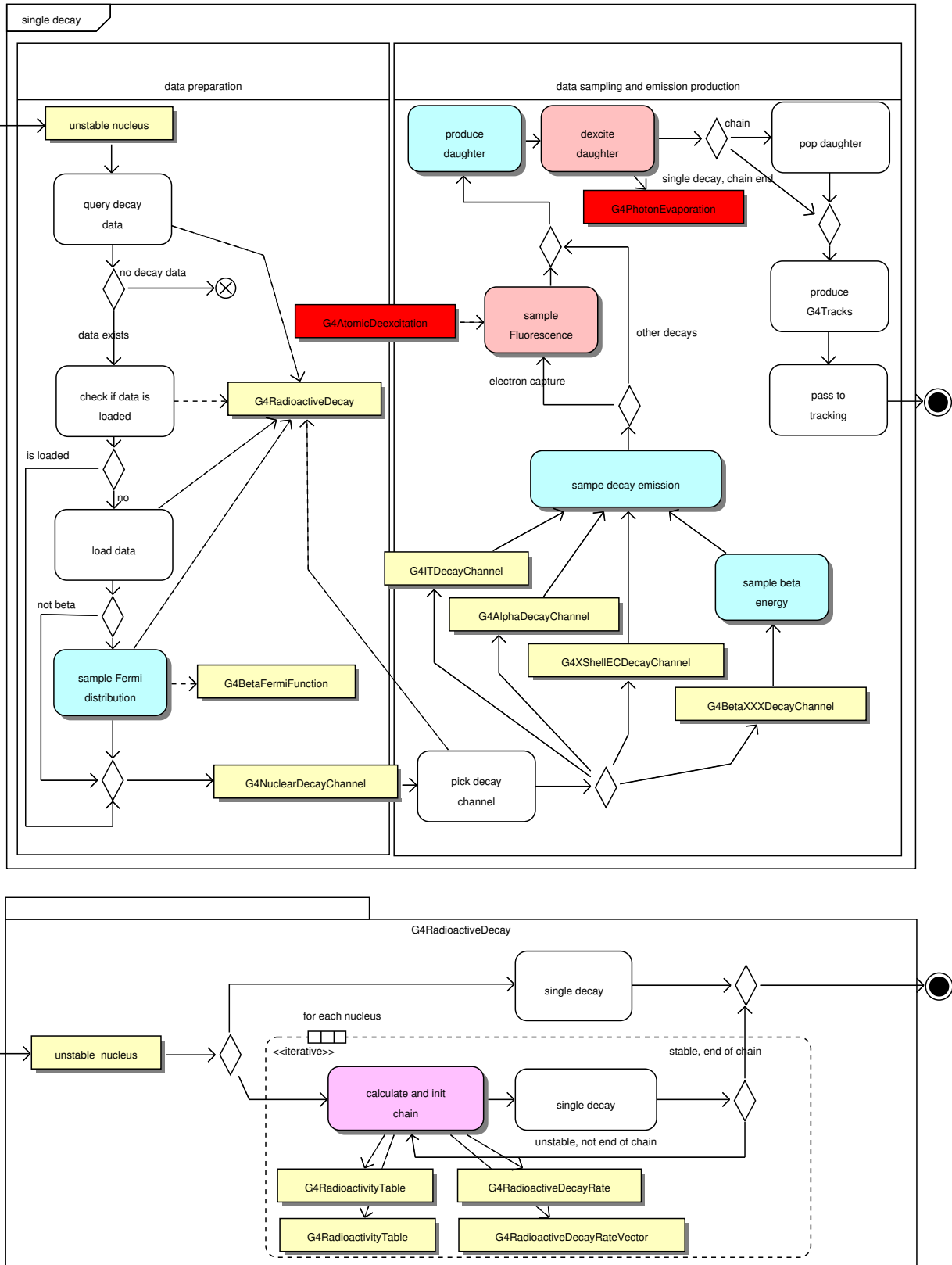[*]   Evaluated Nuclear Structure Data File
[†]   Unified Modeling Language

Figure 30: An UML class diagram for the current radioactive decay code showing the relations between the individual classes. The colors hint at the responsibilities and is matched to the activity diagram in Figure 31, they are: physics simulation (blue), decay chain processing (purple) and not clearly defined (yellow). Data retrieval, initialization and management is provided by the main class (`G4RadioactiveDecay`). The individual decay channels initialize a `G4NuclearDecayChannel` object which includes the physics of all decay types in one class.

Figure 31: An UML activity diagram for the current radioactive code showing how the decay of a nucleus proceeds. The color scheme is matched to the class diagram in Figure 30 and hints at the activity types: physics simulation within the radioactive decay code (blue), physics simulation by other processes(red) and decay chain calculations (purple).

`G4NuclearDecayChannel` class. The `G4XXXDecayChannel` classes only instantiate it differently, with parameters appropriate to the decay.

4. The daughter nucleus produced by the `G4NuclearDecayChannel` class will usually be in an excited state. The deexcitation of the nucleus is delegated to the `G4Photonevaporation` process. This process returns a vector of deexcitation emissions to the `G4NuclearDecayChannel` class, which for isomeric transition decays may also contain conversion electrons. During deexcitation an interaction with shell electrons may occur, which can result in an excited atom.

5. In case of electron capture and internal transition decays the excited atom is then handed over to the separate `G4AtomicDeexcitation` process which returns a vector of fluorescence photons and Auger-electrons. Note that for other decay types this step is omitted even though it is entirely possible that fluorescence emission or Auger electrons are produced as a result of such decays[*].

6. The `G4NuclearDecayChannel` aggregates all decay emission produced so far into a vector structure and returns it to the main `G4RadioactiveDecay` class. If the emission was sampled as part of a decay chain the daughter nucleus is popped from the vector (it decays and is thus non existent at the end of the chain) and the sampling restarts with the daughter nucleus as a new parent. The remaining emission, and in case of non-chain decays or if the end of the chain is reached also the daughter nucleus, is then instantiated into `G4Track` objects and returned to Geant4 tracking.

The above description already highlights that the current code does not follow a strict domain decomposition. Instead two large classes, `G4RadioactiveDecay` and `G4NuclearDecayChannel`, are responsible for many, very different tasks. The `G4RadioactiveDecay` class incorporates responsibilities for data management, data preparation, physics and decay chain calculations. The `G4NuclearDecayChannel` class is responsible for simulating all decay types; each of which has very distinct physics. This makes unit tests nearly impossible and severely inhibits maintenance of the code. This does not necessarily impede the physical correctness of the simulation though. In contrast the energy and momentum conservation behavior of the code, which is discussed in the following may actually lead to incorrect results.
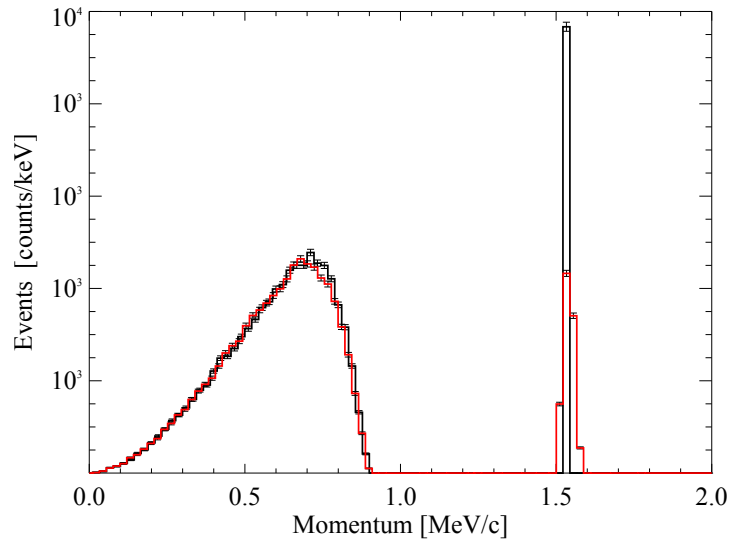
Energy Conservation

For a physically correct outcome, energy should be conserved during the decay, for all decay emission and when deexciting the daughter nucleus. The deexcitation is handled by the `G4Photonevaporation` process which uses a data library different from the radioactive decay process. It is not guaranteed that the level energies tabulated in the two data libraries will be exactly the same. In consequence, a possible deviation has to be taken into account. This is done on three levels:

- If the level energy E_{rad} passed by the radioactive decay code does not correspond to a tabulated level in the `G4Photonevaporation` library, E_{phot}, the nearest level present in the `G4Photonevaporation` database is used to retrieve the possible transitions. The initial deexcitation step occurs from the energy passed by the decay code and will transition to an energy tabulated in the evaporation library. The energy of the first gamma-ray is thus not in accordance with the tabulated evaporation data but deviates by the difference between the tabulated radioactive decay and evaporation library values $\Delta E = E_{\mathrm{rad}} - E_{\mathrm{phot}}$. Further transitions will then result in emissions at energies in accordance with the `G4Photonevaporation` data.

- For all transitions along a deexcitation chain it is checked if the level resulting from the transition is within a tolerance of $1\,\mathrm{keV}$ of ground state. If this is the case the photon energy is set to the energy of the excited level and the nucleus is deexcited to the ground state. Again energy is conserved but the kinetic energy of the emitted photon may not be in accordance with the tabulated data.

---

[*]   At the conclusion of this writing this issue has been fixed in Geant4.9.5.

Figure 32: The simulated momentum distribution of the particles resulting from a ^{22}Na beta-decay (new code: red line, current Geant: black line). At lower momenta the beta-particles are visible. The peak at $\approx 1.5\,\text{MeV/c}$ is the ^{22}Ne daughter nucleus. Due to the recoil resulting from the de-excitation of this nucleus its momentum should be slightly broadened. This is correctly simulated by the new code but not by the current Geant4 simulation.

- The final state's energy is passed back to the radioactive decay code. In case this energy is not 0 keV, but below 1 keV, the daughter nucleus' excitation energy is set to 0 keV. Here energy is not conserved! For larger energies the decay code outputs an excited (possibly meta-stable) daughter nucleus.

Momentum Conservation

The momenta of the gamma-rays and conversion-electrons generated as part of a deexcitation cascade are correctly transferred to the deexciting daughter nucleus by the `G4Photonevaporation` process. The momenta of any fluorescence and Auger-emission produced by the `G4AtomicDeexcitation` process are taken into account by adding the difference of the emissions' summed kinetic energies and the binding energy of the innermost vacated shell to the kinetic energy of the daughter nucleus. This neglects that the emission is not emitted unidirectional but isotropic and recoil momenta must thus be treated as vector quantities. The effect of this shortcoming is shown in Figure 32. Here the simulated particle momenta resulting from a ^{22}Na beta-decay are compared between the current Geant4 code and the code developed as part of this work. At lower momenta the distribution of the beta-emission is visible. The peak at $\approx 1.5\,\text{MeV/c}$ results from the ^{22}Ne daughter nucleus and should show a small amount of broadening due to the recoil resulting from the deexcitation emission. It is evident from the figure that for the current Geant4 code, shown in black, this is not the case.

Decay Chains and Activation in the Current Code

Another important requirement which was articulated in Section 4.3 is the capability to process decay chains and nuclear activation. The current code uses an extended solution of the Bateman equations (Bateman, 1910) to calculate the abundances of all progeny nuclei in a chain starting at a given isotope (Truscott, 2002). The inclusion of the creation of isotopes through activation is possible but requires a manual user input of activation rates even if they are determined by the Monte-Carlo simulation itself. Additionally, a volume specific treatment of activation is missing, which is an important shortcoming, as components consisting of the same materials are not generally subject to the same activation rates.

Concerning decay chains the current code is ineffective as it will always generate the decay emission of all chain members, regardless of if this emission is an intended observable. The performance consequences of this behavior are evaluated in Section 5.6.

Conclusions drawn from the Current Code

It was shown that while the current code fulfills most of the experimental requirements it lacks a consistent software design. This makes extensions difficult, e.g the addition of missing features such as self-consistent long-term activation calculations, radioactive background sources and fast means of simulating the statistical outcome of a large number of decays or decay chains. In conclusion, a reimplementation of the code, which addresses the shortcomings, and is based on a proper problem domain decomposition is beneficial. By following good design principles such a new code would additionally be more maintainable and extensible in order to accommodate future requirements. Accordingly, this path was followed and a new radioactive decay code for Geant4 has been developed as part of this work. This code will be introduced in detail in the following chapters alongside extensive verification and validation studies.

5 A new Radioactive Decay Code for Geant4

The *new* radioactive decay code for Geant4 which is described in this chapter was developed in accordance with the considerations and requirements discussed in the previous chapter. It seamlessly integrates into Geant4 versions 4.9.3 and 4.9.4, although at the moment a C++ compiler capable of selected features (`auto, unordered_map/hash_map`) from the new C++-11 standard is required[*]. Similar to the current Geant4 code this new code retrieves evaluated empirical data from a library based on the popular Evaluated Nuclear Structure Data File (ENSDF; Tuli, 2010), maintained by the National Nuclear Data Center - NNDC and distributed e.g. by the International Atomic Energy Agency. In the following a detailed description of the code will be given. The outline of this description follows the requirements identified as part of the problem domain decomposition in Section 4.5:

- Data management (Section 5.1)

- Sampling of the (discrete) emission resulting from the individual decay and generation of the daughter nucleus (Section 5.3)

- Calculation of the beta-emission spectrum (Section 5.4)

- Calculation of the number of nuclei within a decay chain - may include activation (Section 5.5)

- User interface (will not be covered as it is a purely technical aspect)

- Interface with the Monte-Carlo tool-kit (will not be covered as it is a purely technical aspect)

These requirements have been associated with objects which have well defined responsibilities as documented in the UML class diagram shown in Figure 33. The corresponding activity diagram is shown in Figure 34. Again both diagrams share the same color coding.

5.1 Data Library

The problem domain analysis in Chapter 3.5 yielded that a radioactive decay simulation will need to access empirical and precalculated data. This is necessary because ad-hoc calculations of many quantities are not possible or to computing intensive. As thousands of radioisotopes exists a broad, standardized data library is required. The Evaluated Nuclear Structure Data File (December 2010 version) was found to be well suited. It is in common usage (e.g. as the underlying data library of the popular NuDat online data retrieval system; Sonzogni, 2005), is standardized in a well documented fashion and contains entries for more than 3000 isotopes and parent excitation levels. Additionally, the current Geant4 code uses it as its base library which simplifies comparisons between both codes.

The half-life, gamma energy and intensity values given in ENSDF are generally derived from measured data. In contrast the conversion electron yields are based on theoretical calculations. Additionally, the ENSDF data was extended to include information on fluorescence and Auger electron energies and yields based on the atomic data library distributed with ENSDF, which in turn is taken from a compilation by Schönfeld and Janßen, 1996 which includes empirical data from Bambynek et al., 1972; Bearden and Burr, 1967. An evaluation in Pia et al., 2011 has shown that the latter data compilations as well as more modern derivatives thereof represent the current state-of-the-art for atomic data compilations. In particular, it was found that this empirical data is more accurate than the theory-derived EADL [†](Perkins, Chen, Cullen, and Hubbell, 1991) data used by the current Geant4 atomic deexcitation process, `G4Photonevaporation`.

---

[*]   At the time of this writing the following compilers fulfill these requirements (*with additional boost library): GCC4.4, Intel C++ 11.0*, MSVC 10.0, IBM XLC++ 11.1* (https://wiki.apache.org/stdcxx/C%2B%2B0xCompilerSupport)

[†]   Evaluated Atomic Data Library

Figure 33: An UML class diagram for the new radioactive decay code showing the relations between the individual classes. The colors hint at the responsibilities and are matched to the activity diagram in Figure 34, they are: physics simulation (blue), data management and preparation (orange) and decay chain processing (purple). Each decay type is responsible for simulation its characteristic physics. The deexcitation and fluorescence emission for the statistical simulation approach (green) is produced by the `G4VDecayEmission` base class.
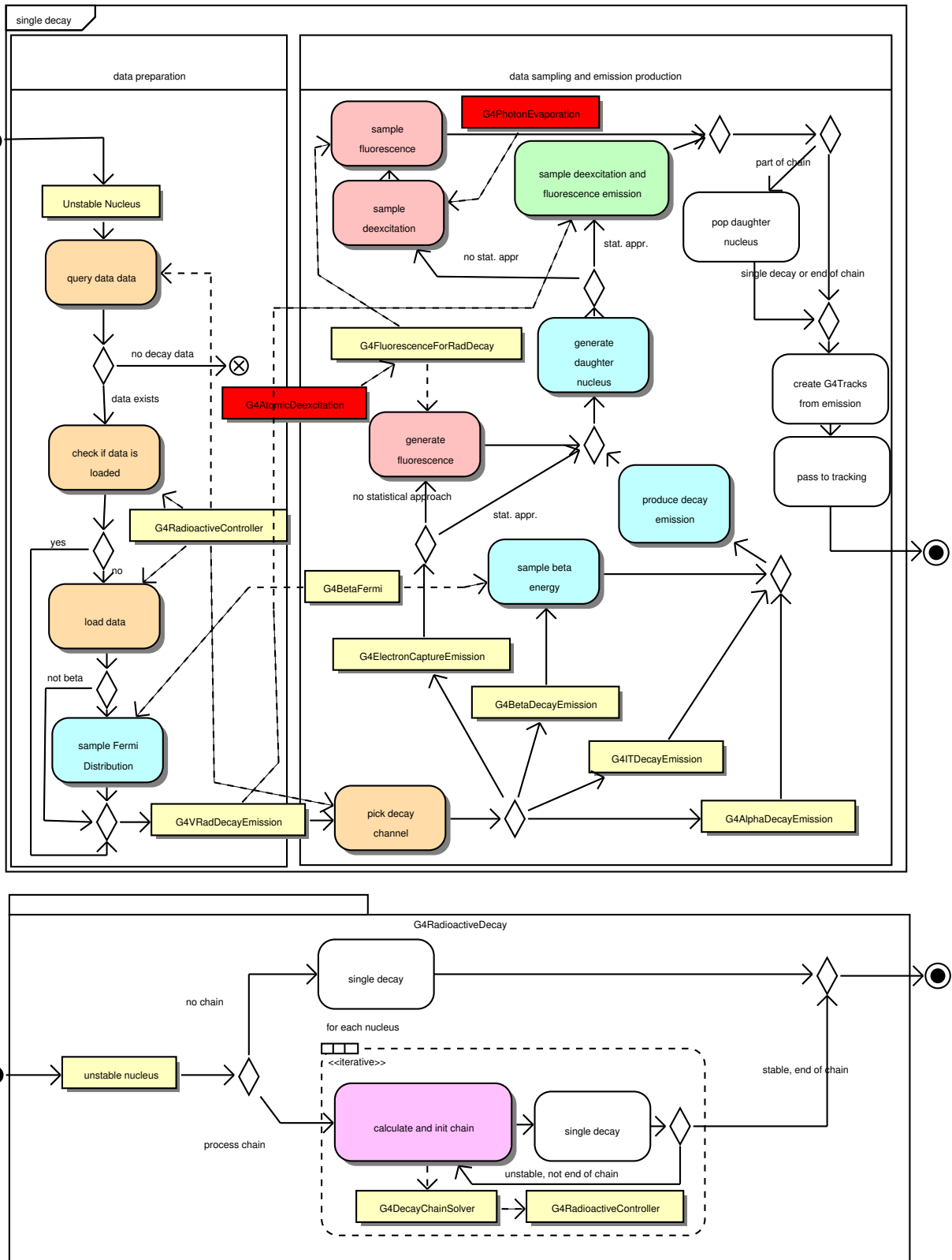
Figure 34: An UML activity diagram for the new radioactive decay code showing how the decay of a nucleus proceeds. The color scheme is matched to the class diagram in Figure 33 and hints at activity types: physics simulation within the radioactive decay (blue), physics simulation by other processes (red), data management and preparation(orange) and decay chain calculations (purple). The emission produced by the statistical decay approach is highlighted in green.

Database Management

Data management for the new code is provided by the `G4RadioactiveController` class which is responsible for all tasks regarding data retrieval, initialization and management. This also includes granting access to the decay data to other classes. The data is loaded from a reprocessed version of ENSDF which is output by a parser written as part of this work. In general the decay database is supplied in plain text and ordered by isotope with a naming scheme following `zZZZ.aAAA` where `ZZZ` is the atomic number and `AAA` the mass number. An example of a library file is shown in Figure 35. It contains four basic types of records:

- **P**arent records. This record type lists the excitation energy of the parent nucleus in the third field and its half-life in seconds in the fourth field. It must precede any valid isotope record and delimits decay channels with different half-lives or excitation energies for a given isotope

- **#** - comment records. Either comments out field headers as is the case in the second line of the example or comments out reference information extracted from the ENSDF file.

- **L**evel records. These records hold information regarding decay channel probabilities and the excitation energy of the daughter nucleus. The third field denotes the decay type (`DT`); the associated branching ratio (`BR`) is given in the fourth field. The excitation energy (`E`) of the daughter nucleus is given in the fifth field, while the sixth field denotes the half-life (`HL`) of this excited level. In case of beta decays the seventh field may give the end-point energy (`EE`) of the beta spectrum in case an entry for this quantity is given in ENSDF. If not the end point energy is calculated from the Q-Value (`QVAL`) of the decay which is given in the eighth field. Fields 9 through 14 give the relative intensities of the different decay types: beta-intensity (`BI`), electron capture intensity (`ECI`) and total beta + electron capture intensity (`TI`), alpha intensity (`AI`), alpha energy (`AE`) and internal transition intensity (`ITI`). The absolute intensity in occurrences per 100 decays is obtained by multiplying the relative intensities with the branching ratio. By using separate fields the number of level records can be reduced if for instance electron capture and β^+-decays result in the same post-decay excitation state. The last three fields give electron capture probabilities for the K-, L- and M- shells (`ECK`, `ECL`, `ECM`). The level record determines the excitation energy and shell vacancies passed to the `G4Photonevaporation` and `G4AtomicDeexcitation` processes.

- **G**amma records contain information needed for the new statistical approach presented in the next section. The "BR" field denotes the intensity of the gamma radiation per 100 decays while the energy of the radiation in given by the "E"-field. The last field again gives the half-life (HL) of the level from which the deexcitation occurs.

- **E**lectron records contain the same information as **G**amma records but this time for conversion electrons.

- Finally **X** and **XA** contain the information given in a **G**amma record for X-ray fluorescence and Auger electron emission.

The data is represented in a fashion that changes in the database will be taken into account by the simulation in a straight forward and implementation-independent way, i.e. when changing emission intensities the user does not have to consider any internal renormalization procedures. This contrasts with the current Geant4 code, where e.g. the radiation intensity is determined by the interplay of three processes with three respective databases (see Section 5.2).

5.2 Statistical vs. Per-Decay Approach

Currently the Geant4 radioactive decay code decays a given unstable nucleus on a per-decay level. This means that deexcitation emission is sampled physically correct for every decay, i.e. taking into account

```
1  P 133BA 0.0          3.31759e+08
2  # I    DT   BR        E        HL        EE        QVAL        BI        ECI        TI        AI
                AE        ITI       ECK       ECL       ECM
3  L 133BA EC   1.0               80.9972   6.28e-09  0           517.4     0          3         3
                0         0         0         0         0         0
4  G 133BA G    34.06             80.9971   6.28e-09
5  E 133BA CE   49.387            45.0125   6.28e-09
6  E 133BA CE   7.35696           75.2828   6.28e-09
7  E 133BA CE   1.51226           79.78     6.28e-09
8
9  ...
10
11 E 133BA CE   0.044676          354.796   1.5e-10
12 X 133BA X_KA1 65.313           30.9728   1.5e-10
13 X 133BA X_KA2 35.3539          30.6251   1.5e-10
14 X 133BA X_KB 23.7372           35        1.5e-10
15 X 133BA X_L  16.477            4.29      1.5e-10
16 XA 133BA A_K  14.7504          25.5      1.5e-10
17 XA 133BA A_L  141.956          3.55      1.5e-10
18 # 133BA   ELC(276G) CORRECTED AS PER F. E. CHUKREEV 1/17/89
19 # 133BA G        Precise EG, IG measurements: 1993Ve06, 1991We08, 1987Mu07,
20 # 133BA G 1985Ku26, 1983Ch11, 1983De11, 1983Yo03, 1981He15, 1980HaYX, 1980VyZZ,
```

Figure 35: An excerpt from a radioactive decay data library file for ^{133}Ba. The first character defines the record type: P - parent record, L - level record, G - gamma record, E - conversion electron record, X - fluorescence or Auger record and # - comment.

if level transitions are allowed or forbidden or occur in cascades. In Chapter 4.3 it was found that experiments often do not observe single decays but measure the statistical outcome of many decays. Accordingly, for the majority of applications this simulation approach induces unnecessary computational overhead. Furthermore, the deexcitation is not handled by the decay process itself, but by a separate process: G4Photonevaporation. While this makes sense from the point that other processes included in Geant4 may also produce an excited nucleus which needs to be deexcited, it also introduces a dependency on a second data library which is not managed by the decay code. In Chapter 4.6 it was already discussed how the interplay of these two databases can result in a violation of energy conservation.

Additionally, the intensity of the deexcitation emission will depend on the tabulated values from both databases, being $I_{\mathrm{rad}} = BR \cdot I_{\mathrm{a} \to \mathrm{b}}$. Here BR is the branching ratio given in the radioactive decay library; and $I_{\mathrm{a} \to \mathrm{b}} = N_0 \cdot p_{\mathrm{a} \to \mathrm{b}}$ is the number of decays N_0 multiplied with the respective probability $p_{\mathrm{a} \to \mathrm{b}}$ for a transition from energy level a to level b; as given in the photon evaporation library. If cascading occurs $I_{\mathrm{a} \to \mathrm{b}}$ is non-trivial as it involves the product of the sum of all transition probabilities $p_{\mathrm{n} \to \mathrm{a}}$ of the N higher energy levels which can fill level a and the probability $p_{\mathrm{a} \to \mathrm{b}}$ of level a transitioning to level b

$$I_{\mathrm{a} \to \mathrm{b}} = N_0 \cdot p_{\mathrm{a} \to \mathrm{b}} \cdot \sum_{n=0}^{N} p_{\mathrm{n} \to \mathrm{a}}. \tag{20}$$

The probability $p_{\mathrm{n} \to \mathrm{a}}$ may again depend on multiple transitions from even higher energy levels leading to additional recursion in Equation 20. It is obvious that this complex interplay of transition probabilities makes it very tedious and error-prone to change the radiation intensity resulting from a specific level transition, e.g. if it is found that the simulation underestimates a certain photo-peak in a spectrum.

The newly developed code circumvents these problems by using a new statistical simulation approach. Here the individual decays are not modeled physically accurately. Rather the accurate simulation of many decays is emphasized. This means that with a statistically sufficient large number of decays, intensities

are correctly reproduced; similar to most experimental scenarios. As will be shown in Section 5.6 this results in significant performance gains. Another benefit is that the delegation to a dedicated deexcitation process becomes obsolete. As both the radiation energies and intensities are given in the ENSDF library they can be included in the radioactive decay data as well. Consequently, all information is sampled from the single consistent data source introduced in Section 5.1. This greatly simplifies editing of the data and ensures consistency with the ENSDF source. In cases where the traditional per-decay approach is needed the new code can default to the existing functionality, also ensuring compatibility and reproducibility for existing applications.

5.3 Discrete Decay Emission

In addition to the deexcitation emission, which is either sampled by the new statistical approach or by the classical delegation to the `G4Photonevaporation` and `G4AtomicDeexcitation` processes, discrete particle emission resulting from the transmutation of the nucleus will occur. The sampling of alpha particles as well as neutrinos resulting from electron capture decays is implemented as a separate object for each decay type taking into account the underlying physics introduced in Chapter 3.5. These objects are also responsible for producing the daughter nucleus.

5.4 The Beta-Fermi-Function - Sampling the Continuous Beta-Spectrum

Beta-decays are unbound three-body decays an the beta particles will have a continuous spectrum. Due to the electrical charge of both the nucleus and the emitted particles this spectrum is slightly shifted towards higher or lower energies. This non-trivial shift which is due to the screening of the nucleus by shell electrons can be taken into account using the Beta-Fermi-function.

$$F(Z,W) = \frac{2(1+S)}{((2S)!)^2}(2p\rho)^{2S-2}e^{\pi\eta}|(S-1+i\eta)!|^2 \tag{21}$$

with $S = (1 - \alpha^2 Z^2)^{1/2}$, $\rho = R/(\hbar/mc)$, the nuclear radius R, the beta-particle momentum p, the nuclear charge Z, the fine structure constant α and $\eta = \pm Ze^2/\hbar V$ where V is the speed of the beta-particle at large distances from the nucleus; the $+(-)$ correspond to an electron and positron respectively (Fermi, 1934).

This function is computationally expensive to calculate which is why several approximations have been developed in the past (Bethe and Bacher, 1936; Hall, 1950; Massey and Mohr, 1933; Nilsson, 1956). In Venkataramaiah et al., 1985, an overview of these approximations is presented, which are generally found to be accurate within 1%, and a simple empirical solution for the Fermi-function is developed; also accurate within 1%. It is this solution which is used for sampling beta-decays in the new radioactive decay code and which will be introduced in this section.

Care was taken that the parameters passed to the Beta-Fermi function are physics-relevant but code-independent. They consist of the atomic charge Z, end-point energy E_p as well as the decay type (β^- or β^+) and optionally forbiddenness. This parameter set is sufficient for many Fermi-function approximations similar to those summarized and developed by *Venkataramaiah et. al*. A substitution of the currently implemented solution with a user-defined function is thus easily possible should it become necessary.

The new code uses the computationally most performant approximation developed by Venkataramaiah *et. al* for calculating the Fermi correction factor $F(Z,E)$ for beta-emission at energy E for an isotope with atomic number Z,
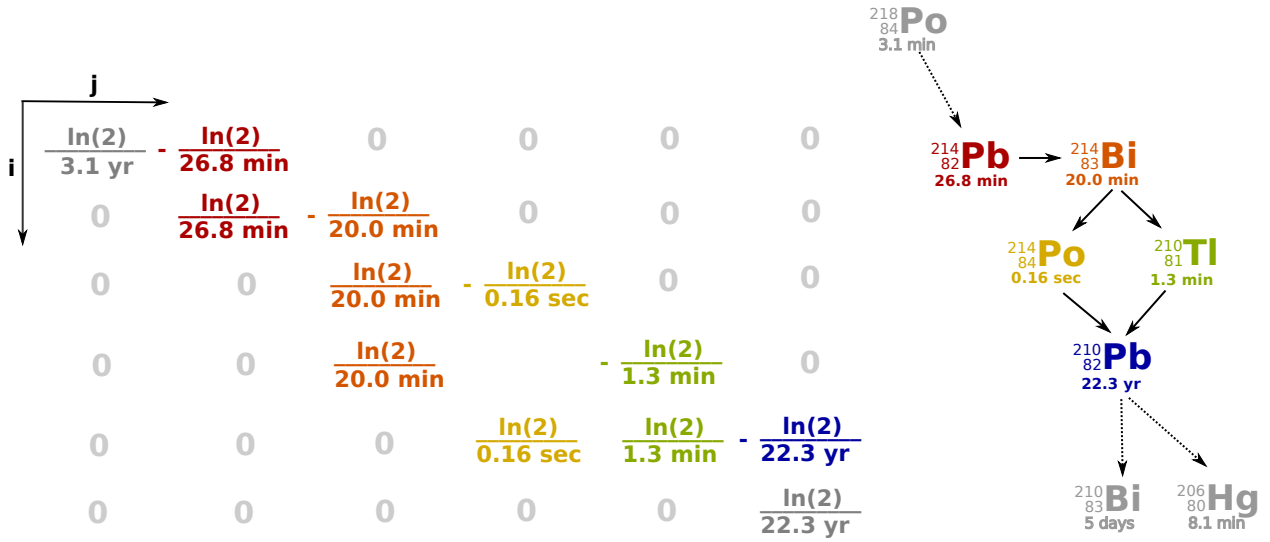
$$F(Z,E) = [A + B/(E-1)]^{\frac{1}{2}}. \tag{22}$$

Figure 36: An illustration of how the Λ-matrix is filled using part of the ^{238}I decay chain as an example.

The constants A and B are determined by linear regression methods using the data of Rose (Rose, 1955) and satisfy

$$A = \begin{cases} 1 + a_0 \exp(b_0 Z) & \text{for } Z \geq 16 \quad (23a) \\ 7.3 \times 10^{-2} Z + 9.4 \times 10^{-1} & \text{for } Z < 16 \quad (23b) \end{cases}$$

with

$$\begin{aligned} a_0 &= 404.56 \times 10^{-3} \\ b_0 &= 73.184 \times 10^{-3} \end{aligned}$$

and

$$B = a Z \exp(bZ) \tag{24}$$

with

$$a = \begin{cases} 5.5465 \times 10^{-3} & \text{for } Z \leq 56 \\ 1.2277 \times 10^{-3} & \text{for } Z > 56 \end{cases}$$

$$b = \begin{cases} 76.929 \times 10^{-3} & \text{for } Z \leq 56 \\ 101.22 \times 10^{-3} & \text{for } Z > 56. \end{cases}$$

The correction factor $F(Z, E)$ is then input into the Beta-Fermi function

$$N(p)\,dp = F(Z, E)\,p^2\,(E_0 - E)^2\,dp \tag{27}$$

where E_0 is the end-point energy of the beta-spectrum, obtained from the tabulated radioactive decay data library, E is the total energy of a beta-particle with momentum p. The results of the above calculations are cached in memory. Consequently the Fermi-function only has to be evaluated once for any given parameter set; subsequent decays will retrieve the necessary data from this cache which significantly improves overall performance.

Isotopes resulting from radioactive decays are often unstable themselves. This leads to chains of subsequent decays until a stable daughter product is reached, examples of which include the ^{232}Th, ^{237}Np and ^{238}U decay chains which frequently occur in reactor fuel cycles and a part of the natural radioactive background. It is often desirable to only simulate those isotopes in a chain which are of interest as observables, either due to their half-life or due to the radiation emitted when they decay. In such a case a full Monte-Carlo simulation of every single decay is very inefficient as most of the time is spent calculating irrelevant quantities. Instead one should only sample the emission resulting from those decay chain members which are actually of interest. This requires determining the number of these nuclei at a specified time. For a system of n nuclei where the ith nucleus-species decays into the $(i+1)$th nucleus-species this calculation can be done by solving a system of differential equations with a general form of

$$
\begin{aligned}
\frac{dN_1(t)}{dt} &= -\lambda_1 N_1(t) \\
\frac{dN_2(t)}{dt} &= \lambda_1 N_1(t) - \lambda_2 N_1(t) \\
&\vdots \\
\frac{dN_n(t)}{dt} &= \lambda_{n-1} N_{n-1}(t) - \lambda_n N_n(t).
\end{aligned}
\tag{28}
$$

Here N_i is the quantity of the ith nucleus-species at time t and λ_i is the corresponding decay constant. These equations can be extended to include a constant per-particle activation rate α_i by substituting λ_i with $k_i = \lambda_i + \alpha_i$. This results in the similar equations

$$
\begin{aligned}
\frac{dN_1(t)}{dt} &= -k_1 N_1(t) \\
\frac{dN_2(t)}{dt} &= \lambda_1 N_1(t) - k_2 N_1(t) \\
&\vdots \\
\frac{dN_n(t)}{dt} &= \lambda_{n-1} N_{n-1}(t) - k_n N_n(t).
\end{aligned}
\tag{29}
$$

A general approach for solving such a set of equations for any number of decay products was first derived by Bateman (Bateman, 1910) in 1910. The above equations have consequently become known as the Bateman equations. One of the main disadvantages of Bateman's original solution is that it does not consider branching, i.e that a parent nucleus can decay to different daughter nuclei via different decay channels. This disadvantage has been overcome by many of the Bateman-derived computational algorithms which exist; with the model in the current radioactive decay code (Truscott, 2002) being one example. These algorithms are generally computationally expensive in the sense that they require recursive loops for each nucleus in a decay chain but may achieve good overall performance if the calculations can be cached and reused.

Algebraic Approach

The code developed as part of this work uses an alternative algebraic approach derived by M. Amaku and coworkers in Amaku, Pascholati, and Vanin, 2010 building upon work by R. J. Onega (Onega, 1969), D. Pressyanov (Pressyanov, 2002), L. Moral and A. F. Pacheco (Moral and Pacheco, 2003) as well as T. M. Senkov (Semkow, 2004) and D. Yuan and W. Kernan (Yuan and Kernan, 2007). Here recursion

occurs only in the initialization phase and not as part of the actual calculation. In this approach the properties governing the decay chain are rewritten into a matrix in Hessenberg form

$$
\Lambda =
\begin{bmatrix}
-k_1 & 0 & 0 & 0 \\
k_1 & -k_2 & 0 & 0 \\
0 & \ddots & \ddots & 0 \\
0 & 0 & k_{n-1} & k_n
\end{bmatrix}
\tag{30}
$$

and a vector $\mathbf{N}(t)$ with

$$
\mathbf{N}(t) =
\begin{bmatrix}
N_1(t) \\
N_2(t) \\
\vdots \\
N_i(t)
\end{bmatrix}
\tag{31}
$$

for which all parameters have the same meanings as in Equations 28 and 29. The system of equations in(29) may then be written as

$$
\frac{d\mathbf{N}}{dt} = \Lambda \mathbf{N}.
\tag{32}
$$

This algebraic approach was originally introduced by Onega in 1969. It was subsequently extended by Yuan and Kernan as well as Semkow to include branching by modifying Λ to

$$
\Lambda =
\begin{bmatrix}
\Lambda_{11} \\
\Lambda_{21} & \Lambda_{22} \\
\vdots & \vdots & \ddots \\
\Lambda_{i1} & \Lambda_{i2} & \cdots & \Lambda_{i,i} \\
\vdots & \vdots & & \vdots & \ddots \\
\Lambda_{n1} & \Lambda_{n2} & \cdots & \Lambda_{ni} & \Lambda_{nn}
\end{bmatrix}
\tag{33}
$$

with

$$
\Lambda_{ij} = k_{i-1} b_{ij}
\tag{34}
$$

for $i > j$ and

$$
\Lambda_{ii} = -k_i.
\tag{35}
$$

In Equation 34 b_{ij} denotes the branching ratio from the jth to the ith component of the decay chain with $\sum_{i=j+1}^{n} b_{ij} = 1$. An example is shown in Figure 36 on page 70. In computational practice Λ can be constructed by iterating through the decay chain and taking activation rates into account if necessary. Because Λ is independent of the actual nuclei numbers it must only be constructed once for each set of nuclei and activations characterizing a given chain. Calculations using different nuclei numbers can reuse these initial matrices as needed. Using the above definitions the number of nuclei of each species in the decay chain is given by

$$
\mathbf{N}(t) = e^{\Lambda t} \mathbf{N}(0)
\tag{36}
$$

which can be rewritten to

$$
\mathbf{N}(t) = C \, e^{\Lambda_d t} \, C^{-1}
\tag{37}
$$

as described by Onega. In Equation 37 C is a square matrix with the nth column consisting of the nth eigenvector of Λ, so that $C = [\mathbf{c}_1, \mathbf{c}_2, \cdots, \mathbf{c}_n]$. C^{-1} is its inverse and Λ_d a diagonal matrix with the elements $\Lambda_{d,nn}$ being the nth eigenvalue of Λ.

M. Amaku and coworkers derive an algorithmic approach for calculating the matrices C, C^{-1} and Λ_d which is computationally less expensive and more accurate than a general approach of numerically diagonalizing the matrix. The elements of $C = [c_{ij}]$ can be calculated with the recurrence expression

$$c_{ij} = \frac{\sum_{k=j}^{i-1} \Lambda_{ik} c_{kj}}{\Lambda_{jj} - \Lambda_{ii}} \tag{38}$$

for $i = 2, \cdots, n$, $j = 1, \cdots, i-1$ and $c_{jj} = 1$. Similarly the elements of $C^{-1} = [c_{ij}^{-1}]$ are given by

$$c_{ij}^{-1} = \sum_{k=j}^{i-1} c_{ik} b_{kj} \tag{39}$$

for $i > j$ and $b_{jj} = 1$. Using C and C^{-1}, Λ_d is given by

$$\Lambda_d = C^{-1} \Lambda C \tag{40}$$

resulting in a general form for Equation 37 of

$$\mathbf{N}(t) = C \begin{bmatrix} e^{-\Lambda_{d,11} t} & & & \\ & e^{-\Lambda_{d,22} t} & & \\ & & \ddots & \\ & & & e^{-\Lambda_{d,nn} t} \end{bmatrix} C^{-1} \mathbf{N}(0). \tag{41}$$

The above equations allow the activation rates to follow any arbitrary time profile which can be evaluated in a physically meaningful fashion, i.e. negative times and singularities do not occur. An example is a step profile, with a constant time invariant activation and a rise in activation rates occurring at certain time intervals. This is for instance the case for near-Earth orbits, when the spacecraft travels through the South Atlantic Anomaly, a region of high proton fluxes.

Implementation of Long Term Activation
In the new code replenishment and generation of unstable isotopes through activation are calculated on a per-volume level, i.e. for each component defined in the detector geometry. A user-space book-keeping class, `G4ActivationBookkeeping`, keeps track of all activations occurring in a given volume. The new material and isotope composition of the volume at a given time is then evaluated by the `G4DecaychainSolver` class. Afterwards material properties are updated within the geometry and the volumes are set as radioactive background sources with an associated activity via the `G4RadDecayVolumeBookkeeping` class. This class is responsible for sampling the radioactive (background) emission which occurs for every primary event; it needs the primary flux as input. Both bookkeeping classes are designed to require minimum custom user code and can be easily integrated into existing applications.

5.6 Computational Performance

Large scale Monte-Carlo simulations may take weeks to compute, even on large computer clusters with thousands of CPUs. Accordingly, inefficient code may easily result in performance penalties in the same order of magnitude, which will not only materialize in lost time but also lost money. The design of the

Figure 37: The ^{233}U decay chain which was simulated as part of the performance tests. The initial isotope of the chain was varied from ^{233}U to ^{213}Bi to test different chain lengths.
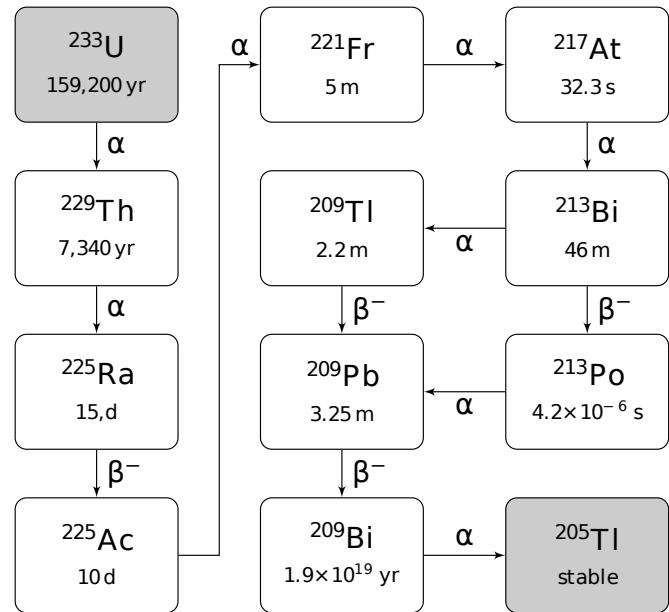
new radioactive decay code keeps this in mind and uses e.g. hash-maps (`std::unordered_map`) after the C++11-standard which allow element access times of $O(1)$ instead of $O(log(n))$ as would be the case for traditional `std::map` containers. In order to estimate the possible performance benefits the new code was compared with the current Geant4 code in three general test scenarios, each of which is commonly encountered in a wide range of applications.

- Decay an isotope $100,000$ times using the classical and the statistical approach.

- Decay a chain of isotopes and sample all emission which has occurred from all isotopes in the chain within a sampling time Δt. Repeat this $10,000$ times.

- Decay a chain of isotopes and sample the emission from a single isotope within the chain occurring within a sampling time Δt Repeat this $10,000$ times.

Each of the above tests was repeated 200 times to ensure that any temporary CPU load by the operating system or other running processes would not bias the results. For the first test the isotopes ^{22}Na(β_+), ^{60}Co(β_-), ^{229}Th(alpha) and ^{133}Ba(EC) were decayed. These were chosen as an exemplary selection of each of the particle emitting decay types. The ^{233}U decay chain which is shown in Figure 37 was chosen for the remaining two tests. The performance for different chain lengths was estimated by varying the initial nucleus within this chain.

The performance tests were run on a 12-core INTEL *XEON* machine at $2.93\,$GHz operating under Ubuntu 10.10 *Maverick Merecat* and an, except for the decay code, unaltered version of *Geant4.9.4-p01*. The *GCC 4.4.5* compiler[*] with Geant4 standard optimization flags was used for compilation; the C++11 extensions were enabled. Within the performance test application the radioactive decay was the only physics process included, thus guaranteeing that no other processes to which the decay emission might be subject to in subsequent tracking would influence the results. The geometry was empty except for a "world" volume consisting of a vacuum filled box with $10\,$m side length.

Single Decay Performance

Figure 38 shows the relative performance change for the single decay tests with respect to the runtime the current code requires for the test. In most scenarios the new statistical approach is significantly faster. An exception are isotopes which have a large number of deexcitation emissions such as ^{229}Th. Here the linear increase of sampling time with the number of emissions results in a performance penalty.

---

[*]   Gnu Compiler Compilation
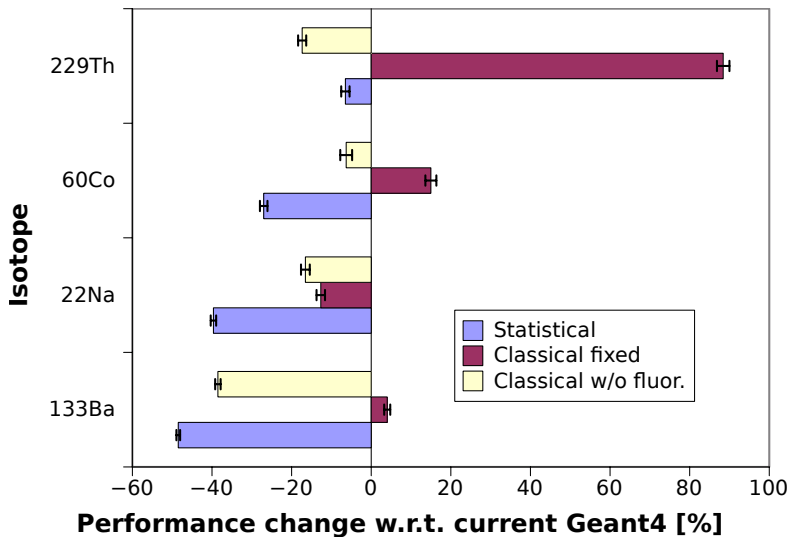
Figure 38: Relative performance change when using the new code with respect to the runtime of the current Geant4 code. Each simulation consisted of $100,000$ decays and was repeated 200 times. Three different sampling techniques are shown: statistical approach, classical approach and classical approach without post-decay fluorescence production. This last approach resembles the current Geant4 implementation.

When comparing the classical approach for decay emission production, i.e. delegation to `G4Photonevaporation` and `G4AtomicDeexcitation`, two scenarios were distinguished. In the first case, labeled "classical fixed" in the figure, the vacant shell index, which may be output by the `G4Photonevaporation` process at the end of deexcitation, is passed to the `G4AtomicDeexcitation` process for X-ray and Auger-electron production. This is done for all decay types.

As the current Geant4 code does not pass the shell index except for internal transition decays, a second scenario labeled "classical w/o fluor." in the figure was evaluated[*]. It is apparent from the figure, especially for ^{229}Th-decays, that the switch to the physically more meaningful behavior, i.e always passing a shell index to `G4AtomicDeexcitation`, results in a severe performance penalty. If a full treatment of X-ray and Auger-electron emission is needed and simulation performance is critical the author thus strongly recommends the use of the new statistical approach.

Decay Chain Performance

The decay chain performance comparison is shown in Figure 39. Here one should consider that the current Geant4 code does not take into account the time at which the chain emission is to be sampled at. Instead it is in the user's responsibility to keep track of relevant emission. This behavior results in a severe performance penalty because much of the sampled emission may actually not be of interest at all. The new code samples the decay chain in such a way that only emissions occurring after a given time period are actually produced. This explains the increase in computing time needed by the new code between ^{233}U as the initial isotope and ^{229}Th. As is shown in Figure 37, thorium has a much shorter half-life than uranium. Since the time period over which the emission from the chain is sampled remains fixed at 3×10^{13} s $= 95120$ years much less uranium than thorium will have decayed. This also reduces the number of subsequent decays within the chain and hence much less emission has to be sampled.

If only the emission of a single isotope within a chain is of interest, the behavior of both codes is similarly divergent. Again the current Geant4 inefficiently samples all occurring emission, regardless of the importance for the simulation result. Instead the user must identify this emission and discard of the rest. In contrast the new code allows to select individual isotopes within a given chain. Only the emission resulting from such decays will be sampled and passed to tracking. In Figure 39 this scenario is shown by the two single data points labeled "End of chain - C" for the new code with classical deexcitation sampling and "End of chain - S" for the new code with statistical deexcitation sampling. The time needed by the

---

[*]   At the time of this writing this bug has been fixed in Geant4.9.5.

Figure 39: Absolute performance of the new code and the current Geant4 code when decaying the ^{233}U decay chain. The chain length was varied by setting different initial isotopes. The lines are shown as a visual guidance. The uncertainties are sufficiently small as to not be distinguishable in the plot.
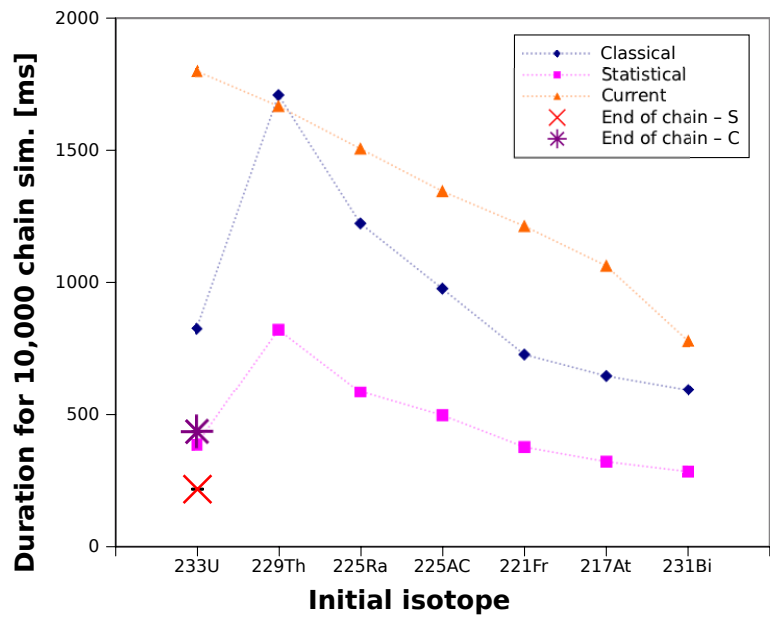
current code is given by the respective ^{233}U data point. In total the performance gain for decay chains is $\approx 800\%$ when using statistical sampling and still $\approx 450\%$ for classical deexcitation sampling.

6 Verification and Validation of the Radioactive Decay Simulation in Geant4

The estimates obtained from simulations like those for the IXO/ATHENA background critically rely on uncertainty quantifications of the involved models. Especially if a new code is developed it must be thoroughly tested. In order to quantify the accuracy of the newly developed decay code, and also the existing software, two different evaluations where performed. In a first step the accuracy of both codes was *verified* by comparing them with the ENSDF library which both used as empirical and precalculated data input. In a second step a concrete application example consisting of the model of a high purity germanium detector (HPE), was used to experimentally *validate* both codes.

The main difference between the two approaches it that even though much of the ENSDF data is based upon measurements, a significant fraction is also theory derived, and neither data types have been independently evaluated by the author. Accordingly, the ENSDF data is taken "as is". In particular, this means that no validity or consistency checks have been performed on the data before usage. The purpose of *verification* is now to ascertain that *"the software and its associated products conform to requirements [...] for all life cycle activities* during each life cycle process [...]; satisfy standards, practices, and conventions during life cycle processes; and successfully complete each life cycle activity and satisfy all the criteria for initiating succeeding life cycle activities [...]."* (IEEE, 2005).

With respect to the radioactive decay simulation this corresponds to the software being able to sample decays in accordance with its input data (the data of 3000+ isotopes in the ENSDF file) and correctly interact with the Geant4 Monte-Carlo toolkit it is embedded in. As such the verification is application independent as neither a detector geometry definition or other processes occurring during particle tracking are of interest.

In contrast the *validation* measurements were performed within our team and detailed knowledge about the experiment is available. The validation measurements resemble a "real–world" application example of an experiment which uses a High-Purity Germanium (HPGe) detector. By comparing a simulation of this detector with measurements it is validated if an application using the radioactive decay software can correctly model the experiment and the governing physical laws. In more technical terms validations thus *"provid[e] evidence that the software and its associated products satisfy system requirements allocated to software at the end of each life cycle activity, solve the right problem (e.g., correctly model physical laws, [...]), and satisfy intended use and user needs."* (IEEE, 2005). For a general purpose tool-kit like Geant4 such a validation will usually be application-specific because it will model the specific experiment with which the validation data was measured. Nevertheless results may be transferable to other use-cases as well.

6.1 Verification with ENSDF Data

Because the verification was performed on a more "atomic" level it will be discussed first. The validation measurements are presented in Section 6.2. Additional verifications and validations were also performed for the long-term activation simulation. These are presented separately in Section 6.3.1.

6.1.1 Evaluated Data Preparation

The ENSDF library contains two general types of data: such which was directly derived from measurements (mainly gamma-ray energies and intensities as well as beta-decay end point energies) and such which is based on theoretical calculations (mainly fluorescence, Auger- and conversion electron data). The fluorescence and Auger emission data is furthermore based on additional data sources as was discussed in Chapter 5.1.

The energy and intensity values for both data types were extracted from the ENSDF using the RADLIST program (Burrows, 1988). By using this tested ENSDF-parser it was assured that no errors were introduced into the evaluated data during the automated conversion.

---

* A *life cycle activity* is the sum of tasks a software should fulfill.

6.1.2 Simulated Data Preparation

The ENSDF file contains data on over 3000 isotopes and excitation energies. Each of these isotopes was decayed a simulated 10^6 times. In the underlying Geant4 simulation only the decay process had been enabled and aside from a vacuum filled world volume the geometry was otherwise empty. For each decay the resulting radiation and particles along with their kinetic energy were recorded decay type dependent in two separate histograms. The first histogram ranged from $0\,\mathrm{keV} - 30\,\mathrm{keV}$ with a binning size of $0.05\,\mathrm{keV\,keV}$; the second histogram ranged from $0 - 30,000\,\mathrm{keV}$ with a binning size of $0.2\,\mathrm{keV}$. These two binning schemes were chosen in order to properly distinguish discrete radiation a nearby energies in the X-ray and gamma-ray energy regime. Beta-emission was distinguished from conversion and Auger-electrons by modifying the decay codes to produce *geantinos** instead of beta-particles.

With this simulation approach 2910 parent excitation levels and isotopes were simulated for the current Geant4 code with radioactive decay database version 3.3. For the new code, based on a newer ENSDF file, 3040 simulations using the new statistical approach were conducted, an additional 130 excitation levels and isotopes.

6.1.3 Data Analysis

The large number of isotopes simulated results in a large number of a datasets which needs to be included in the analysis. This makes manual processing a tedious task, which is why an automated analysis routine was written in IDL. This routine takes the level and particle energies from the evaluated data as an initial estimate E_0 for where simulated emission may be present. In the proximity of this initial energy estimate the data is then scanned for emission events within an interval of $E_0 \pm 0.5\,\mathrm{keV}$ at energies below $30\,\mathrm{keV}$ and $E_0 \pm 5.0\,\mathrm{keV}$ at higher energies. If discrete emission contained in a single histogram bin is found the intensity of the emission I is given by

$$I = \frac{N_{\mathrm{Events/bin}}}{N_{\mathrm{sim}}} \tag{42}$$

with an uncertainty of $\sqrt{N_{\mathrm{Events/bin}}}/N_{\mathrm{sim}}$. The energy uncertainty is determined by the binning size. It is possible that events are distributed over multiple neighboring bins due to the fact that recoil from previous emission is transferred to the deexciting nucleus. In such a case the intensity is calculated from the sum of events in the affected bins. Should the evaluated data indicate that emission at a slightly different energy may have also contributed to this sum, the intensities of both emissions as given in the evaluated data are summed for further analysis. For the emission energy the median energy of all affected bins is used; accordingly, its corresponding uncertainty is given by the median deviation.

The previous steps result in radiation energy and intensity values for both the evaluated and simulated data. From these absolute and relative energy and intensity deviations can be calculated, making overall comparisons and comparisons of individual isotopes, such as the ones measured as part of the validation, possible.

For beta-emission it was chosen to compare the end-point energies of the beta-spectrum. These are tabulated in the evaluated data sets but need to be determined from the simulated data by performing a least-squares fit to the spectrum using e.g. the Beta-Fermi function described in Sec. 4.6. It should be stressed, that this introduces a model dependency into the results, which is why a validation of the simulated beta-spectrum against experimental data should be done whenever possible. Performing such a comparison for every simulated isotope would be beyond the scope of this paper as it can not be automated due to the lack of compiled experimental data.

The accuracy and stability of the automated analysis was assessed with a complete set of simulations using the new statistical approach. These simulations were not compared to the RADLIST output but to the output of the parser used for reprocessing the ENSDF into the radioactive decay library. Ideally, one

---

* In Geant4 geantinos are particles which do not interact with anything. The only process relevant to them is transportation.
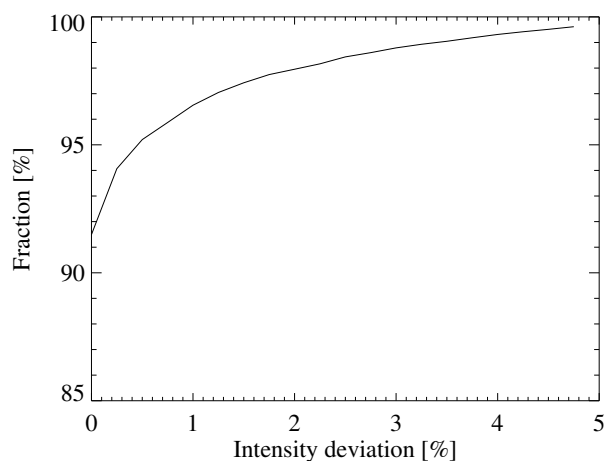
Figure 40: The percentage of simulated emission intensity deviations as output by the automated analysis routines when compared to the ENSDF-derived simulation input. A "perfect" analysis would show zero deviations. Due to emission lines at nearby energies this is not the case, as these lines cannot always be distinguished leading to an inaccurate determination of the corresponding intensities.

would expect a perfect match of the simulation with its input. More realistically some intensity deviations are expected for those cases where nearby emission impedes the automated analysis. Additionally, energy deviations in the order of one bin width will necessarily occur. As is apparent from Figure 40, 99% of all simulated emission is within an intensity deviation of 3% from the simulation input. The automated analysis can thus be considered sufficiently stable and precise for identifying global trends in the accuracy of the decay codes.

6.1.4 Verification Results

The following verification results focus on identifying global trends in the accuracy of the decay codes and exploring the regions in which a simulation can be expected to give reliable results. Nuclide charts have been used to efficiently convey a maximum amount of information. They are aided by contour plots for identifying individual trends dependent on specific parameters. A contrasting, detailed comparison of selected isotopes is performed as part of the validation measurements presented in Section 6.2.

Estimate of the Verification Uncertainties

Due to the "global" nature of the following results it is unfeasible to attach uncertainties to individual values. Nevertheless, knowledge of the intrinsic errors on an equally global level is important to determine the informational value of the presented data. For the radiation energy the uncertainty is determined by the binning scheme used for the simulation output (the energy uncertainties in ENSDF are negligible). This results in $\Delta E = 0.05\,\mathrm{keV}$ at energies below $30\,\mathrm{keV}$ and $\Delta E = 0.2\,\mathrm{keV}$ at higher energies. On should note that these bin widths where chosen keeping the finite energy resolution of radiation detectors in mind which is often at best a few $10\,\mathrm{eV}$. Accordingly, the evaluated energy values in ENSDF due not have significantly lower uncertainties either. In consequence, smaller bin widths would have resulted in significant amounts of additional data but not much informational gain.

For the intensity uncertainty the matter is a more sophisticated. Here it makes sense to compare the relative intensity deviations, not absolute intensities, as the correct simulation of weak peaks might be of the same interest to an experimentalist as that of a strong peak is. Accordingly, knowledge of the relative intensity deviation uncertainty is required. If the relative intensity deviation, δI, is given by

$$\delta I = \frac{I_{\mathrm{sim}} - I_{\mathrm{meas}}}{I_{\mathrm{meas}}} \tag{43}$$

Figure 41: The distribution of the relative uncertainties of the observed deviations between simulated and evaluated radiation intensities with respect to the level intensity. The contour levels correspond to the percentile of values at at given deviation error with respect to the number of values at a given level intensity. At higher intensities, values are more sparse resulting in the visible "single box" contours.
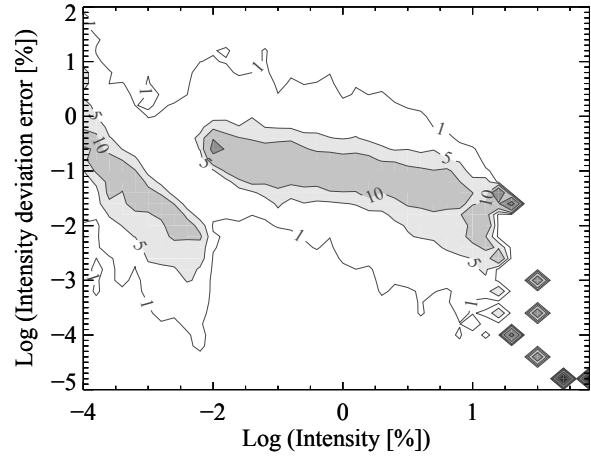
the corresponding uncertainty is

$$\Delta(\delta I) = \sqrt{\left(\frac{1}{I_{\text{meas}}} \cdot \Delta I_{\text{sim}}\right)^2 + \left(-\frac{I_{\text{sim}}}{I_{\text{meas}}^2} \cdot \Delta I_{\text{meas}}\right)^2} \tag{44}$$

where "sim" denotes simulated intensities and corresponding uncertainties while "meas" identifies the measured values.

Figure 41 shows a compilation of the observed intensity deviation uncertainties for the complete set of isotopes included in the verification. As is apparent from the figure even at low intensities the uncertainties are in an acceptable range below 10% for the majority of the data. This should be accurate enough for most applications; considering that the accuracy of many physics processes in Geant4 is in the same order of magnitude (see Wright et al., 2006 and Chapter 3.3).

Intensity Deviations

Figure 42 shows the line intensity accuracy of the current Geant4 code and the new code employing the single database statistical approach when compared to ENSDF data. As is apparent from the figure, both codes reproduce the gamma- and alpha-emission intensities given in ENSDF reasonably well for the majority of isotopes. The mean deviation $(I_{\text{exp}} - I_{\text{sim}})/I_{\text{exp}}$ amounts to $8.57 \pm 2.22\%$ for gamma-rays and $2.47 \pm 2.26\%$ for alpha-emission when using the current code. For the new code the mean deviation is minimal with $1.85 \pm 2.07\%$ for gamma-rays and $5.61 \pm 2.62\%$ for alpha-emission. The outliers present in the simulations using the new code can be explained by the way the ENSDF data is parsed into the radioactive data library. In cases where multiple datasets describing the same emission exist, the parser is tuned to favor experimentally determined data or if such a distinction is not possible use the first available data set. In contrast the RADLIST program preferably uses theoretical data according to the documentation (Burrows, 1988). Additionally, the parser is currently not capable of handling all variants of non-standard ENSDF entries. A result a small number of isotopes have not been simulated.

It is further apparent from the figure that the current Geant4 code has problems reproducing the ENSDF intensities for conversion electrons. This manifests itself in an overall deviation of $35.67 \pm 6.32\%$ compared to a $9.54 \pm 0.98\%$ for the new code.

For the current Geant4 code the gamma- and conversion electron intensity deviations must be attributed to the `G4Photonevaporation` process, to which the production of this emission is delegated. A comprehensive validation of this process would go beyond the scope of this work and avoiding the problem by modifying the conversion probabilities is usually unfeasible as it would require altering both the `G4Photonevaporation` and `G4RadioactiveDecay` libraries. The non-trivial interplay of the transition probabilities given therein usually makes this prohibitively tedious as is discussed in Chapter 4.6.

Accordingly, the newly developed code should be favored for application scenarios depending on the correct simulation of isotopes for which large intensity deviations were found.

In case of fluorescence and Auger emission it is evident from Figure 43 that the deviations between evaluated ENSDF intensities and those produced by current Geant4 code are even larger. For X-ray emissions the mean intensity deviation amounts to 52.64±1.97%; for Auger-electron emission to 52.57± 0.96%. Similar to the scenario described above not the radioactive decay code alone is responsible for the observed offsets but its interplay with the `G4AtomicDeexcitation` process. It is interesting to note that the deviations are largest for the isotopes on the upper-left of the nuclide chart; isotopes which usually decay via electron capture. This substantiates the assumption that the `G4AtomicDeexcitation` is the source of the severest deviations — it is called by the current code if electron capture data is present in the radioactive decay library (see Chapter 4.6 for details). The new code again yields better results with the new statistical approach. Here the mean deviation amounts to $4.09 \pm 1.78\%$ for X-ray emission and $1.34 \pm 1.16\%$ for Auger electron emission. This is a more than 10-fold improvement with respect to the current Geant4 code. Especially for X-ray detectors sensitive in this energy range, such as IXO and ATHENA, this can be regarded as a crucial improvement.

Discrete Energy Deviations

Many of the applications introduced in Chapter 4.3 identify studied isotopes using the (photo-peak) energy of the emitted radiation. In consequence, any Monte-Carlo simulation of such an experiment needs to accurately emit gamma and X-ray radiation, Auger- and conversion-electrons as well as alpha particles at their respective discrete energies.

The comparisons shown in Figures 44 and 45 lead to the conclusion that for the current Geant4 code X-ray and Auger electrons are generally emitted at an energy which is within 0.2 keV of the evaluated value. Using the new code this already good value further improves to below 0.1 keV, which is close to the Fano-limited energy resolution of silicon detectors (e.g. $\approx 150\,\text{eV}@5.9\,\text{keV}$). At higher energies and for alpha particles as well a conversion electrons the observed energy deviation is below 0.5 keV for the current Geant4 code and better than 0.2 keV when using the new code, which close to the energy resolution of many semiconductor detectors (Perez-Andujar and Pibida, 2004) and well beneath the resolving capabilities of scintillation based devices.

The outliers present in the comparison of the new code with ENSDF are due to the fact the ENSDF parser for the radioactive decay library preferably uses experimental data in case were multiple data sets for an isotope are present while the RADLIST program which was used to parse the ENSDF comparison data prefers theoretical data (Burrows, 1988). Within both energy ranges no energy dependence of the energy deviation was observed. Depending on the absolute energy precision required a user should check the level energies given in the radioactive decay and `G4Photonevaporation` databases and determine if the values therein are consistent with the expectations.

Beta Decays

In contrast to the previous comparisons beta-decays result in a continuous spectrum. A comparison of the spectral shape is not possible with ENSDF data as only the mean energy and the end point energy of the spectrum are usually given. While the mean energy is usually derived from a model the end-point energy is often obtained from measurement and was accordingly chosen for the comparison. Because these simulations output the complete beta-particle spectrum, the end-point values have been obtained by fitting the beta decay function implemented in the radioactive decay code to the data. As is exemplary shown for the current code in Figure 46 the accuracy of the simulation deteriorates in the energy range between 2000 keV and 6000 keV. This is due to the fact that many isotopes feature multiple decay channels with different end-point energies in this range. Their superposition makes the automated analysis less stable, which also reflects itself in the larger uncertainties shown in Figure 46. Figure 47 shows the end-point energy deviations on a per-isotope basis displayed as nuclide charts for both the current and the new decay code.
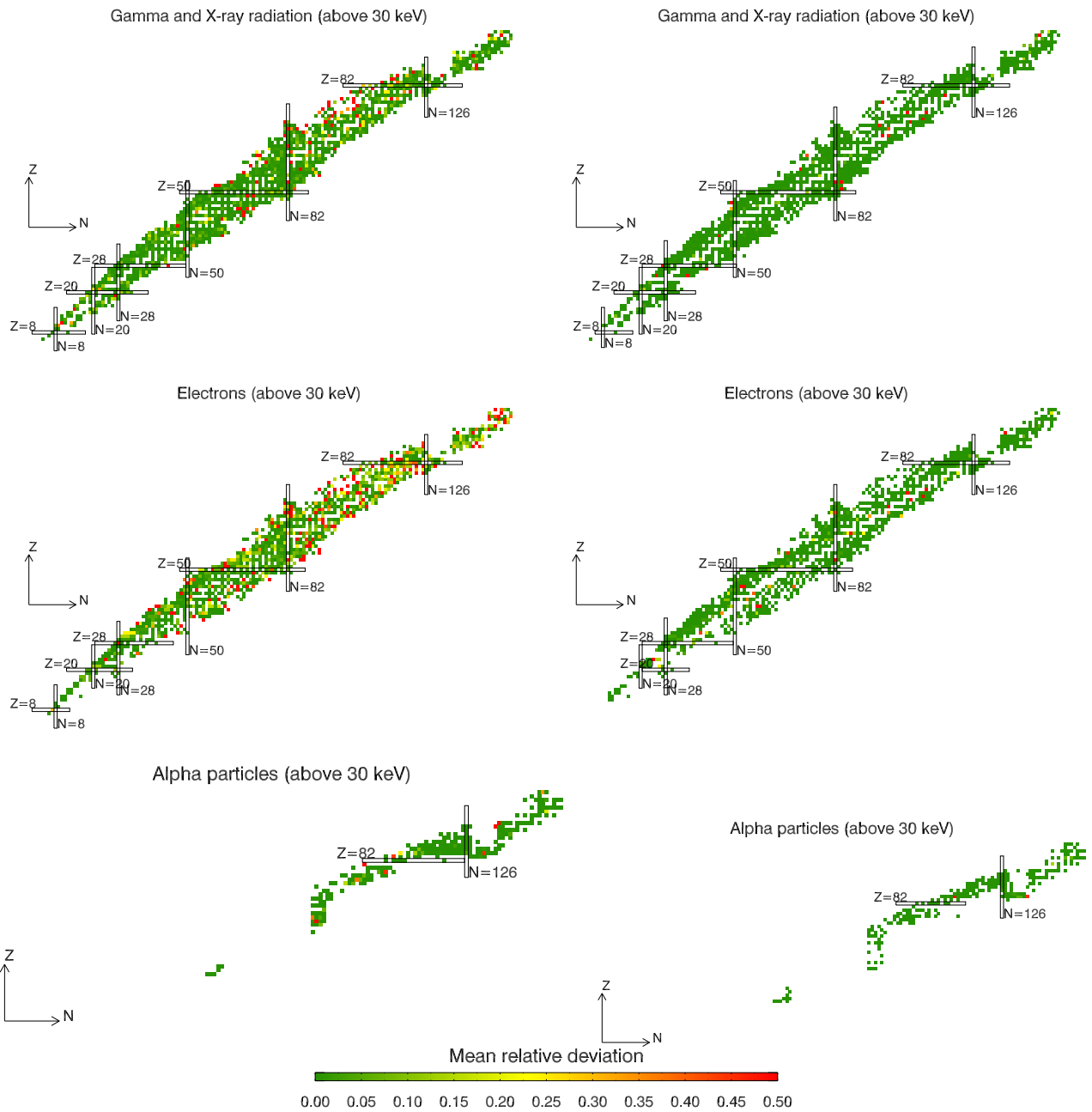
Figure 42: Nuclide charts showing the median relative intensity deviations per isotope for gamma (top), conversion-electron (middle) and alpha (bottom) emission. Simulations using the current Geant4 code are shown on the left; simulations using the new code and employing the statistical approach are shown on the right.
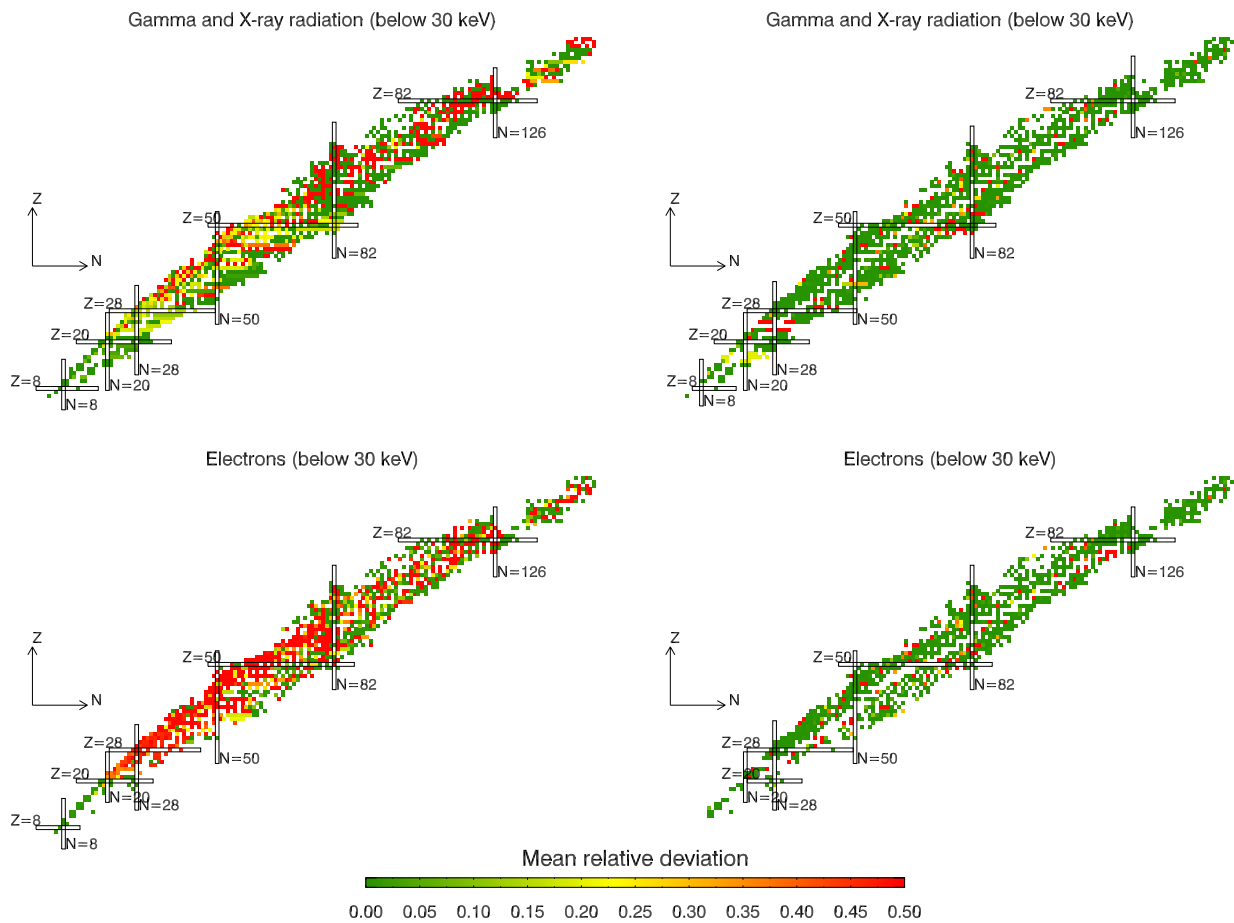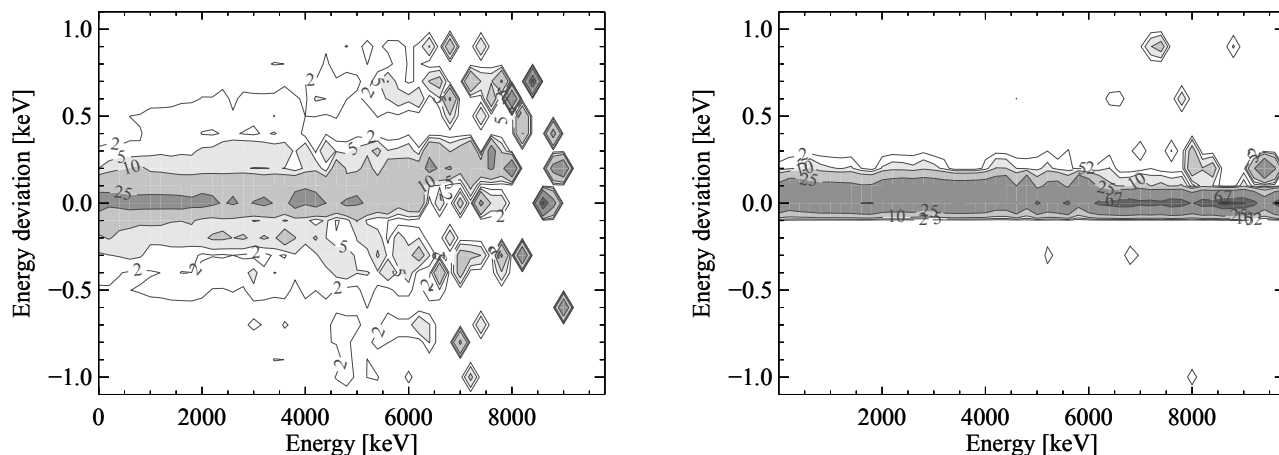
Figure 43: Nuclide charts showing the median relative intensity deviations per isotope for X-ray (top) and Auger-electron (bottom) emission. Simulations using the current Geant4 code are shown on the left; simulations using the new code and employing the statistical approach are shown on the right.

Figure 44: The distribution of the absolute energy deviation of simulated emission lines when compared to ENSDF data with respect to the radiation energy for all level energies. The contour levels correspond to the percentile of values at a given energy deviation with respect to the number of values at a given radiation energy. At higher energies evaluated values are more sparse resulting in fractured contours. The current Geant4 code is shown on the left, the new code with the statistical approach on the right.
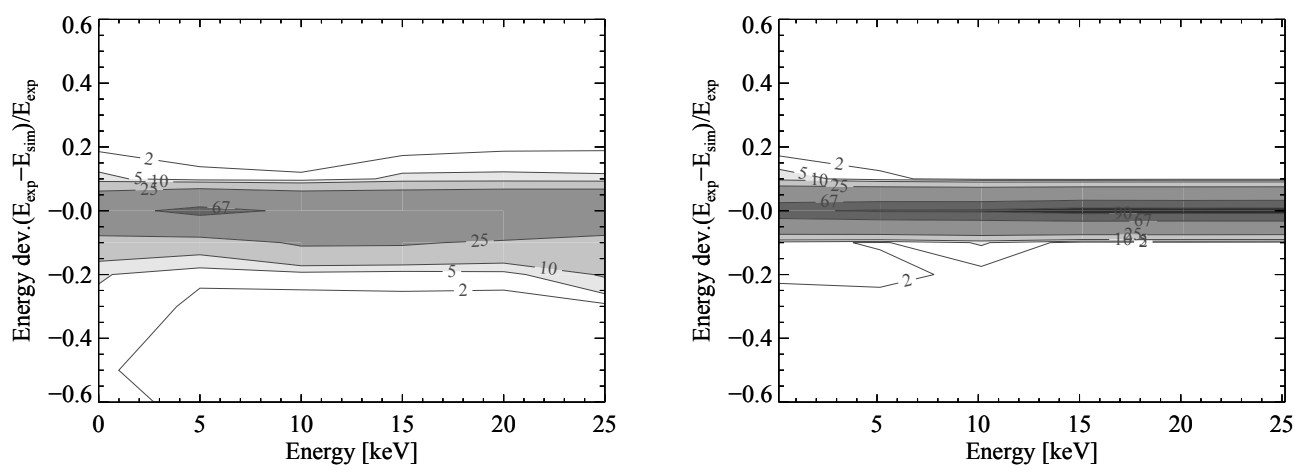
Figure 45: The distribution of the absolute energy deviation of simulated emission lines when compared to ENSDF data with respect to the radiation energy for level energies below $25\,\mathrm{keV}$. The contour levels correspond to the percentile of values at a given energy deviation with respect to the number of values at a given radiation energy. The current Geant4 code is shown on the left, the new code using the statistical approach on the right.
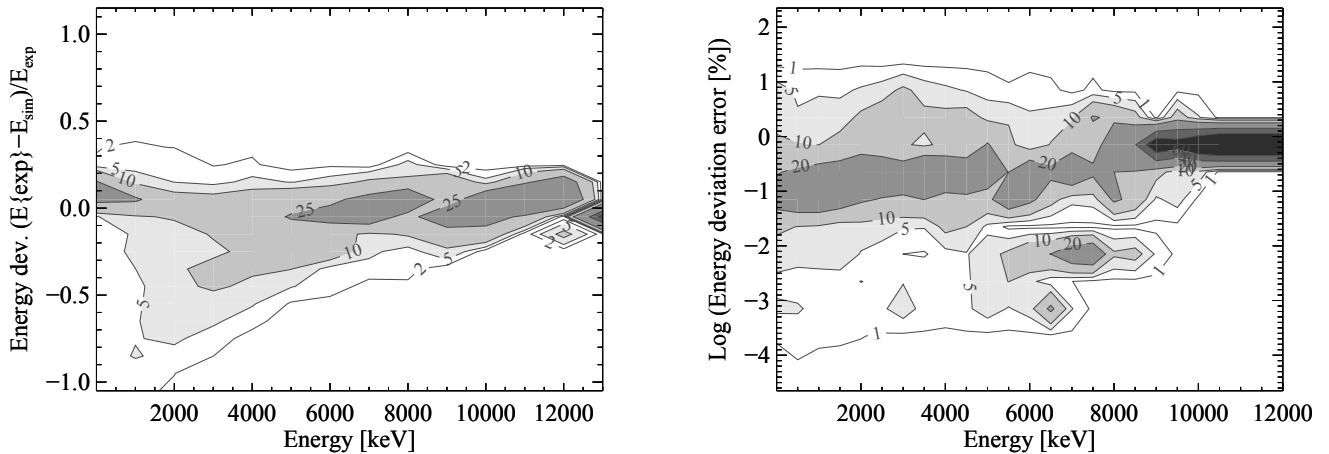
Figure 46: Left panel: The distribution of relative beta-decay end point energy deviation with respect to the end-point energy. The contour levels correspond to the percentile of values at given relative energy deviation with respect to the number of values at a given end-point energy. Right panel: the distribution of relative energy deviation uncertainties with respect to the end-point energy. The contour levels correspond to the percentile of values at given endpoint energy deviation error with respect to the number of values at a given end-point energy.

Overall a median end-point energy deviation of $23.42 \pm 1.41\%$ for β^- emission and $36.94 \pm 5.59\%$ for β^+ emission was observed when simulating with the current Geant4 code. The new code shows significant improvements for β^- emission ($13.99 \pm 1.92\%$ deviation). For β^+ emission the performance of the current code is matched by the new code with a deviation of $37.49 \pm 1.21\%$. The largest deviations occur at high atomic numbers where the currently used Beta-Fermi Function is less accurate (Venkataramaiah et al., 1985). However, in contrast to the existing code users can easily implement their own Fermi-function in such cases.

As a consequence of the instable analysis routines with respect to beta-emission and the fact that a spectral comparison is not possible, the results presented here are shown for completeness only. Individual verification should be performed if necessary, examples of which are given in Section 6.2.

6.1.5 Conclusions from the Verification Tests & Outlook

The verification presented in this section has led to the identification of two important trends for the radioactive decay codes in Geant4:

- Both codes are capable of reproducing the evaluated ENSDF intensities of gamma-radiation within a deviation of $\approx 20\%$. Especially the current code exhibits problems in the X-ray regime and when simulating Auger- and conversion electrons. It was found that this behavior has to be attributed to the `G4Photonevaporation` process in case of conversion electrons and the `G4AtomicDeexcitation` process for Auger and X-ray fluorescence emissions. It should be noted that the underlying atomic data libraries of these processes partially deviate from those of ENSDF and need not necessarily be considered state-of-the-art anymore. If ENSDF conformity is required the new code should be used.

- Both codes reproduce the discrete radiation and particle energies within the energy resolution of common detectors. Additionally, these values are readily accessible in the underlying databases.

A comparison of Beta-emission end-point energies has also been presented but is not as accurate as the results for discrete emission are. Further research on this subject would be worthwhile for application scenarios for which such emission is of importance.
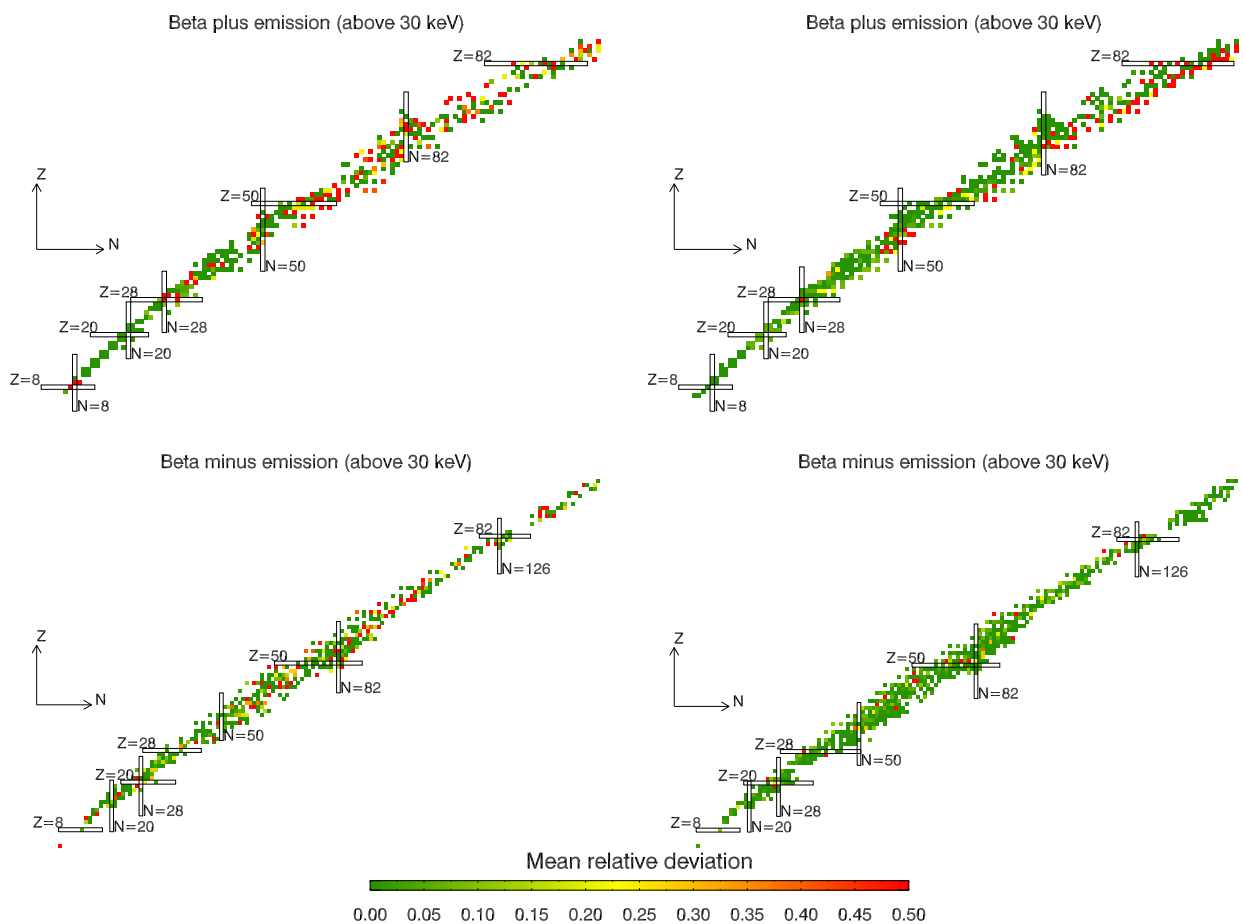
Figure 47: Nuclide charts showing the median relative beta-decay end-point energy deviation per isotope for β^+ (top) and β^- (bottom) emission. Simulations using the current Geant4 code are shown on the left; simulations using the new code and employing the statistical approach are shown on the right.

Figure 48: The experimental setup consisting of a HPGe detector which is placed inside the hollow lead shielding blocks in the center left part of the image. These blocks are the outer part of a collimator which additionally consists of a tin and a copper tube, placed around the cylindrical detector head. Additional steel shielding can be seen on the tables. The source was suspended in front of the detector by a thin wire. Not visible is the detector's dewar.

6.2 Validation Measurements

In this section validation measurements with a High Purity Germanium detector (HPGe) are presented. The comparison data was taken at Oak Ridge National labs by Zane W. Bell. The experimental setup chosen was kept as simple as possible in order to minimize the chance of introducing uncertainties and deviations into the simulation model. It consists of an Ortec 70 mm diameter pop-top germanium detector with parameters as shown in Figure 49. The dimensions were obtained through private communication with the manufacturer.

The detector head was situated inside a shielding, consisting of hollowed lead blocks, as is shown in Figure 48. Inside the shielding two additional collimator tubes were concentrically placed around the detector head; one made of copper ($\varnothing = 10.165$ cm, thickness 3.4 mm) and a second out of tin ($\varnothing = 10.3$ cm, thickness 1.35 mm). The tubes were aligned with the dewar facing edge of the lead blocks and are each 30.4 cm long. As will be shown later this collimator effectively shields against source radiation which has scattered off the laboratory's walls, ceiling or equipment therein.

Additional shielding of the detector's field of view was provided by steel shot filled boxes and a steel plate which were placed upon the tables supporting the detector and had the form of two perpendicular walls. Both the detector's dewar and the lead collimator parts were placed on borated wax blocks; the first supported by a wooden crate, the latter situated on top of the steel table. The radioactive samples consisted of 6 different calibrations sources (Eckart&Ziegler type D): ^{22}Na, ^{54}Mn, ^{57}Co, ^{60}Co, ^{133}Ba, ^{137}Cs. These were suspended on a wire situated 30 cm in front of the detector head and centered on the detector's horizontal axis. The calibrated activities and decay properties of these sources are summarized in Table 6. Table 9 additionally lists the intensities and energy positions of their most prominent photopeaks. All sources are enclosed in a circular plastic disc with the dimensions of the disc obtained from the manufacturer.

Each of the above sources was measured for a detector live time of 10 min. Before and after the set of source measurements a 10 min background measurement was performed. Spectra were recorded using a multichannel analyzer with 8096 channels attached to to a data acquisition PC. After the measurements the mean of the two background spectra was normalized to the source measurement time and subtracted from the source spectra prior to any further analysis.

Experimental Data Analysis
The measured and background-subtracted spectra were analyzed using the *HYPERMET* program introduced in Phillips and Marlow, 1976. HYPERMET performs least square fits to the data. From these fits it obtains parameters such as photo-peak height, area and width but also pile-up related characteristics.

Table 6: Properties of the measured calibration sources on the calibration date. The half-lives were obtained from NuDat.

Isotope	Reference activity	Half-life	Activity	Decay type
^{22}Na	37.0 kBq (06/2006)	2.603 y	15.6 kBq	β^+
^{54}Mn	37.0 kBq (06/2006)	312.120 d	2.7 kBq	EC
^{57}Co	37.0 kBq (06/2006)	271.740 d	1.8 kBq	EC
^{60}Co	37.0 kBq (06/2006)	1925.280 d	24.1 kBq	β^-
^{133}Ba	37.0 kBq (05/2006)	10.551 y	29.7 kBq	EC
^{137}Cs	37.0 kBq (06/2006)	30.080 y	34.3 kBq	β^-

Figure 49: A sketch of the HPGe-detector head: **1** Mount cup length, **2** Distance end cap – crystal, **3** Mount cup base, **4** Beryllium entrance window, **5** Mylar insulator, **6** Crystal end radius, **7** Outer dead layer thickness, **8** Inner dead layer thickness and bore size, **9** Mount cup thickness. Dimensions were obtained from private communication.
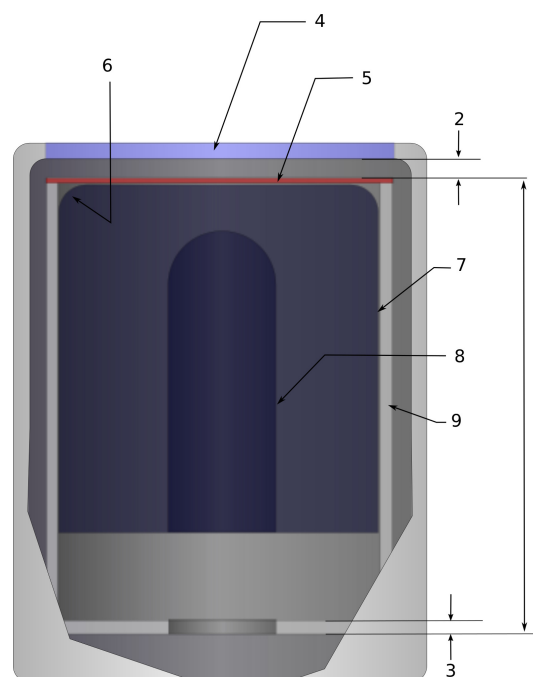
Figure 50: The upper part of the plot shows the measured ^{133}Ba photo-peaks at 79.61 keV and 80.99 keV (dots). Also shown are the background and peak models fitted to the data using HYPERMET. The background consists of a constant linear part (lower dashed line) and a step-function modeling the step of the Compton component (upper dashed line). The lower energy peak is shown dotted, while the solid line is the sum of the second peak and the other components. The low-energy exponential tail is not distinguishable for these peaks. The lower part shows the residuals in terms of σ uncertainties (solid area: 1σ, lines: 3σ).
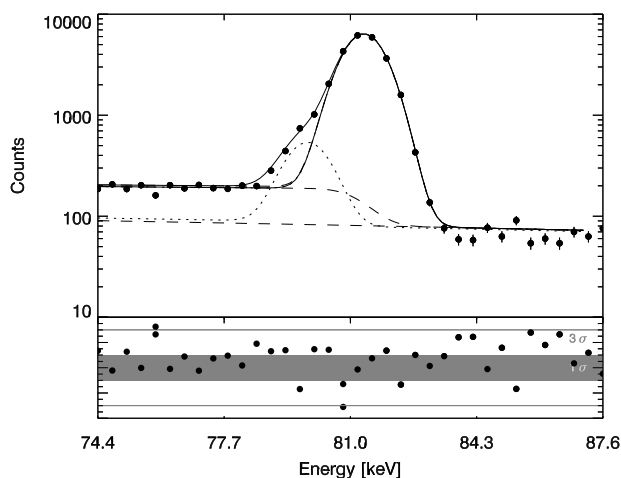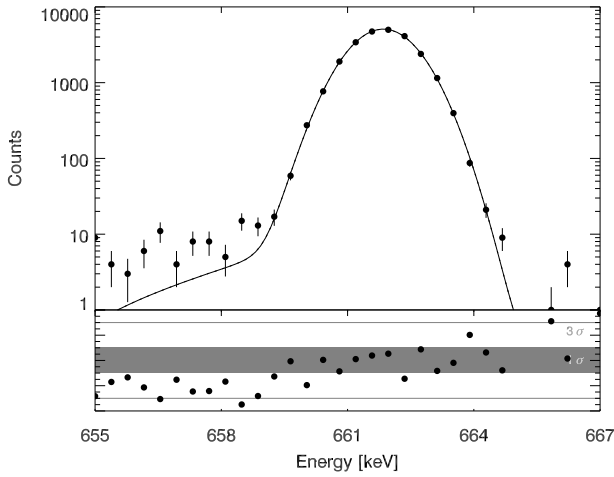
Figure 51: The upper part of the plot shows the measured ^{137}Cs photo-peak at 661.66 keV (dots). Also shown is the model fitted to the data using HYPER-MET (solid line). Clearly visible is the exponential tail towards low energies, which is added to the Gaussian peak. For the ^{137}Cs source this feature is stronger than for the other isotopes as it higher activity leads to more pile-up. The lower part shows the residuals in terms of σ uncertainties (solid area: 1σ, lines: 3σ).

A short summary of the fit functions used by the program is presented in the following in the order of decreasing importance. The dominating features are exemplary shown in Figures 50 and 51.

1. Ideally, gamma rays of a given energy would result in a sharp spectral line when registering in a detector. Due to its finite energy resolution a detector registers a broadened peak instead. This peak usually includes a Gaussian component,

$$G(x) = A \cdot \exp\left(-\frac{x - x_c}{\sigma}\right)^2 \tag{45}$$

with amplitude A, position x, center x_c and the energy resolution defining width σ. For Germanium-detectors the width usually is a function of the squared gamma-ray energy as is shown in Figure 52. Two examples of these peak shapes are shown in Figures 50 and 51.

2. Incomplete charge collection moves events from the full photo-peak energy towards lower energies, adding an exponentially decaying component, $d(x) = \exp(x - x_c)/\beta$, with slope β, to the peak. Folded with Gaussian noise of width γ this yields

$$D(x) = \alpha \exp\left(\frac{x - x_c}{\beta}\right) \times \frac{1}{2}\text{erfc}\left(\frac{x - x_c}{\gamma} + \frac{\gamma}{2\beta}\right) \tag{46}$$

where α is a normalization factor to the amplitude A of the photo-peak and x_c is the position of the photo-peak's center; $\text{erfc}(u)$ is the complementary error function. The parameters α and β may vary with energy. To account for this the a polynomial model was fitted to the parameters obtained from photo-peaks at different energies as shown in Figure 53. This polynomial was then used to determine the parameter's values at arbitrary energies. Figure 51 exemplary shows the strong exponential tail of the ^{137}Cd photo-peak at 661.66 keV.

3. Very strong photo-peaks may exhibit an additional, longer exponential tail, $T(x)$, at energies below the peak which can be attributed to surface effects and will also influence peaks lying at lower energies

$$T(x) = \tau A \exp\left(\frac{x - x_c}{\nu}\right) \times \frac{1}{2}\text{erfc}\left(\frac{x - x_c}{\mu} + \frac{\mu}{2\nu}\right). \tag{47}$$

The slope parameter ν is usually one to two orders of magnitude larger than β while the relative amplitude τ is one to three orders smaller (Phillips and Marlow, 1976). The width of the Gaussian is again determined by μ.
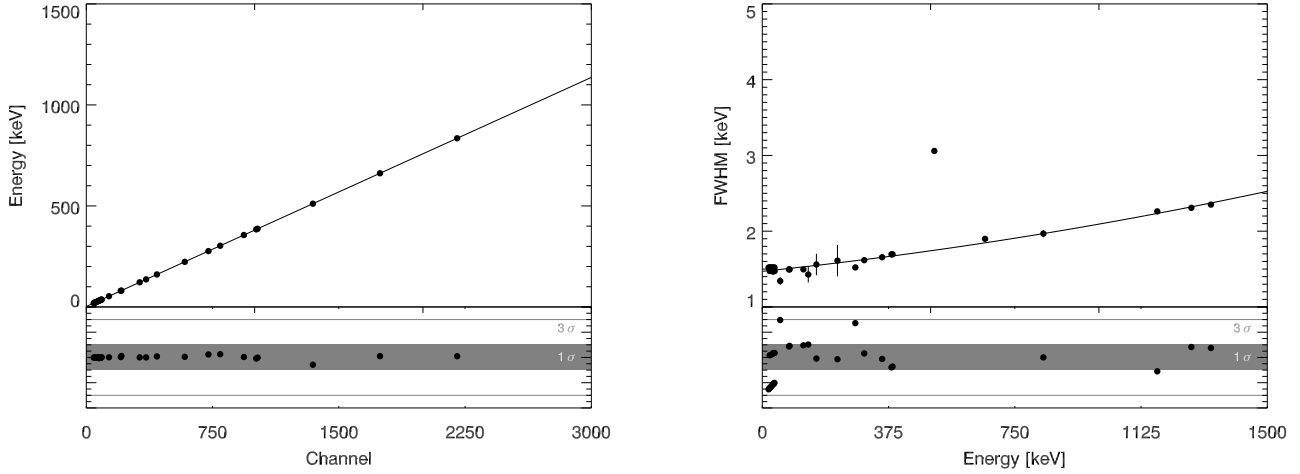
Figure 52: Left panel: The energy calibration for the HPGe detector. The photo-peak locations in channels as determined with HYPERMET are compared to energy values taken from NuDat (filled circles). Also shown is a second order polynomial fit to the data (solid line). Right panel: The measured peak FWHM for all isotopes (filled circles). The stray point is the 511 keV pair-production peak, which has a much broader width than the photo-peaks. Also shown is a second degree polynomial model fitted to the data which was used to determine the detector resolution at arbitrary energies. The lower panels of both plots show the respective residuals in terms of σ uncertainties (solid area: 1σ, lines: 3σ).

4. Gamma-rays can Compton scatter within the detector or into the detector from surrounding materials. These scattered events manifest themselves in an ledge or discontinuity in the background above or below the photo-peak energies. A step of amplitude S in the spectrum which is folded with Gaussian noise of width δ can be modeled as

$$C(X) = S \times \frac{1}{2}\mathrm{erfc}\left(\frac{x - x_c}{\delta}\right). \tag{48}$$

5. Finally, the effects on the continuum of peaks at higher energies can often be modeled by a nearly linear background within a few peak widths on either side of a photo-peak. This component can be mathematically represented with a polynomial function

$$B(x) = a + b\left(x - x_c\right) + c\left(x - x_c\right)^2. \tag{49}$$

The total background for a peak is then given by the sum of components 3 to 5, whereby the background from peaks at higher energies may contribute to the background of peaks at lower energies. On top of this background the actual peak (component 1) and corresponding exponential tail (2) have to be added.

Tables 7 and 8 summarize the parameters determined by fitting the prominent photo-peaks of the measured isotopes with HYPERMET. The widths mentioned above, σ, γ, δ and μ, are set identically by the program. The energy calibration presented in the tables was performed by comparing the identified photo-peaks with reference data from NuDat(Sonzogni, 2005). A second order polynomial was then fitted to this data as shown in Figure 52. In this way each channel number was mapped to a corresponding energy.

Table 7: Peak and background parameters obtained by fitting the measured data with the HYPER-MET program. The 1σ uncertainties are determined from a variable metric method described in Phillips and Marlow, 1976.

	E [keV]	Channel	A	σ	Area	alpha	beta
[22]Na	1274.55 ± 0.10	3366.57 ± 0.10	2041 ± 20	5.44 ± 0.04	11812 ± 105	0.09 ± 0.15	0.26 ± 0.49
[54]Mn	834.87 ± 0.06	2203.08 ± 0.09	411 ± 26	4.63 ± 0.11	2081 ± 54	0.60 ± 0.01	0.34 ± 0.36
[57]Co	122.06 ± 0.03	317.05 ± 0.04	763 ± 23	3.52 ± 0.08	2863 ± 80	0.49 ± 0.27	0.20 ± 0.22
	136.48 ± 0.05	355.20 ± 0.13	85 ± 8	3.63 ± 0.25	338 ± 22	0.25 ± 0.26	1.00 ± 0.01
[60]Co	1174.23 ± 0.07	3098.50 ± 0.04	1996 ± 45	5.33 ± 0.06	11603 ± 112	0.60 ± 0.01	0.39 ± 0.11
	1332.50 ± 0.09	3520.01 ± 0.05	1748 ± 64	5.54 ± 0.07	10770 ± 117	0.28 ± 0.52	0.59 ± 0.23
[133]Ba	27.98 ± 0.11	68.16 ± 0.29	301 ± 33	3.58 ± 0.04	1446 ± 154	0.60 ± 0.00	1.00 ± 0.00
	30.77 ± 0.02	75.54 ± 0.02	11931 ± 204	3.58 ± 0.04	57391 ± 1061	0.60 ± 0.00	1.00 ± 0.00
	32.66 ± 0.28	80.54 ± 0.74	121 ± 34	3.58 ± 0.04	582 ± 161	0.60 ± 0.00	1.00 ± 0.00
	35.00 ± 0.03	86.72 ± 0.07	2793 ± 113	3.58 ± 0.04	13437 ± 471	0.60 ± 0.00	1.00 ± 0.00
	36.10 ± 0.15	89.65 ± 0.40	265 ± 78	3.58 ± 0.04	1272 ± 373	0.60 ± 0.00	1.00 ± 0.00
	53.16 ± 0.03	134.77 ± 0.05	410 ± 18	3.16 ± 0.12	1380 ± 52	0.26 ± 0.78	0.17 ± 6.17
	79.53 ± 0.05	204.55 ± 0.13	455 ± 38	3.52 ± 0.03	1706 ± 131	0.41 ± 0.16	0.10 ± 0.02
	81.01 ± 0.02	208.45 ± 0.02	6251 ± 68	3.52 ± 0.03	23428 ± 232	0.41 ± 0.16	0.10 ± 0.02
	160.78 ± 0.06	419.49 ± 0.14	94 ± 8	3.68 ± 0.33	466 ± 43	0.60 ± 0.00	1.00 ± 0.00
	223.32 ± 0.10	584.95 ± 0.28	64 ± 10	3.79 ± 0.49	257 ± 43	0.27 ± 0.88	0.17 ± 8.02
	276.41 ± 0.02	725.41 ± 0.04	876 ± 26	3.58 ± 0.08	3342 ± 82	0.35 ± 4.21	0.18 ± 4.83
	302.85 ± 0.01	795.36 ± 0.03	1951 ± 45	3.81 ± 0.06	7909 ± 144	0.58 ± 0.24	0.19 ± 0.36
	356.01 ± 0.01	936.01 ± 0.02	5965 ± 69	3.90 ± 0.03	24774 ± 234	0.52 ± 0.30	0.22 ± 0.48
	383.84 ± 0.02	1009.62 ± 0.04	793 ± 20	3.99 ± 0.07	3407 ± 68	0.06 ± 0.00	0.63 ± 0.58
	386.89 ± 0.11	1017.68 ± 0.28	19 ± 2	3.99 ± 0.07	83 ± 11	0.06 ± 0.00	0.63 ± 0.58
[137]Cs	29.01 ± 0.20	70.89 ± 0.51	30 ± 7	3.47 ± 0.09	139 ± 29	0.60 ± 0.08	1.00 ± 0.00
	32.01 ± 0.04	78.83 ± 0.07	878 ± 43	3.46 ± 0.11	3929 ± 86	0.49 ± 0.20	1.00 ± 0.02
	36.50 ± 0.05	90.70 ± 0.11	191 ± 11	3.47 ± 0.09	890 ± 49	0.60 ± 0.08	1.00 ± 0.00
	661.65 ± 0.03	1744.69 ± 0.02	5088 ± 46	4.47 ± 0.03	24222 ± 198	0.11 ± 0.90	0.14 ± 0.37

Table 8: Peak and background parameters obtained by fitting the measured data with the HYPERMET program. Note that the reduced χ^2 is given, i.e. $\chi^2/d.o.f$. The 1σ uncertainties are determined from a variable metric method described in Phillips and Marlow, 1976.

	E [keV]	a	b	c	Σ	τ	ν	χ^2
^{22}Na	1274.55 ± 0.10	0.01 ± 0.15	0.01 ± 0.01	0.00 ± 0.00	0.00 ± 0.00	0.01 ± 0.01	2.78 ± 1.48	0.9
^{54}Mn	834.87 ± 0.06	0.60 ± 0.45	-0.01 ± 0.02	0.00 ± 0.00	0.00 ± 0.00	0.00 ± 0.00	0.00 ± 0.00	1.3
^{57}Co	122.06 ± 0.03	0.00 ± 0.01	0.04 ± 0.04	0.00 ± 0.00	0.01 ± 0.00	0.00 ± 0.00	0.00 ± 0.00	2.2
	136.48 ± 0.05	0.94 ± 0.73	0.01 ± 0.04	0.00 ± 0.00	0.00 ± 0.00	0.00 ± 0.00	0.00 ± 0.00	1.5
^{60}Co	1174.23 ± 0.07	2.81 ± 9.98	0.27 ± 0.34	0.00 ± 0.00	0.01 ± 0.00	0.00 ± 0.00	11.7 ± 20.5	1.1
	1332.50 ± 0.09	3.17 ± 0.80	-0.06 ± 0.03	0.00 ± 0.00	0.01 ± 0.00	0.00 ± 0.00	0.00 ± 0.00	1.3
^{133}Ba	27.98 ± 0.11	335.19 ± 7.82	-4.28 ± 0.22	0.00 ± 0.00	-0.02 ± 0.00	0.00 ± 0.00	1.00 ± 0.00	8.6
	30.77 ± 0.02	335.19 ± 7.82	-4.28 ± 0.22	0.00 ± 0.00	-0.02 ± 0.00	0.00 ± 0.00	1.00 ± 0.00	8.6
	32.66 ± 0.28	335.19 ± 7.82	-4.28 ± 0.22	0.00 ± 0.00	-0.02 ± 0.00	0.00 ± 0.00	1.00 ± 0.00	8.6
	35.00 ± 0.03	335.19 ± 7.82	-4.28 ± 0.22	0.00 ± 0.00	-0.02 ± 0.00	0.00 ± 0.00	1.00 ± 0.00	8.6
	36.10 ± 0.15	335.19 ± 7.82	-4.28 ± 0.22	0.00 ± 0.00	-0.02 ± 0.00	0.00 ± 0.00	1.00 ± 0.00	8.6
	53.16 ± 0.03	70.32 ± 3.57	0.48 ± 0.21	0.00 ± 0.00	0.00 ± 0.00	0.00 ± 0.00	0.00 ± 0.00	1.4
	79.53 ± 0.05	80.60 ± 23.96	-0.53 ± 0.77	0.00 ± 0.00	0.02 ± 0.00	0.00 ± 0.00	1.00 ± 0.00	1.7
	81.01 ± 0.02	80.60 ± 23.96	-0.53 ± 0.77	0.00 ± 0.00	0.02 ± 0.00	0.00 ± 0.00	1.00 ± 0.00	1.7
	160.78 ± 0.06	127.26 ± 4.08	-0.68 ± 0.31	0.00 ± 0.00	0.00 ± 0.00	0.00 ± 0.00	0.00 ± 0.00	0.7
	223.32 ± 0.10	70.11 ± 4.43	-0.08 ± 0.32	0.00 ± 0.00	0.00 ± 0.00	0.00 ± 0.00	0.00 ± 0.00	1.5
	276.41 ± 0.02	54.62 ± 3.25	-0.11 ± 0.20	0.00 ± 0.00	0.00 ± 0.00	0.00 ± 0.00	0.00 ± 0.00	1.8
	302.85 ± 0.01	43.40 ± 5.86	-0.05 ± 0.21	0.00 ± 0.00	0.00 ± 0.00	0.01 ± 0.01	2.50 ± 0.09	2.3
	356.01 ± 0.01	9.89 ± 5.25	-0.13 ± 0.19	0.00 ± 0.00	0.00 ± 0.00	0.00 ± 0.00	5.23 ± 4.59	2.2
	383.84 ± 0.02	0.00 ± 0.01	0.02 ± 0.02	0.00 ± 0.00	0.01 ± 0.00	0.00 ± 0.00	1.00 ± 0.00	1.3
	386.89 ± 0.11	0.00 ± 0.01	0.02 ± 0.02	0.00 ± 0.00	0.01 ± 0.00	0.00 ± 0.00	1.00 ± 0.00	1.3
^{137}Cs	29.01 ± 0.20	33.56 ± 2.35	0.09 ± 0.06	0.00 ± 0.00	0.00 ± 0.00	0.00 ± 0.00	0.00 ± 0.00	1.7
	32.01 ± 0.04	42.56 ± 3.77	-0.08 ± 0.14	0.00 ± 0.00	0.00 ± 0.00	0.00 ± 0.00	0.00 ± 0.00	1.7
	36.50 ± 0.05	33.56 ± 2.35	0.09 ± 0.06	0.00 ± 0.00	0.00 ± 0.00	0.00 ± 0.00	0.00 ± 0.00	1.7
	661.65 ± 0.03	0.00 ± 0.01	0.03 ± 0.02	0.00 ± 0.00	0.00 ± 0.00	0.00 ± 0.00	7.14 ± 5.26	1.6
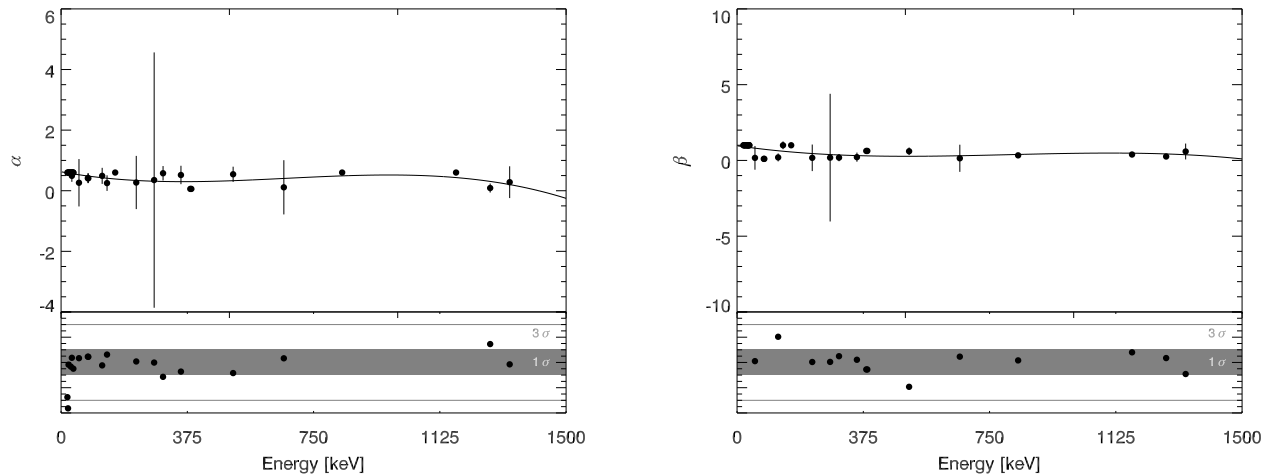
Figure 53: A compilation of the fit parameters defining the normalization (α, left panel) and slope of the exponential tail (β, right panel) for the measured photo-peaks (filled circles). Also shown is a third degree polynomial model fitted to the data which was used to determine the parameters at arbitrary energies. The lower part shows the respective residuals in terms of σ uncertainties (solid area: 1σ, lines: 3σ).

6.2.1 A Review of the Verification Results for the Measured Sources

Before proceeding with a detailed simulation of the experimental setup introduced in Section 6.2 it is worthwhile to have a more detailed look at the individual ENSDF-verification results of the measured isotopes which result from the work presented in Chapter 6.1.4. Any energy or intensity deviations present in these "atomic" tests would also ab initio manifest themselves in the output of the validation simulations. These deviations might be subsequently enhanced or suppressed by additional physical processes occurring during further tracking of the radiation and particles through the geometric model. Nevertheless, they give an initial estimate of the accuracy which can be expected from the simulation.

Gamma Emission

An overview of the simulation verification results for the gamma- and X-ray emission resulting from decays of the measured isotopes is given in Table 9. Above 50 keV the radiation intensity deviations produced by both the current and the new code are below 5%; for the new code this is also true at lower (X-ray) energies. Deviations of this order of magnitude are thus to be expected for the validation simulations. Additional offsets may be introduced by the following influences

- Inherent uncertainties in other simulated processes such as Compton-scattering (modeled as multiple scattering in the simulation), pair-production and the photo-electric effect.

- Small geometrical details, which cannot be inferred from measurement, e.g. the dead layer of the Germanium-crystal or the thickness of the radioactive deposit in the source.

- The lab room, which was simplified for the simulation model, will introduce backscattered events onto the detector.

- Inaccurate modeling of the experimental detector's response function. Geant4 does not simulate semi-conductor physics nor are the effects of the read-out electronics included in the Monte-Carlo simulation. Thus the response has to be inferred from the measurements and modeled as part of the data analysis.

Table 9: The results of the verification in Section 6.1.4 for the isotopes measured as part of the validation. Results for the current Geant4 radioactive decay code (cur.) and the new code (new) with respect to ENSDF evaluated data are shown. Uncertainties of 0.00 denote that uncertainties are present, but below the two significant digits given. The intensity deviation is given by $(I_{\mathrm{ref}} - I_{\mathrm{sim}})/I_{\mathrm{ref}}$.

Isotope	Energy[keV]	Intensity [%]	Cur. energy dev. [keV]	Cur. intensity dev	New energy dev. [keV]	New intensity dev.
^{22}Na	1274.54 ± 0.01	$99.94 \pm 1.40 \times 10^{-02}$	$(1.37 \pm 2.00) \times 10^{-01}$	-0.00 ± 0.00	$(1.37 \pm 2.00) \times 10^{-01}$	0.00 ± 0.00
^{54}Mn	834.85 ± 0.00	$99.98 \pm 1.00 \times 10^{-02}$	$(0.48 \pm 2.00) \times 10^{-01}$	0.00 ± 0.00	$0.23 \pm 2.00 \times 10^{-01}$	0.00 ± 0.00
^{57}Co	14.41 ± 0.00	$9.16 \pm 1.50 \times 10^{-01}$	$(1.29 \pm 5.00) \times 10^{-02}$	0.00 ± 0.00	$(1.29 \pm 5.00) \times 10^{-02}$	0.00 ± 0.00
	122.06 ± 0.00	$85.60 \pm 1.70 \times 10^{+00}$	$(0.61 \pm 2.00) \times 10^{-01}$	-0.00 ± 0.00	$(0.61 \pm 2.00) \times 10^{-01}$	-0.00 ± 0.00
	136.47 ± 0.00	$10.68 \pm 8.00 \times 10^{-02}$	$(0.74 \pm 2.00) \times 10^{-01}$	0.03 ± 0.00	$(0.74 \pm 2.00) \times 10^{-01}$	0.00 ± 0.00
^{60}Co	1173.23 ± 0.00	$99.85 \pm 3.00 \times 10^{-02}$	$(0.28 \pm 2.00) \times 10^{-01}$	-0.00 ± 0.00	$(0.13 \pm 2.00) \times 10^{-01}$	-0.00 ± 0.00
	1332.49 ± 0.00	$99.98 \pm 6.00 \times 10^{-04}$	$(0.92 \pm 2.00) \times 10^{-01}$	-0.00 ± 0.00	$(0.18 \pm 2.00) \times 10^{-01}$	-0.00 ± 0.00
^{137}Cs	283.50 ± 1.00	$(0.00 \pm 0.00) \times 10^{+00}$	$(0.10 \pm 1.02) \times 10^{+00}$	0.14 ± 0.00	$(0.10 \pm 1.02) \times 10^{+00}$	0.01 ± 0.00
	661.66 ± 0.00	$85.10 \pm 2.00 \times 10^{+00}$	$(0.57 \pm 2.00) \times 10^{-01}$	0.00 ± 0.00	$(0.57 \pm 2.00) \times 10^{-01}$	-0.00 ± 0.00
^{133}Ba	30.63 ± 0.00	$33.70 \pm 1.00 \times 10^{+00}$	$(-1.75 \pm 2.00) \times 10^{-01}$	-0.52 ± 0.00	$(-1.75 \pm 2.00) \times 10^{-01}$	-0.01 ± 0.00
	30.97 ± 0.00	$62.20 \pm 1.80 \times 10^{+00}$	$(1.73 \pm 2.00) \times 10^{-01}$	0.17 ± 0.00	$(1.73 \pm 2.00) \times 10^{-01}$	-0.02 ± 0.00
	$35.00 \pm$ –	$22.60 \pm 7.00 \times 10^{-01}$	$(0.20 \pm\ –\ ) \times 10^{+00}$	0.59 ± 0.00	$(0.00 \pm\ –\ ) \times 10^{+00}$	-0.05 ± 0.00
	53.16 ± 0.00	$2.20 \pm 2.20 \times 10^{-02}$	$(1.62 \pm 2.00) \times 10^{-01}$	0.04 ± 0.00	$(1.62 \pm 2.00) \times 10^{-01}$	-0.01 ± 0.00
	79.61 ± 0.00	$2.62 \pm 6.00 \times 10^{-02}$	$(0.14 \pm 2.00) \times 10^{-01}$	0.01 ± 0.00	$(0.14 \pm 2.00) \times 10^{-01}$	-0.00 ± 0.00
	81.00 ± 0.00	$34.10 \pm 3.00 \times 10^{-01}$	$(1.97 \pm 2.00) \times 10^{-01}$	0.02 ± 0.00	$(1.97 \pm 2.00) \times 10^{-01}$	0.00 ± 0.00
	160.61 ± 0.00	$(645.00 \pm 8.00) \times 10^{-03}$	$(0.11 \pm 2.00) \times 10^{-01}$	0.03 ± 0.00	$(0.11 \pm 2.00) \times 10^{-01}$	0.01 ± 0.00
	223.24 ± 0.00	$(45.00 \pm 4.00) \times 10^{-02}$	$(0.37 \pm 2.00) \times 10^{-01}$	0.03 ± 0.00	$(0.37 \pm 2.00) \times 10^{-01}$	0.02 ± 0.00
	276.40 ± 0.00	$7.16 \pm 2.20 \times 10^{-02}$	$(2.00 \pm 2.00) \times 10^{-01}$	0.04 ± 0.00	$(2.00 \pm 2.00) \times 10^{-01}$	-0.00 ± 0.00
	302.85 ± 0.01	$18.33 \pm 6.00 \times 10^{-02}$	$(0.51 \pm 2.00) \times 10^{-01}$	0.02 ± 0.00	$(0.51 \pm 2.00) \times 10^{-01}$	-0.00 ± 0.00
	356.01 ± 0.00	$62.05 \pm 1.90 \times 10^{-01}$	$(0.13 \pm 2.00) \times 10^{-01}$	0.04 ± 0.00	$(0.13 \pm 2.00) \times 10^{-01}$	-0.00 ± 0.00
	383.85 ± 0.01	$8.94 \pm 3.00 \times 10^{-03}$	$(0.48 \pm 2.00) \times 10^{-01}$	0.02 ± 0.00	$(0.48 \pm 2.00) \times 10^{-01}$	0.00 ± 0.00

Isotope	Current code		New code	
	K-S	A-D	K-S	A-D
^{60}Co	0.016	0.002	0.322	0.168
^{137}Cs	0.117	0.013	0.828	0.429
^{22}Na	1.000	0.884	1.000	0.950

Table 10: Kolmogorov-Smirnov (K-S) and Anderson-Darling (A-D) goodness of fit tests for the three beta-decaying isotopes which are part of the validation. The significance levels α of the statistics are given. Values of $\alpha \approx 1$ indicate that the simulation represents the experimental data well.

- Knowledge about the absolute intensity of the measured isotopes which is needed to normalize the simulation to the experiment. The date of the reference measurements is known with a precision of one month with an additional error of up to 5% for the magnitude of the activity.

It is to be expected that geometrical uncertainties will have stronger effects on the simulation outcome at lower energies. In the X-ray regime even small variations in entrance window, dead layer or radioactive deposit thickness may lead to large changes in the transmission of such radiation. As will be shown later the influence of the lab room is negligible due to the collimator used for the measurements.

Beta-Emission

The isotopes ^{60}Co and ^{137}Cs produce electrons through β-decays while the ^{22}Na decay results in the production of positrons. For completeness, a comparison of the simulated beta-spectra of these isotopes with experimental data from Hansen and Spernol, 1968; Hsue, Langer, and Tang, 1966; Wenninger, Stiewe, and Leutz, 1968 was made, even though the experimental setup is not sensitive to beta-emission. The individual comparisons are shown in Figure 6.2.1. For each isotope the goodness of the fit of the simulated data with respect to the measured data was quantified using Kolmogorov-Smirnov (Massey, 1951) and Anderson-Darling tests (Anderson and Darling, 1954). Table 10 summarizes the significance levels α resulting from these tests. A significance level of $\alpha \approx 1$ indicates that the two datasets are sufficiently similar. The results show that the new radioactive decay simulation models the experimental data more accurately for the three isotopes in question. Even better agreement may be reached by use of isotope-specific Beta-Fermi functions, a possibility foreseen in the new code's design.

6.2.2 Geant4 Simulations of the HPGe Detector Measurements

The validation simulations were run on Geant4 version 4.9.4-p01 with the native radioactive decay code and with the new code using the statistical approach. Each isotope was decayed 5×10^6 times and the energy deposits in the germanium crystal were recorded. The resulting data was analyzed with custom IDL programs after processing it to include the detector response. Details on the data analysis and preparation will be given after an introduction of the geometrical model used for the simulations.

6.2.3 Geometrical Model for the Validation Simulations

It was shown in previous works (e.g. Hurtado, Garcia-Tenorio, and Garcia-Leon, 2009, Hurtado, García-León, and García-Tenorio, 2004, Laborie, Le Petit, Abt, and Girard, 2002, Golovko, Iacob, and Hardy, 2008, Bissaldi et al., 2009), that the simulation outcome might critically be influenced even by small geometrical details, such as the dead layer thickness or accurate modeling of the laboratory room. Accordingly, appropriate care was taken to model the detector with an adequate level of detail. Besides the detector head, this model also included the attached dewar, the lead, tin and copper collimator parts as well as the tables and additional shielding thereon. The measurement for these parts were either
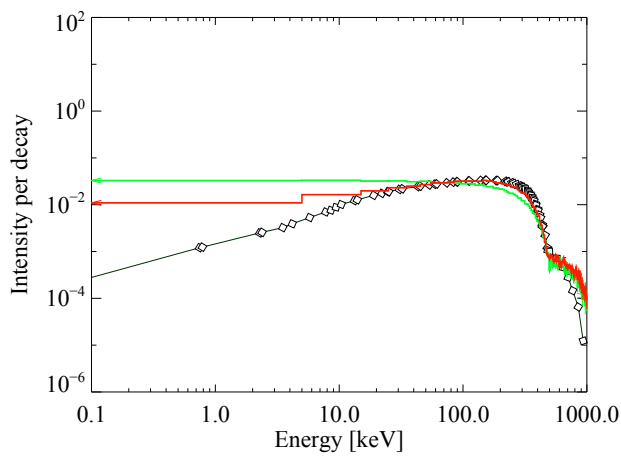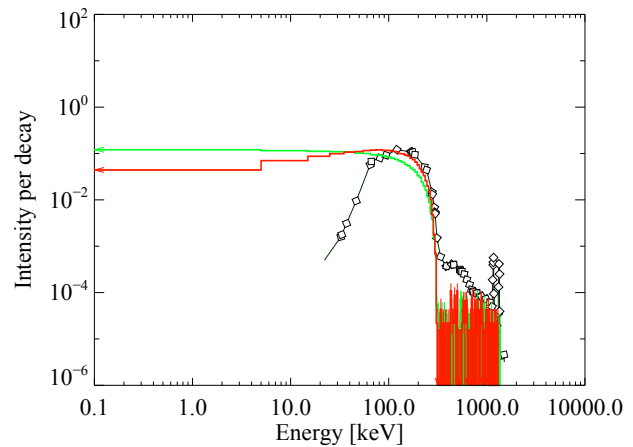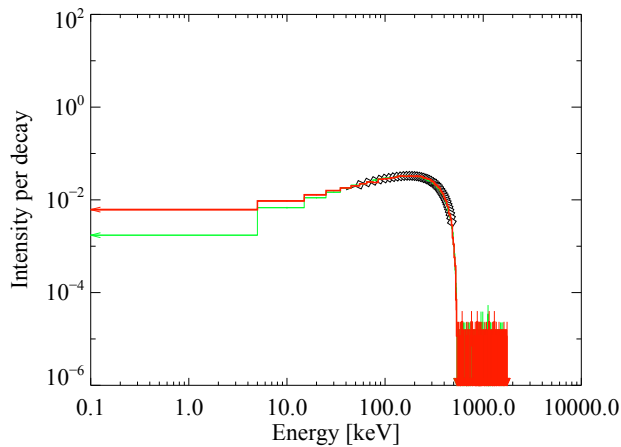
Figure 54: A comparison of the beta-spectrum produced by the new (red line) and current (blue line) radioactive decay simulations with experimental data (diamonds). Three isotopes were compared: ^{22}Na (top left), ^{60}Co (top right) and ^{137}Cs (bottom left). In the order of the mentioning the experimental data was taken from Hansen and Spernol, 1968; Hsue, Langer, and Tang, 1966; Wenninger, Stiewe, and Leutz, 1968.

obtained directly from the setup or acquired from the detector manufacturer. An image of the simulation model is shown in Figure 55.

In contrast to previous works it was not intended to iterate through different implementations of the geometric model with the purpose of finding an optimal representation; i.e. fudge the simulation. Such a procedure would have opposed the goal of validating how well the simulation can reproduce experimental results if optimization possibilities by comparison with measured data do not exist. A scenario which is common during the development phase of a new detector.

A single exception was made from such a completely self-consistent approach: the (non-measurable) thickness of the radioactive material in the source was allowed to vary by as much as 50%. This improved the simulation's capability to reproduce the X-ray fluorescence lines of ^{133}Ba (-50% thickness) and ^{137}Ca (-20% thickness) at energies below 40 keV.

One could further content that the use of a measured response function* of the data preparation for the analysis violates a self-consistent approach. This is not necessarily the case if the detector response can be obtained from measurements of detector prototypes, even if measurements of the final detector in its intended environment (e.g. space) are not possible.

Another point of concern was how accurate the model of the lab room would need to be. Other authors (e.g. Bissaldi et al., 2009) have found that gamma-rays scattered from the ceiling, floor and wall can contribute in the order of 10% to the radiation registered by the detector. For the experimental setup used as part of this work the contribution was found to lie below 3%; a fact which can be attributed to the use of a collimator. Accordingly, the room was modeled in a simplified fashion, consisting of concrete

---

* In this meaning: including the finite energy resolution of the detector and the incomplete charge collection effects as characterized with HYPERMET.
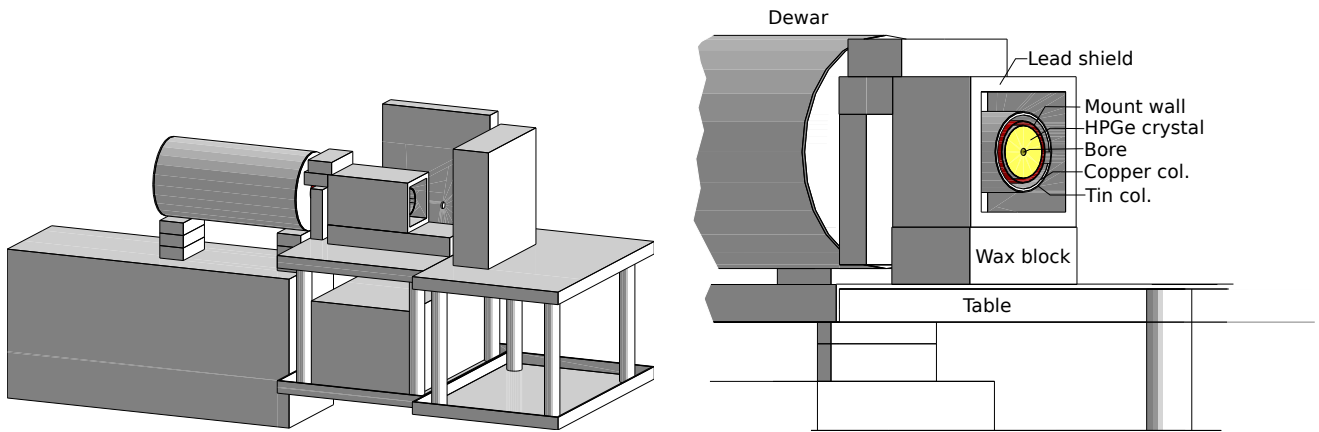
Figure 55: The geometrical model of the HPGe detector as implemented in the Geant4 simulation. The detector is inside the hollow lead blocks at the image center, its dewar extends to the left and sits on top of borated wax blocks, which in turn are placed upon a wooden crate. The shielding is placed on top of two steel tables. The left panel shows the full setup without the model of the laboratory room. The right panel shows a detailed view in which the front part of the lead shielding, collimator and detector head have been cut off in order to illustrate the interior design.

walls, floor and ceiling. Laboratory equipment other than the detector and the tables it was placed upon was not included into the simulation.

6.2.4 Simulation Analysis & Response Modeling

The raw data output by the Monte-Carlo simulation consists of an event list which includes the primary event number, the energy deposited in the crystal and the particle type. For the analysis and the final comparison this event list needs to be transferred into a spectrum and the detector response needs to be taken into account. In accordance with the experimental data a 8192 channel binning scheme was used. Afterwards the detector's response characteristics were applied to the now binned data. Using the parameter sets shown in Tables 7 and 8 as well as Figures 52 and 53 the inverse of the HYPERMET analysis was performed on the data; in effect turning the idealized spectrum from the simulation in to a spectrum affected by a finite energy resolution, incomplete charge collection effects and electronic noise. Effects due to Compton scattering did not have to taken into account in this step, as the scattering is already modeled as part of the Geant4 simulation. During all processing steps it was assured that the sum of events in the spectrum stays constant; accordingly, photo-peak intensities will not be altered by the above procedure. The reprocessed spectra were then analyzed using the HYPERMET program in the same fashion the experimental data had been analyzed; accordingly yielding a familiar set of parameters which could be used for comparisons.

6.2.5 Validation Results

As was described in the previous section the simulated data needs to be reprocessed to match the experimental detectors response. Especially for the regions around the photo-peaks this will lead to a substantial change in the appearance of the spectra as the ideal energy resolution output by the Monte-Carlo simulation is replaced by Gaussian shaped peaks with added pile-up. Owing to this fact the comparison with the measured data is subdivided into an analysis of the photo-peak regions and an analysis of the complete spectra including the Compton-scattered continuum.

Photo Peaks

It has been discussed in Chapter 4.3 that most applications influenced by radioactive decays will measure the properties of the resulting photo-peaks. Commonly these parameters are the peak width, peak energy and the peak intensity; all of which are also part of the HYPERMET analysis. A comparison of the peak width does not make much sense in the context of the data preparation approach used in this work. As the width is determined by the response function applied to the simulated data after the Monte-Carlo simulation which in turn is modeled after the measured response, no additional information on the accuracy of the simulation would be gained. In contrast the latter two parameters, energy and intensity, are fully determined by the Geant4-simulation, e.g the radioactive decay code and the underlying data libraries. Figures 57, 58 and 59 show a comparison between experimental and simulated data for the photo-peak regions of the measured isotopes. Simulations with both the current and the new radioactive decay code are shown in the Figures; a quantitative overview of the results is given in Tables 11 and 12.

The curved shape of the residuals in some plots indicates a mismatch between simulated and measured peak positions. Taking into account the "absolute" energy positions given in NuDat and shown as vertical dashed lines in the figures these deviations are found to be the result of the binning scheme. They are exaggerated in the residual plots if the peak maximums fall into neighboring bins. Quantitatively the peak positions obtained with Hypermet show a median energy deviation of -0.20 ± 0.05 keV for the current Geant4 code and -0.18 ± 0.05 keV for the new code. Taking the evaluated energy positions as a reference, these offsets are well within the mean bin width of ≈ 0.3 keV per channel. In consequence, both codes model the peak positions equally well within the binning-scheme determined uncertainties.

The observed peak area/intensity deviations between the measured data and both codes are summarized in Figure 56 and Table 12. Additionally, taking into account the individual peak comparisons shown in Figures 57, 58 and 59 it is apparent that both codes are generally capable of reproducing the measured photo-peaks within 3σ error bounds. In summary, the photo-peak areas resulting from the new code deviate from the measurements by a mean of $4.01 \pm 3.57\%$. With a mean deviation of $8.65 \pm 4.56\%$ the current Geant4 code performs a factor of ≈ 2 worse.

One should note however, that the larger deviation of the current Geant4 code is mainly due to its poor performance at low energies. In the X-ray regime below 40 keV the code exhibits a mean peak area deviation of $16.27 \pm 5.64\%$, which is more than double as high as that of the new code at $6.73 \pm 2.52\%$. As the geometric model was kept the same for all simulations these larger deviations are likely to be due to the physics implementation in the code. This assumption is supported by the fact that the errors are much larger for ^{133}Ba than they are for ^{137}Cs (compare Figures 58 and 58). Interestingly these two isotopes are handled differently by the current radioactive decay code as they have different decay types. ^{133}Ba decays via electron capture. In accordance with the code analysis presented in Section 4.6 electron capture decays involve delegation of deexcitation emission production to both the `G4Photonevaporation` and `G4AtomicDeexcitation` processes; the latter handling the fluorescence emission occurring when the vacated inner electron shell is filled by outer shell electrons. In the case of ^{137}Cs, which is a beta-emitter, the second delegation is not performed for the majority of decays; the production of fluorescence emission is then exclusively in the responsibility of the `G4Photonevaporation` process. This leads to the conclusion that the observed deviations are at least partially due to the `G4AtomicDeexcitation` process; a finding which is in accordance to the verification results presented in Section 6.1.4.

Radioactive Decay Induced Continuum

The continuum is often of lesser importance to applications which aim to directly measure radioactive decays. In contrast its correct estimate can be crucial to such experiments where radiation from radioactive decays is not the intended observable but an unwanted background. Photo peaks are usually well distinguishable in measured data, an extended continuum is not, and will be superimposed on the actual observables. If it is too strong it might obscure an intended source altogether. Hence a correct simulation of the radioactive continuum will be of great importance to the IXO and ATHENA missions.

Table 11: The energy deviations of the photo-peak positions when comparing the current Geant4 radioactive decay code and the new code with the measured data given in the first column.

	E [keV]	ΔE_{old} [keV]	ΔE_{new} [keV]
^{22}Na	1274.74 ± 0.07	0.06 ± 0.11	0.06 ± 0.11
^{54}Mn	834.95 ± 0.04	0.10 ± 0.06	0.10 ± 0.06
^{57}Co	122.05 ± 0.02	-0.36 ± 0.03	-0.36 ± 0.03
	136.48 ± 0.05	-0.30 ± 0.06	-0.31 ± 0.06
^{60}Co	1173.41 ± 0.06	-0.01 ± 0.09	-0.02 ± 0.09
	1332.73 ± 0.07	0.24 ± 0.12	0.24 ± 0.12
^{133}Ba	30.75 ± 0.03	-0.56 ± 0.04	-0.48 ± 0.04
	35.98 ± 0.08	0.66 ± 0.09	0.84 ± 0.09
	79.53 ± 0.05	-0.02 ± 0.08	0.03 ± 0.07
	81.01 ± 0.02	-0.20 ± 0.03	-0.19 ± 0.03
	276.42 ± 0.02	-0.23 ± 0.02	-0.23 ± 0.03
	302.85 ± 0.01	-0.26 ± 0.02	-0.24 ± 0.02
	356.01 ± 0.01	-0.39 ± 0.01	-0.38 ± 0.01
	383.84 ± 0.02	-0.14 ± 0.02	-0.14 ± 0.03
^{137}Cs	32.03 ± 0.03	-0.32 ± 0.05	-0.32 ± 0.05
	36.50 ± 0.05	-0.28 ± 0.07	-0.18 ± 0.06
	661.69 ± 0.03	-0.07 ± 0.04	-0.07 ± 0.04

Table 12: The photo-peak area deviations when comparing the current Geant4 radioactive decay code and the new code with the measured data. The first column give the measured energies of the compared peaks.

	E [keV]	ΔI_{old} [%]	ΔI_{new} [%]
^{22}Na	1274.74 ± 0.07	-4.70 ± 3.42	-5.35 ± 2.95
^{54}Mn	834.95 ± 0.04	4.26 ± 1.63	1.96 ± 6.53
^{57}Co	122.05 ± 0.02	8.26 ± 3.60	-11.05 ± 3.44
	136.48 ± 0.05	10.67 ± 9.75	-1.40 ± 9.82
^{60}Co	1173.41 ± 0.06	-11.47 ± 2.93	0.47 ± 2.97
	1332.73 ± 0.07	-13.40 ± 3.02	-7.34 ± 2.96
^{133}Ba	30.75 ± 0.03	-29.94 ± 14.91	15.12 ± 0.17
	81.01 ± 0.02	-28.50 ± 2.36	-1.71 ± 11.17
	276.42 ± 0.02	0.57 ± 7.72	-4.24 ± 7.16
	302.85 ± 0.01	3.39 ± 5.18	2.03 ± 4.81
	356.01 ± 0.01	1.09 ± 2.88	-2.23 ± 2.66
	383.84 ± 0.02	4.59 ± 21.66	-3.12 ± 7.38
^{137}Cs	32.03 ± 0.03	-5.72 ± 3.51	4.19 ± 3.07
	36.50 ± 0.05	0.91 ± 8.16	5.91 ± 6.81
	661.69 ± 0.03	-19.69 ± 1.25	1.98 ± 1.27
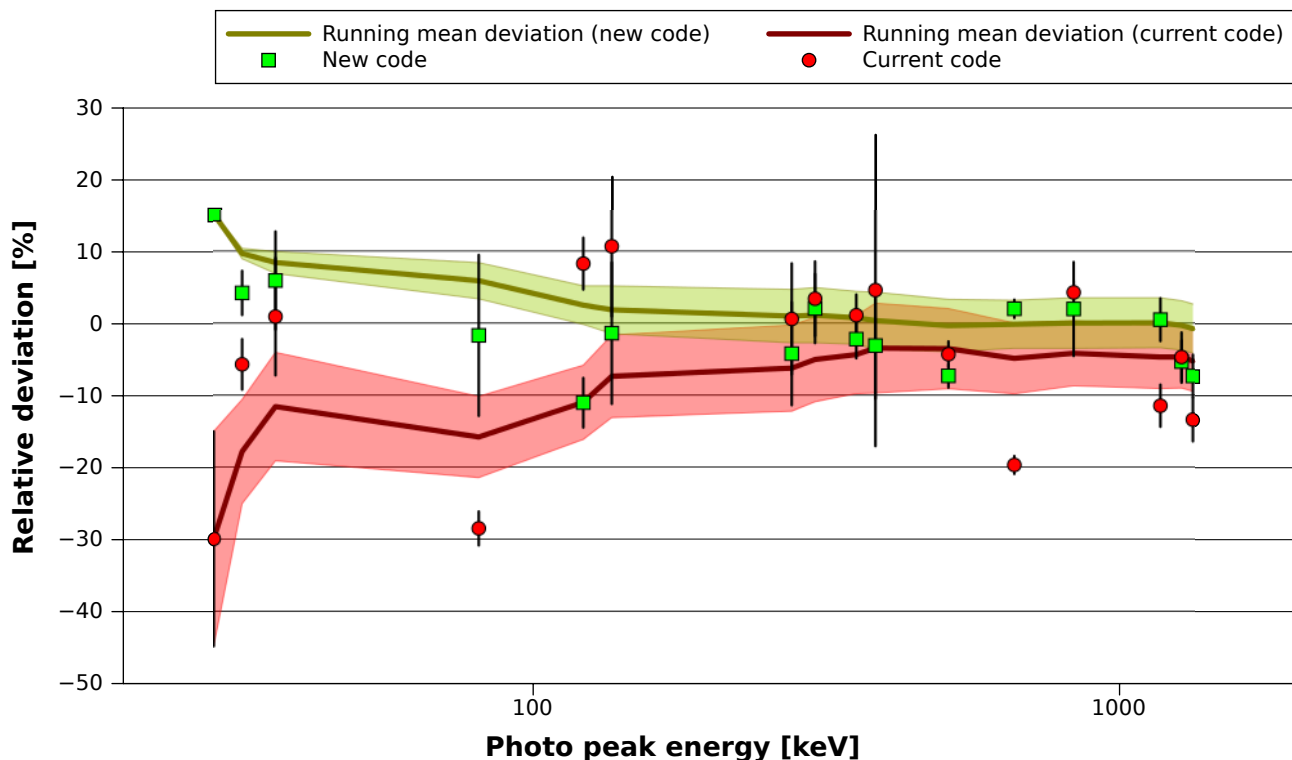
Figure 56: The deviations of photo-peak areas when comparing the current Geant4 radioactive decay code(red circles) and and the new code (green squares) with measured data. The green (new code) and red (current code) lines give the running mean deviation, the shaded areas the uncertainty thereof. It is apparent that the new code is more accurate over the complete energy range.

It is worthwhile to mention that the shape of the continuum is much more effected by processes other than the radioactive decays, such as Compton or Rayleigh scattering. Nevertheless, in an otherwise background free detector, its flux would be completely determined by the photo-peak intensities and activity of the radioactive isotope. Likewise, the position of the Compton edges is determined by the full-energy position of the photo-peak. These facts strongly motivate a comparison of the continuum as part of a validation for the radioactive decay code; a task which is often neglected (see Table 5 in the introduction of this Chapter).

The methods and possibilities of HYPERMET are unsuited for such a comparison; it provides parameters for the near-peak continuum at most. Instead of parameterizing the continuum shape or intensity by use of models an absolute comparison was performed. Accordingly, the residuals shown in Figures 60, 61 and 62 yield information about the observed flux deviations. By defining energy ranges in the spectrum as the continuum, mean deviation values were calculated. These are given in Table 13. It is apparent that both codes, new and current, are generally capable of reproducing the measurements within 3σ uncertainties or deviations of less than 30%. The single exception is ^{57}Co, for which the continuum extends entirely at energies below 100 keV. This is in accordance with the observed photo peak intensity deviations at low energies where the current Geant4 code was also found not capable of reproducing the measurements well.

6.2.6 Discussion of Results and Conclusions drawn from the Validation Measurements

The validation measurements performed as part of this work have shown that both the current Geant4 decay code and the newly developed decay code are capable of reproducing measurements with a High Purity germanium within 3 sigma uncertainties. For the photo-peaks this manifests itself in relative
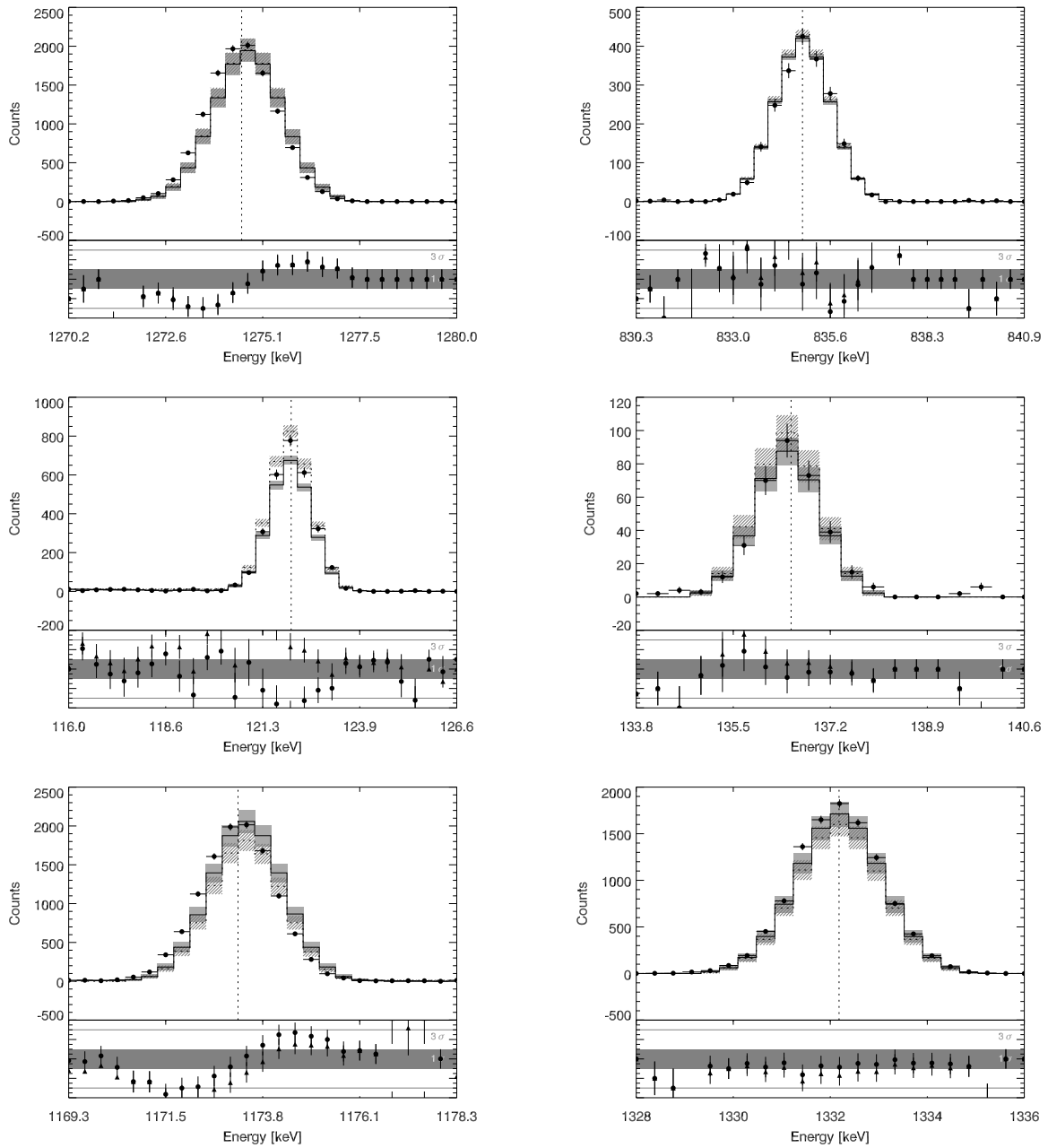
Figure 57: A comparison of the simulated and measured photo-peak regions. From top left to bottom right the following isotopes and peaks are shown: $^{22}\mathrm{Na}_{1274.54\,\mathrm{keV}}$, $^{54}\mathrm{Mn}_{834.85\,\mathrm{keV}}$, $^{57}\mathrm{Co}_{122.06\,\mathrm{keV}}$, $^{57}\mathrm{Co}_{136.47\,\mathrm{keV}}$, $^{60}\mathrm{Co}_{1173.23\,\mathrm{keV}}$ and $^{60}\mathrm{Co}_{1332.49\,\mathrm{keV}}$. Simulations using the current Geant4 code (dashed line, hatched $1\,\sigma$ errors) and the new code (solid line, filled $1\,\sigma$ errors) are compared. The lower panel shows the residuals (triangles: current Geant4 code, circles: the new code) in terms of σ uncertainties (solid area: 1σ, lines: 3σ). The vertical dashed lines mark the literature values for the peak energies.
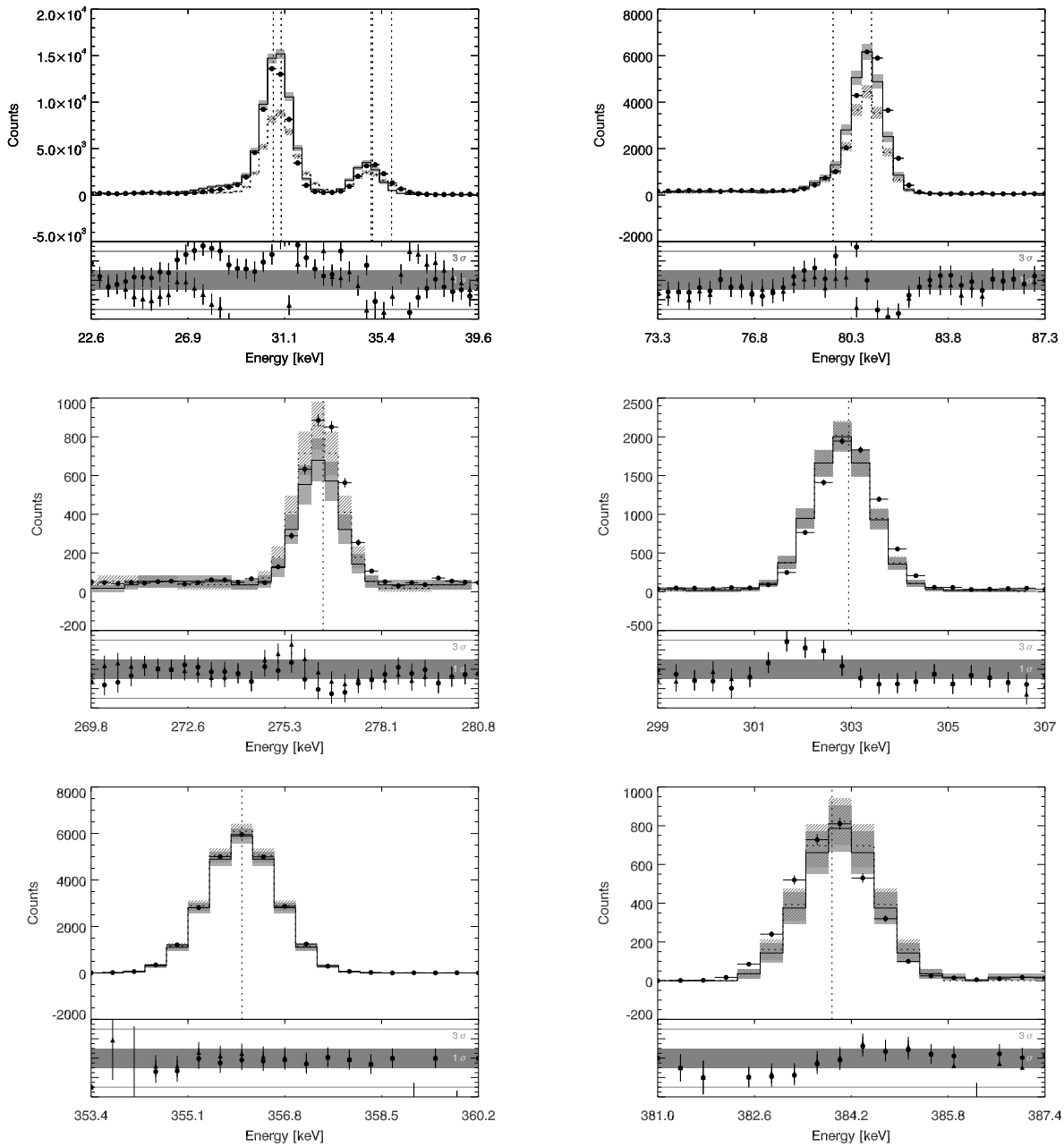
Figure 58: A comparison of the simulated and measured photo-peak regions. From top left to bottom right the following isotopes and peaks are shown: $^{133}\text{Ba}_{30.63-35.82\,\text{keV}}$, $^{133}\text{Ba}_{79.61\&80.99\,\text{keV}}$, $^{133}\text{Ba}_{276.40\,\text{keV}}$, $^{133}\text{Ba}_{302.85\,\text{keV}}$, $^{133}\text{Ba}_{356.01\,\text{keV}}$ and $^{133}\text{Ba}_{383.85\,\text{keV}}$. Simulations using the current Geant4 code (dashed line, hatched 1σ errors) and the new code (solid line, filled 1σ errors) are compared. The lower panel shows the residuals (triangles: current Geant4 code, circles: the new code) in terms of σ uncertainties (solid area: 1σ, lines: 3σ). The vertical dashed lines mark the literature values for the peak energies.
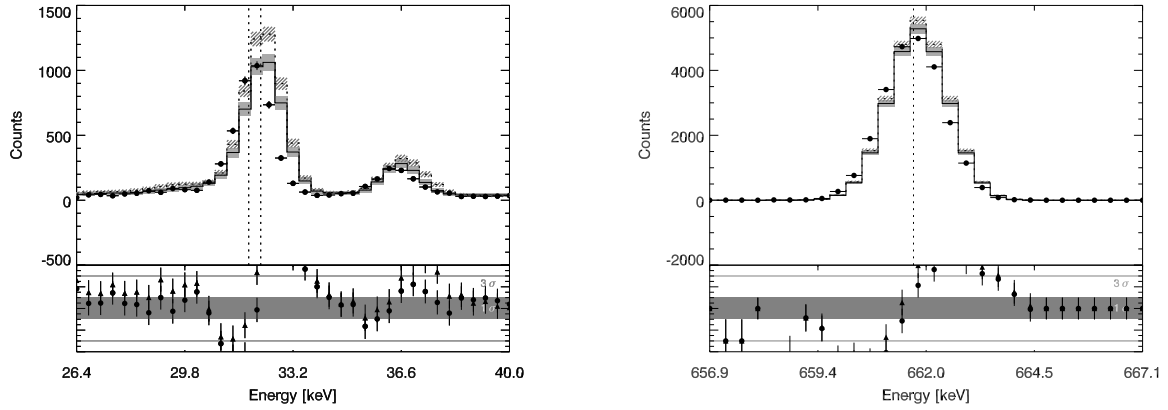
Figure 59: Comparison of the simulated and measured photo-peak regions. From top left to bottom right the following isotopes and peaks are shown: $^{137}Cs_{31.82-37.26\,keV}$ and $^{137}Cs_{661.66\,keV}$. Simulations using the current Geant4 code (dashed line, hatched $1\,\sigma$ errors) and the new code (solid line, filled $1\,\sigma$ errors) are compared. The lower panel shows the residuals (triangles: current Geant4 code, circles: the new code) in terms of σ uncertainties (solid area: 1σ, lines: 3σ). The vertical dashed lines mark the literature values for the peak energies.

Table 13: A compilation of the mean continuum deviations observed between simulations and measurement. The range column gives the energy range(s) which were defined as the continuum.

		Mean deviation [%]	
Isotope	Range [keV]	New code	Current code
^{22}Na	$30-500,\,520-1050$	22.82 ± 1.92	24.74 ± 1.90
^{133}Ba	$100-250$	7.09 ± 1.33	16.62 ± 1.33
^{137}Cs	$30-500$	13.77 ± 1.36	11.55 ± 1.73
^{57}Co	$30-100$	28.15 ± 2.14	74.45 ± 2.85
^{60}Co	$30-1100$	17.08 ± 1.59	26.31 ± 1.57
^{54}Mn	$30-700$	15.08 ± 1.79	15.36 ± 1.42

intensity deviations of less than $15.12\pm0.17\%$ (new code) and less than $29.94\pm14.91\%$ (current code). This is in accordance with those results presented in previous works (Table 5) where no iterative adjustment to the simulation geometry was performed. The deviation of the continuum regions, which are of great importance for low background applications, is in the same order of magnitude and generally also within a $3\,\sigma$ uncertainty level.

Especially for the photo-peak comparison the correct modeling of the detector response was found to be crucial. Additionally, it was observed that initial intensity deviations, resulting from the radioactive decay code, will influence the outcome of the detailed detector simulation. This leads to the conclusion that Geant4 can reliably simulate radioactive decays, even in complex geometries, within an error of $\approx 20-30\%$, if the following prerequisites are met:

- The detector and components in its proximity are modeled with appropriate accuracy.

- The values within the radioactive decay library are consistent with evaluated data. Especially for X-ray emission the new code shows better agreement in this respect.

- The detector response function is well known and applied to the simulated data.

One should note that fulfilling the last point is not always adequately possible for a detector in its early design stage.
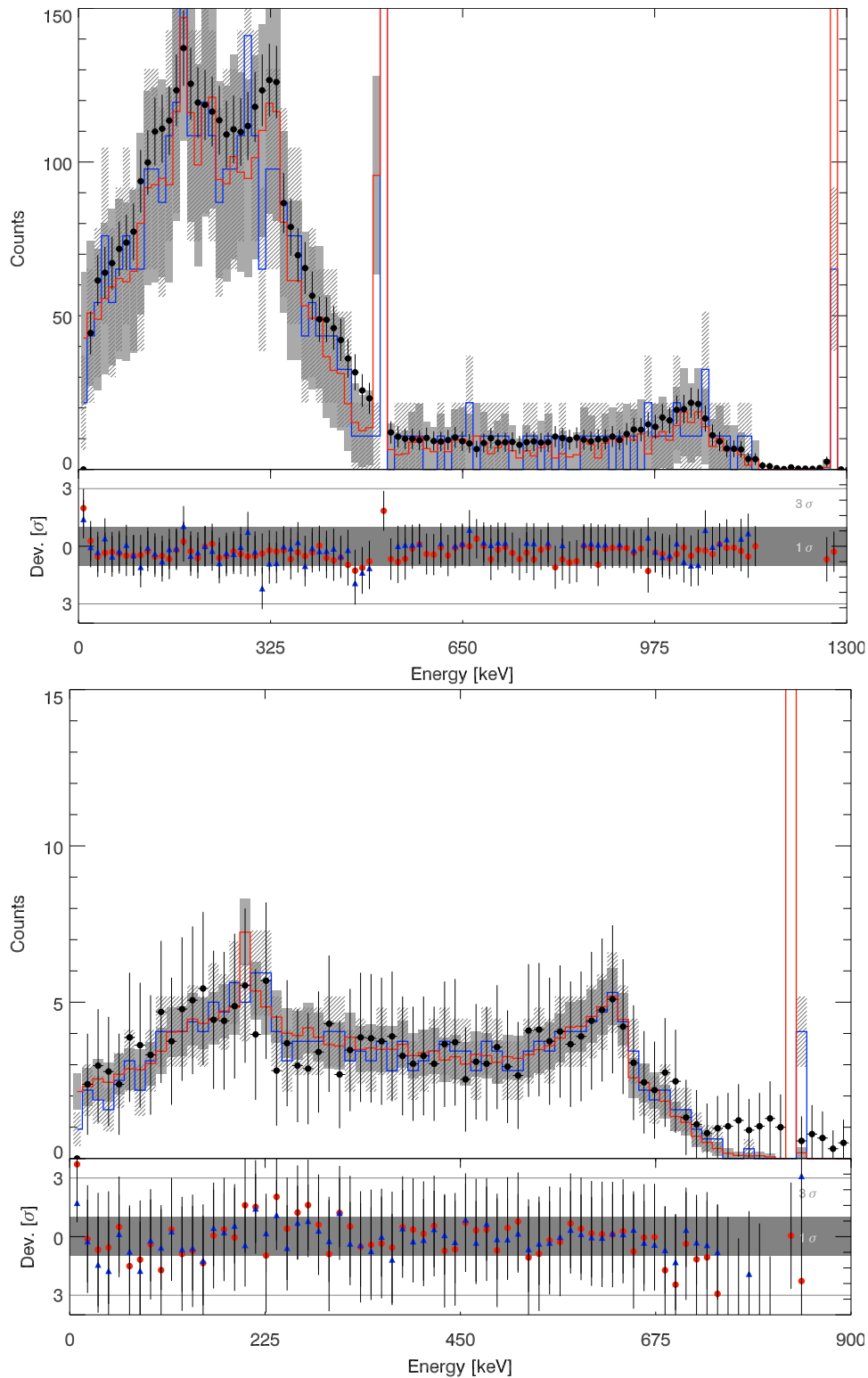
Figure 60: Comparison of the complete simulated and measured spectra showing the simulations' repro-
duction of the continuum. The following isotopes are shown: ^{22}Na (top) and ^{54}Mn (bottom).
Simulations using the current Geant4 code (blue line, hatched 1σ errors) and the new code
(red line, filled 1σ errors) are compared. The lower panel shows the residuals (blue trian-
gles: current Geant4 code, red circles: the new code) in terms of σ uncertainties (solid area:
1σ, lines: 3σ). Note that the y-axis was limited in range in order to accentuate details of the
spectrum.
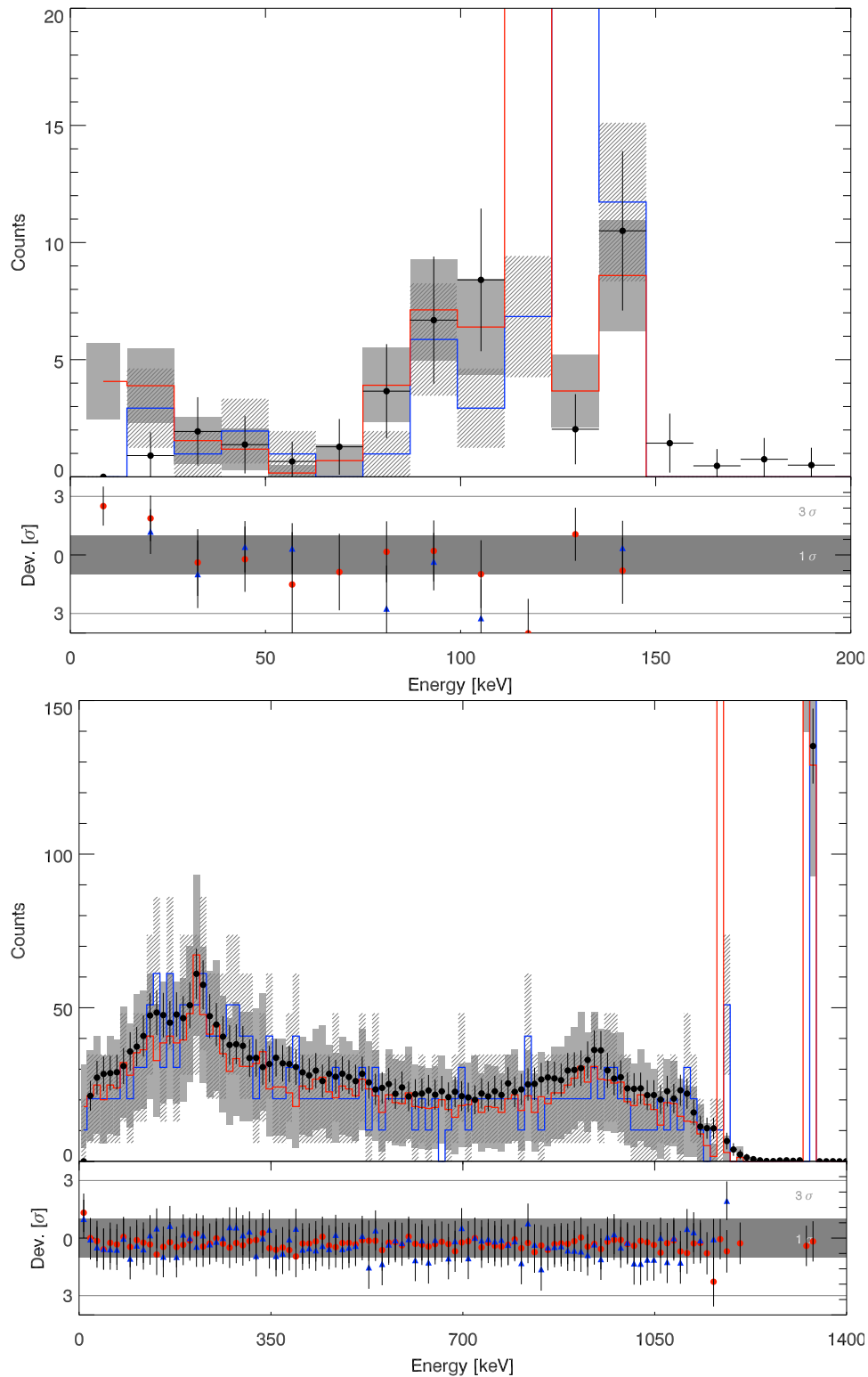
Figure 61: Comparison of the complete simulated and measured spectra showing the simulations' reproduction of the continuum. The following isotopes and peaks are shown: ^{57}Co (top) and ^{60}Co (bottom). Simulations using the current Geant4 code (blue line, hatched 1σ errors) and the new code (red line, filled 1σ errors) are compared. The lower panel shows the residuals (blue triangles: current Geant4 code, red circles: the new code) in terms of σ uncertainties (solid area: 1σ, lines: 3σ). Note that the y-axis was limited in range in order to accentuate details of the spectrum.
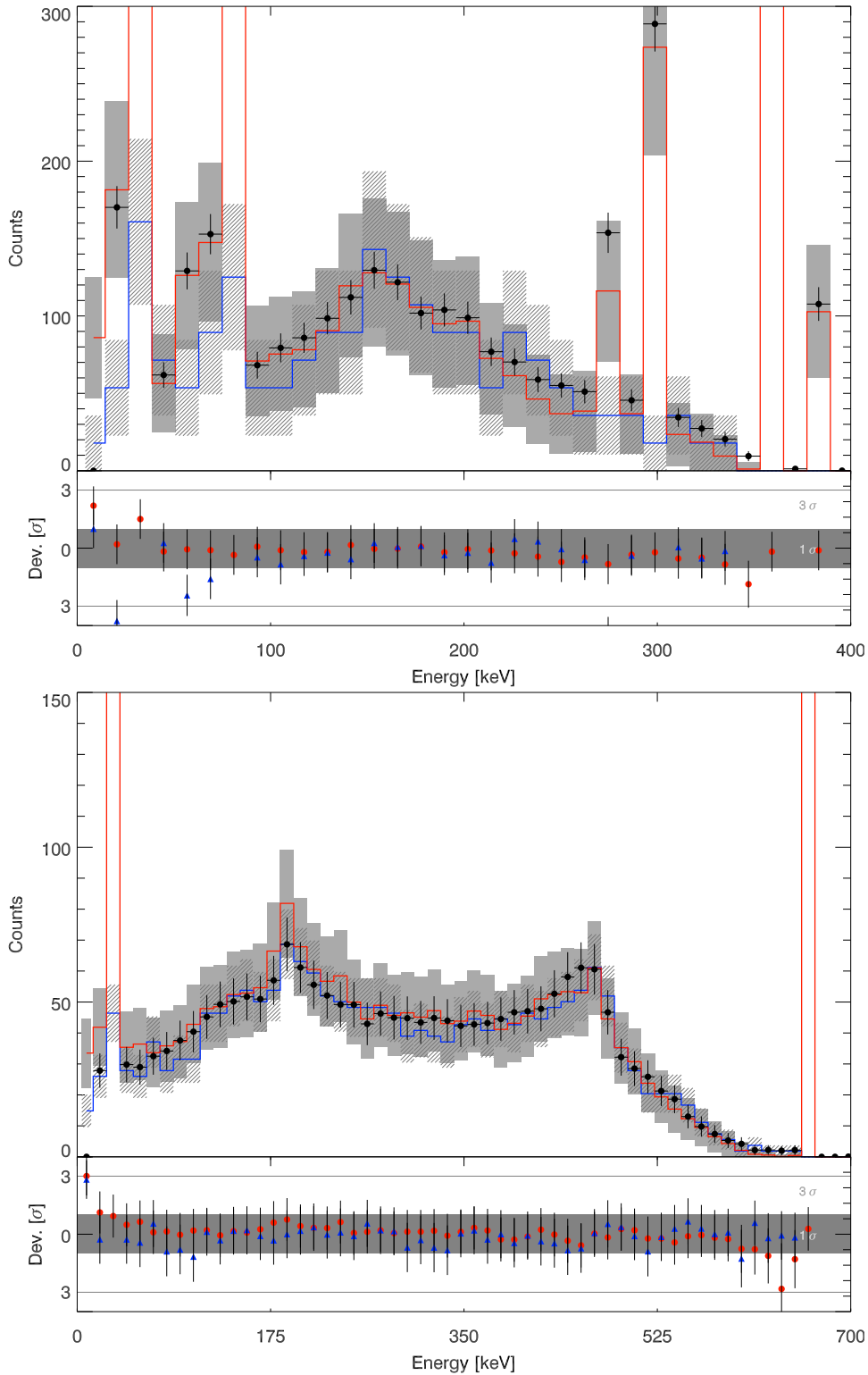
Figure 62: Comparison of the complete simulated and measured spectra showing the simulations' reproduction of the continuum. The following isotopes and peaks are shown: ^{133}Ba (top) and ^{137}Cs (bottom). Simulations using the current Geant4 code (blue line, hatched 1σ errors) and the new code (red line, filled 1σ errors) are compared. The lower panel shows the residuals (blue triangles: current Geant4 code, red circles: the new code) in terms of σ uncertainties (solid area: 1σ, lines: 3σ). Note that the y-axis was limited in range in order to accentuate details of the spectrum.

Element	Mass fraction
Hydrogen	0.1047
Oxygen	0.5785
Magnesium	0.0157
aluminium	0.0317
Silicon	0.2115
Calcium	0.0479
Iron	0.0100
Europium	3.7×10^{-8}
Cobalt	8.26×10^{-7}

Table 14: Mass fractions of the elements constituting to the concrete block used in the long-term activation verification. The isotope composition of the individual elements was set to natural abundances. Due to rounding errors the individual fractions do not sum to unity.

6.3 Verification and Validation of the Long-term Activation Simulation

The newly developed radioactive decay simulation for Geant4 includes possibilities to model the isotope build-up associated with long-term activation. These models take the activation rate per atom for a given material and volume as input and use the decay chain algorithm presented in Chapter 5.5 to calculate the isotope composition of the material at a given time in the future. The activation rates are acquired from the Monte-Carlo simulation itself; the only required user-input is the primary particle flux, which is needed to relate the number of emitted primaries with a time span.

The long-term activation code outputs an *XML** file containing the new material composition on a per volume basis. This information is used as input for a second simulation run, in which the new material composition is set in the geometry and the corresponding volumes have decay activities associated. During this second simulation run these volumes will act as radioactive background sources which produce the long-term-activation induced radiation. In the following a verification of the isotope abundance calculation and a validation of an application using the new long-term activation code are presented.

6.3.1 Verification with Tabulated Data

The reliability of the long-term activation extension of the new radioactive decay code was verified by simulating the irradiation of a concrete block with $10\,\text{MeV}$ neutrons at a flux of $10^5\,\text{s}^{-1}$ for $50\,\text{h}$. This cubic block had an edge length of $60\,\text{cm}$ and was subdivided into $5 \times 5 \times 5$ sub-volumes. For each of these smaller volumes the activation and material composition was tracked. This information was used as input for a second simulation in which the sub-volumes were now defined as background sources, the activity of which was sampled every $100\,\text{s}$.

The initial composition of the concrete is shown in Table 14. Figure 63 shows the time evolution of the different isotopes' activities after neutron activation as produced by the simulation in comparison with expected activities calculated from ENSDF tabulated data. This calculation was done by using the same activation rates which are input into the long-term activation code to calculate the isotopic composition after the irradiation. Based on this new isotope abundance the development of the isotope-specific activity over time was calculated. The results of these manual calculations are represented by the solid lines in the figures. One should note that the data is idealized as no statistical distribution of the activity was taken into account. In the simulation the activity is drawn from a Gaussian distribution centered on this idealized activity. Accordingly, the scattering of the data points around the calculated data is intended and part of the model. In conclusion, the simulation is in good agreement with the verification calculations. One should note that this simple verification scenario is commonly encountered in applications concerning the activation of particle accelerator or reactor walls.

---

*   Extensible Markup Language

Figure 63: Time development of the activity of different isotopes in a concrete block after 50 h of irradiation with 10 MeV neutrons. The data points are from a Geant4 simulation using our new radioactive decay code. The solid lines represent activities calculated using ENSDF tabulated data and the initial isotope composition of the concrete as input.
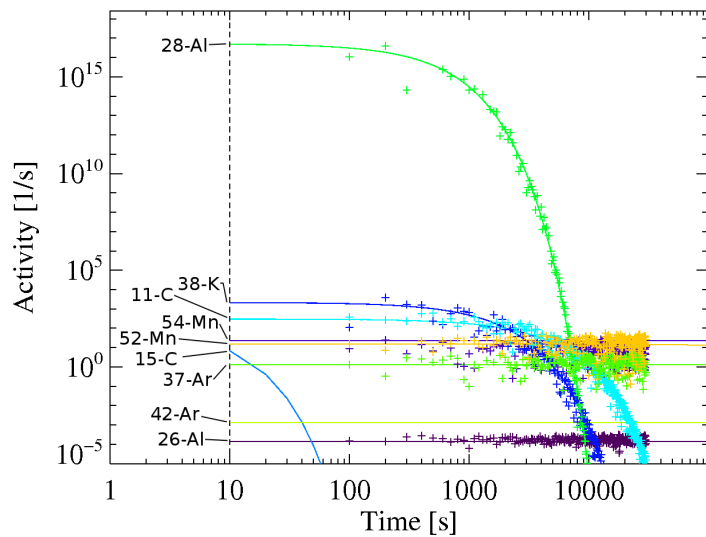
Figure 64: A sketch of the geometry used for the validation of the long-term activation code with STS-53 data. The center blue box is the 3×3 inch NaI crystal. It is surrounded by a mass dummy of the Space Shuttles hull and shielding, which is between $5\,\mathrm{g\,cm^{-2}} - 33\,\mathrm{g\,cm^{-2}}$ at the mid-deck locker location of the crystal. This was approximated by an aluminium box with a wall strength of 10 cm.
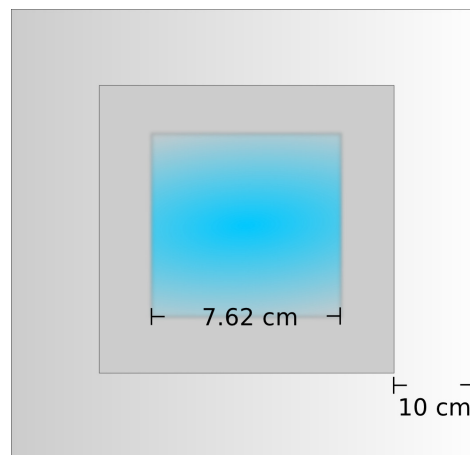
6.3.2 Validation with STS-53 CREAM Data

The Cosmic Radiation Environment & Activation Monitor (CREAM) (Dyer et al., 1992) was flown in the mid-deck locker of the STS[*]-53 Space Shuttle mission. The experiment included a cubic $3 \times 3 \times 3$ inch sodium iodide (NaI) scintillator crystal, which was kept inside the locker during the mission. Here it was irradiated by cosmic ray particle penetrating the shuttle's hull and interior structures. This irradiation resulted in the activation of the material. After the shuttle had landed the crystal was quickly bonded with a photomultiplier tube in order to detect scintillation photons produced by the decay radiation from the activated isotopes. The induced radioactivity was then measured 22.6 and 182 hours after touchdown. Using the resulting spectra the isotopic composition after activation could be deduced. Due to the different half-lives of the various radio-nuclei a characteristic shift of the photo-peak intensities with respect to the measurement time was observed.

Because the quality of a long-term activation code is mainly determined by the correct time evolution of an initial sample of radio-nuclei subject to activation, the CREAM NaI-crystal measurements represent an excellent validation possibility. Due to the simple setup of the experiment the simulation geometry was intentionally kept simple too. It consisted of the crystal enclosed in a hollow aluminium block with a wall thickness of 10 cm. This corresponds to the mean shielding thickness around the mid-deck locker which is between $5\mathrm{g\,cm^{-2}} - 33\,\mathrm{g\,cm^{-2}}$ (Dyer et al., 1992). A sketch of the geometry is shown in Figure 64.

---

[*]   Space Transport System

This setup was irradiated with protons emitted from a virtual sphere geometry, as described in Chapter 3.2. The energy and flux of these protons follows a cosmic ray spectrum calculated with the CREME96 code and using the orbital parameters of the STS-53 mission, i.e an apogee of 381 km, a perigee of 372 km, an inclination of 57° and a mission duration of 7 days (NASA, 2012). The launch date was set to December 2nd, 1992. The physics list was same as used for the IXO and ATHENA simulations: G4Livermore-EM physics and a modified *QGSP_BI_HP* hadronics list. The scintillation process and thus optical photons where not modeled. After the occurrence of 50,000 activations the irradiation simulation was concluded with an activity calculation by the new long-term activation code for the crystal after 22.6 and 182 hours respectively. The results from the activation simulation and calculation were input into as second simulation run. This time the NaI crystal was modeled as a radioactive source. In this simulation the energy deposits resulting from decays within the crystal were written out.

For the analysis the energy deposit data was binned into a histogram with a bin width of 100 keV, a the finite energy resolution of the detector was included by folding this histogram with a Gaussian ($\sigma = 200$ keV). The data was then normalized according the procedure introduced in Chapter 3.2 and compared with experimental data taken from similar comparisons by *Dyer et al.* in Dyer et al., 1994. The spectra resulting from a simulated measurement 22.6 hours and 182 hours after the simulated end of activation (i.e. Space Shuttle touchdown) are shown in Figure 65. It is apparent from the figures that the simulations agree well with the measurements. A comparison of the photo-peaks shows that the same isotopes are produced in the experiment and the simulation, with the exception of ^{111}In and ^{126}In. This deviation was found to result from the hadronic activation physics and not the long-term activation code, i.e. the production of ^{111}In is underestimated by the hadronic models while the production of ^{126}In is overestimated. The change in individual peak intensities of the ^{124}I and ^{126}I group as well as the complete decay of the ^{123}In peak with time are modeled correctly.

The remaining deviations are assumed to result from the extremely simplified simulation, which neither included a correct treatment of the detector energy resolution, nor the production of scintillation photons. The latter of which clearly manifests itself in the absence of the Iodine absorption edges in the simulated data.

Nevertheless, this simple validation provides a self-consistent estimate not only of the long-term activation and radioactive decay code accuracy but also of the complete IXO/ATHENA physics processes. In those parts of the spectra which are not influenced by the discussed response and activation issues the deviation is generally below 50% and the continuum deviates less than 20%.

6.4 Conclusion on Radioactive Decay Physics in Geant4

In this and the previous chapters the requirements for radioactive decay simulations as part of a Monte-Carlo toolkit have been discussed. The current Geant4 code was found not to fulfill all these requirements. Due to the current code's design, which makes maintenance of and extensions to the code tedious it was chosen to develop a new radioactive decay code for Geant4. After an introduction of the new code's design and underlying programming, verification and validation tests as well as performance estimates were presented for both codes. In general it was found that the new code is more performant in all three fields. Both the verification with ENSDF and the validation measurements with a HPGe detector show $5 - 50\%$ lower intensity deviations for the new code with respect to the current code when compared to evaluated and measured data. This observation is especially frequent at lower energies in the X-ray regime and for conversion and Auger-electrons. At the same time the new code offers speed gains of up to 50% and has the capability of self-consistently modeling long-term activation buildup within a single Geant4 simulation; a feature which was verified and validated with Space Shuttle measurements and was found to be consistent with expectations.

In summary, these features make the new code ideal for low background simulations such as those for IXO and ATHENA. Not only does it outperform the existing Geant4 code, it also is more accurate in the critical energy range below 40 keV.
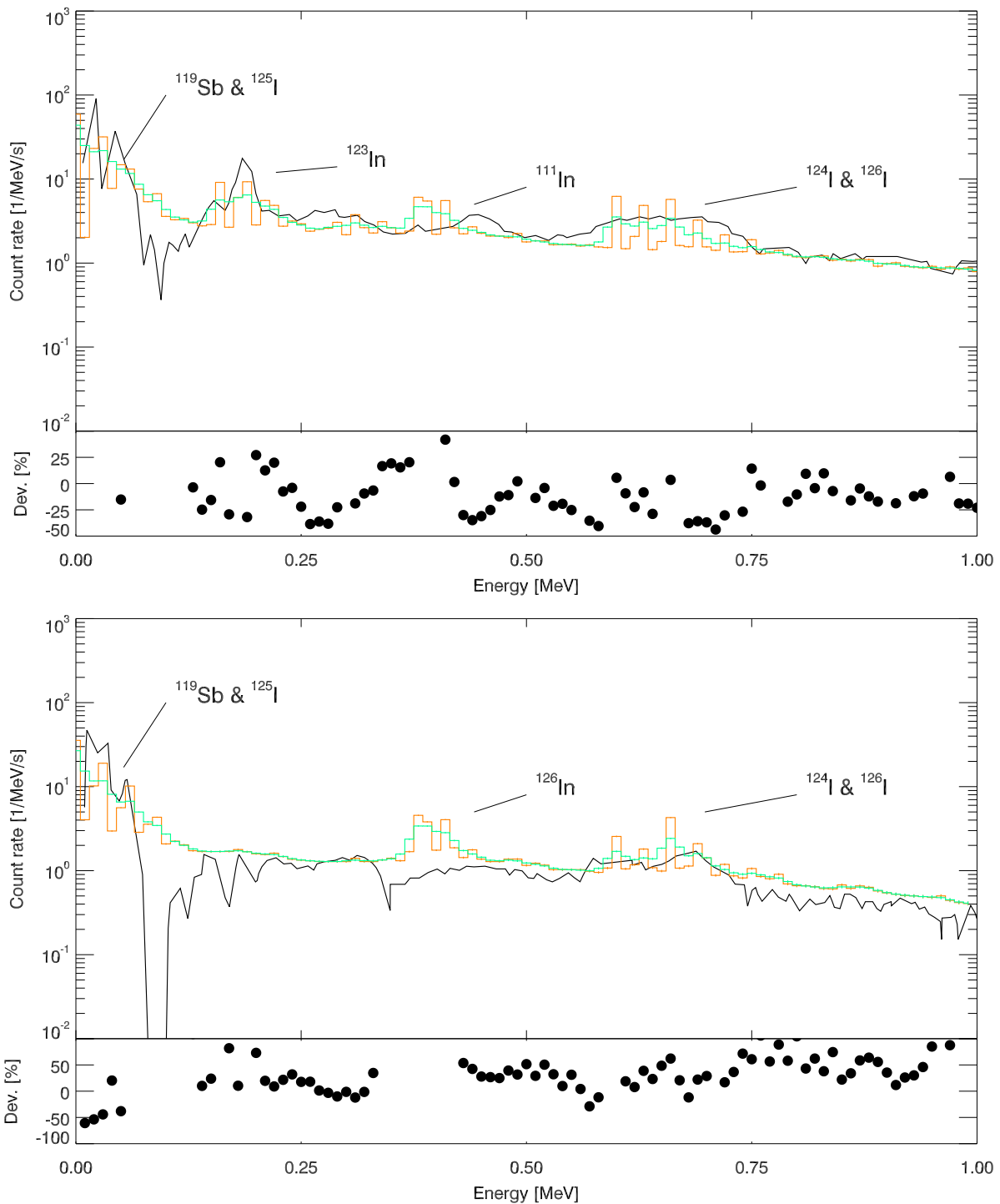
Figure 65: A comparison of the simulated irradiation and subsequent decay measurements of a NaI crystal which was part of the CREAM experimental package on board the STS-53 mission with experimental data (black solid line) taken from Dyer et al., 1994 . The top plot shows a spectrum of the induced radioactivity measured 22.6 hours after touchdown of the shuttle, the bottom plot a measurement 182 hours after touchdown. The orange solid line represents the raw simulated data, the green solid line this data after application of a 200 keV wide Gaussian PSF. The lower panels shows the relative deviation between the response adjusted simulation and the experimental data. The uncertainties for the spectra in the top panels are sufficiently small as to not be distinguishable. The experimental data source does not include uncertainties which is why none could be attached to it and the corresponding deviation values.

Another important point for IXO/ATHENA-style design phase simulations has been addressed by the validation measurements. The uncertainty for a known detector design without the possibility of optimizing/calibrating the simulation geometry has been quantified at $\approx$ 20%. This is valuable input for determining the accuracy of the IXO/ATHENA simulation, which will be presented in the next chapter.

Figure 66: The simulated IXO WFI quantum efficiency (black solid line) compared with the modeled quantum efficiency (red line) published in Treis et al., 2009b. The lower panel shows the relative deviation between simulation and model.
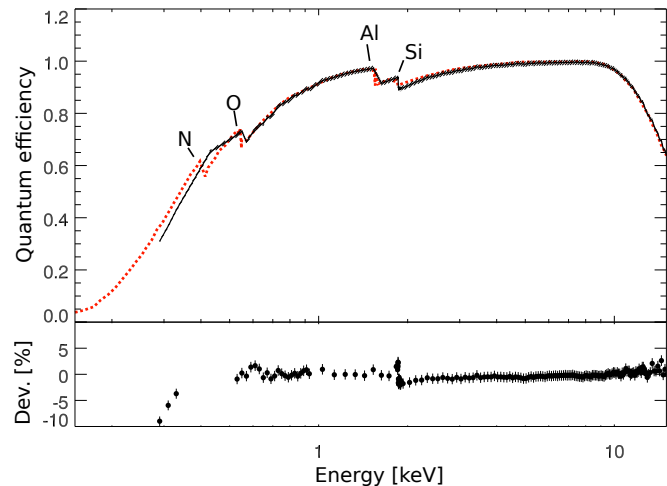
7 Background of the IXO/ATHENA WFI

The previous chapters have deviated from the original goal of estimating the IXO/ATHENA particle induced background. This had become necessary as it was found in the introduction to the IXO/ATHENA simulation environment in Chapter 3.3 that the Geant4 radioactive decay code does not provide an adequate means of simulating the delayed background component. This assessment has led the development of a new radioactive decay code and an extensive validation and verification effort thereof (Chapters 3.5–6.2). Concurrently to this software development estimates for the prompt background component of the IXO and ATHENA WFI have been performed. These are presented in this chapter alongside the delayed background results for ATHENA. The delayed results make use of the aforementioned work.

The background simulation results will mainly focus on the newer ATHENA design. This is due to two reasons: The ATHENA and IXO Wide Field Imager designs are sufficiently similar that results on topics such as pattern suppression performance and background constituents are equally valid for both missions. Additionally, the ATHENA simulations use the newest code developments of both the simulation framework, analysis routines and radioactive decay code. Due to the long run duration of individual simulations it was refrained from rerunning the IXO geometry with this code. Instead references to IXO will be given whenever appropriate and many of the preparatory simulations presented here are based on the IXO geometry.

7.1 Quantum Efficiency

The correct simulation of the WFI's quantum efficiency was verified in a similar fashion as presented in Chapter 3.5 for the validation of the simulation environment with XMM Newton data. For the IXO WFI the simulated data was compared with the modeled efficiency given in Treis et al., 2009b. As is apparent from Figure 66 simulation and model are in good agreement. The main absorption edges are correctly reproduced by the simulation and the absolute efficiency is modeled with and accuracy of > 90%.

7.2 Graded-Z Shielding Performance

The graded-Z shielding is one of the key ATHENA/IXO design features. Optimally it suppresses all fluorescence emission within the detector energy range resulting in a flat, easy to model background. A good estimate of the shielding's performance is thus of great importance. The initial optimization of the shielding was carried out using the Geant4 based MULASSIS software and the same plane approximations of the shielding used for the initial qualification of the background input spectrum. The characteristics of the optimized shielding were then confirmed by a simulation of the complete geometry within the IXO/ATHENA simulation environment.

Figure 67 shows the plane approximation results for the optimized graded-Z shielding with layer thicknesses as given in Table 3. As is apparent from the figure the graded-Z shielding in the given configuration
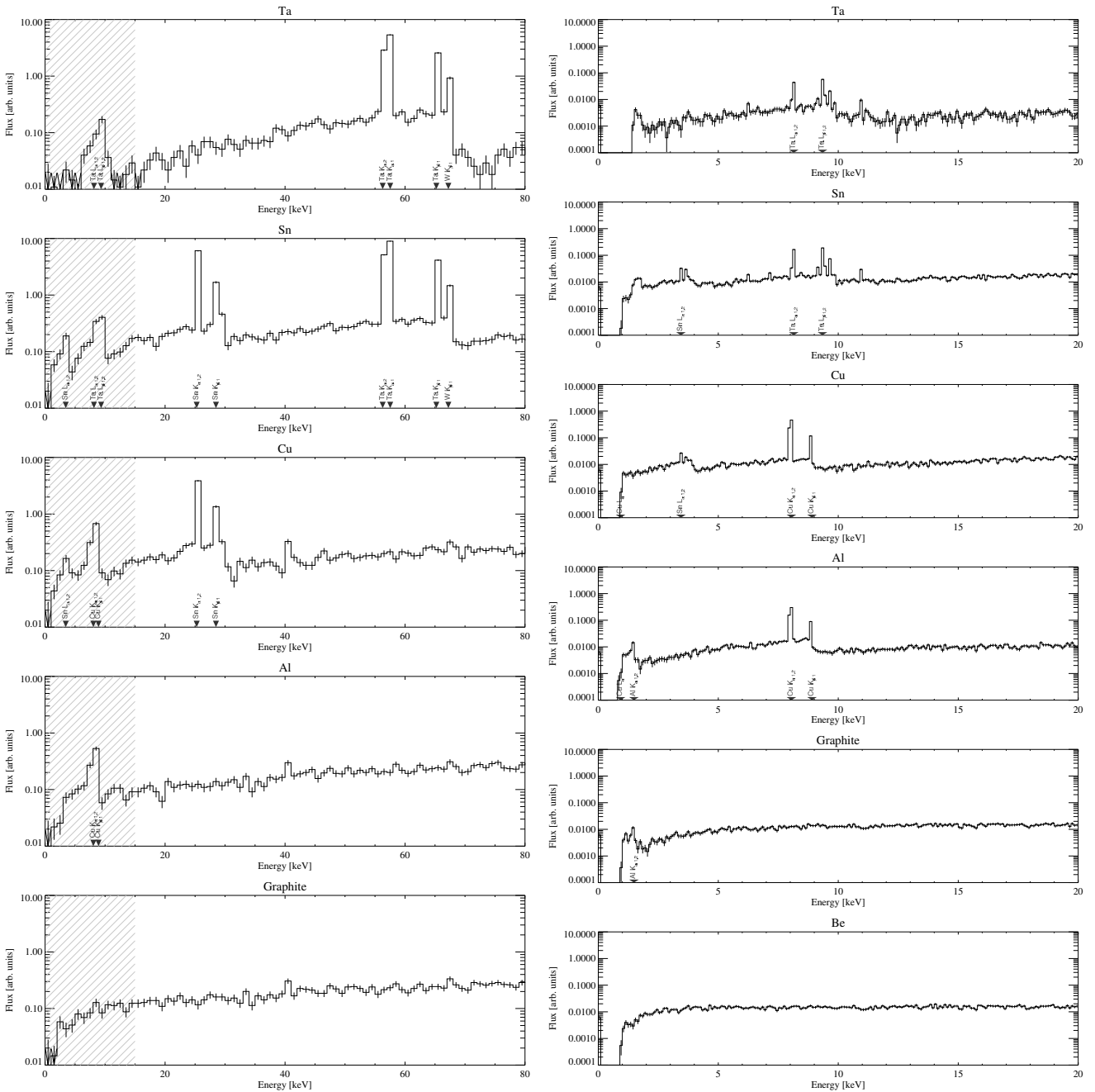
Figure 67: Performance of the IXO/ATHENA graded-Z shielding. The spectra show the X-ray flux behind the subsequent shielding layers; with the bottommost being the flux incident on the detector. As the DePFET-based WFI has a quantum efficiency near 1 for large parts of the energy range ($0.1 - 15\,$keV) most of the radiation within this range will be detected. Left panel: spectra extended past the detector energy range (shaded area) which highlight the fluorescence emission from the outer shielding layers (Ta, Sn). Right panel: more detailed view of the WFI energy range. An additional Beryllium layer was added to further suppress the Al- and C-fluorescence emission. Note that MULASSIS has a cutoff energy of $0.9\,$keV.

Figure 68: The simulated ATHENA background spectrum using the optimized graded-Z shielding and after pattern recognition and background reduction processing. In the simulation a molybdenum cold finger was placed behind the sensitive detector area. The presence of Si-$K_{\alpha+\beta}$ emission (dashed line) results from neighboring pixels and the ASICs. Carbon and beryllium emission originates from the ceramic detector mounting and the beryllium shielding layer. Also note the Fe-absorption edge at $\approx 6.8\,\mathrm{keV}$, which results for the Invar-made, iron-rich detector frame.
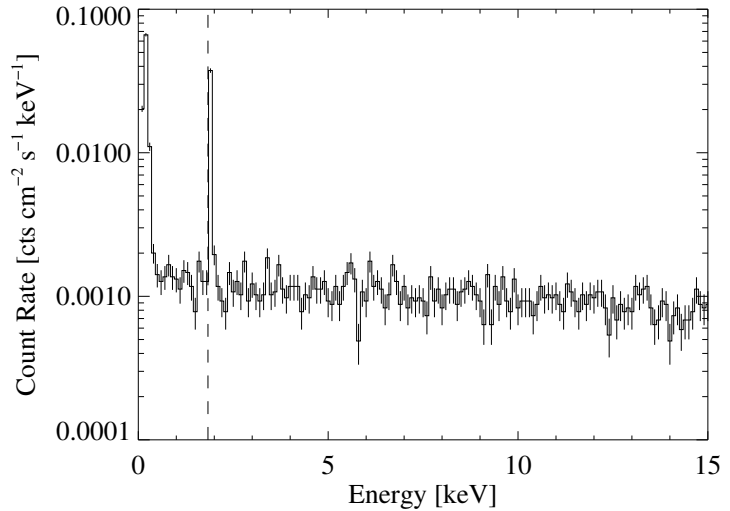
effectively suppresses all fluorescence emission behind the innermost Beryllium layer. Furthermore, the spectra presented in the figure confirm that fluorescence emission from the intermediate shielding layers is correctly produced via PIXE. The results of a full ATHENA simulation are shown in Figure 68 and confirm the plane approximation findings: the detector background is free from fluorescence emission of heavier elements. Not unexpectedly three emission lines can be distinguished in the full simulation which includes the pixelized detector and detector components inside the shielding:

- The Silicon $K_{\alpha+\beta}$-lines at $1.739\,\mathrm{keV}$ and $1.835\,\mathrm{keV}$ respectively. These originate from neighboring pixels and the ASICs in proximity of the detector.

- The Carbon K_{α}-line at $0.277\,\mathrm{keV}$. While the emission from the carbon-rich shielding layer is suppressed the sensitive detector part is mounted on a carbon rich carrier board which is in turn held in place by a carbon-containing ceramic mountings; both of which are not shielded from the detector.

- The Beryllium K_{α}-line at $0.108\,\mathrm{keV}$ resulting from the Beryllium shielding layer. This emission is at the lower bound of the detector energy range and will thus be uncritical for most observations.

In conclusion, it was confirmed that the graded-Z shielding effectively suppresses fluorescence emission; thereby greatly simplifying the (detector) background models needed for observation analysis.

7.3 Pattern Detection as a Means of Background Reduction

Particles such as electrons and protons incident on the WFI can deposit energy in multiple pixels of the detector. Pixel patterns resulting from these events can frequently be distinguished from those patterns resulting from actual X-ray radiation. An overview of such valid patterns and their occurrence in the background component is shown in Figure 25 and Table 15. Further background identification is carried out by excluding events where the total energy deposit of a pattern is above $20\,\mathrm{keV}$; the energy at which the reflectivity and thus focusing ability of the ATHENA mirrors rapidly decreases (Friedrich et al., 2012).

Because of the two distinctive classes of patterns occurring the simulated overall raw instrument background of $0.0957 \pm 0.0002\,\mathrm{cts\,keV^{-1}\,cm^{-2}\,s^{-1}}$ can be greatly reduced by $> 99\%$ if all patterns from the observation which cannot be attributed to X-rays are excluded. This can be done frame-wise by discarding a complete frame whenever an invalid pattern is detected. In case of IXO and ATHENA this
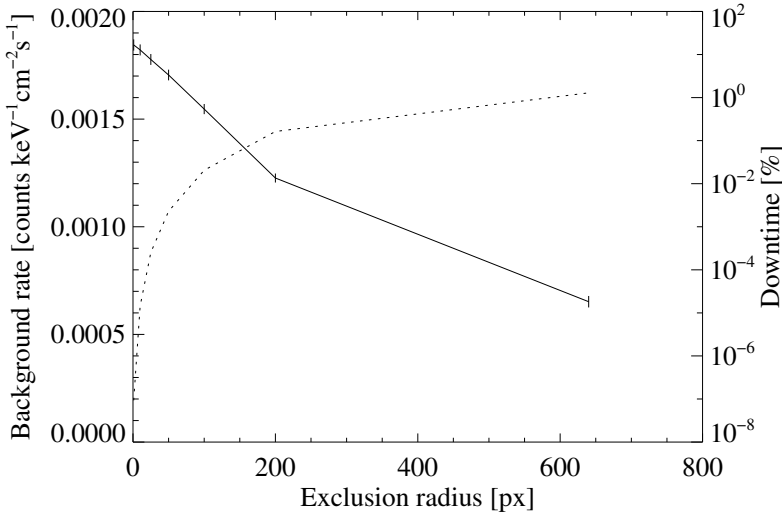
Figure 69: The effect of the exclusion radius size on the background rate (solid line) and dead time (dashed line). The comparison was done using an ATHENA simulation with a molybdenum cold finger design.

Table 15: Occurrence of different background pattern types and how often they are considered valid or non-valid background patterns.

Pattern	Occurrence [%]	Non-valid [%]	Valid [%]
Singles	31.11	85.18	14.82
Doubles	25.43	99.36	0.64
Triples	20.12	99.99	0.01
Quadruples	12.00	100.00	0.00
N>4	11.34	100.00	0.00

approach results in a dead time of $\approx$ 1.6% because frames with identified background are lost for science observation.

Another approach is to only exclude additional events (radially) positioned around an identified invalid pattern. Figure 69 shows the effects of the size of such exclusion radii on the background rate and dead time for an ATHENA simulation with a molybdenum cold finger design. It is apparent from the figure that the background rates quickly drop as a result of introducing exclusion radii and level out if nearly the complete frame is masked. This behavior can be explained by the fact that the secondary particles produced when a cosmic ray traverses the detector components are emitted at relatively small angles from the primaries trajectory. The small angles are due to the fact that particles able to penetrate the shielding need to have energies of at least a few MeV and are thus not scattered much before interacting with the sensitive volume.

The larger the exclusion radius the more background events from such a shower will be rejected. At a 640 px exclusion radius more than half a frame area is dropped and the dead time accordingly approaches the full frame-dropping value. For most observations this is acceptable but because the exclusion radius size can be implemented variably, one order of magnitude lower dead times at the cost of only twice as high background rates are possible. A summary of dead times for different cold finger designs is given in Table 17. In both cases the dead times are much shorter than what would be expected from an anti-coincidence of similar performance as it was planned for SIMBOL-X (Hauf, 2009a; Tenzer et al., 2009). Here dead times above 10% of the total observation time occur.

7.4 Influence of the XMS and Surrounding Satellite Components

The influence of the surrounding satellite components on the background estimates was evaluated at an early point of the work for IXO. The reasoning was that if these components could be excluded the virtual source sphere can be reduced in size while still enclosing the complete simulation geometry. This would
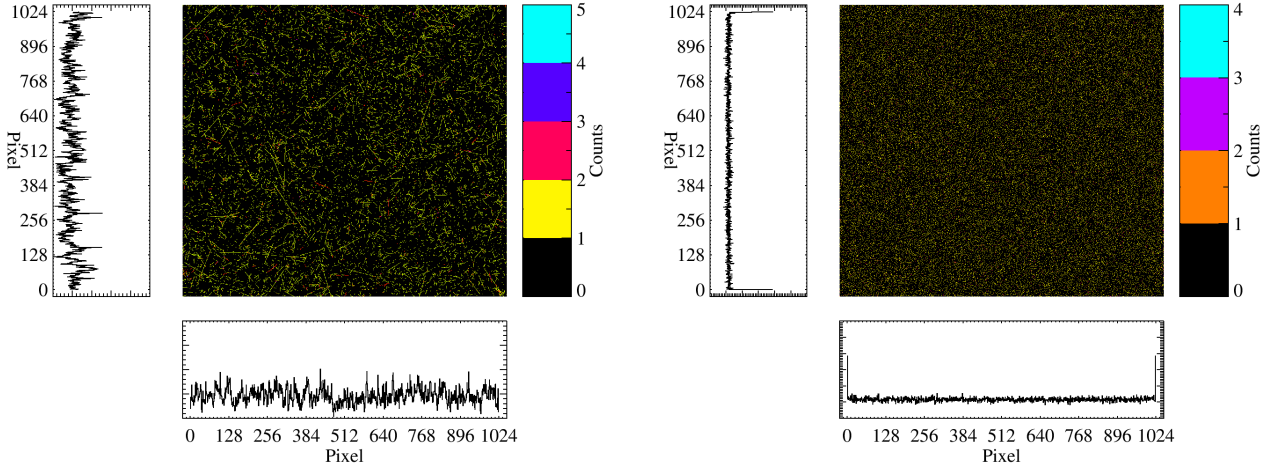
Figure 70: A comparison of two IXO simulations done with Geant4.9.1. The left panel shows an integral image of the IXO background resulting from a simulation of 10^6 primary protons without the satellite structures and the XMS. The right panel shows a similar image for a simulation resulting from 10^7 primaries which included the satellite components and the XMS. Note that the background is homogeneous in both images (within the statistical limits) and that no evidence of the XMS' presence is seen.

lead to a decrease in computing times for a given number of primary events because particles would hit background relevant components within the geometry.

The largest single component in the simplified satellite geometry implemented as part of this study is the X-ray Micro-calorimeter Spectrometer (XMS). With a mass of over 200 kg (Herder et al., 2010), mainly due to the required cryogenic system, the XMS is the most likely structure to influence the WFI background.

Figure 70 shows a comparison of integrated background images from two IXO simulations: one with the XMS and satellite components, the second without. It is evident from the figure that both geometrical setups result in a nearly homogeneous background which is unaffected by the presence of the XMS. This observation is supported by the background rates resulting from these two simulations, $(4.03 \pm 0.31) \times 10^3 \, \mathrm{cts \, cm^{-2} \, s^{-1} \, keV^{-1}}$ (w/o XMS) and $(3.66 \pm 0.06) \times 10^3 \, \mathrm{cts \, cm^{-2} \, s^{-1} \, keV^{-1}}$ (with XMS), which are compatible with each other.

In conclusion, it was found that the presence of the XMS and other satellite components has minimal influence on the detector background. More importantly does it not introduce inhomogeneities into the background. In consequence, both the satellite and the XMS have been excluded from most of the following simulations in order to reduce processing times.

7.5 Influence of the Realistic Entrance Window Model

As part of a further refinement of the IXO geometric model optical and UV-filter layers were added to the wafer as part of a realistic entrance window representation at the time of transitioning the simulation environment to Geant4.9.3. These layers are a few nanometers in thickness; a geometrical extend which is at the limit of Geant4's applicability. By default the secondary production threshold is set to 250 eV for photons and 990 eV for other particles. As a result, secondary electrons which would be produced in the thin layers are not created and tracked. Instead their corresponding energy is deposited at the point of production. This results in the behavior highlighted in the left panel of Figure 71 which shows a cut through the entrance window including the mentioned filter layers. The sharp peak visible in the histogram showing the energy deposition results from such secondaries which are not tracked further throughout the volume.
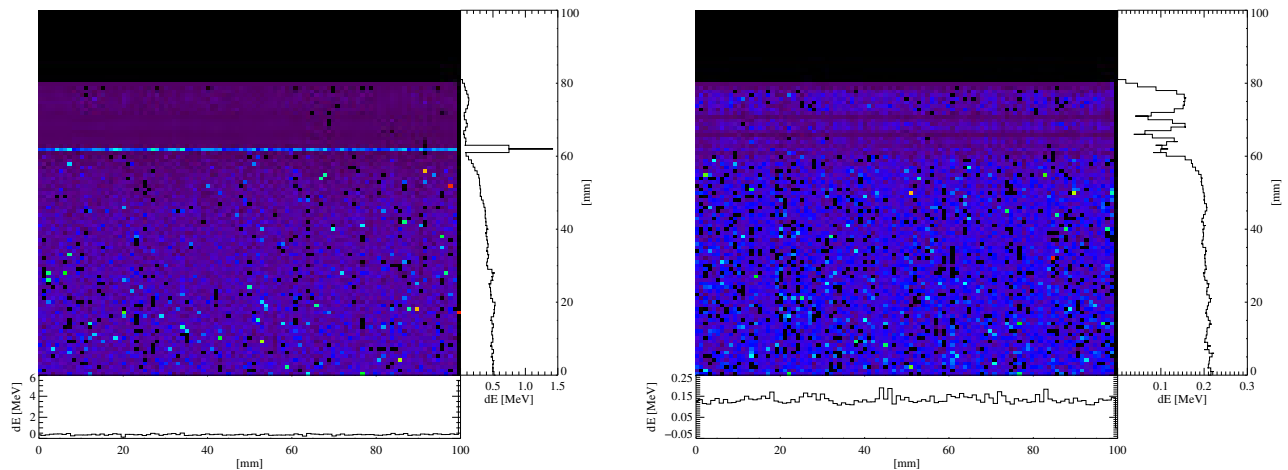
Figure 71: A comparison of the effects of secondary production thresholds on the energy deposition in the optical and UV-filter layers of the realistic entrance window. Both panels show a cut through the entrance window and histograms of the position dependent energy deposits. Note the sharp peak in energy deposition in the left panel when using the standard secondary production threshold of 990 eV. In comparison the energy deposition in the right panel, with a decreased threshold of 100 eV is more continuous and the positions of the layers are distinguishable.

The right panel shows the effects of forcing secondary production for all particles down to 100 eV by using the `G4ProductionCutsTable::GetProductionCutsTable()->SetEnergyRange()` command. The distinctive peak vanishes and instead a continuous energy deposit, with clearly visible layer boundaries is observed. While the distinguishable layers are simulation artifact due to the limited step size, the continuous behavior is physical as it shows that scattering takes place. Accordingly, the secondary production threshold was lowered for all subsequent simulations.

The addition of the layers does not influence the raw, pre-pattern rejection, background flux in case the standard secondary production threshold is set (Table 16). If the lower threshold is applied an increase of 16.3% is observed. This is evidence that the standard threshold value actually inhibited secondary production. Not as intuitively explicable is the behavior of the background rates with filters after pattern rejection has been applied. One would expect that the rate stays constant or increases in accordance with the raw rate. Instead a decrease is observed which necessitates that the effectiveness of the pattern detection algorithms has increased with respect to the layer-less simulations. Figure 72 hints to why this is the case. It is apparent from the figure that especially the secondary electron flux shows an increase in raw rates and a decrease in post rejection rates. As will be shown in Section 7.6 secondary electrons are the most important constituent of the background, accounting for over 90% of the emission. Accordingly, the changes in electron rates strongly influence the overall background. The filter layers now lead to additional scattering of secondary electrons, moving them to shallower incidence angles with respect to the silicon-surface (Figure 73). In consequence, the electrons are more likely to deposit energy in more than one pixel. This results in a higher chance for the occurrence of invalid patterns which are detected by the pattern rejection algorithms and in turn effectively reduces the background rate.

In conclusion, the addition of the filter layers to the simulation results in a more realistic entrance window design and has a positive impact on the background rate. Nevertheless one should be aware of the fact that forcing the secondary production threshold to a lower energy may result in unvalidated behavior of the simulation.

Figure 72: Relative change of particle fluxes before an after pattern rejection with filter layers in comparison to a simulation without these layers.
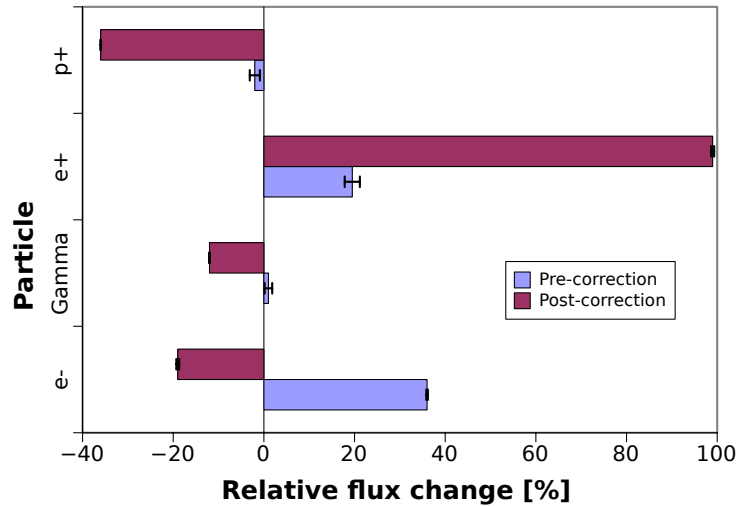
Table 16: The influence of the filter layers with standard secondary production threshold and lower production threshold on the raw background rate and the background rate after pattern rejection has been applied.

	No layers	Layers with standard threshold	Layers with low threshold
Raw rate	922.45 ± 1.54	922.97 ± 1.60	1072.61 ± 2.31
Cor. rate	24.35 ± 0.54	19.73 ± 0.32	10.87 ± 0.36

7.6 Background Constituents and Origin

In order to explore further background reduction possibilities the constituents and origin of the background radiation were identified. As is apparent from Figures 74 and 75 the background is dominated by secondary electrons which originate mainly from the shielding and detector housing near the field of view. In contrast, the origin of the gamma radiation is distributed more evenly within the detector geometry. This radiation manifests itself in the Si-$K_{\alpha,\beta}$, C-K_α and Be-K_α-lines visible in the spectra shown in Figures 74 and 68.

The homogeneous origin of the gamma radiation when compared to the secondary electrons is due to the fact that the electrons are more easily shielded from detection by material between their production points and the sensitive area. As a consequence only electrons with high energies or those produced near component edges in proximity to the field of view reach the pixelized area.

Figure 75 also identifies the production positions of positrons and neutrons which either influence the background directly, or more commonly with the secondary radiation they stimulate. The occurrence of these particles can be attributed to hadronic interactions which also lead to nuclear activations and subsequent radioactive decays. Accordingly, they occur mainly in higher-Z materials such as the tantalum component of the graded-Z shielding and the molybdenum cold finger.

In addition to the spatial origin of the secondary particles the processes via which they interact were studied. Again slices through the IXO detector model were created, but this time interaction types not particles were distinguished. These interaction distributions are shown in Figure 76. It is apparent from the figure, that the majority of interactions occurs in the high-Z materials of the HXI and its surrounding anti-coincidence unit as well as in the graded-Z shielding (bright red and orange in the figure). The occurrence of the electromagnetic processes is strongly material and density dependent but distributed similarly over all process types. In contrast, the occurrence of hadronic processes, such as neutron and proton scattering, is more homogeneously distributed over the geometry. In conclusion, these studies yield a more detailed insight to how the secondary particles identified at the beginning of this section
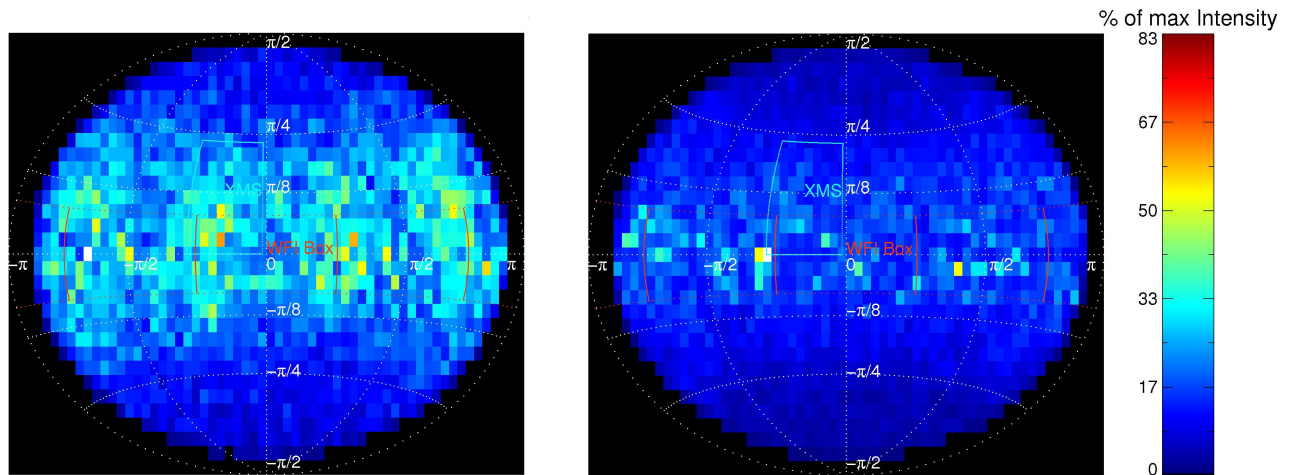
Figure 73: A comparison of the incidence angles of secondary electron when sampled from the center of the WFI. The left panel shows a simulation without the optical and UV-filter layers, the right panel a simulation including these layers. The addition of the filters results in majority of secondary electrons hitting the detector at shallower angles. The positions of different satellite components and detector components are marked in the plots.
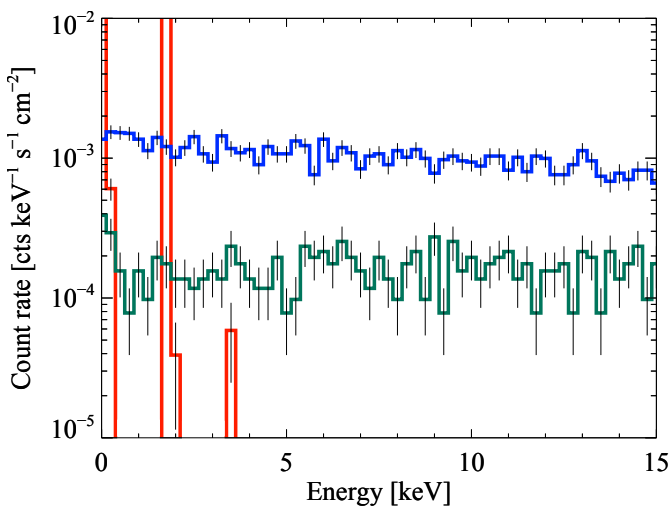
Figure 74: The constituents of the ATHENA Wide Field Imager background for a 165×10^6 primary proton simulation with a molybdenum cold finger: secondary electrons (blue), gamma radiation (red) and other particles (green). Note that the fluorescence line intensity extends beyond the count rate range shown in the spectrum.

are produced. The material dependent production yields of these particles are confirmed. As a result, high-Z materials should be avoided in the vicinity of the sensitive area.

7.7 Suppression of Secondary Electrons

In the previous section secondary electrons have been identified as the dominant background source. A large fraction of these are produced in the graded-Z shielding, as is apparent from Figure 75. Significant reductions in the background rate can thus be expected if either the number of electrons produced or their influence on the detector can be limited. Sacrificing shielding thickness in order to decrease secondary electron production at the cost of reintroducing fluorescence emission into the background spectrum is clearly not an optimal solution.

Hence the second possibility of reducing the electrons' impact onto the detector should be investigated. Basically this can be achieved in two possible ways: stopping/shielding the electrons before they reach the sensitive area or altering the secondary electron spectrum in such a way that they deposit less energy in the detector's energy range. Because electrons are charged particles, electromagnetic fields provide
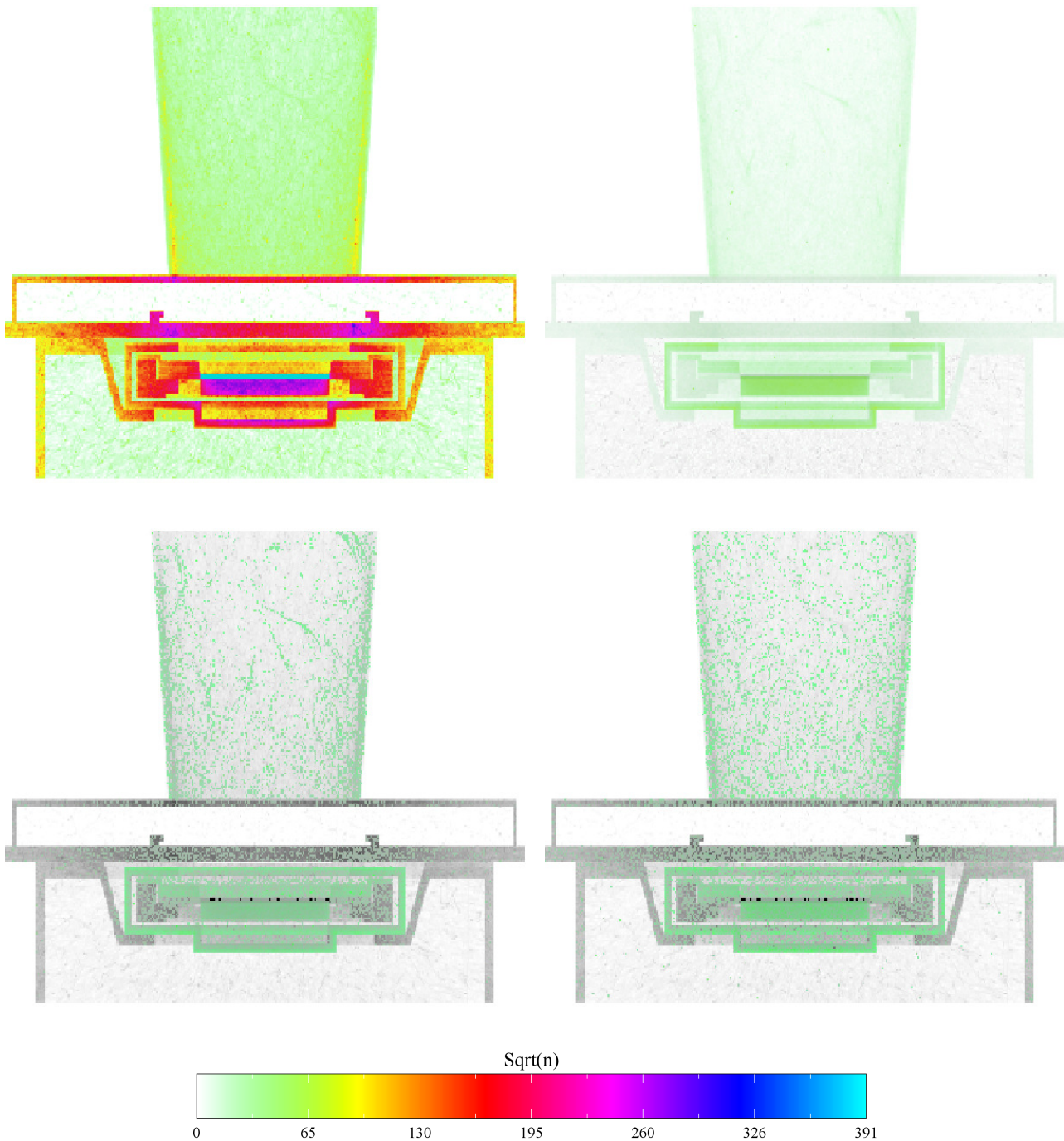
Figure 75: Origins of the secondary electron (top left), gamma (top right), positron (bottom left) and neutron (bottom right) emission registered in Wide Field Imager in terms of the number of created particles (n) for a simulation of 165×10^6 primary protons. Displayed is a $50\,\mathrm{mm}$ thick slice through the x-z plane of the detector. The detector geometry is underlaid in gray; the resolution of the grid is $1\,\mathrm{mm}$. It is apparent that secondary electrons which influence the background are mainly produced near the FOV edges, especially the aluminium mounting plate (areas underneath the baffle), the non FOV side of the graded-Z shielding (towards the bottom of the image) and the cold finger (pink-purple block at the center). The wafer itself can be seen in bright blue. Gamma radiation originates mainly as fluorescence emission from the shielding layers but also from the cold finger. Neutron a positron production occurs mainly in the components consisting of higher Z materials such as the outer graded-Z layers and the molybdenum cold finger. Note that for protons and positrons the colors have been intensified by 100%.
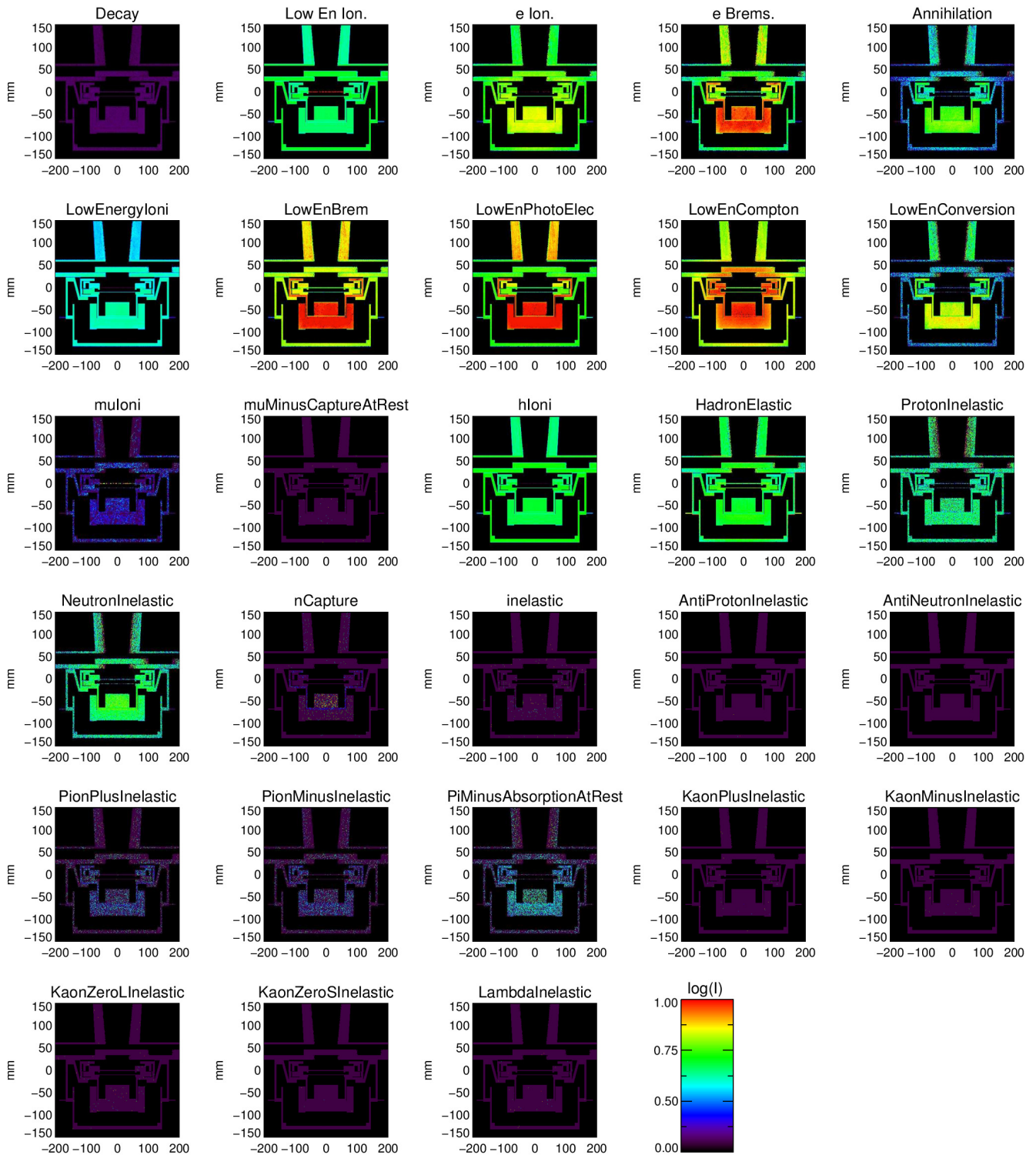
Figure 76: The spatial distribution of interactions with respect to the involved Geant4 processes. Shown are $5\,\mathrm{cm}$ thick slices through the IXO geometry and the occurrence of secondary interactions (the Geant4 process name is given) occur. The look up table gives the relative number of interactions in a column of $1 \times 1 \times 50\,\mathrm{mm}^3$ and is normalized to unity. Electron interaction occur mainly in the HXI and surrounding anti-coincidence unit.

an ample way of altering their energy spectrum, by either decreasing or increasing their kinetic energy. Accordingly, the influence of an electric field on the electron background component was investigated. The two designs studied are shown in Figure 26.

- The field was implemented to extend between the inner- and outermost grading-Z layers in such a way that a negative polarity slows the electrons (inner layer on negative potential) and a positive polarity accelerates them (inner layer on positive potential).

- An additional 0.1 mm thin graphite anode was added at a distance of 0.4 mm from the innermost graded-Z layer which would then act as the corresponding cathode. The field extends in the empty space between the two. The anode could be realized as a meshed structure, within the simulation this was implemented by decreasing the density of the graphite to 5% of the solid state density.

Both these scenarios are considered mechanically feasible as insulating layers can be easily worked into the graded-Z components. The required high field strengths will make them electronically challenging though.

Figure 77 shows the effect of different field strengths and polarities on the background rate for an ATHENA simulation with a molybdenum cold finger. Both field designs were studied. As is apparent from the figure a decelerating field (negative polarity) actually leads to an increase in background rates. The reason for this is that the secondary electron spectrum extends well beyond the detector energy range. Thus higher energy electrons will always replace those which are inhibited by the electric field.

The "accelerating field" approach is more promising and can lead to significant reductions of the background rate as is shown in Figure 77. In this case an electromagnetic field is used to accelerate the secondary electrons to energies above the detectable energy range. As a consequence they will be classified as background events with a higher probability. This significantly reduces the background rates by $\approx 60\%$ when electric field strengths above 200 kV/cm are employed corresponding to a potential difference of ≈ 80 kV from the anode to the cathode.

The shows oscillations of the background rate for field strengths between $0 - 40$ kV/cm can be attributed to the filter layer materials' different mean free inelastic scattering lengths for electrons. At a few nm they are in the same order of magnitude as the thicknesses of these layers. Electrons with lower energies have a short mean free path length and accordingly loose more energy due to scattering and deposit less of their initial energy in the sensitive area. They are thus less likely to trigger the background rejection threshold of 20 keV per pattern. With increasing field strength and electron energies, the energy loss through scattering is reduced for a given layer. At a certain field strength an electron energy is reached where even multiply scattered particles will retain sufficient energy to trigger background rejection. As three layers exist on the FOV side of the detector, three oscillations in detection efficiency are to be expected with increasing field strength. Additionally, within each layer volume only a small number of simulation and thus evaluation steps occur, leading to a "discretized" result of the simulation. This further amplifies the observed oscillatory behavior. Hence the oscillations are a combination of "real" physics and simulation artifacts.

7.8 Influence of Long Term Activation and Radioactive Decays

Cosmic ray protons interacting with the satellite and detector components may lead to the transmutation of elements thereby producing previously not occurring stable and instable nuclei. Instable nuclei will subsequently undergo radioactive decays and depending on the decay type emit detectable electron, positron, alpha or gamma radiation. If the production rate of an element through cosmogenic activation is above its decay rate the element will built up over time. This leads to an increase of decay activity and corresponding radiation over the mission duration. Likewise some elements may reach an equilibrium state if the production and decay rates are equal. Using the extensions to Geant4 described in Chapter 3.5 the additional delayed WFI background due to activation was estimated at $(0.21 \pm 0.05) \times 10^{-4}$ cts keV^{-1} cm^{-2} s^{-1} or about 5% of the prompt decay background after a mission
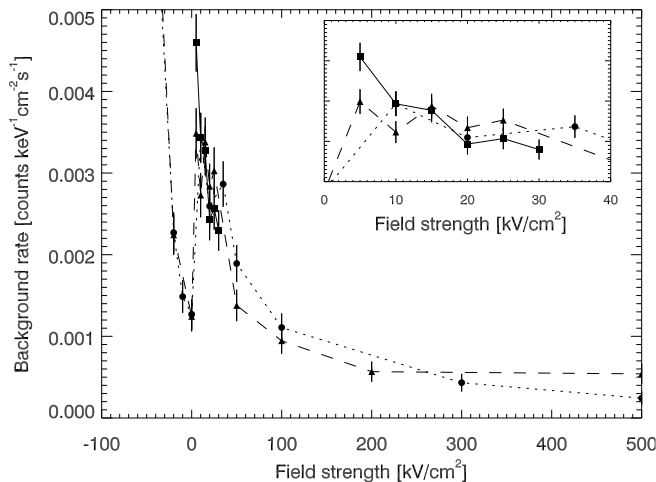
Figure 77: Effect of an electric field on the background rate (200 px radial exclusion) implemented in two designs: within the graded-Z shielding, the innermost layer is the anode, the outermost layer the cathode (circles); between the innermost graded-Z layer and an inner-lying graphite mesh anode 4 mm apart (triangles). The influence of the filter layers on the wafer was studied with a layer-free simulation of the second design (squares). The inset shows the region were oscillations of the background rate occur (see text for details).
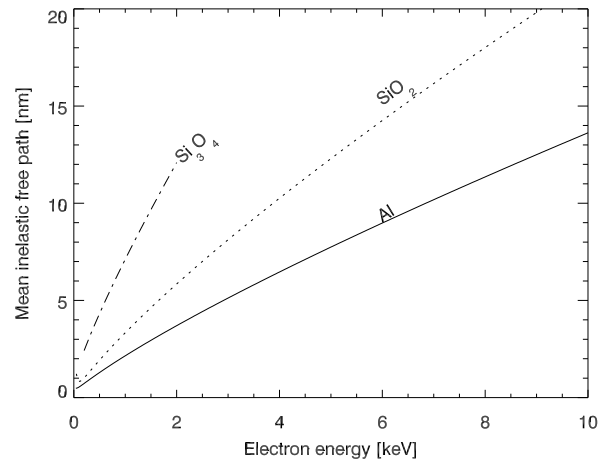
Figure 78: Mean inelastic free path of electrons incident on the materials the filter and carrier layers consist of. The different scattering properties correspond to the three oscillation peaks observed for the dependency between background rate and field strength. Electrons accelerated to higher energies by the electric field will subsequently be less affected by scattering and energy losses in these layers, thus depositing more energy in the detector — favorably above the detector energy range (see text for details). Data was calculated using *NIST Electron Inelastic-Mean-Free-Path Database: Version 1.2.*

duration of 10 years. As is apparent from Figure 79 this additional background has a flat, fluorescence emission free spectrum similar to that of the prompt background shown in Figure 68.

Comparison with Previous Missions

To the author's best knowledge no detailed long term studies of the cosmogenic activation induced background of X-ray telescopes such as XMM Newton or Chandra exist. For semiconductor detectors the accuracy of our simulations and the newly developed activation code was instead estimated by comparing against CGRO OSSE[*] data and simulations from Dyer et al., 1996 as well as simulations for the Wind TGRS[†] instrument presented in Weidenspointner et al., 2004. Both works present activation induced background rates for the surrounding detector structures and thus allow for a detector type independent comparison. Additionally, both the CGRO and the WIND observatories contain high-Z materials; similar to the Tantalum and tin in the IXO/ATHENA graded-Z shielding. These similarities are sufficient to allow for an order of magnitude comparison and consistency check of the IXO/ATHENA results, complimenting the explicit validation with Space Shuttle CREAM data presented in Chapter 6.3.2.

[*]   The Oriented Scintillation Spectrometer Experiment on-board the Compton Gamma Ray Observatory (Schoenfelder et al., 1993)

[†]   The Transient Gamma-Ray Spectrometer of the Global Geospace Science satellite Wind (Ogilvie and Desch, 1997)

Figure 79: The simulated delayed, activation induced ATHENA background spectrum using the optimized graded-Z shielding and after pattern recognition and background reduction processing. For the simulation a molybdenum cold finger was placed behind the sensitive detector area. The presence of Si-$K_{\alpha+\beta}$ emission (dashed line) results from neighboring pixels and the ASICs. Carbon and beryllium emission originates from the ceramic detector mounting and the beryllium shielding layer. Also note the Fe-absorption edge at $\approx$ 6.8 keV, which results for the Invar-made, iron-rich detector frame.
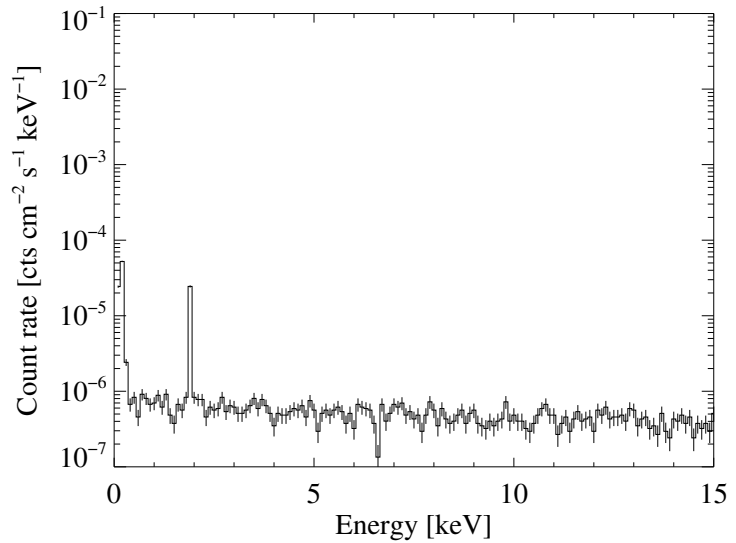
In Dyer et al., 1996, an activation induced background rate of $\approx$ 0.1 cts keV^{-1} s^{-1} – 5 cts keV^{-1} s^{-1} in the energy range from $0 - 20$ keV is reported. Taking into account the OSSE effective area of 2620 cm^2(Cameron et al., 1992) this corresponds to an activation induced background rate of $\approx$ 0.38×10^{-4} cts keV^{-1} cm^{-2} s^{-1} – 19.08×10^{-4} cts keV^{-1} cm^{-2} s^{-1}. For the TGRS detector Weidenspointner et al., 2004 report simulated activation induced rates of $\approx$ 3×10^{-3} cts keV^{-1} s^{-1} for the WIND spacecraft and $\approx$ 2×10^{-2} cts keV^{-1} s^{-1} for the TGRS detector at 40 keV. Again taking into account the detector surface area this yields background rates of $\approx$ 0.19×10^{-4} cts keV^{-1} cm^{-2} s^{-1} and $\approx$ 1.25×10^{-4} cts keV^{-1} cm^{-2} s^{-1} respectively.

Keeping in mind the large differences between the two gamma ray missions and the IXO/ATHENA spacecraft (e.g. detector type, energy range, shielding and orbit) it is found that the simulated ATHENA delayed background is in the same order of magnitude as the measured rates of the COMPTEL and WIND spacecraft.

Buildup of individual Components and Spatial Dependency

Figure 80 shows the origins of the activation induced radiation for electrons and gamma rays. The strongest sources are the graded-Z shielding and the cold finger which. This is consistent with the majority of the prompt neutron and positron production also occurring there (Figure 75). The decay radiation resulting from the activated nuclei has maximum energies of a few MeV and thus is even more limited to originating near the edges of the FOV if it is to reach the detector. This fact reflects itself in the figure, which shows that the most of the registered emission is produced at these locations.

Figures 81 and 82 show the activation rates and activities after 10 years mission time for two large detector components, the detector spring plate and the graded-Z shielding. The figures are supplemented by Figure 83 which shows the time-dependent activity build-up of these components. As is apparent from the figures maximum activities of $\approx$ 10 Bq occur after a 10 year mission duration. Taking into account the surface area of the activated components ($\approx$ 700 cm^2 for the tantalum layer) this reduces to a decay rate of $\approx$ 0.015 decays cm^{-2} s^{-1} per unit area, which is two orders of magnitude less than the prompt proton flux of 2.38 protons cm^{-2} s^{-1}. The is in accordance with the two order of magnitude difference

Sqrt(n)

0	65	130	195	260	326	391
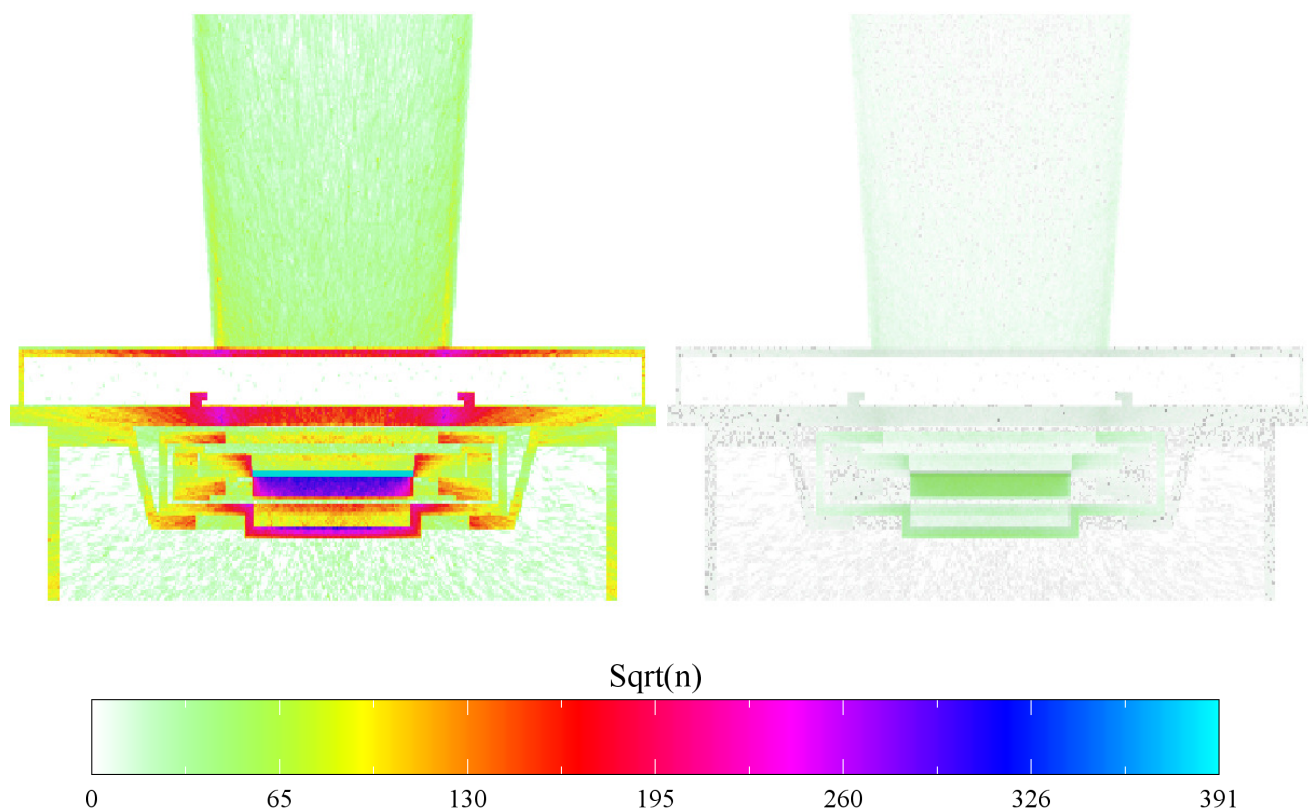
Figure 80: Origins of the delayed, activation induced secondary electron (left) and gamma (right) emission registered in Wide Field Imager for a simulation of 165×10^6 primary protons displayed for a $50\,\text{mm}$ thick slice through the x-z plane of the detector. The detector geometry is underlaid in gray; the resolution of the grid is $1\,\text{mm}$. It is apparent, that secondary electrons which influence the background are mainly produced near the FOV edges, especially the aluminium mounting plate (areas underneath the baffle), the non FOV side of the graded-Z shielding (towards the bottom of the image) and the cold finger (green block at center). The wafer itself can be seen in bright red. Gamma radiation originates mainly as fluorescence emission from the shielding layers but also from the cold finger. Neutron a positron production occurs mainly in the components with higher Z materials such as the outer graded-Z layers and the molybdenum cold finger.

observed for the prompt and delayed background rates, $(6.21\pm0.15)\times10^{-4}\,\text{cts}\,\text{keV}^{-1}\,\text{cm}^{-2}\,\text{s}^{-1}$ compared to $(0.21\pm0.05)\times10^{-4}\,\text{cts}\,\text{keV}^{-1}\,\text{cm}^{-2}\,\text{s}^{-1}$.

The oscillations visible for tantalum in Figure 83 are due to numerical instabilities. These occur if an insufficient number isotopes of a given species is created as a result of the initial activation simulation. The resulting activations per atoms rate is then near the numerical precision limit of the calculation. This manifests itself as the observed oscillatory behavior. It can be avoided by running a longer activation simulation with an accordingly larger statistical sample size. Due to the fact that the isotopes in question have a relatively low activity of $\approx 5 \times 10^{-5}\,\text{decays}\,\text{cm}^{-2}\,\text{s}^{-1}$ and hence will not significantly influence the detector background it was refrained from investing this additional computational time.
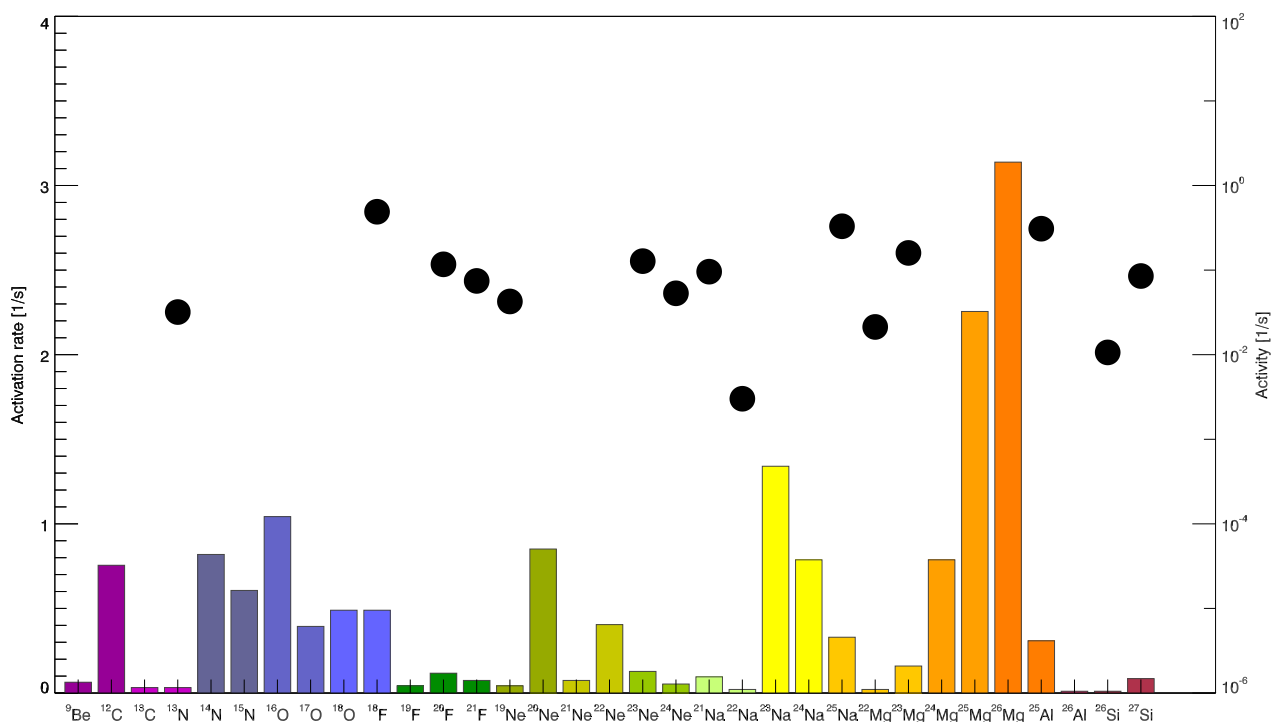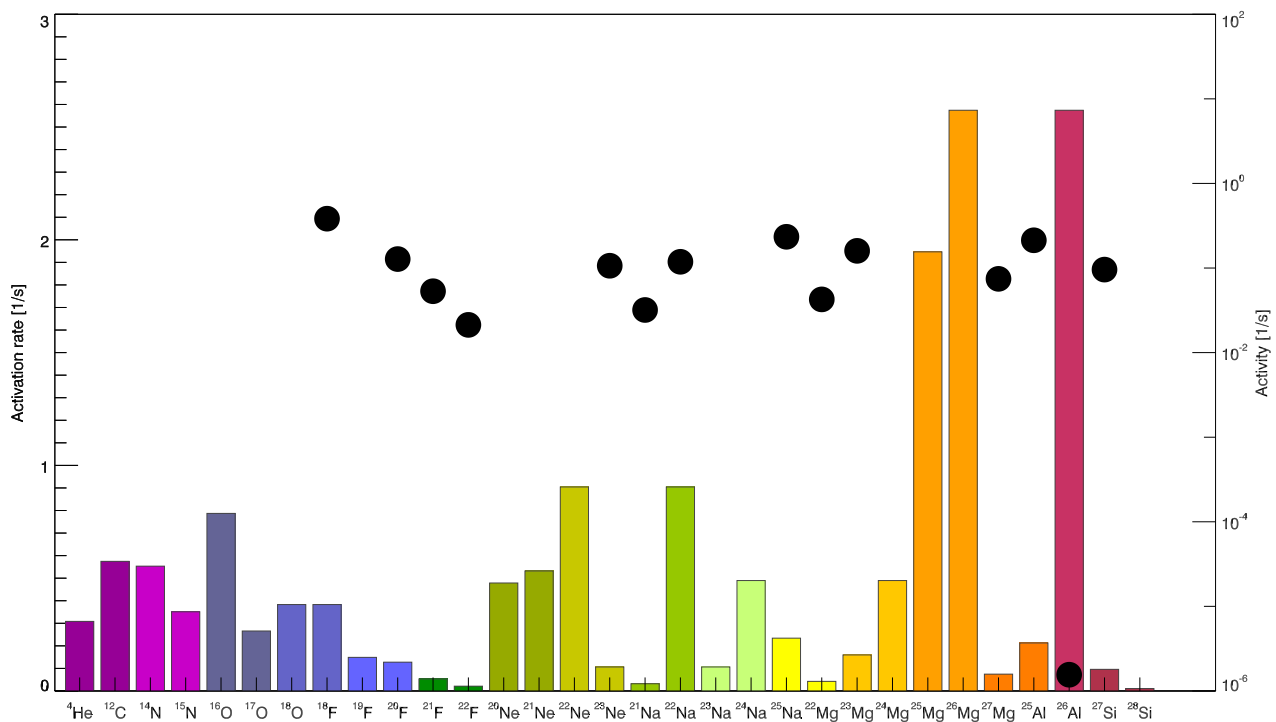
Figure 81: Activation rates (bars, left axis) and activities (filled circles, right axis) after a 10 year mission time for the two largest simulated WFI structures, the base plate and the mounting plate both made from aluminium. The colors of the bars corresponds to the activity build-up plots shown in Figure 83.
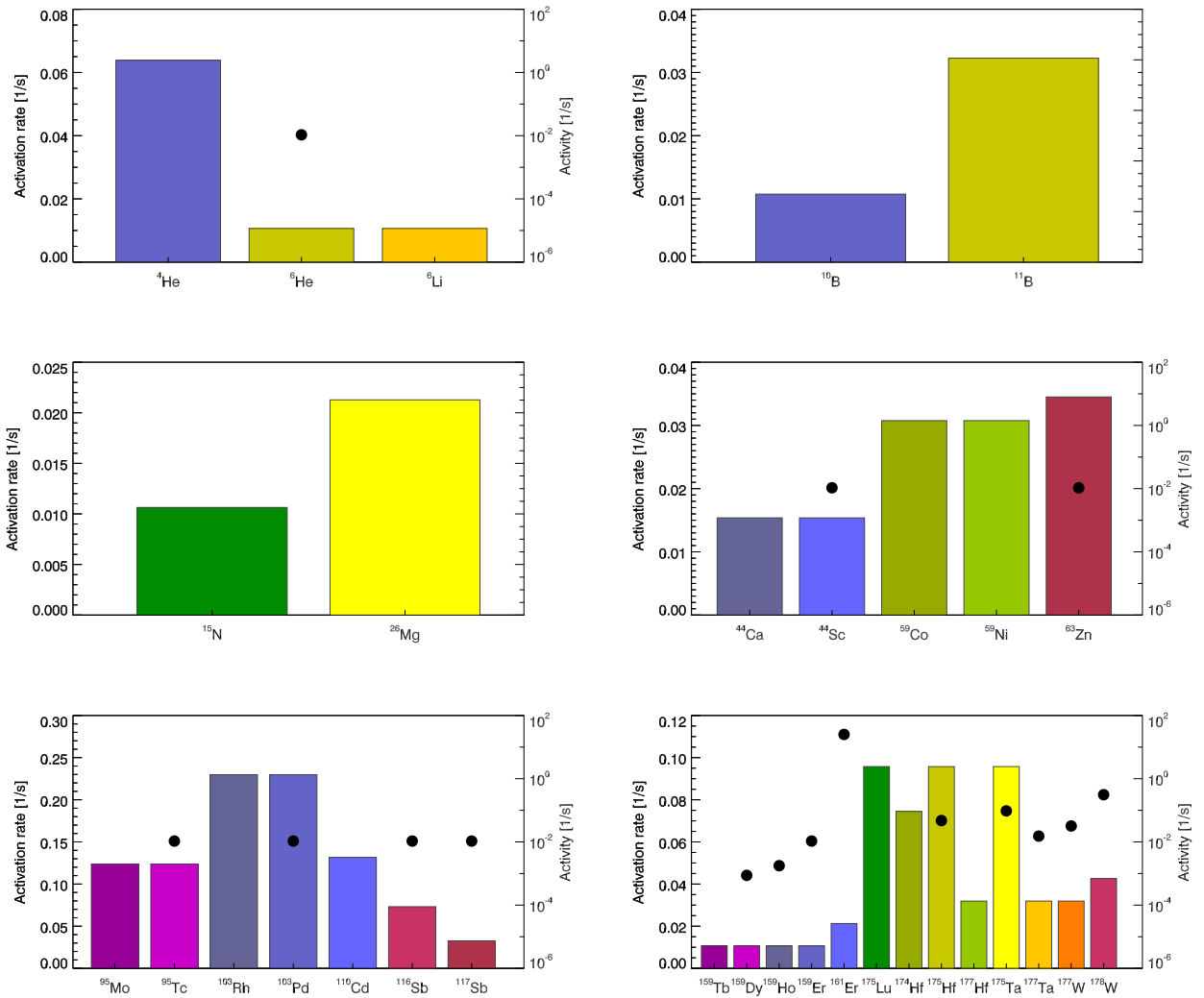
Figure 82: Activation rates (bars, left axis) and activities (filled circles, right axis) after a $10\,\mathrm{year}$ mission time for the graded-Z shielding layers. From top left to bottom right these are made from beryllium, graphite (no activation of instable isotopes), aluminium (no activation of instable isotopes), copper, tin and tantalum. The colors of the bars corresponds to the activity build-up plots shown in Figure 83.
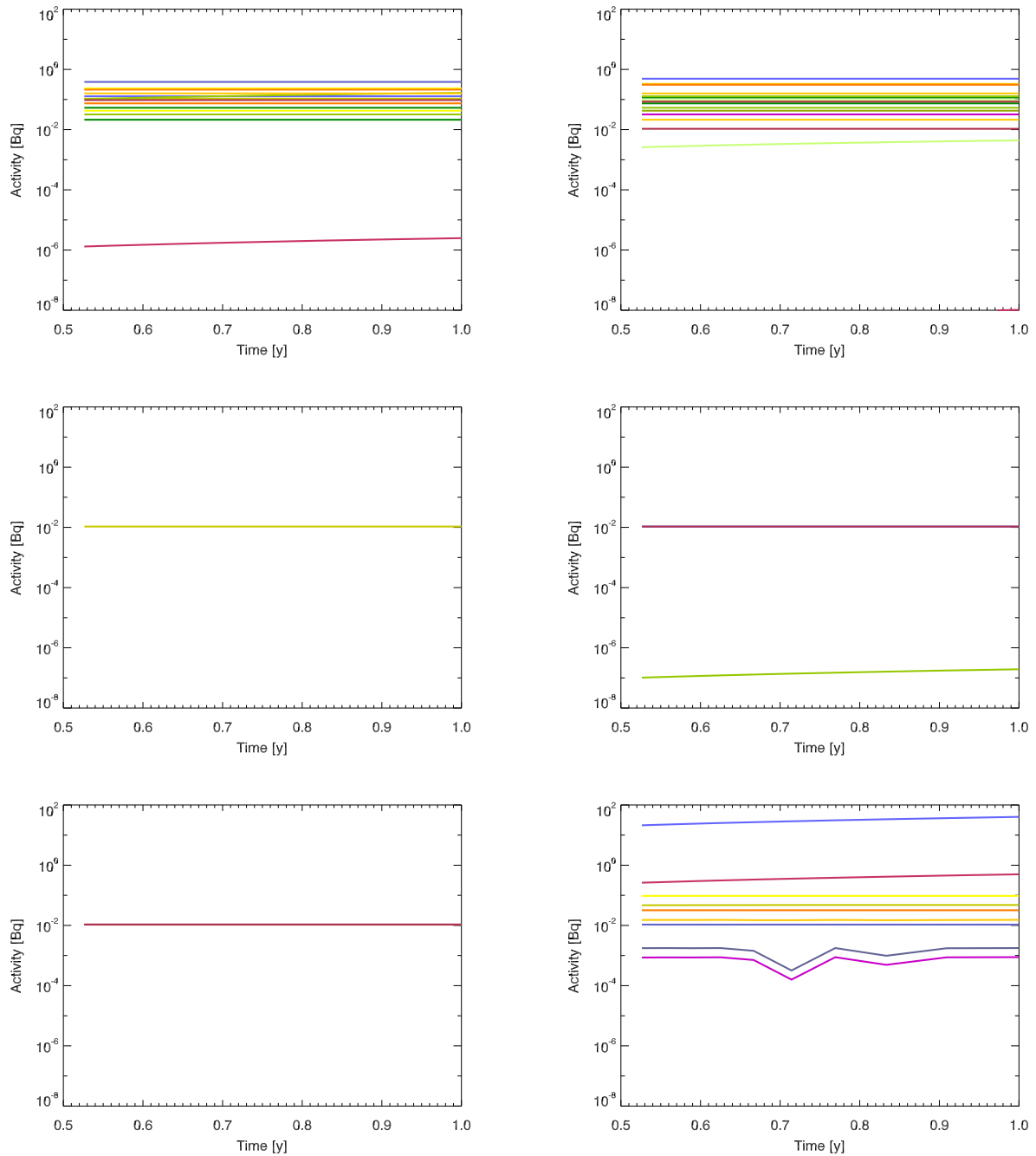
Figure 83: Activity buildup over a mission duration of 10 years of the two largest WFI components, the base plate (top left) and the mounting plate (top right) as well as the graded-Z shielding layers made from beryllium (center left), copper (center right), tin (bottom left) and tantalum (bottom right). The colors of the bars corresponds to the activation rate plots shown in Figures 81 and 82. The oscillations visible in plot for tantalum are due to numerical instabilities (see text).
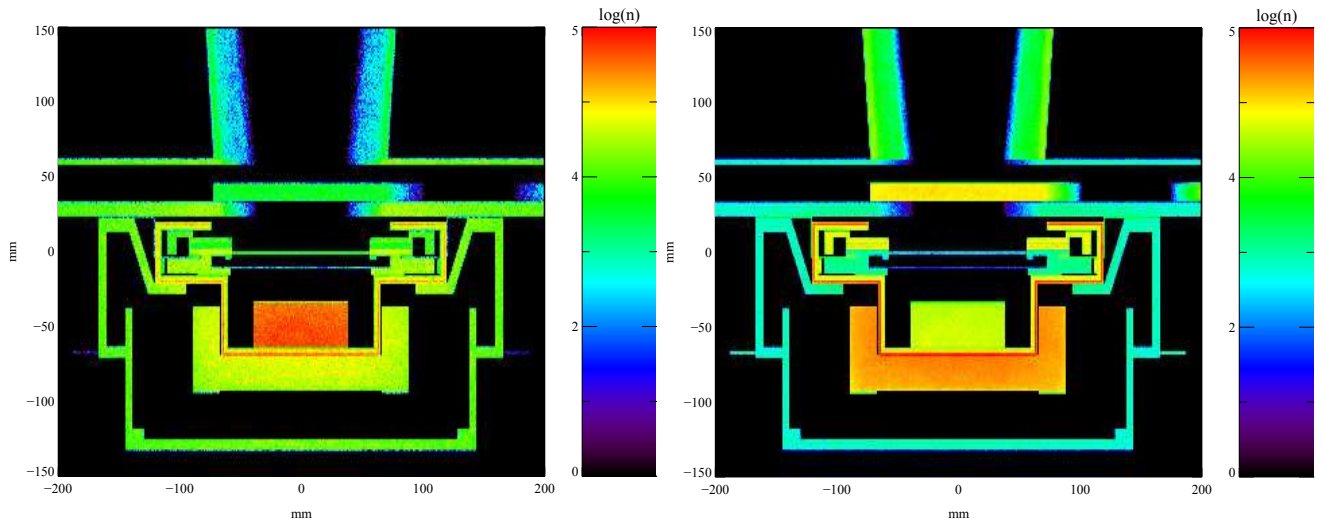
Figure 84: A cut through the IXO simulation geometry showing the production location of secondary electrons resulting from low energy ionization process with energies below $1\,\mathrm{keV}$ and between $1\,\mathrm{keV} - 10\,\mathrm{keV}$. For the plot it was not distinguished between radiation which actually reaches the detector and such which does not. The bright red area at the center of the left panel is the HXI. Also clearly distinguishable is the outer-most graded-Z shielding layer consisting of tantalum.

7.9 Influence of the Cold Finger, HXI and Comparison of ATHENA and IXO

A summary of the simulated background rates including different cold finger designs and a comparison with IXO simulations is shown in Table 17. As is apparent from the table (and somewhat counter-intuitive) the presence of a cold finger directly underneath the sensitive detector area does not necessarily increase the background rates but can even lead to a decrease (e.g. for silicon-carbite and graphite cold fingers when applying a radial exclusion rejection algorithm). This is due to the fact that these low-Z materials have small proton-interaction cross-sections, thus inducing little additional secondary background while at the same time shielding the detector backside from radiation originating from other components. In consequence, they effectively increase the thickness of the second innermost carbon graded-Z shielding layer.

If complete frames with identified invalid patterns are dropped, the differences between different cold finger materials decrease. This leads to the conclusion that mainly radiation resulting in single pattern events is shielded by the carbon-rich cold finger designs. These events would not be detected as background by the pattern recognition algorithms.

In comparison with IXO simulations it was found that the ATHENA simulations, all of which do not include the Hard X-ray Imager (HXI), are consistent with IXO simulations without this detector. The cadmium-zinc-tellurium made HXI can exemplary be seen as a component made of high-Z material. Additionally, it is located within the graded-Z shielding and in proximity to the detector. It increases the background by 48.75%, mainly due to the production of additional secondary electrons as is exemplary shown in Figure 84. High-Z materials within the graded-Z shielding should thus be avoided whenever possible as it is the case for ATHENA.

7.10 Conclusion of Background Results & Comparison to Existing Missions

In the previous sections it was shown that the ATHENA background is fluorescence emission free with a rate between $\approx 6 \times 10^{-4}\,\mathrm{cts\,keV^{-1}\,cm^{-2}\,s^{-1}} - 13 \times 10^{-4}\,\mathrm{cts\,keV^{-1}\,cm^{-2}\,s^{-1}}$, depending on the parameters used in for the background rejection algorithms. Secondary electrons have further been identified as the dominating source and two reduction designs employing electric fields have been studied. These are ca-

Table 17: Comparison of final ATHENA (Geant4.9.4-p1) and IXO (Geant4.9.3) background simulations including different cold finger designs in the energy range of $0.1\,\mathrm{keV} - -15\,\mathrm{keV}$ and $0.25\,\mathrm{keV} - -15\,\mathrm{keV}$. For the total background rate a delayed component of $(0.21 \pm 0.05) \times 10^{-4}\,\mathrm{cts\,keV^{-1}\,cm^{-2}\,s^{-1}}$ needs to be added. All results are after pattern recognition processing with either an exclusion radius of $200\,\mathrm{px}$ (marked A) or complete frame dropping (B). All count rates are given in units of $10^{-4}\,\mathrm{cts\,keV^{-1}\,cm^{-2}\,s^{-1}}$. For IXO not all parameters were studied at the time.

	Baseline		IXO	
	Fast	Slow	HXI	no HXI
Primaries	150×10^6	150×10^6	100×10^6	100×10^6
R/O rate [fps]	1562.5	781.25	400.00	400.00
Raw flux 0.1-15 keV	829.43 ± 1.73	829.43 ± 1.73	872.23 ± 1.88	693.91 ± 1.87
Cor. flux 0.1-15 keV (A)	12.23 ± 0.21	12.22 ± 0.21	18.98 ± 0.3	12.76 ± 0.26
Rejection eff. [%]	97.53 ± 0.12	98.53 ± 0.12	97.82 ± 0.22	98.16 ± 0.13
Dead-time[%]	0.16	0.16	–	–
Rel. change[%]	0.0	-0.08	55.19	4.33
Cor. flux 0.1-15 keV B)	6.21 ± 0.15	6.21 ± 0.15	15.62 ± 0.24	9.39 ± 0.22
Rejection eff. [%]	97.53 ± 0.12	98.53 ± 0.12	97.82 ± 0.22	98.16 ± 0.13
Dead-time[%]	1.30	1.30	–	–
Rel. change[%]	0.0	-0.08	27.71	-23.22
Raw flux 0.25-15 keV	809.24 ± 1.72	809.23 ± 1.72		
Cor. flux 0.25-15 keV	9.77 ± 0.19	9.76 ± 0.19		
Rejection eff. [%]	98.79 ± 0.12	98.80 ± 0.12		
Rel. change[%]	-20.11	-20.20		

	ATHENA w. cold finger			
	molybdenum	SiC	Graphite	copper
Primaries	150×10^6	40×10^6	40×10^6	40×10^6
R/O rate [fps]	1562.5	1562.5	1562.5	1562.5
Raw flux 0.1-15 keV	916.65 ± 1.82	807.78 ± 3.30	784.43 ± 3.76	860.90 ± 3.41
Cor. flux 0.1-15 keV (A)	12.22 ± 0.21	11.32 ± 0.39	11.60 ± 0.46	12.50 ± 0.41
Rejection eff. [%]	98.63 ± 0.12	98.60 ± 0.23	98.52 ± 0.27	98.55 ± 0.23
Dead-time[%]	0.16	0.16	0.16	0.16
Rel. change[%]	0.08	-7.44	-5.15	2.21
Cor. flux 0.1-15 keV (B)	6.21 ± 0.15	6.65 ± 0.30	6.72 ± 0.35	6.62 ± 0.30
Rejection eff. [%]	99.29 ± 0.12	99.12 ± 0.23	99.14 ± 0.27	99.23 ± 0.23
Dead-time[%]	1.30	1.34	1.36	1.30
Rel. change[%]	-49.22	-45.63	-45.05	-45.87
Raw flux 0.25-15 keV	893.69 ± 1.80	787.56 ± 3.28	764.18 ± 3.73	837.88 ± 3.38
Cor. flux 0.25-15 keV	9.02 ± 0.18	8.76 ± 0.35	8.86 ± 0.40	9.29 ± 0.36
Rejection eff. [%]	98.99 ± 0.12	98.89 ± 2.33	98.84 ± 0.27	98.89 ± 2.29
Rel. change[%]	-26.25	-28.37	-27.56	-24.04
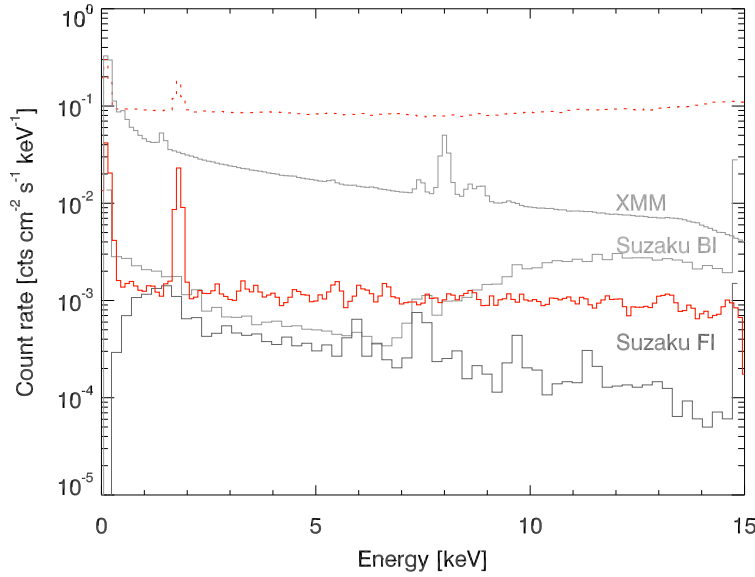
Figure 85: Comparison between the simulated ATHENA energy spectrum before pattern rejection (dashed red line) and thereafter (solid red line). Both simulated spectra have an energy resolution of 125 eV applied. Additionally, measured XMM Newton EPIC, Suzaku front-illuminated and Suzaku back-illuminated spectra are shown.

pable of reducing the overall background to $\approx 1 \times 10^{-4}\,\mathrm{cts\,keV^{-1}\,cm^{-2}\,s^{-1}} - 3 \times 10^{-4}\,\mathrm{cts\,keV^{-1}\,cm^{-2}\,s^{-1}}$, again depending on the background rejection algorithm parameters.

Figure 85 shows a comparison of the ATHENA background with measured XMM Newton and Suzaku background spectra. The estimates show that ATHENA will perform considerably better than XMM and as well as the Suzaku mission. One should note that both the XMM Newton and Suzaku spectra were taken in the intermediate phase of the solar cycle. In contrast, the ATHENA rate was simulated for the solar activity minimum corresponding to a cosmic ray maximum. It can thus be seen as an upper bound for the WFI background.

Additional uncertainties were identified throughout this work, either from literature studies or verification and validation of the simulation. For the simulated hadronic physics they are generally in the order of 30%. The quantum efficiency was validated to be accurate within 10%. Finally the long term activation code was validated with Space Shuttle data and found to be accurate within 20% – 50%. Taking these uncertainties into account and adding the contribution of the long-term activation, $(0.21 \pm 0.05) \times 10^{-4}\,\mathrm{cts\,keV^{-1}\,cm^{-2}\,s^{-1}}$, to the current ATHENA background rate, $(6.21 \pm 0.15) \times 10^{-4}\,\mathrm{cts\,keV^{-1}\,cm^{-2}\,s^{-1}}$ yields an overall upper count rate bound of $(6.42 \pm 2.03) \times 10^{-4}\,\mathrm{cts\,keV^{-1}\,cm^{-2}\,s^{-1}}$ as a final background estimate. This is well within the ATHENA science requirements of $\approx 10^{-3}\,\mathrm{cts\,kev^{-1}\,cm^{-2}\,s^{-1}}$ and can be further reduced to $(2.70 \pm 2.67) \times 10^{-4}\,\mathrm{cts\,keV^{-1}\,cm^{-2}\,s^{-1}}$ if secondary electrons are suppressed via an electric field (Section 7.7).

8 Conclusion and Outlook

In this work it has been shown that the particle induced background goals for the IXO and ATHENA missions of $10^{-4}\,\mathrm{cts\,keV^{-1}\,cm^{-2}\,s^{-1}} - 10^{-3}\,\mathrm{cts\,keV^{-1}\,cm^{-2}\,s^{-1}}$ are feasible. Using Geant4 Monte-Carlos simulations a background flux of $(6.42 \pm 2.03) \times 10^{-4}\,\mathrm{cts\,keV^{-1}\,cm^{-2}\,s^{-1}}$ has been estimated for the ATHENA mission with the possibility of a further reduction to $(2.70 \pm 2.67) \times 10^{-4}\,\mathrm{cts\,keV^{-1}\,cm^{-2}\,s^{-1}}$ in case the novel electric field approach discussed in Chapter 7.7 is employed.

These estimates were produced by using a Geant4 simulation framework which has been validated against XMM Newton measurements (Chapter 3.5) and Space Shuttle activation measurements with the CREAM experiment (Chapter 6.3.2). A separate validation and verification of the Geant4 radioactive decay code has been performed and a new radioactive decay code including a self-consistent long-term activation simulation has been created (Chapters 6 and 5.5). All validations and verifications show maximum deviations below $\approx 50\%$, which is in the same order of magnitude as those found in literature studies (Chapter 3.3). These additional uncertainties have been added to the statistical uncertainty for the above background estimates. In the course of the studies a variety of background reduction possibilities have been studied:

- The introduction of a graded-Z shielding, similar to the one originally studied for the SIMBOL-X mission. This shielding consists of tantalum, tin, copper, aluminum, graphite and beryllium layers (listed from the outside) and effectively suppresses fluorescence emission from surrounding satellite components. Such unwanted emission is for instance visible in the background spectra of XMM Newton (Chapter 3.5). Another effect of the shielding is that it efficiently blocks solar protons with energies below $\approx 5\,\mathrm{MeV}$. This finding was confirmed for energies below $18\,\mathrm{MeV}$ by measurements at the GSI PHELIX laser using TNSA accelerated protons (Chapter 2.2.1 and Neff et al., 2011). In consequence, the solar flux variability at these energies does not have to be taken into account in the IXO/ATHENA background model.

- Different background recognition and rejection schemes were studied (Chapter 7.3). These are based on the fact that particle induced background events which register on a pixel detector often result in pixel patterns distinguishable from X-rays. Using a pattern recognition algorithm such events are identified, leading to background rejection efficiencies of $> 99\%$.

  In addition to rejecting only invalidated patterns the implications of broader rejection schemes were studied. Using the assumption that the interaction of a proton with the detector's components will often result in multiple secondary particles complete frames were rejected in case an invalid pattern had been identified. This approach further reduces the background from $\approx 40 \times 10^{-4}\,\mathrm{cts\,keV^{-1}\,cm^{-2}\,s^{-1}}$ to $\approx 6 \times 10^{-4}\,\mathrm{cts\,keV^{-1}\,cm^{-2}\,s^{-1}}$ but results in a dead-time of $\approx 1.5\%$. In a further step the rejection scheme was changed to excluding radial areas around invalidated patterns. For an exclusion radius of 200 pixels this reduces the dead-time by an order of magnitude to $\approx 0.16\%$ while only doubling the background rate to $\approx 12 \times 10^{-4}\,\mathrm{cts\,keV^{-1}\,cm^{-2}\,s^{-1}}$. As the exclusion radius may be implemented variably, this latter approach is deemed the most flexible and efficient.

- The use of an electric field as a means of background reduction. A detailed characterization of the background constituents has resulted in the observation that secondary electrons originating from the graded-Z shielding are the dominant background component (Chapter 7.6). Using an electric field these electrons are accelerated to energies above the WFI's energy range. This approach reduces the background flux to $(2.70 \pm 2.67) \times 10^{-4}\,\mathrm{cts\,keV^{-1}\,cm^{-2}\,s^{-1}}$.

Each of the studied background reduction schemes can be individually implemented. Nevertheless the observed reductions are a consequence of the interplay of all three schemes: the characteristics of the secondary electrons produced in the graded-Z shielding and affected by the electric field influence the detection efficiency of the pattern recognition algorithms.
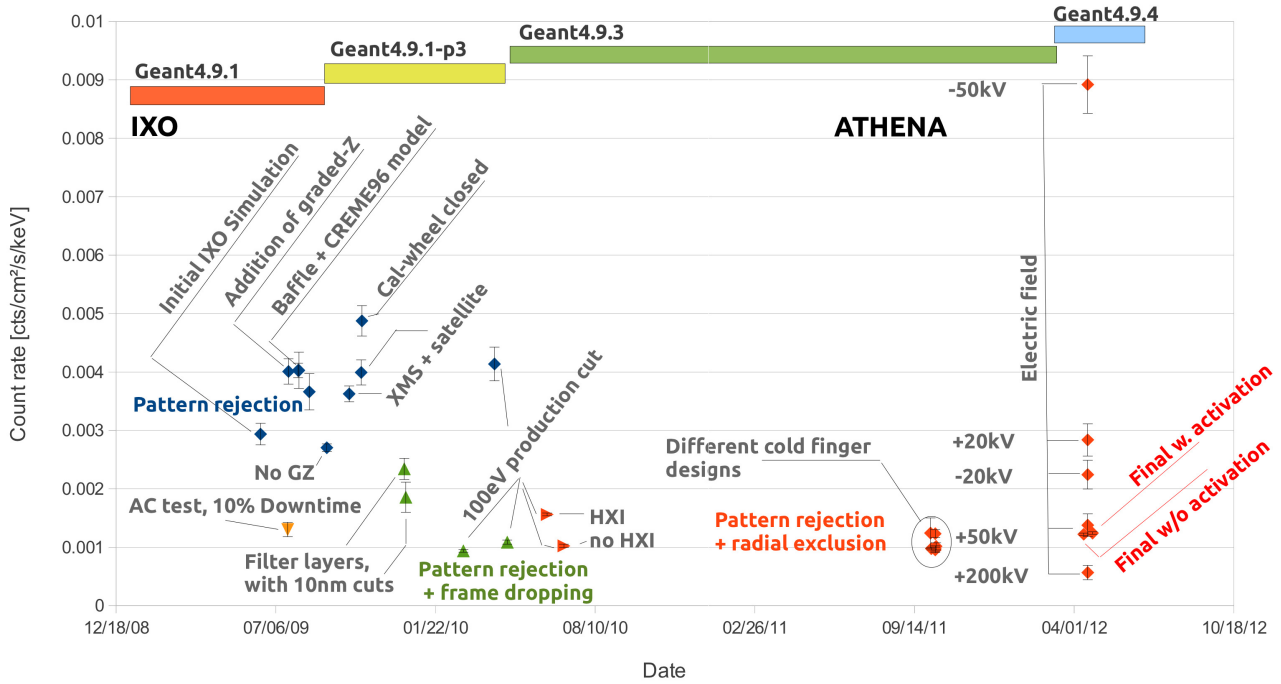
Figure 86: A compilation of background rate from important milestones in the IXO and ATHENA simulations. The color of the data points indicates different background rejection algorithms.

In order to estimate the influence of the delayed background component which results from the cosmogenic activation of detector structures and the subsequent decay of instable isotopes a new radioactive decay code for Geant4 has been developed (Chapter 3.5). This had become necessary due to the fact that the capabilities of the current Geant4 code are inadequate for the IXO/ATHENA application domain. The new code is based upon an evaluation of experimental requirements (Chapter 4.3) which has led to the implementation of a novel statistical sampling approach (Chapter 5.2), thereby reflecting experimental reality, as most experiments are not sensitive to individual decays. An extensive verification with ENSDF data for over 3000 isotopes has shown that in comparison to the current Geant4 code the new code is up to 50% more accurate at X-ray energies and still 20% more accurate at higher energies. These results have been confirmed by validation measurements with a HPGe detector. At the same time the new code offers significant performance gains of up to 50% for single decays and up to 800% for decay chains (Chapter 5.6).

The new code includes a self-consistent longterm activation simulation, which makes manual user input of activation rates unnecessary. The models used therein have been validated with a complete simulation of the CREAM experiment aboard the STS-53 Space Shuttle mission, which studied the on-orbit activation of a NaI cube (Chapter 6.3.2). By applying this code to the IXO/ATHENA background simulation an estimate for the delayed background of $(0.21 \pm 0.05) \times 10^{-4}\,\mathrm{cts\,keV^{-1}\,cm^{-2}\,s^{-1}}$ after a 10 year mission time has been obtained. In summary the delayed and prompt background, $(6.21 \pm 0.15) \times 10^{-4}\,\mathrm{cts\,keV^{-1}\,cm^{-2}\,s^{-1}}$ yield the aforementioned total background rate of $(6.42 \pm 2.03) \times 10^{-4}\,\mathrm{cts\,keV^{-1}\,cm^{-2}\,s^{-1}}$.

It is important to note that the presented background estimates are the outcome of a continuous progression of the simulation environment and detector design over a time span of three years. During this time a close collaboration with the detector development team at Max-Planck-Institut für extraterrestrische Physik and at Max-Planck-Halbleiterlabor has ensured that the background optimization results are technically feasible. The most important milestones of this development are summarized in Figure 86. It is apparent from the figure that the results follow a consistent explicable trend. Together

with the validations and verifications presented in the previous chapters the gives confidence in the simulations and the resulting estimates and observations.

8.1 Outlook

At the conclusion of this writing the ATHENA mission had just been canceled by ESA in favor of a solar system mission to Jupiter's moons (ESA, 2012). While this is regretful in terms of the science opportunities both IXO and ATHENA would have supplied, it does not relativize the results of this work in any way. JUICE's instruments will operate in the harsh Jovian radiation environment and as a consequence a correct estimate of the detector background and long term activation similar to the one presented will be needed.

JUICE is just one example where the results produced as part of this work and the newly developed code can be applied. Other application domains range from material sciences, medial physics, reactor facilities and particle accelerators to intense light sources and homeland security. In general any experiment influenced by radioactive decays which is to be modeled in Geant4 will benefit from the extensive verification and validation studies and novel sampling approaches presented.

More specifically the studied background reduction schemes are applicable for a wide range of silicon pixel detectors, space-borne and ground-based alike. As experiments become more and more sensitive, the need for efficient background reduction will increase. Within this context the sound design of the newly developed code, based on a proper problem domain analysis, is a valuable asset. It facilitates extensions which might become necessary as part of future developments and novel application requirements.

List of Figures

List of Tables

References

Aalseth, C. E. et al. (2002). "The CERN Axion Solar Telescope (CAST)". In: *Nuclear Physics B Proceedings Supplements*. Vol. 110, pp. 85–87.

Achterberg, A. et al. (2006). "First year performance of the IceCube neutrino telescope". In: *Astroparticle Physics* 26.3, pp. 155 –173.

Acquafredda, R. et al. (2009). "The OPERA experiment in the CERN to Gran Sasso neutrino beam". In: *Journal of Instrumentation* 4, p. 4018.

Agostinelli, S. et al. (2003). "Geant4 – a simulation toolkit". In: *Nuclear Instruments and Methods in Physics Research Section A: Accelerators, Spectrometers, Detectors and Associated Equipment* 506.3, pp. 250 –303.

Allen, J. S. (Feb. 1939). "The Emission of Secondary Electrons from Metals Bombarded with Protons". In: *Phys. Rev.* 55, pp. 336–339.

Allison, J. et al. (2006). "Geant4 developments and applications". In: *IEEE Transactions on Nuclear Science* 53, pp. 270–278.

Amaku, M., P. R. Pascholati, and V. R. Vanin (2010). "Decay chain differential equations: Solution through matrix algebra". In: *Computer Physics Communications* 181, pp. 21–23.

Anderson, T. W. and D. A. Darling (1954). "A Test of Goodness of Fit". In: *Journal of the American Statistical Association* 49.268, pp. 765–769.

Apostolakis, J. et al. (2009). *Geant4 simulation of nuclear spallation reactions*.

Apostolakis, J. et al. (2009). "Progress in hadronic physics modelling in Geant4". In: *J. Phys.: Conf. Ser.* 160.1, p. 012073.

Aschenbach, B. (2009). "Realization of X-ray telescopes-from design to performance". In: *Experimental Astronomy* 26, pp. 95–109.

Aschenbach, B. et al. (2000). "Imaging performance of the XMM-Newton x-ray telescopes". In: *Society of Photo-Optical Instrumentation Engineers (SPIE) Conference Series*. Ed. by J. E. T. . B. Aschenbach. Vol. 4012. Society of Photo-Optical Instrumentation Engineers (SPIE) Conference Series, pp. 731–739.

Astbury, A. and D. Axen (2006). *Comparison of GEANT4 Simulation of Atmospheric Cosmic Rays with Measured Terrestrial Muon and Neutron Spectra*. Tech. rep.

Augelli, M. et al. (Dec. 2009). "Inter-Comparison and Validation of Geant4 Photon Interaction Models". In: *ArXiv e-prints*. arXiv:`0912.1724` [`physics.comp-ph`].

Bambynek, W. et al. (1972). "X-Ray Fluorescence Yields, Auger, and Coster-Kronig Transition Probabilities". In: *Reviews of Modern Physics* 44, pp. 716–813.

Band, I., M. Trzhaskovskaya, and M. Listengarten (1976). "Internal conversion coefficients for atomic numbers $Z \leq 30$". In: *Atomic Data and Nuclear Data Tables* 18.5, pp. 433 –457.

Barcons, X. et al. (2011). "International X-ray Observatory (IXO) Assessment Study Report for the ESA Cosmic Vision 2015-2025". In: *ArXiv e-prints*.

Barret, D. et al. (Feb. 2011). *IXO - Revealing the physics of the hot Universe*.

Barret, D. et al. (2010). "The High Time Resolution Spectrometer (HTRS) aboard the International X-ray Observatory (IXO)". In: ed. by M. Arnaud, S. S. Murray, and T. Takahashi. Vol. 7732. 1. San Diego, California, USA: SPIE, p. 77321M.

Bateman, H. (1910). "The solution of a system of differential equations occurring in the theory of radioactive transformations". In: *Proc. Cambridge Philos. Soc* 15, p. 423.

Bavdaz, M. et al. (July 2006). "The XEUS x-ray telescope". In: *Society of Photo-Optical Instrumentation Engineers (SPIE) Conference Series*. Vol. 6266. Society of Photo-Optical Instrumentation Engineers (SPIE) Conference Series.

Bavdaz, M. et al. (2011). "ESA-led ATHENA/IXO optics development status". In: *SPIE Proc.* 8147.1, p. 81470C.

Bearden, J. A. and A. F. Burr (Jan. 1967). "Reevaluation of X-Ray Atomic Energy Levels". In: *Rev. Mod. Phys.* 39, pp. 125–142.

Bellazzini, R. et al. (2010). "A polarimeter for IXO". In: *X-ray Polarimetry: A New Window in Astrophysics by Ronaldo Bellazzini, Enrico Costa, Giorgio Matt and Gianpiero Tagliaferri. Cambridge University Press, 2010. ISBN: 9780521191845, p. 269*, p. 269.

Bequerel, H. (1896). "Sur les Radiations Invisible Emises par les Corps Phosphorescence". In: *Comptes Rendus*.

Bethe, H. A. and R. F. Bacher (Apr. 1936). "Nuclear Physics A. Stationary States of Nuclei". In: *Reviews of Modern Physics* 8, pp. 82–229.

Bhat, M. R. (1991). "Evaluated Nuclear Structure Data File (ENSDF)". In: International conference on nuclear data for science and technology.

Bissaldi, E. et al. (2009). "Ground-based calibration and characterization of the Fermi gamma-ray burst monitor detectors". In: *Experimental Astronomy* 24. 10.1007/s10686-008-9135-4, pp. 47–88.

Boella, G. et al. (Apr. 1997). "BeppoSAX, the wide band mission for X-ray astronomy". In: *AAPS jounal* 122, pp. 299–307.

Bombelli, L. et al. (Oct. 2008). "Fast DEPFET read-out for the SIMBOL-X low energy detector". In: *Nuclear Science Symposium Conference Record, 2008. NSS '08. IEEE*, pp. 1772 –1777.

Borovsky, J. E., D. J. McComas, and B. L. Barraclough (1988). "The secondary-electron yield measured for 5–24 MeV protons on aluminum-oxide and gold targets". In: *Nuclear Instruments and Methods in Physics Research Section B: Beam Interactions with Materials and Atoms* 30.2, pp. 191 –195.

Boyko, I. (Oct. 2008). *Comparison of Geant4 hadron generators with data: a critical appraisal*. Tech. rep. arXiv:0810.1396. Comments: Proceedings of the 34th International Conference on High Energy Physics.

Bradt, H. V. D. and J. E. McClintock (1983). "The optical counterparts of compact galactic X-ray sources". In: *Annual review of astronomy and astrophysics* 21, pp. 13–66.

Briesmeister, J. F. (1986). *MCNP : a general Monte Carlo code for neutron and photon transport*. 3. Los Alamos National Laboratory. Los Alamos.

Broad, W. J. (1984). "Golden Age of Astronomy Peers To Edge of Universe". In: *New York Times*.

Burrows, T. W. (1988). *The Program RADLST*. Tech. rep. BNL-NSC-52142. Brookhaven National Laboratory.

Cameron, R. A. et al. (1992). "Operation and performance of the OSSE instrument". In: *NASA Conference Publication*. Ed. by . B. D. C. R. Shrader N. Gehrels. Vol. 3137. NASA Conference Publication, pp. 3–14.

Capogni, M., S. L. Meo, and A. Fazio (2010). "Simulation of radioactive decay in GEANT Monte Carlo codes: Comparison between spectra and efficiencies computed with sch2for and G4RadioactiveDecay". In: *Applied Radiation and Isotopes* 68.7-8. Proceedings of the 17th International Conference on Radionuclide Metrology and its Applications (ICRM 2009), pp. 1428 –1432.

Chen, Y., T. P. Li, and M. Wu (1997). "Imaging by an Optimizing Method". In: *Astronomical Data Analysis Software and Systems VI*. Ed. by G. H. . H. Payne. Vol. 125. Astronomical Society of the Pacific Conference Series, p. 178.

Arnaud, M., S. S. Murray, and T. Takahashi, eds. (2010). *Silicon pore x-ray optics for IXO*. Vol. 7732. 1. San Diego, California, USA: SPIE, 77321F.

Cooke, B. A. et al. (1978). "The Ariel V /SSI/ catalogue of high galactic latitude /absolute value of B greater than 10 deg/ X-ray sources". In: *Monthly Notices of the Royal Astronomical Society* 182, pp. 489–515.

Croff, A. G. (1983). "ORIGEN2: A versatile computer code for calculating the nuclide compositions and characteristics of nuclear materials". In: *Nucl. Technol.* 62.3.

Dehaes, J. C. and A. Dubus (1993). "Proportionality between the secondary electron yield and the electronic stopping power for proton impact on aluminium". In: *Nuclear Instruments and Methods in Physics Research Section B: Beam Interactions with Materials and Atoms* 78.1–4, pp. 255 –259.

Dotti, A., A. Lupi, and C. Roda (2006). "Results from ATLAS Tile Calorimeter: a comparison between data and Geant4 simulation". In: *Nucl. Phys. B, Proc. Suppl.* 150, pp. 106–109.

Dyer, C. S. et al. (June 1994). "Calculations and observations of induced radioactivity in spaceborne materials". In: *IEEE Transactions on Nuclear Science* 41, pp. 438–444.

Dyer, C. et al. (Dec. 1992). "Radiation environment measurements on Shuttle missions using the CREAM experiment". In: *Nuclear Science, IEEE Transactions on* 39.6, pp. 1809 –1816.

Dyer, C. et al. (1996). "Secondary radiation environments in heavy space vehicles and instruments". In: *Advances in Space Research* 17.2. Proceedings of the Meetings F2.6 and F2.7 of COSPAR Scientific Commission F which was held during the Thirtieth COSPAR Scientific Assembly, pp. 53 –58.

ESA (May 2012). *JUICE is Europe's next large science mission*.

ESA (2012). *The XMM User's Handbook*.

Elvis, M. et al. (1978). "Seyfert galaxies as X-ray sources". In: *Monthly Notices of the Royal Astronomical Society* 183, pp. 129–157.

Fassò, A., A. Ferrari, P. R. Sala, and J. Ranft (2001). "FLUKA: Status and Prospects for Hadronic Applications". In: *Advanced Monte Carlo for Radiation Physics, Particle Transport Simulation and Applications*. Ed. by F. B. A. Kling, p. 955.

Feldman, U., G. A. Doschek, W. E. Behring, and K. J. H. Phillips (Apr. 1996). "Electron Temperature, Emission Measure, and X-Ray Flux in A2 to X2 X-Ray Class Solar Flares". In: *The Astrophysical Journal* 460, p. 1034.

Ferguson, C (Feb. 2000). *General purpose Source Particle Module for Geant4/SPARSET*. Technical Note, UoS-GSPM-Tech, Issue 1.1.

Fermi, E. (1934). "Versuch einer Theorie der Beta-Strahlen. I". In: *Zeitschrift für Physik A Hadrons and Nuclei* 88 (3). 10.1007/BF01351864, pp. 161–177.

Ferrando, P. et al. (Feb. 2004). "SIMBOL-X: a new-generation hard x-ray telescope". In: *Society of Photo-Optical Instrumentation Engineers (SPIE) Conference Series*. Ed. by O. Citterio and S. L. O'Dell. Vol. 5168. Society of Photo-Optical Instrumentation Engineers (SPIE) Conference Series, pp. 65–76. eprint: `arXiv:astro-ph/0309424`.

Feynman, R. P. (Sept. 1965). "The Feynman Lectures on Physics; Vol. I". In: *American Journal of Physics* 33, pp. 750–752.

Folger, G., V. N. Ivanchenko, and J. P. Wellisch (Sept. 2004). "The Binary Cascade". In: *European Physical Journal A* 21, pp. 407–417.

Folger, G. and J. P. Wellisch (June 2003). "String Parton Models in Geant4". In: *ArXiv Nuclear Theory e-prints*. eprint: `arXiv:nucl-th/0306007`.

Forman, W. et al. (1978). "The fourth Uhuru catalog of X-ray sources." In: *The Astrophysical Journals* 38, pp. 357–412.

Forman, W. et al. (1979). "X-ray observations of galaxies in the Virgo cluster". In: *The Astrophysical Journall* 234, pp. L27–L31.

Freyberg, M. J. et al. (Feb. 2004). "EPIC pn-CCD detector aboard XMM-Newton: status of the background calibration". In: *Society of Photo-Optical Instrumentation Engineers (SPIE) Conference Series*. Ed. by K. A. Flanagan and O. H. W. Siegmund. Vol. 5165. Society of Photo-Optical Instrumentation Engineers (SPIE) Conference Series, pp. 112–122.

Friedrich, P. et al. (2012). *ATHENA Optics -Based on Silicon Pore Optics (SPO)*. First German ATHENA Science Workshop, January 13, 2012, Garching, Germany.

Fukuda, S. et al. (2003). "The Super-Kamiokande detector". In: *Nuclear Instruments and Methods in Physics Research Section A: Accelerators, Spectrometers, Detectors and Associated Equipment* 501.2–3, pp. 418 –462.

Gaisser, T. K. (1991). *Cosmic Rays and Particle Physics*. Ed. by T. K. Gaisser.

Garmire, G. P. et al. (2003). "Advanced CCD imaging spectrometer (ACIS) instrument on the Chandra X-ray Observatory". In: *Society of Photo-Optical Instrumentation Engineers (SPIE) Conference Series*. Ed. by J. E. T. . H. D. Tananbaum. Vol. 4851. Society of Photo-Optical Instrumentation Engineers (SPIE) Conference Series, pp. 28–44.

Geant4 collaboration (2012). *Geant4 User Documentation*.

Gharbi, F. (2011). "Inhomogeneity effects on HPGe gamma spectrometry detection efficiency using Monte Carlo technique". In: *Nuclear Instruments and Methods in Physics Research Section A: Accelerators, Spectrometers, Detectors and Associated Equipment* 654.1, pp. 266 –271.

Ghigo, M. et al. (2010). "Hot slumping glass technology for the grazing incidence optics of future missions with particular reference to IXO". In: *Space Telescopes and Instrumentation 2010: Ultraviolet to Gamma Ray* 7732.1. Ed. by M. Arnaud, S. S. Murray, and T. Takahashi, p. 77320C.

Giacconi, R. et al. (1971a). "Discovery of Periodic X-Ray Pulsations in Centaurus X-3 from UHURU". In: *The Astrophysical Journall* 167, p. L67.

Giacconi, R. et al. (1971b). "Uhuru Mission Overview". In: *APJ* 165, 27b.

Giacconi, R. et al. (1979). "The Einstein /HEAO 2/ X-ray Observatory". In: *The Astrophysical Journal* 230, pp. 540–550.

Giacconi, R., H. Gursky, F. R. Paolini, and B. B. Rossi (Dec. 1962). "Evidence for x Rays From Sources Outside the Solar System". In: *Phys. Rev. Lett.* 9, pp. 439–443.

Giacri-Mauborgne, M.-L. et al. (2005). "Status of the Photonuclear Data Library for CINDER'90". In: *International Conference on Nuclear Data for Science and Technology*. Vol. 769. American Institute of Physics Conference Series, pp. 195–198.

Golovko, V., V. Iacob, and J. Hardy (2008). "The use of Geant4 for simulations of a plastic -detector and its application to efficiency calibration". In: *Nuclear Instruments and Methods in Physics Research Section A: Accelerators, Spectrometers, Detectors and Associated Equipment* 594.2, pp. 266 –272.

Gondoin, P. et al. (1998). "Calibration of the first XXM flight mirror module: II. Effective area". In: *Society of Photo-Optical Instrumentation Engineers (SPIE) Conference Series*. Ed. by R. B. H. . A. B. Walker. Vol. 3444. Society of Photo-Optical Instrumentation Engineers (SPIE) Conference Series, pp. 290–301.

Gruber, D. E., J. L. Matteson, L. E. Peterson, and G. V. Jung (1999). "The Spectrum of Diffuse Cosmic Hard X-Rays Measured with HEAO 1". In: *The Astrophysical Journal* 520.1, p. 124.

Guatelli, S. et al. (June 2007). "Validation of Geant4 Atomic Relaxation Against the NIST Physical Reference Data". In: *IEEE Transactions on Nuclear Science* 54, pp. 594–603.

Guatelli, S. et al. (June 2007). "Validation of Geant4 Atomic Relaxation Against the NIST Physical Reference Data". In: *Nuclear Science, IEEE Transactions on* 54.3, pp. 594 –603.

Hager, R. and E. Seltzer (1968). "Internal conversion tables part I: K-, L-, M-shell conversion coefficients for Z=30 to Z=103". In: *Nuclear Data Sheets. Section A* 4.1-2, pp. 1 –11.

Hall, H. (Aug. 1950). "On the Evaluation of the Fermi β-Distribution Function". In: *Physical Review* 79, pp. 745–745.

Hansen, H. H. and A. Spernol (Apr. 1968). "Some investigations on the decay of ^{60}Co". In: *Zeitschrift fur Physik* 209, pp. 111–118.

Harnden Jr., F. R. and F. D. Seward (1984). "Einstein observations of the Crab nebula pulsar". In: *The Astrophysical Journal* 283, pp. 279–285.

Hauf, S. (May 2009a). *Simulating and Optimizing the Simbol-X Detector Background*. 6. Geant 4 Space Users Workshop, Madrid, Spanien.

Hauf, S. (Mar. 2009b). "Simulation on the SIMBOL-X Detector Background". MA thesis. TU Darmstadt.

Heinrich, W. (1994). "Cosmic rays and their interactions with the geomagnetic field and shielding material". In: *Radiation Physics and Chemistry* 43.1–2, pp. 19 –34.

Heinrich, W. and A. Spill (Aug. 1979). "Geomagnetic shielding of cosmic rays for different satellite orbits". In: *Journal of Geophysical Research* 84, pp. 4401–4404.

Heirtzler, J. (2002). "The future of the South Atlantic anomaly and implications for radiation damage in space". In: *Journal of Atmospheric and Solar-Terrestrial Physics* 64.16. Space Weather Effects on Technological Systems, pp. 1701 –1708.

Hendricks, J. S. (2003). "MCNPX version 2.5.c". In: American Nuclear Society.

Herder, J. W. den et al. (2010). "The x-ray microcalorimeter spectrometer onboard of IXO". In: *Space Telescopes and Instrumentation 2010: Ultraviolet to Gamma Ray* 7732.1, 77321H. Ed. by M. Arnaud, S. S. Murray, and T. Takahashi, 77321H.

Hickox, R. C. and M. Markevitch (2006). "Absolute Measurement of the Unresolved Cosmic X-Ray Background in the 0.5-8 keV Band with Chandra". In: *The Astrophysical Journal* 645.1, p. 95.

Hsue, S., L. Langer, and S. Tang (1966). "Precise determination of the shape of the twice forbidden beta spectrum of 137Cs". In: *Nuclear Physics* 86.1, pp. 47 –55.

Hurtado, S., R. Garcia-Tenorio, and M. Garcia-Leon (June 2009). "Coincidence Summing Corrections in Gamma-Ray Spectrometry Using GEANT4 Code". In: *Nuclear Science, IEEE Transactions on* 56.3, pp. 1531 –1536.

Hurtado, S., M. García-León, and R. García-Tenorio (2004). "GEANT4 code for simulation of a germanium gamma-ray detector and its application to efficiency calibration". In: *Nuclear Instruments and Methods in Physics Research A* 518, pp. 764–774.

IEEE (2005). "IEEE Standard for Software Verification and Validation". In: *IEEE Std 1012-2004 (Revision of IEEE Std 1012-1998)*, pp. 1 –110.

Jansen, F. et al. (2001). "XMM-Newton observatory. I. The spacecraft and operations". In: *Astronomy and Astrophysics* 365, pp. L1–L6.

Kelley, R. L. et al. (2009). "The X-Ray Microcalorimeter Spectrometer for the International X-Ray Observatory". In: *AIP Conference Proceedings* 1185.1. Ed. by B. Young, B. Cabrera, and A. Miller, pp. 757–760.

Kirsch, M. G. F. et al. (Feb. 2004). "Timing accuracy and capabilities of XMM-Newton". In: *Society of Photo-Optical Instrumentation Engineers (SPIE) Conference Series*. Ed. by K. A. Flanagan and O. H. W. Siegmund. Vol. 5165. Society of Photo-Optical Instrumentation Engineers (SPIE) Conference Series, pp. 85–95.

Klose, C. (May 2007). "Simulation zum Detektorhintergrund des Röntgensatelliten SIMBOL-X". Diplomarbeit. MA thesis. TU Darmstadt.

Koyama, K. (1988). "X-ray observations with the GINGA satellite". In: *Comments on Astrophysics* 12, pp. 287–302.

Laborie, J.-M., G. Le Petit, D. Abt, and M. Girard (2002). "Monte Carlo calculation of the efficiency response of a low-background well-type HPGe detector". In: *Nuclear Instruments and Methods in Physics Research Section A: Accelerators, Spectrometers, Detectors and Associated Equipment* 479.2–3, pp. 618 –630.

Lechner, A., A. Mantero, M. G. Pia, and M. Sudhakar (Oct. 2008). "Validation of Geant4 X-ray fluorescence transitions - validation of Geant4 electromagnetic models against calorimetry measurements in the energy range up to 1 MeV". In: *Nuclear Science Symposium Conference Record, 2008. NSS '08. IEEE*, pp. 2869 –2876.

Lechner, P. et al. (2003). "X-ray imaging spectrometers in present and future satellite missions". In: *Nuclear Instruments and Methods in Physics Research A* 509, pp. 302–314.

Lei, F. et al. (Dec. 2002). "MULASSIS: a geant4-based multilayered shielding simulation tool". In: *IEEE Transactions on Nuclear Science* 49, pp. 2788–2793.

Lei, F., S. Rason, K. Ford, and P. Morris (Sept. 2009). "Validation of Geant4-based dose computational tools with REEF experiments". In: *Radiation and Its Effects on Components and Systems (RADECS), 2009 European Conference on*, pp. 440 –445.

Lin, R. P. (1985). "Energetic solar electrons in the interplanetary medium". In: *Solar Physics* 100. 10.1007/BF00158444, pp. 537–561.

Lisse, C. M. et al. (1996). "Discovery of X-ray and Extreme Ultraviolet Emission from Comet C/Hyakutake 1996 B2". In: *Science* 274.5285, pp. 205–209.

Luo, B. et al. (2008). "The Chandra Deep Field-South Survey: 2 Ms Source Catalogs". In: *The Astrophysical Journal Supplement Series* 179.1, p. 19.

Maccacaro, T. et al. (1988). "The X-ray spectra of the extragalactic sources in the Einstein extended medium sensitivity survey". In: *The Astrophysical Journal* 326, pp. 680–690.

Marshall, F. E. et al. (1980). "The diffuse X-ray background spectrum from 3 to 50 keV". In: *The Astrophysical Journal* 235, pp. 4–10.

Marshall, F. J. and G. W. Clark (1984). "SAS 3 survey of the soft X-ray background". In: *The Astrophysical Journal* 287, pp. 633–652.

Martin-Carrillo, A. et al. (2012). "The relative and absolute timing accuracy of the EPIC-pn camera on XMM-Newton, from X-ray pulsations of the Crab and other pulsars". In: *ArXiv e-prints*.

Massey, F. J. (1951). "The Kolmogorov-Smirnov Test for Goodness of Fit". In: *Journal of the American Statistical Association* 46.253, pp. 68–78.

Massey, H. S. W. and C. B. O. Mohr (Aug. 1933). "Free Paths and Transport Phenomena in Gases and the Quantum Theory of Collisions. I. The Rigid Sphere Model". In: *Royal Society of London Proceedings Series A* 141, pp. 434–453.

McEntaffer, R. L. et al. (2009). "Off-plane x-ray grating spectrometer for the International X-ray Observatory". In: *Society of Photo-Optical Instrumentation Engineers (SPIE) Conference Series*. Vol. 7360. Society of Photo-Optical Instrumentation Engineers (SPIE) Conference Series.

McNamara, A., H. Heijnis, D. Fierro, and M. Reinhard (2012). "The determination of the efficiency of a Compton suppressed HPGe detector using Monte Carlo simulations". In: *Journal of Environmental Radioactivity* 106.0, pp. 1–7.

Mitchell, R. J. and J. L. Culhane (1977). "Detection of iron line emission in the Ariel V X-ray spectrum of the Centaurus cluster of galaxies". In: *Monthly Notices of the Royal Astronomical Society* 178, 75P–80P.

Mitsuda, K. et al. (2007). "The X-Ray Observatory Suzaku". In: *Publications of the Astronomical Society of Japan* 59, pp. 1–7.

Moral, L. and A. F. Pacheco (2003). "Algebraic approach to the radioactive decay equations". In: *American Journal of Physics* 71, pp. 684–686.

Moses, D., W. Droege, P. Meyer, and P. Evenson (Nov. 1989). "Characteristics of energetic solar flare electron spectra". In: *The Astrophysical Journal* 346, pp. 523–530.

Mysid (Apr. 2012). *Electromagnetic transmittance, or opacity, of the Earth's atmosphere.*

NASA (May 2012). *Mission Archives – STS–53*. http://www.nasa.gov/mission_pages/shuttle/shuttlemissions/arch 53.html.

NASA (2012a). *Satellite Showcase: Uhuru.*

NASA (2012b). *The Chandra Proposers' Observatory Guide.*

NASA (2012c). *The HEAO-1 Satellite.*

NASA (2012d). *The Third Small Astronomy Satellite (SAS-3).*

NASA/ESA (Apr. 2012). *Orbit of James Webb Space Telescope.*

NIST. *NIST Electron Inelastic-Mean-Free-Path Database: Version 1.2*. http://www.nist.gov/srd/nist71.cfm.

Nakazawa, K. et al. (2010). "The hard x-ray imager onboard IXO". In: *Society of Photo-Optical Instrumentation Engineers (SPIE) Conference Series*. Vol. 7732. Society of Photo-Optical Instrumentation Engineers (SPIE) Conference Series.

Neff, S. et al. (Oct. 2011). "An activation experiment with laser-accelerated high-energy protons to optimize the graded-z shield design for the IXO/ATHENA satellite missions". In: *Nuclear Science Symposium and Medical Imaging Conference (NSS/MIC), 2011 IEEE*, pp. 1194 –1196.

Nilsson, S. (May 1956). "On the Coulomb effect for the internal bremsstrahlung accompanying beta decay". In: *JJournal*, pp. 467–77.

Ogilvie, K. and M. Desch (1997). "The WIND spacecraft and its early scientific results". In: *Advances in Space Research* 20.4–5. Results of the IASTP Program, pp. 559 –568.

Onega, R. J. (1969). "Radioactivity Calculations". In: *American Journal of Physics* 37.10, pp. 1019–1022.

Perez-Andujar, A. and L. Pibida (2004). "Performance of CdTe, HPGe and NaI(Tl) detectors for radioactivity measurements". In: *Applied Radiation and Isotopes* 60.1, pp. 41 –47.

Perkins, S. T., M. H. Chen, D. E. Cullen, and J. H. Hubbell (1991). *Tables and graphs of atomic subshell and relaxation data derived from the LLNL Evaluated Atomic Data Library (EADL), Z=1-100*. Livermore, CA: Lawrence Livermore Nat. Lab.

Pfeffermann, E. et al. (2004). "Lessons learned from the EPIC pn-CCD camera for future missions". In: *Mem. Soc. Astron. Italiana* 75, p. 555.

Phillips, G. W. and K. W. Marlow (1976). "Automatic analysis of gamma-ray spectra from germanium detectors". In: *Nuclear Instruments and Methods* 137.3, pp. 525 –536.

Pia, M. G. et al. (Dec. 2009). "PIXE Simulation With Geant4". In: *IEEE Transactions on Nuclear Science* 56, pp. 3614–3649.

Pia, M. G. et al. (Sept. 2011). "Evaluation of atomic electron binding energies for Monte Carlo particle transport". In: *ArXiv e-prints*. arXiv:1109.6079 [physics.comp-ph].

Pia, M. et al. (Dec. 2009). "PIXE Simulation With Geant4". In: *Nuclear Science, IEEE Transactions on* 56.6, pp. 3614 –3649.

Piccinotti, G. et al. (1982). "A complete X-ray sample of the high-latitude /absolute value of B greater than 20 deg/ sky from HEAO 1 A-2 - Log N-log S and luminosity functions". In: *The Astrophysical Journal* 253, pp. 485–503.

Pilbratt, G. L. et al. (July 2010). "Herschel Space Observatory. An ESA facility for far-infrared and submillimetre astronomy". In: *Astronomy and Astrophysics* 518, L1, p. L1. arXiv:1005.5331 [astro-ph.IM].

Porro, M. et al. (Nov. 2007). "ASTEROID: A new 64 channel ASIC for source follower based readout of the MIXS DEPFET arrays on BepiColombo". In: *Nuclear Science Symposium Conference Record, 2007. NSS '07. IEEE*. Vol. 3, pp. 2392 –2397.

Pressyanov, D. S. (2002). "Short solution of the radioactive decay chain equations". In: *American Journal of Physics* 70, pp. 444–445.

Ribon, F. et al. (2004). "Geant4 hadronic physics validation with LHC test-beam data: first conclusions". In:

Ribon, F. et al. (2010). *Status of Geant4 hadronic physics for the simulation of LHC experiments at the start of LHC physics program*.

Rose, M. E. (1955). *Beta-and gamma-ray spectroscopy*. Ed. by K. Sieghahn. North Holland Publishing Company, Amsterdam.

Rösel, F., H. M. Fries, K. Alder, and H. C. Pauli (1978). "Internal conversion coefficients for all atomic shells". In: *Atomic Data and Nuclear Data Tables* 21.2-3, pp. 91 –289.

Schartel, N. (2008). "XMM-Newton: The next decade". In: *Astronomische Nachrichten* 329.2, pp. 111–113.

Schartel, N. (2009). "Ten Years XMM-Newton: Scientific Achievements and Future Prospects". In: *Chandra's First Decade of Discovery*. Ed. by . D. S. S. Wolk A. Fruscione.

Schoenfelder, V. et al. (1993). "Instrument description and performance of the Imaging Gamma-Ray Telescope COMPTEL aboard the Compton Gamma-Ray Observatory". In: *APSJ* 86, pp. 657–692.

Schönfeld, E. and H. Janßen (Feb. 1996). "Evaluation of atomic shell data". In: *Nuclear Instruments and Methods in Physics Research A* 369, pp. 527–533.

Schreier, E. J., P. Gorenstein, and E. D. Feigelson (1982). "High-resolution X-ray observations of M87 - Nucleus, jet and radio halo". In: *The Astrophysical Journal* 261, pp. 42–50.

Schwartz, D. A. et al. (2000). "Absolute effective area of the Chandra high-resolution mirror assembly (HRMA)". In: *Society of Photo-Optical Instrumentation Engineers (SPIE) Conference Series*. Ed. by J. E. T. . B. Aschenbach. Vol. 4012. Society of Photo-Optical Instrumentation Engineers (SPIE) Conference Series, pp. 28–40.

Semkow, T. M. (2004). "Comment on "Algebraic approach to the radioactive decay equations," by L. Moral and A. F. Pacheco [Am. J. Phys. 71 (7), 684-686 (2003)]". In: *American Journal of Physics* 72, pp. 410–411.

Seo, E. S. et al. (1991). "Measurement of cosmic-ray proton and helium spectra during the 1987 solar minimum". In: *APJ* 378, pp. 763–772.

Shea, M. A. and D. F. Smart (1990). "A summary of major solar proton events". In: *Solar Physics* 127 (2). 10.1007/BF00152170, pp. 297–320.

Sonzogni, A. A. (2005). "NuDat 2.0: Nuclear Structure and Decay Data on the Internet". In: *AIP Conference Proceedings* 769.1. Ed. by R. C. Haight, M. B. Chadwick, T. Kawano, and P. Talou, pp. 574–577.

Stefanescu, A. et al. (2010). "The Wide Field Imager of the International X-ray Observatory". In: *Nuclear Instruments and Methods in Physics Research A* 624, pp. 533–539.

Stocke, J. T. et al. (1991). "The Einstein Observatory Extended Medium-Sensitivity Survey. II - The optical identifications". In: *The Astrophysical Journals* 76, pp. 813–874.

Strüder, L et al. (2000). "The European Photon Imaging Camera on XMM-Newton: The pn-CCD camera". In: *Astronomy and Astrophysics* 365, pp. 18–26.

Strüder, L. et al. (2003). "pnCCDs on XMM-Newton–42 months in orbit". In: *Nuclear Instruments and Methods in Physics Research Section A: Accelerators, Spectrometers, Detectors and Associated Equipment* 512.1-2. Proceedings of the 9th European Symposium on Semiconductor Detectors: New Developments on Radiation Detectors, pp. 386 –400.

Swank, J. H. et al. (1977). "Spectral evolution of a long X-ray burst". In: *The Astrophysical Journall* 212, pp. L73–L76.

Swartz, D. A., S. J. Wolk, and A. Fruscione (2010). "Chandra's first decade of discovery". In: *Proceedings of the National Academy of Sciences* 107.16, pp. 7127–7134.

Tanaka, Y., H. Inoue, and S. S. Holt (1994). "The X-ray astronomy satellite ASCA". In: *Publications of the Astronomical Society of Japan* 46, pp. L37–L41.

Tananbaum, H. D. et al. (Oct. 1999). "Constellation X-ray mission: implementation concept and science overview". In: *Society of Photo-Optical Instrumentation Engineers (SPIE) Conference Series*. Ed. by O. H. Siegmund and K. A. Flanagan. Vol. 3765. Society of Photo-Optical Instrumentation Engineers (SPIE) Conference Series, pp. 62–72.

Tenzer, C., E. Kendziorra, and A. Santangelo (Aug. 2008). "Monte-Carlo background simulations of present and future detectors in x-ray astronomy". In: *Society of Photo-Optical Instrumentation Engineers (SPIE) Conference Series*. Vol. 7011. Society of Photo-Optical Instrumentation Engineers (SPIE) Conference Series.

Tenzer, C. et al. (2006). "Monte Carlo simulations of Stacked X-ray Detectors as Designed for SIMBOL-X". In: *Space Telescopes and Instrumentation II: Ultraviolet to Gamma Ray*. Ed. by M. J. L. Turner and G. Hasinger. Vol. 6266.

Tenzer, C. et al. (2009). "Status of the Simbol-X Background Simulation Activities". In: *American Institute of Physics Conference Series*. Ed. by J. R. . P. Ferrando. Vol. 1126. American Institute of Physics Conference Series, pp. 75–78.

Toor, A. and F. D. Seward (1974). "The Crab Nebula as a calibration source for X-ray astronomy". In: *The Astronomical Journal* 79, pp. 995–999.

Treis, J et al. (2009a). "Pixel detectors for x-ray imaging spectroscopy in space". In: *Journal of Instrumentation* 4.03, P03012.

Treis, J. et al. (2009b). "The wide field imager for the International X-ray Observatory". In: *Society of Photo-Optical Instrumentation Engineers (SPIE) Conference Series*. Vol. 7435. Society of Photo-Optical Instrumentation Engineers (SPIE) Conference Series.

Trümper, J (1982). "The ROSAT mission". In: *Advances in Space Research* 2.4, pp. 241 –249.

Truscott, P. (2002). *Treatment of Radioactive Decay in Geant4*. Tech. rep. Qinetiq.

Tuli, J. (Dec. 2010). *Evaluated Nuclear Structure Data File (ENSDF)*.

Tuohy, I. R., W. M. Burton, and D. H. Clark (1982). "The peculiar X-ray morphology of the supernova remnant G292.0+1.8 - Evidence for an asymmetric supernova explosion". In: *The Astrophysical Journall* 260, pp. L65–L68.

Tuohy, I. and G. Garmire (1980). "Discovery of a compact X-ray source at the center of the supernova remnant RCW 103". In: *The Astrophysical Journall* 239, pp. L107–L110.

Turner, M. J. L. et al. (2001). "The European Photon Imaging Camera on XMM-Newton: The MOS cameras : The MOS cameras". In: *Astronomy and Astrophysics* 365, pp. L27–L35.

Tylka, A. J. et al. (Dec. 1997). "CREME96: a revision of the C_osmic R_ay E_ffects on M_icro-E_lectronics code". In: *IEEE Transactions on Nuclear Science* 44, pp. 2150–2160.

Venkataramaiah, P et al. (1985). "A simple relation for the Fermi function". In: *Journal of Physics G: Nuclear Physics* 11.3, p. 359.

Vidmar, T et al. (2008). "An intercomparison of Monte Carlo codes used in gamma-ray spectrometry". In: *Applied Radiation and Isotopes* 66.6–7. Proceedings of the 16th International Conference on Radionuclide Metrology and its Applications, pp. 764 –768.

Voges, W. et al. (1999). "The ROSAT all-sky survey bright source catalogue". In: *Astronomy and Astrophysics* 349, pp. 389–405.

Voges, W. et al. (2000). "ROSAT all-sky survey faint source catalogue." In: *International Astronomical Union Circulars* 7432, p. 1.

Vrtilek, S. D. et al. (1991). "The Einstein objective grating spectrometer survey of galactic binary X-ray sources". In: *The Astrophysical Journals* 76, pp. 1127–1167.

Weidenspointner, G et al. (2004). "MGGPOD: a Monte Carlo suite for modelling instrumental backgrounds in [gamma]-ray astronomy and its application to Wind/TGRS and INTEGRAL/SPI". In: *New Astronomy Reviews* 48.1-4. Astronomy with Radioactivities IV and Filling the Sensitivity Gap in MeV Astronomy, pp. 227 –230.

Weidenspointner, G., M. G. Pia, and A. Zoglauer (Oct. 2008). "Application of the Geant4 PIXE implementation for space missions new models for PIXE simulation with Geant4". In: *Nuclear Science Symposium Conference Record, 2008. NSS '08. IEEE*, pp. 2877 –2884.

Weisskopf, M. C. et al. (2002). "An Overview of the Performance and Scientific Results from the Chandra XâĂŘRay Observatory". In: *Publications of the Astronomical Society of the Pacific* 114.791, pp. 1–24.

Weisskopf, M. C. et al. (2010). "On Calibrations Using the Crab Nebula and Models of the Nebular X-Ray Emission". In: *The Astrophysical Journal* 713, pp. 912–919.

Weisskopf, M. C. et al. (2000). "Discovery of Spatial and Spectral Structure in the X-Ray Emission from the Crab Nebula". In: *The Astrophysical Journal Letters* 536.2, p. L81.

Wellisch, J. P. (2005). *Hadronic physics simulation engines for Geant4.* Tech. rep. Proceedings of The Monte Carlo Method: Versatility Unbounded in a Dynamic Computing World.

Wenninger, H., J. Stiewe, and H. Leutz (1968). "The 22Na positon spectrum". In: *Nuclear Physics A* 109.3, pp. 561 –576.

Wikipedia.org (May 2012). *FLOPS*.

Wilson, W. B. et al. (1995). "Recent development of the CINDER'90 transmutation code and data library for actinide transmutation studies". In: Global '95, Versailles (France).

Wolter, H. (1952). "Spiegelsysteme streifenden Einfalls als abbildende Optiken für Röntgenstrahlen". In: *Annalen der Physik* 445.1-2, pp. 94–114.

Wright, D. H. et al. (Oct. 2006). "Recent Developments and Validations in Geant4 Hadronic Physics". In: *Calorimetry in High Energy Physics: XII*. Ed. by S. R. Magill and R. Yoshida. Vol. 867. American Institute of Physics Conference Series, pp. 479–486.

Yuan, D. and W. Kernan (2007). "Explicit solutions for exit-only radioactive decay chains". In: *Journal of Applied Physics* 101.9, p. 094907.

Zhang, C. et al. (2006). "Development of DEPFET Macropixel detectors". In: *Nuclear Instruments and Methods in Physics Research Section A: Accelerators, Spectrometers, Detectors and Associated Equipment* 568.1. New Developments in Radiation Detectors, Proceedings of the 10th European Symposium on Semiconductor Detector, 10th European Symposium on Semiconductor Detectors, pp. 207 –216.
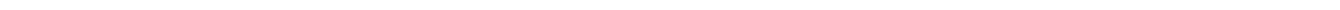
Publications and Conference Presentations

- S. Hauf. Background Simulations of the Wide Field Imager of the ATHENA X-ray Observatory. Poster at IEEE NSS MIC 2011, Valencia, Spain, October 2011.

- S. Hauf. R&D on the Geant4 Radioactive Decay Physics. Talk at 13th ICATPP, Villa Olmo, Como, Italy, October 2011.

- S. Hauf, M. Kuster, M. Grazia Pia, D. H. H. Hoffmann, P. Lang, S. Neff, A. Stefanescu, and L. Strüder. Background Simulations of the Wide Field Imager of the ATHENA X-Ray u Observatory. ArXiv e-prints, November 2011.

- M. Augelli, M. Begalli, M. Han, S. Hauf, C.-H. Kim, M. Kuster, M. Grazia Pia, L. Quintieri, P. Saracco, H. Seo, M. Sudhakar, G. Weidenspointner, and A. Zoglauer. Data libraries as a collaborative tool across Monte Carlo codes. ArXiv e-prints, December 2010.

- M. Augelli, M. Begalli, M. Han, S. Hauf, C. H. Kim, M. Kuster, M. G. Pia, P. Queiroz Filho, L. Quintieri, P. Saracco, H. Seo, D. Souza Santos, G. Weidenspointner, and A. Zoglauer. Environmental Adaptability and Mutants: Exploring New Concepts in Particle Transport for Multi-Scale Simulation. ArXiv e-prints, November 2010.

- M. Augelli, S. Hauf, M. Kuster, M. Han, C. H. Kim, M. G. Pia, L. Quintieri, H. Seo, P. Saracco, G. Weidenspointner, and A. Zoglauer. New Physics Data Libraries for Monte Carlo Transport. ArXiv e-prints, December 2010.

- S. Hauf. R&D on the Geant4 Radioactive Decay Physics. DPG Frühjahrstagung, Bonn, April 2010.

- S. Hauf. Simulationen zum IXO WFI Detektorhintergrund. DPG Frühjahrstagung, Bonn, April 2010.

- S. Hauf, M. Kuster, D. H. H. Hoffmann, Z. W. Bell, M. G. Pia, G. Weidenspointner, and A. Zoglauer. Radioactive decay simulation with Geant4: experimental benchmarks and developments for X-ray astronomy applications. ArXiv e-prints, December 2010.

- M. Augelli, M. Begalli, T. Evans, E. Gargioni, S. Hauf, C. H. Kim, M. Kuster, M. G. Pia, P. Queiroz Filho, L. Quintieri, P. Saracco, D. Souza Santos, G. Weidenspointner, and A. Zoglauer. Geant4-related R&D for new particle transport methods. ArXiv e-prints, Decem ber 2009.

- S. Hauf. Simulating and Optimizing the Simbol-X Detector Background. Geant4 Space Users Workshop, Madrid, Spain, May 2009.

- S. Hauf. Simulations on the SIMBOL-X Detector Background. Master's thesis, TU Darmstadt, March 2009.

- S. Hauf, M. Kuster, M. G. Pia, Z. Bell, U. Briel, R. Chipaux, D. H. H. Hoffmann, E. Kendziorra, P. Laurent, L. Strüder, C. Tenzer, G. Weidenspointer, and A. Zoglauer. Progress and Validation of Geant4 Based Radioactive Decay Simulation Using the Examples of Simbol-X and IXO. ArXiv e-prints, December 2009.

- C. Tenzer, U. Briel, A. Bulgarelli, R. Chipaux, A. Claret, G. Cusumano, E. Dell'Orto, V. Fioretti, L. Foschini, S. Hauf, E. Kendziorra, M. Kuster, P. Laurent, and A. Tiengo. Status of the Simbol-X Background Simulation Activities. AIP Conference Proceedings 2009.

Invited Talks
- S. Hauf. Simulating and optimizing the IXO detector background. Invited Talk, Max-Planck- Institute for Extraterrestrial Physics - MPE, Garching, Germany, November 2010.

Curriculum Vitae

Personal data

Name:	Steffen Hauf
Birthday:	30/11/1983
Birth place:	Darmstadt, DE
Nationality:	German
Address:	Zimmerstr. 9
	64283 Darmstadt
Parents:	Hans Jürgen Hauf
	Doris Hauf, nee Blümel

Education

April 2009	Master of Science in Physics, TU Darmstadt, DE
April 2007	Bachelor of Science in Physics, TU Darmstadt, DE
October 2004 – July 2005	Erasmus stipend, Bristol, UK
May 2003	German Abitur, majors in Physics and English, Gernsheim, DE

Professional experience

Spring 2008 – present	Ph.D. candidate TU Darmstadt
Summer 2005 – spring 2008	Student contact, foreign relations office, TU Darmstadt
Summer 2003 – spring 2004	Youth center worker, town of Stockstadt
Summer 2002 – present	Freelance programmer and designer

Acknowledgements